BARYON EXCHANGE REACTIONS IN π^-p SCATTERING AT 4 GeV/c

Daniel Lee Scharre

Lawrence Berkeley Laboratory
University of California
Berkeley, California 94720

1 April 1977

ABSTRACT

An experiment designed to study baryon exchange reactions in π^-p scattering at 4 GeV/c is discussed. The experiment was performed at the Bevatron and utilized a streamer chamber and a downstream spectrometer which consisted of two scintillation counter hodoscopes and a Cerenkov counter to define the fast proton trigger, and two planes of spark chambers to provide improved resolution on the forward track. Analysis of meson production in the reactions

$$\pi^-p \to pM^-$$

$$\pi^-p \to p\pi^-M^0$$

$$\pi^-p \to \Lambda^0M^0$$

is discussed for backward production of meson systems M^- and M^0. Differential cross sections and decay distributions (where applicable) for π^-, ρ^-, ρ^0, f^0, ω^0, η^0, and K^{*0} production are discussed. Upper limits for A_1^-, A_2^-, and B^- production are given. Baryon resonance production and limits on exotic meson production are briefly discussed.

Acknowledgments

I would like to thank my research adviser, Dr. Robert Ely, and my colleagues, Drs. George Gidal, Pier Oddone, and John Chapman, for their advice, encouragement, and most of all their tolerance and good humor. I am grateful to Peggy Fox for typing this lengthy manuscript. Finally, I would like to thank the scanning and measuring staff and other support personnel without whose efforts the successful completion of this work would have been impossible.

Work performed under the auspices of the U. S. Energy Research and Development Administration.

Table of Contents

List of Figures

List of Tables

I. Introduction

Due to the relatively small cross sections involved, very little data probing baryon exchange reactions is available in comparison to meson exchange reactions. In order to examine these baryon exchange reactions, an experiment involving $\pi^- p$ interactions at 4 GeV/c incident momentum was run. In this thesis, the experiment and the results of the analysis of the data from the experiment is discussed. The high sensitivity obtained in the experiment results from the utilization of a triggered streamer chamber and downstream spectrometer. The trigger required either a fast forward proton (evidence for baryon exchange) or a fast forward K^+ (not discussed in this thesis). The trigger also included events in which a fast forward Λ^0 decayed and produced a forward proton.

Approximately 380,000 frames (88 rolls of film) were exposed on each of three views taken of streamer chamber events. Of these, approximately 313,000 frames were determined to be acceptable for measurement. With a trigger cross section of about 1 mb, this provides an effective sensitivity of approximately 300 events/μb. The analysis described in this thesis is a result of the measurement of 64% of the 2-prong data, 76% of the 4-prong data, and 98% of the data in which a visible vee is observed to decay within the streamer chamber. 52000 2-prong events, 47000 4-prong events, and 6600 visible vee events have been measured.

The primary motivation for this experiment was to do a detailed analysis of baryon exchange reactions at a statistical level greater than was previously available. It was desired to do analysis involving all of the particles in the final state, thus a 4π detector was required. Topics of interest to be included in the analysis program relate to the resonances produced in such reactions, along with their differential cross

sections and decay angular distributions. The results of such an analysis provides information relevant to an understanding of the production mechanisms involved in baryon exchange reactions. A detailed discussion of baryon exchange reactions, with emphasis on the Regge exchange formalism, is given in Ch. II. Also included in that chapter is a review of experiments which have previously examined πp baryon exchange processes.

Within the overall framework of baryon exchange reactions, there are a few areas of special interest. The first concerns the existence of the A_1 meson. The observed A_1 enhancement has the quantum numbers $J^{PC} = 1^{++}$, a combination required by the quark model, but all previous experimental analyses have indicated that the A_1 enhancement is nonresonant. Theoretical models have indicated that baryon exchange processes might be better adapted to a search for resonant A_1 production than the diffractive processes in which the A_1 enhancement has been observed. A discussion of the A_1 and the relevance of baryon exchange to the problem is discussed in Ch. II.

The existence of exotic mesons (i.e., mesons which cannot be constructed from a quark-antiquark pair) is another open question for which there are theoretical reasons to expect that a search in baryon exchange reactions is more likely to yield positive results than a search in meson exchange reactions. This problem is also discussed in Ch. II.

In Ch. III is a description of the experimental layout. The streamer chamber, spectrometer, and trigger system are discussed. In Ch. IV is a discussion of the data handling and processing. Ch. V discusses the cross section calculation. This involves the determination of the beam flux, the

trigger acceptance, and inefficiencies involved with both the hardware and the data processing. Ch. VI describes the analysis of the following seven reactions:

$$\pi^- p \to \pi^- p \tag{1}$$

$$\pi^- p \to \pi^- p\pi^0 \tag{2}$$

$$\pi^- p \to K^- pK^0 \tag{3}$$

$$\pi^- p \to \pi^-\pi^-\pi^+ p \tag{4}$$

$$\pi^- p \to \pi^-\pi^-\pi^+ p\pi^0 \tag{5}$$

$$\pi^- p \to \pi^- K^- K^+ p \tag{6}$$

$$\pi^- p \to \pi^- K^+ \Lambda^0. \tag{7}$$

In reactions (1)-(6), the proton is required to be fast (i.e., it is responsible for the trigger). In reaction (7), the Λ^0 is required to be fast. Differential cross sections and decay distributions (where applicable) for π^-, ρ^-, ρ^0, f^0, ω^0, η^0, and K^{*0} production are discussed. Upper limits for A_1^-, A_2^-, and B^- production are given. Baryon resonance production and limits on exotic meson production are briefly discussed.

II. Historical and Theoretical Background

A. Backward Scattering

1. Regge exchange phenomenology

An interaction in which two particles in the initial state yields two particles in the final state can be kinematically described by two variables. A useful choice consists of two of the three relativistically invariant Mandelstam variables s, t, and u. Such an interaction is shown in Fig. 1, where a and b are the initial state particles and c and d are the final state particles. The Mandelstam variables are defined by the equations

$$s = (p_a + p_b)^2 = (p_c + p_d)^2$$

$$t = (p_c - p_a)^2 = (p_d - p_b)^2$$

$$u = (p_d - p_a)^2 = (p_c - p_b)^2,$$

where p_a, p_b, p_c, and p_d are the 4-momenta of particles a, b, c, and d respectively. These variables are not independent and

$$s + t + u = m_a^2 + m_b^2 + m_c^2 + m_d^2,$$

where m_a, m_b, m_c, and m_d are the masses of particles a, b, c, and d. In defining the variables t and u, an ambiguity exists in the particle assignments. Generally, particle c is chosen to be similar to particle a, and particle d similar to particle b. For instance, in the case of meson-baryon scattering, the specific case which will be dealt with in the remainder of this section, if the initial state meson is chosen to be particle a, then particle c will be the final state meson. Likewise, particles b and d are the baryons.

If a phenomenological Lagrangian for the strong interaction is assumed which allows only 3-point coupling at the vertices, three lowest order

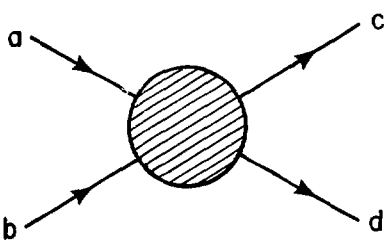

XBL 771-253

Fig. 1

Feynman diagrams can be drawn to represent the reaction

$$a + b \rightarrow c + d.$$

These are shown in Fig. 2. Fig. 2(a) represents s-channel (direct channel) scattering, where the square of the mass of the intermediate particle is given by s. The quantum numbers of this intermediate particle (charge, baryon number, hypercharge, and isospin) are those which are accessible to both the state comprised of a + b and the state comprised of c + d. In meson-baryon scattering, this intermediate particle is a baryon. For values of $\sqrt{s}$ not much larger than the masses involved, a reasonable interpretation of the data can be made within the framework of this model by describing the amplitude for the reaction in terms of a sum of a small number of terms. Each of these terms corresponds to an amplitude for a possible angular momentum state of the intermediate particle.

Fig. 2(b) represents t-channel (forward) exchange scattering where t is the square of the mass of the exchanged particle. Note that in the physical region, the intermediate particle is far from the mass shell. To overcome certain fundamental problems involved with the exchange of a single pole, it is necessary to use Reggeized exchanges. A Reggeized exchange consists essentially of contributions from an infinite series of poles, all possessing the same quantum numbers except spin, resulting in a description of the scattering amplitude in terms of a Regge trajectory and the residue along that trajectory. This trajectory relates α, the angular momentum, to t, and passes through the correct spin assignments when t is greater than zero and equal to the square of the mass of a particle on the trajectory. For t in the physical region and close to zero (compared to the masses involved), and s large, the Regge exchange model provides a good description of the scattering. The quantum numbers of the exchanged

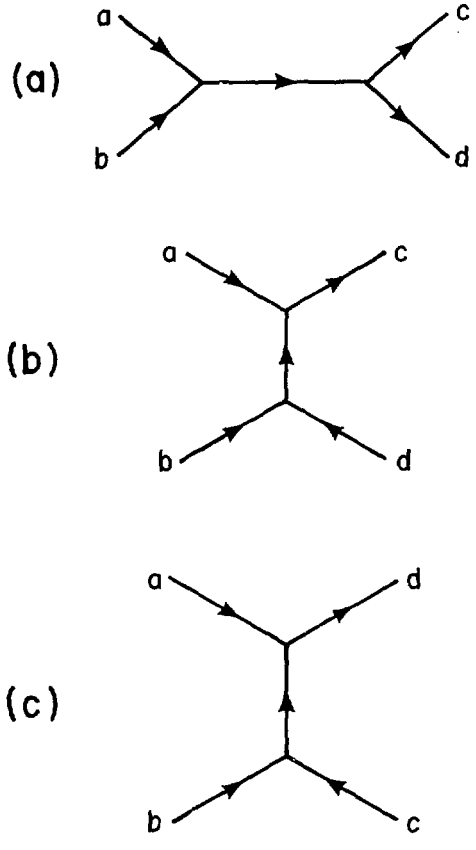

XBL 771-251

Fig. 2

trajectory are those which are accessible to the states $\bar{a} + c$ and $b + \bar{d}$, where the bar above the particle name identifies it as the charge conjugate particle. In the specific case of meson-baryon scattering, the exchanged trajectory is a meson trajectory.

Figure 2(c) represents u-channel (backward) exchange scattering where the square of the mass of the exchanged particle is given by u. Reggeization of the exchange leads to a description in terms of baryon trajectories. The quantum numbers of the exchanged trajectory are those which are accessible to $\bar{a} + d$ and $b + \bar{c}$. For s large and u close to zero, the u-channel exchange model provides a good description of the scattering amplitude. According to the tenets of duality, all three descriptions of the scattering amplitude are equally valid. However, for reactions in a kinematic region near the boundary of the physical region, at least one of the invariants is near its kinematic limit. It is generally easier to adequately describe the data in terms of an exchange in the channel in which the invariant is near its kinematic limit rather than in terms of one of the other channels.

The Regge exchange model establishes a framework for the description of reactions in terms of t-channel or u-channel exchange. This model predicts certain characteristics of the amplitudes and the relationships between different amplitudes. I will not go into the details of the model or its predictions here since an excellent discussion is given by Barger and Cline[1], but will only mention a few pertinent points relevant to this experiment.

The first point regards the functional dependence of the cross section with s. The amplitude for the reaction involving the exchange of a single

fermion trajectory is

$$A = \beta(\sqrt{u}) \frac{1}{\Gamma(\alpha(\sqrt{u})+1/2)} \frac{1+\tau e^{-i\pi(\alpha(\sqrt{u})-1/2)}}{\sin\pi(\alpha(\sqrt{u})-1/2)} \left(\frac{s-t}{2s_0}\right)^{\alpha(\sqrt{u})-1/2}, \qquad (8)$$

where

$\alpha(\sqrt{u})$ = Regge trajectory

$\beta(\sqrt{u})$ = residue of the trajectory

$\tau = (-1)^{J-1/2}$ = signature of the trajectory

J = spin of a fermion lying on the trajectory

s_0 = normalization energy.

Γ refers to the common gamma function. For each trajectory, there is a MacDowell reflection which has the same signature, but opposite parity, which must be included in the amplitude. It is obtained from the original amplitude by the transformations

$$\alpha(\sqrt{u}) \to \alpha(-\sqrt{u})$$

$$\beta(\sqrt{u}) \to -\beta(-\sqrt{u}).$$

The cross section is given by

$$\frac{d\sigma}{du} = \frac{1}{32\pi s} \sum_i |A_i|^2,$$

where only terms of first order in $\frac{1}{s}$ are kept, and where $\sum_i$ refers to the sum over different Regge amplitudes. If a single trajectory is assumed to dominate, the cross section near u=0 is given by

$$\frac{d\sigma}{du} \sim s^{\alpha(\sqrt{u})+\alpha(-\sqrt{u})-2}.$$

If the assumption is made that $\alpha(\sqrt{u})$ is a function only of $(\sqrt{u})^2$, then

$$\alpha(\sqrt{u}) = \alpha(-\sqrt{u})$$

and

$$\frac{d\sigma}{du} \sim s^{2\alpha(\sqrt{u})-2} \quad . \tag{9}$$

The functional dependence of the trajectories themselves will be discussed later.

Another point of interest is the functional dependence of the cross section with u. Since the residue factor, $\beta(\sqrt{u})$, is unknown, the u-dependence is not predicted by the theory. Experimentally, it has been found that peaking is exhibited in the backward direction (with the exception of those cases in which there is a possible zero at a production angle of 180^0 in the center of mass) which can be expressed functionally as

$$\frac{d\sigma}{du} \sim e^{bu}$$

or

$$\frac{d\sigma}{du} \sim e^{bu'}$$

at fixed s. The variable u' is given by

$$u' = u - u_{max},$$

and the slope parameter b is generally 3-4 GeV^{-2}. This same peaking is also seen in forward reactions which can be described in terms of Regge amplitudes (corresponding to meson trajectory exchange) similar to that given in Eq. (8). The backward cross sections are generally at least an order of magnitude smaller than the corresponding forward cross sections, and the slope smaller by at least a factor of two.

Another prediction of Regge theory is the existence of zeros in the scattering amplitude at certain values of u. The signature term

$$\zeta = \frac{1 + \tau\, e^{-i\pi(\alpha-1/2)}}{\sin \pi(\alpha - 1/2)}$$

from the amplitude given in Eq. (8) is seen to provide a pole at all values of α such that

$$(\alpha - 1/2)\ \imath = +\ 1.$$

The gamma function in the denominator of Eq. (8) provides a zero for all values of α such that

$$(\alpha + 1/2) < 0$$

but integral (i.e., $\alpha = -1/2, -3/2, \ldots$). The pole from the signature factor and this zero cancel at right signature points (called nonsense points since the angular momentum takes on an unphysical value), but there is only a zero at the wrong signature nonsense points. This dip structure at wrong signature nonsense points has been observed in some t-channel and u-channel reactions, but there is still some question regarding the validity of this interpretation.

2. Application to this experiment

The experiment described in this thesis is intended to explore the baryon exchange domain, s is not too small, nearly 9, and u from the incoming pion to the outgoing proton is close to 0. However, there are two complications which must be considered in the analysis. First, the experimental conditions are far from asymptotic ($s \to \infty$, $t \to \infty$). Thus, although it is expected that the main body of the data may be explained by u-channel baryon exchange processes, there will still be some background from direct channel reactions as will be shown later in this section.

There may also be tails due to t-channel exchange reactions. The other complication arises when inelastic reactions are considered. In elastic scattering, there are only two final state particles, and it is a fairly simple matter to draw a diagram, as in Fig. 2, to describe the reaction. When additional particles are added to the final state, problems arise as to which vertices the additional particles are to be assigned, and whether or not the reaction is more accurately described by a diagram with more than two vertices. Since it is not feasible to explore the question of diagrams with more than two vertices with the data available, the assumption will generally be made that all processes can be described by a single exchange between two vertices. The vertex assignment of the final state particles will be made on the basis of evidence of resonant production and backward peaking.

Restricting the discussion to the specific case of $\pi^- p$ scattering, various diagrams representing reactions of interest are shown in Fig. 3. If it is assumed that only the proton is produced forward (i.e., is coupled to the top or pion vertex) as in Fig. 3(a), isotopic spin invariance requires that the exchanged trajectory be a delta trajectory. M^- refers to the meson system recoiling from the proton, and could consist of a single π^- or any other negatively charged meson system with Y=0. If instead, it is assumed that a neutral or negatively charged baryon system (denoted by B^0 or B^-) is produced at the top vertex (e.g., $p\pi^-$ or $p\pi^-\pi^-$), exchanged nucleon and delta trajectories are allowed by isotopic spin invariance as shown in Fig. 3(b). Consideration of similar diagrams shows that producing any positively charged baryon system B^+ requires the exchanged trajectory to be a delta trajectory as in the case of a single forward proton. Production of a doubly charged baryon resonance at the

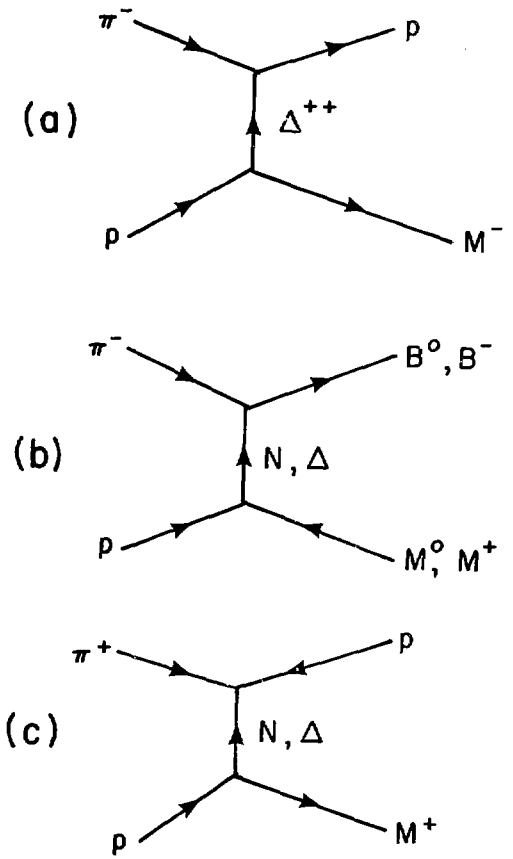

XBL 771-252

Fig. 3

top vertex (e.g., $\Delta^{++}(1232)$) is not allowed by any known exchange, but requires the exchange of a trajectory with exotic quantum numbers (I=5/2). For comparison, Fig. 3(c) shows a π^+ induced reaction yielding a forward proton. In this case, the exchange of both nucleon and delta trajectories is allowed, as opposed to the π^- induced reaction in which only delta exchange is allowed.

In considering nucleon exchange, the most obvious candidate for a trajectory is the one on which the N(939) lies, called the N_α trajectory. (An α trajectory contains a $J^P = \frac{1}{2}^+$ resonance, a β contains a $J^P = \frac{1}{2}^-$ resonance, a γ contains a $J^P = \frac{3}{2}^-$ resonance, and a δ contains a $J^P = \frac{3}{2}^+$ resonance.) The trajectory has the approximate functional form[1]

$$\alpha(\sqrt{u}) \simeq -\ 0.4 + 1.0\ (\sqrt{u})^2,$$

where u is in units of GeV^2. Regge lore has it that this trajectory (and the MacDowell reflected trajectory N_β) is the nucleon trajectory that contributes most to the amplitudes for the reactions being discussed. The principal delta trajectory is assumed to be the Δ_δ trajectory on which the $\Delta(1232)$ lies. The functional form of this trajectory is given by[1]

$$\alpha(\sqrt{u}) \simeq 0.15 + 0.9\ (\sqrt{u})^2.$$

The functional forms of these trajectories were obtained by analysis of the Chew-Frautschi plot.

Elastic $\pi^+ p$ and $\pi^- p$ scattering has been analyzed in terms of exchanges of these two trajectories, and gives quantitatively correct results.[2] Later analyses of charge exchange data, polarization data, and data from other reactions have shown that the simple model employing the exchange of these two Regge poles is not satisfactory. Various attempts to make a satisfactory fit to the data have included Regge cuts in addition to

poles, effects due to absorption, and other trajectories playing roles of secondary importance (for instance the N_γ trajectory on which the N(1520) lies). I will not discuss this in detail since it leads too far astray from the present discussion. It is mentioned only to show that the situation is not perfectly understood. An excellent description of various models which have been suggested and the problems encountered is given by Storrow and Winbow.[3]

In addition to those events in which a fast proton is directly produced, some events will occur in which a fast lambda is produced at the top vertex and decays into $p\pi^-$, the proton triggering the event. These events can be described in terms of u-channel exchange in which a baryon with Y=0 is exchanged. In Fig. 4 are shown two exchange diagrams for reactions in which a fast lambda is produced. If a Λ^0 is produced at the top vertex as in Fig. 4(a), only a Σ trajectory is allowed by isotopic spin invariance. The K^0 at the bottom vertex could be any neutral K^* system. If a Σ^- or any other negatively charged Y=0 baryon resonance is produced at the top vertex as in Fig. 4(b), both Λ and Σ trajectory exchange is allowed.

In this case, there are even more trajectories to consider since the octet has both Λ and Σ resonances. The important Λ trajectories[4] are postulated to be the Λ_α (on which the $\Lambda(1116)$ lies) and the Λ_γ (on which the $\Lambda(1520)$ lies). The important Σ trajectories[5] are postulated to be the Σ_α (on which the $\Sigma(1193)$ lies) and the Σ_γ (on which the $\Sigma(1670)$ lies).

The s dependence of baryon exchange reactions at fixed u can be determined from the functional form of the trajectory. For u near zero, the value of α for the various Y=0 and Y=1 trajectories varies between

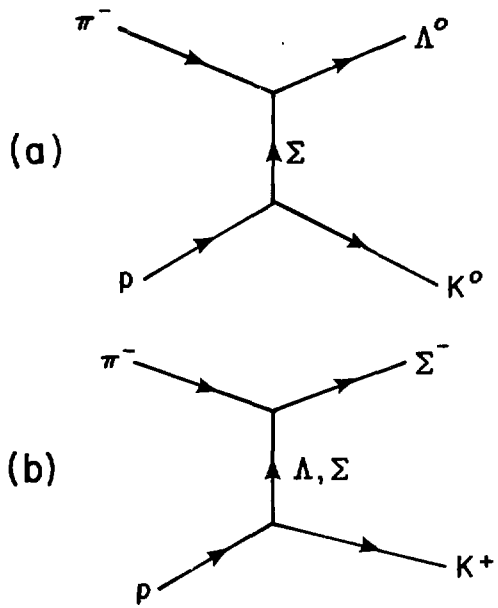

XBL 771-257

Fig. 4

approximately 0 and -1. Applying Eq. (9), this gives an s dependence at fixed u of

$$\frac{d\sigma}{du} \sim s^{-n},$$

where n is between 2 and 4.

3. Previous experiments

The backward scattering experiments on which the most data is available are those dealing with the elastic scattering of π^+ and π^- on p. In Table I are listed some recent backward elastic scattering experiments. In column I, π^- refers to π^-p elastic scattering, π^+ refers to π^+p elastic scattering, and π^0 refers to charge exchange scattering,

$$\pi^- p \rightarrow \pi^0 n,$$

which is included in the table for completeness.

In examining the results of these experiments, a number of important points become apparent. First, even though there is considerable backward peaking at momenta above approximately 3 GeV/c indicating the effects of u-channel exchange processes, there is still significant background due to direct chanel processes up to at least 5 GeV/c. In π^- backward elastic scattering, this is shown clearly in the data of Kormanyos et al.[7], where the differential cross section at 180^0 was measured for π^- lab momenta between 1.6 and 5.3 GeV/c. Considerable structure as a function of lab momentum is evident throughout the accessible momentum range. In particular, a peak due to direct channel production of the $\Lambda(2850)$ is seen near 4 GeV/c. A similar analysis of π^+p backward elastic differential cross section data between 2 and 6 GeV/c done by Baker et al.[16] shows similar structure due to s-channel effects, possibly all the way up to 6 GeV/c

Table I. $\pi^{\pm}p$ backward elastic and charge exchange scattering experiments.

Reaction	Lab momentum (GeV/c)	Reference
π^-	1.6 - 5.3	6, 7
π^-	2.15 - 6.0	8
π^-	2.3 - 6.0	9
π^-	2.38 - 3.00	10
π^-	2.77	11
π^-	3, 4	12
π^-	3.0,5.1	13
π^-	3.25	14
π^-	8, 16	15
π^+	2 - 6	16
π^+	5	17
π^-, π^+	2.85, 3.30, 3.55	18, 19, 20
π^-, π^+	3.55	21
π^-, π^+	4, 6, 8	22
π^-, π^+	4, 8	23
π^-, π^+	5.9 - 17.1	24, 25, 26
π^0	1.55 - 3.8	27
π^0	1.8 - 5.0	28
π^0	2 - 6	29
π^0	4, 6, 8, 11	30
π^0	5.9, 10.1, 13.8	31
π^0	6	32

momentum. As is expected, the same effect is seen in the charge exchange reaction.[28] Thus, it is expected that in this experiment at 4 GeV/c, some s-channel effects will be present, both in the elastic and inelastic reactions. Presumably, t-channel effects will also be present, particularly in the production of high mass resonances where the separation between u' = 0 and t' = 0 ($t' = t - t_{max}$) is not large.

The next observation of interest that can be made regards the relative cross sections for π^+ and π^- backward elastic scattering. The π^+ elastic differential cross section at 180^0 is considerably larger than the π^- elastic differential cross section at 180^0. Various experiments in which the two cross sections are compared are listed in Table II, along with the differential cross section ratios which were determined. It is seen that the π^+ elastic differential cross section is at least 5 times larger than the π^- elastic differential cross section at 180^0. This difference can be understood by considering the u-channel isotopic spin relations for the two amplitudes:

$$f(\pi^-) = f(\Delta)$$

$$f(\pi^+) = \frac{1}{3}[f(\Delta) + 2f(N)],$$

where $f(\pi^-)$ and $f(\pi^+)$ are the amplitudes for π^- and π^+ backward elastic scattering and $f(\Delta)$ and $f(N)$ are the amplitudes for u-channel Δ_δ exchange and N_α exchange. It is assumed that no other trajectories contribute to the reactions. The π^- reaction requires delta exchange as stated earlier, and the π^+ reaction is dominated by nucleon exchange. Thus, the data indicate that for scattering at 180^0 the nucleon coupling to the πN vertex is considerably stronger than the delta coupling at that vertex.

Another obvious difference between the two differential cross sections

Table II. Comparison of $\pi^+ p$ and $\pi^- p$ elastic differential cross sections at 180^o.

Lab momentum (GeV/c)	$\frac{d\sigma}{d\Omega}_{+} / \frac{d\sigma}{d\Omega}_{-}$ at 180^o	Reference
3.30	6.1 ± 1.4	20
3.55	8.0 ± 1.1	20
3.55	7.4 ± 1.0	21
4, 8	∿ 5	23
5.9, 9.9, 13.7	∿ 4	24, 25, 26

is that the π^- cross section falls off slowly with u,

$$\frac{d\sigma}{du} \sim e^{4u},$$

whereas the π^+ cross section falls off more steeply with u and has a dip at u $\approx$ -0.15 GeV^2, at which point the π^+ cross section is considerably smaller than the π^- cross section. This dip has been explained in terms of a wrong signature nonsense zero in the N_{α} amplitude at this point on the trajectory. The validity of this interpretation of the dip has since come under fire due to the lack of corroborating evidence.

Some analysis of backward inelastic reactions has also been done. Listed in Table III are some relevant reactions induced by π^- and π^+ on nucleons. I will not discuss the results in detail here, but will make comparisons with the relevant reactions in Ch. VI where the analysis of this experiment is discussed. Note that the listing of a reaction in Table III does not necessarily imply observation of that reaction. Often only upper limits on cross sections are quoted.

A few points regarding the results of some of these inelastic experiments which are relevant to the previous discussion of the elastic experiments will be mentioned. In the backward ρ production experiments of Hagopian et al.[37], Baton et al.[11], and Johnson et al.[39], the backward cross section for the reaction

$$\pi^- p \rightarrow p\rho^-$$

is smaller than that for the reaction

$$\pi^- p \rightarrow n\rho^0;$$

by a factor of approximately 4 at 4 GeV/c.[39] This is consistent with the inference made from the elastic differential cross section data that delta exchange is suppressed relative to nucleon exchange. Another point

Table III. $\pi^{\pm}N$ backward inelastic scattering experiments.

Reaction	Lab momentum (GeV/c)	Reference
$\pi^- p \to p\rho^-$	1.80 - 3.25	14, 33
$\pi^- p \to n\eta^0$	2 - 6	34
$\pi^- p \to \Delta^+\pi^-$, $\Delta^-\pi^+$	2.15 - 6	35, 36
$\pi^- p \to p\rho^-$, $n\rho^0$	2.3	37
$\pi^- p \to p\rho^-$, pA_1^-, pA_2^-, pB	2.45	38
$\pi^- p \to p\rho^-$, $n\rho^0$, $\Delta^-\pi^+$	2.77	11
$\pi^- p \to p\rho^-$, $n\rho^0$, $\Delta^-\pi^+$, $N^{*+}(1700)\pi^-$	4	39
$\pi^- p \to n\eta^0$	5.9, 10.1, 13.8	31
$\pi^- p \to p\rho^-$, pA_1^-, pA_2^-	8, 16	40, 41
$\pi^- p \to pA_1^-$, pA_2^-, $p\pi^-\rho^0$, $p\pi^- f^0$	8	42, 43
$\pi^+ p \to p\rho^+$, pB^+, $\Delta^{++}\pi^0$, $\Delta^{++}\eta^0$, $\Delta^{++}\rho^0$, $\Delta^{++}\omega^0$, $N^{*+}(1600)\pi^+$	5	17, 44
$\pi^+ p \to p\rho^+$	5.2	45
$\pi^+ n \to p\rho^0$, $p\omega^0$	2.15	46
$\pi^+ n \to p\rho^0$, pf^0, $p\omega^0$	4	47
$\pi^+ n \to p\rho^0$, pf^0	6	48

relevant to ρ production which is particularly evident in the reaction

$$\pi^+ p \rightarrow p\rho^+$$

done at 5.2 GeV/c by Carlson et al.[45] is that there is no dip in the u distribution as there is for backward $\pi^+ p$ elastic scattering, but instead the differential cross section falls off like e^{3u}. Nucleon exchange is expected to dominate both of these reactions, thus it appears that a dip at the wrong signature nonsense point on the nucleon trajectory cannot always be expected.

The dominance of nucleon exchange over delta exchange is again supported by comparison of the reactions

$$\pi^- p \rightarrow \Delta^- \pi^+$$

and

$$\pi^- p \rightarrow \Delta^+ \pi^-$$

in the backward region. In various experiments [35, 11, 39] which measured the cross sections for these two reactions, Δ^- production (which can be produced by nucleon exchange) was found to have a larger cross section than Δ^+ production (which requires delta exchange).

Since forward Λ^0 production will be briefly examined in this thesis, a list of previous experiments relevant to Λ^0 production is given. In Table IV are listed those reactions in which a π^- beam incident on a proton target produces a forward Λ^0.

B. A_1 Production

The lack of concrete evidence for the existence of the A_1 meson has long been a problem for the standard quark model. The A_1 meson is the axial vector meson ($J^P = 1^+$) with quantum numbers I=1 and C=+1. The reason that

Table IV. Λ^0 production in π^-p scattering experiments.

Reaction	Lab momentum (GeV/c)	Reference
$\pi^-p \to \Lambda^0K^0$	4, 6.2	49
$\pi^-p \to \Lambda^0K^0$	5	50
$\pi^-p \to \Lambda^0K^0$	5, 7, 12	51
$\pi^-p \to \Lambda^0K^0$, $\Lambda^0K^{*0}(890)$	8, 10.7	52
$\pi^-p \to \Lambda^0K^0$, $\Lambda^0K^{*0}(890)$	8	53

the nonexistence of the A_1 poses such a problem is that it is required by the standard quark model with SU(3). (Inclusion of SU(4) at this time adds an unnecessary complication.) The basic quark model prescribes that the allowed meson multiplets are those of a quark-antiquark system (i.e., a spin $\frac{1}{2}$ fermion-antifermion system). Thus, the following relationships between the quark angular momentum states and the quantum numbers of the resonance can be established:

$$\bar{J} = \bar{L} + \bar{S} \tag{10}$$

$$P = (-1)^{L+1} \tag{11}$$

$$C = (-1)^{L+S}, \tag{12}$$

where $\bar{L}$ is the orbital angular momentum of the quark-antiquark system, $\bar{S}$ is the spin of the quark-antiquark system, and $\bar{J}$ is the spin of the resonant state. Note that S is either 0 or 1. In addition, the multiplet structure of the meson states (see discussion in following section) requires that each meson be a member of a nonet (an octet plus a singlet), all members having the same quantum numbers.

If the states with L=0 and S=0 are considered, $J^{PC} = 0^{-+}$. This is the well established nonet which contains the π. With S=1, $J^{PC}=1^{--}$. This nonet, containing the ρ, is also well established. For states with L=1, the situation is not as encouraging. For S=0, $J^{PC} = 1^{+-}$. The B meson is the I=1 member of the octet. The $I=\frac{1}{2}$ member, generally referred to as Q_B, is not well established and will be discussed later. There is no evidence for the isoscalar members. For S=1, there are three values of J which can be produced by vector angular momentum addition; J=0,1, and 2. The $J^{PC} = 2^{++}$ nonet is well established with the A_2 as the isovector member. The $J^{PC} = 1^{++}$ nonet is the multiplet in which the A_1 falls.

There are candidates for the other mesons in the nonet, but none are conclusively established. Finally, there is the $J^{PC} = 0^{++}$ octet which is composed of states which are difficult to establish completely as resonances. The situation for the L=1 mesons is shown in Table V where the completely established states are underlined. Since some of the states do exist, it is expected that all of them should exist, and hence the desire to prove the existence of the A_1.

In diffractive processes such as

$$\pi^- N \rightarrow (\pi\pi\pi)^- N,$$

a wide enhancement peaked near 1.10 GeV in the 3π invariant mass distribution has been observed which decays primarily into $\rho\pi$. This enhancement has been designated the A_1, although the correspondence between this enhancement and the resonant state referred to earlier as the A_1 has certainly not been established. Typical of reactions in which there was early observation of this enhancement was the reaction[54]

$$\pi^+ p \rightarrow \pi^-\pi^+\pi^+ p$$

at 3.65 Gev/c incident π^+ momentum where an enhancement covering the region of both the A_1^+ and the A_2^+ (not resolved) was seen to decay into $\rho^0\pi^+$. A similar experiment[55] examining the same reaction at 4 GeV/c incident momentum did resolve the two peaks and observed an A_1^+ with mass at approximately 1.08 GeV and width of about 0.08 GeV. The A_1 enhancement has been seen in many subsequent experiments[56], generally at a mass near 1.10 GeV but with widths varying from under 0.05 GeV to over 0.30 GeV.

As more statistics became available in reactions of this type, it became possible to do partial wave analyses[57] of the data. This type of

Table V. L=1 quark model resonances.

S	J^{PC}	I=1	I=1/2	I=0	
0	1^{+-}	B	Q_B	-	-
1	0^{++}	δ	κ	ϵ	S^*
1	1^{++}	A_1	Q_A	D	E
1	2^{++}	A_2	K^{**}	f	f'

Table VI. Comparison of differential cross section slope parameters in missing mass experiment of Anderson et al. (Refs. 15, 40, 41).

Reaction	Slope parameter
$\pi^- p \to p\pi^-$	4.23 ± 0.40
$\pi^- p \to p\rho^-$	4.44 ± 0.60
$\pi^- p \to pA_1^-$	16.9 ± 6.8
$\pi^- p \to pA_2^-$	4.00 ± 1.32

analysis made possible the determination of not only the magnitudes of the amplitudes of various spin states, but also the relative phases between the amplitudes. Since the number of parameters involved in such an analysis is large, it is necessary to make some simplifying assumptions in the analysis. First, factorization is assumed. The NN vertex is assumed to be independent of the π - 3π vertex. The interaction is assumed to be described by a diagram with two vertices and there are no pions at the nucleon vertex. Secondly, it is assumed that the 3π decay proceeds through isobars into $\rho\pi$, $\epsilon\pi$, and $f\pi$, and then the dipion system independently decays. Thirdly, the assumption is generally made that the production amplitude of the 3π system does not depend on the manner in which the 3π system decays. Fourthly, there is an upper limit placed on the angular momentum states allowed. Finally, the effects of subchannel unitarity are generally ignored (though some recent analyses include a unitarity requirement). After establishing the amplitudes to be included in the analysis, a maximum likelihood fit is made to either the amplitudes or the density matrix elements of the 3π system.

Due to the many assumptions and approximations made, the validity of these analyses is not totally convincing. Nonetheless, some of the results are interesting. One such isobar analysis was done[58] with data from reaction (4),

$$\pi^- p \rightarrow \pi^-\pi^-\pi^+ p, \tag{4}$$

in the forward region, in which data from a number of experiments with beam momentum between 5 and 25 GeV/c was utilized. The analysis showed a large $J^P = 1^+$ signal that decayed via S wave to $\rho\pi$, corresponding to the A_1 peak. Although it is not possible to obtain the absolute phase of an amplitude, it

is possible to obtain the phase relative to another amplitude which is presumed to be slowly varying. No phase variation of the 1^+ amplitude, as would be expected for a Breit-Wigner resonance, was observed. In order to demonstrate that this method of analysis will display the correct amplitude variation for at least some Breit-Wigner resonances, a partial wave analysis of a portion of the same data was done in the region of the A_2[59]. The A_2 showed a characteristic Breit-Wigner amplitude line shape in the 2^+ amplitude which decayed via D wave into $\rho\pi$. The phase of this amplitude relative to a presumably slowly varying amplitude varied in a manner consistent with a Breit-Wigner amplitude. The fact that the A_2 amplitude behaves as is expected lends credibility to the results of the A_1 analysis. Other similar analyses[60,61] of 3π diffractive data showed A_2 signals which displayed Breit-Wigner resonance behavior, whereas the A_1 showed a peak at approximately 1.10 GeV with a width of approximately 0.30 GeV but no phase variation. Thus, it appears that only a small part, if any, of the A_1 enhancement corresponds to a $J^P = 1^+$ resonance.

An alternative explanation for the A_1 enhancement was proposed by Deck[62] before the nonresonant behavior of the A_1 was established by partial wave analysis. He interpreted the enhancement as a kinematical effect. He assumed that the reaction associated with the observed $\rho\pi$ peak proceeded principally via peripheral collisions which are dominated by the one-pion exchange diagram given in Fig. 5(a). An improvement on this model was made by replacing the one-pion exchange amplitude by Reggeized amplitudes.[63] The diagrams associated with the Reggeized Deck model are shown in Figs. 5(b) and (c), where it is seen that the amplitude is diffractive in nature. A similar model was utilized by Ascoli[64] to generate Monte Carlo events which were analyzed by his partial wave analysis program and compared with the

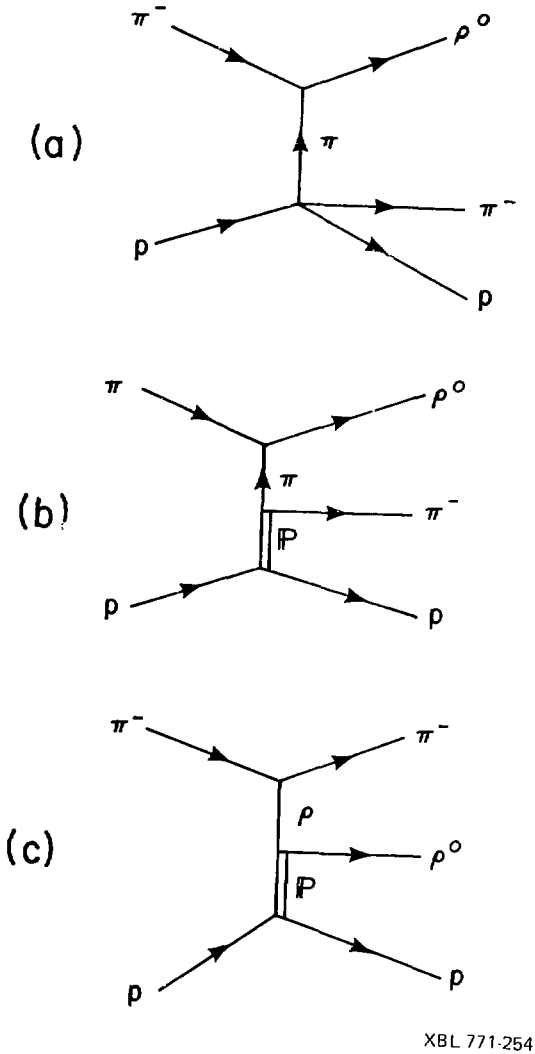

XBL 771-254

Fig. 5

experimental data. The amplitudes resulting from the Monte Carlo simulation of the Deck amplitudes compared well with the data, which confirms the relevance of the Deck model in explaining the A_1 enhancement.

Various models have been proposed which include a resonant 1^+ amplitude in addition to the Deck amplitude in an effort to comply with the quark model. It is possible to construct amplitudes which result in a lack of phase variation of the total amplitude. One such model[65] predicts a resonant A_1 with a mass of 1.30 GeV and a width of 0.24 GeV which fits the data well.

Many of the problems in isolating the resonant A_1 disappear if reactions are examined in which the Deck mechanism is inoperative. Examples of such reactions are charge exchange reactions, hypercharge exchange reactions, and baryon exchange reactions. One charge exchange reaction which has undergone partial wave analysis[66] of the 3π state is

$$\pi^+ n \to \pi^+\pi^+\pi^- p$$

at 4 Gev/c. Significant η^0, ω^0, and A_2^0 production was seen, but there was no evidence for production of a peak in the 1^+ partial wave. However, it is not required that the resonant A_1 appear at the same mass as the Deck enhancement, and an A_1 above 1.30 GeV in mass would not be observed in this experiment. Another reaction in which the 3π final state was analyzed[67,68] was

$$\pi^+ p \to \pi^+\pi^+\pi^- A_2^{++}$$

at 7 GeV/c. Again there was no evidence for an A_1. An A_2 cross section of 53 ± 7 μb for $|t| < 0.8$ GeV^2 and $1.16 \leq M_{A_2} \leq 1.28$ GeV was measured. For an A_1 satisfying the same conditions, an upper limit of 2 μb was set for a resonance of width less than or equal to 0.15 GeV.

A few baryon exchange reactions have been analyzed for evidence of A_1 production as mentioned in the previous section. Evidence for backward A_1 production is claimed in a 16 GeV/c missing mass experiment done by Anderson et al.[41] in which a fast forward proton defined the trigger. However, since the peak was only seen in a missing mass spectrum, it was impossible to determine the spin and parity of the state, or even the decay mode. The mass peaks at 1.115 ± 0.020 GeV and the enhancement has a width of $0.098 \begin{smallmatrix} + 0.045 \\ - 0.020 \end{smallmatrix}$ GeV. The total cross section extrapolated to the entire backward hemisphere is $\sigma_T = 0.35 \begin{smallmatrix} + 0.87 \\ - 0.28 \end{smallmatrix}$ μb. The differential cross section as a function of u is parameterized as

$$\frac{d\sigma}{du} \sim e^{(16.9 \pm 6.8)\, u'}.$$

The value of the slope parameter is very large for a baryon exchange reaction. A comparison with the slope parameters of other reactions observed in the same experiment is shown in Table VI. The small cross section (just over one standard deviation in significance) and the abnormal u distribution make the interpretation of the enchancement as the A_1 questionable. These inconclusive results provided part of the motivation for later baryon exchange experiments (including this one).

Another experiment at 8 GeV/c in which reaction (4) was analyzed[42,43] utilized a streamer chamber to observe the final state resulting from a fast proton trigger. No evidence for A_1^- production was seen, and a 95% confidence level upper limit of 0.93 μb was set. If it is assumed that delta exchange cross sections fall off as $S^{-2.5}$ as predicted by Regge theory, then this upper limit, when extrapolated to 16 GeV/c, is smaller than the cross section observed by Anderson et al.

The results of the various experiments attempting to observe A_1 production indicate that either the A_1 does not exist or it does not couple as strongly to pions and baryons as might be expected. This is in contradiction to theoretical predictions that the A_1 should be produced with a cross section, both in meson exchange reactions and baryon exchange reactions, comparable to cross sections of other meson resonances such as the ρ and the A_2.[69,70]

Observation of other members belonging to the 1^+ multiplet would further strengthen the requirement of the existence of the A_1. The strange member of the octet is commonly associated with the Q enhancement observed in the reactions

$$K^- p \to (K\pi\pi)^- p.$$

The enhancement is very similar to the 3π enhancement and can be explained in terms of a Deck diffractive model. A recent experiment[71,72] at 13 GeV/c claims two resonances with relative phase variations consistent with Breit-Wigner amplitudes in the 1^+ partial wave. The Q_1 at 1.30 GeV has a width of 0.3 GeV and decays primarily into ρK. The Q_2 at 1.40 GeV has a width of 0.16 GeV and decays primarily into $K^*\pi$. These two states are presumably mixtures of the strange partners of the A_1 and the B, the Q_A and Q_B states. However, a recent analysis involving a unitary Deck model with coupled ρK and $K^*\pi$ channels[73] gives a satisfactory description of the experimental data with only one resonance, the Q_B. Thus, the situation with the Q states remains the same.

With the discovery of a new quark flavor (charm), the opportunity to observe new members of the 1^+ multiplet (now a 15-plet plus a singlet rather than an octet plus a singlet) arises. Of particular interest are those intermediate states produced by radiative decays of the ψ'.[74] The

three states $\chi(3415)$, $\chi(3500)$, and $\chi(3550)$, have properties consistent with spin assignments of $J^P = 0^+$, 1^+, and 2^+ and I=0. If the $\chi(3500)$ can be conclusively established as the SU(4) partner of the A_1, the problem of the A_1 becomes even more severe.

C. Exotic Meson Production

1. Quark model and duality

An exotic elementary particle is defined to be a particle which cannot fit into the conventional quark model in which mesons consist of a $q\bar{q}$ pair (q being the generic designation used to specify any one of the four quarks), and baryons consist of three quarks, qqq. As will be seen shortly, the production of exotic mesons is particularly pertinent to this experiment, so the discussion will be restricted to mesons for the remainder of this section.

According to the quark model, the three quarks comprise a triplet in the SU(3) group theoretical description. (Despite the fact that SU(3) has now been apparently superseded by SU(4), SU(3) still provides a valid description in the limit that charm is not excited. In addition, the SU(3) multiplet scheme is more familiar and easier to deal with.) Thus, a $q\bar{q}$ pair can be combined in a manner which can be described in terms of multiplication of two elements of the group

$$3 \otimes \bar{3} = 1 + 8,$$

where 3, 1, and 8 represent irreducible representations of SU(3) and the bar above a representation indicates the conjugate representation. Hence, the mesons produced by a $q\bar{q}$ pair must be members of either octets or singlets. All well established mesons can be described as members of either a singlet or an octet.

If an exotic is not composed of a $q\bar{q}$ pair, the next most complicated system is two pairs. (A system containing no quarks but only gluons would be exotic, but there would be no way of determining its exotic nature by its quantum numbers.) In this case, the allowed irreducible representations are given by

$$(1 + 8) \times (1 + 8) = 1 + 1 + 8 + 8 + 8 + 8 + 10 + \overline{10} + 27.$$

Thus, exotic mesons are expected to occupy higher order multiplets than ordinary mesons. These higher order multiplets contain states with isospin and hypercharge which do not occur in singlet or octet representations. For instance, members of the 27-plet include a state with I=2 and a state with Y=2. One can imagine exotic systems composed of three or more pairs of quarks which would produce even larger multiplets.

Note that some exotic mesons are members of singlets and octets. In such an instance, there is no way to differentiate exotic mesons from ordinary mesons by the SU(3) representation, but there are some combinations of quantum numbers which are allowed for exotic mesons but not for ordinary mesons. Mesons with these particular combinations of quantum numbers are called "abnormal charge conjugation" states since the J^{PC} quantum number combination is not allowed for a $q\bar{q}$ pair. Eqs. (10)-(12) relate the meson quantum numbers to the $q\bar{q}$ angular momentum state. Combining a quark and an antiquark in all possible ways, it is impossible to produce natural parity states (i.e., states with $P = (-1)^J$) with $CP = -1$ and the $J^P = 0^-$ state with $CP = +1$. Thus, mesons with quantum numbers $J^{PC} = 0^{+-}$, 1^{-+}, 2^{+-},... are not allowed and hence can only be produced by exotic quark combinations. No mesons with these exotic quantum number combinations have yet been established.

The pertinence of the discussion on exotic mesons to this experiment lies with the fact that there are theoretical reasons for expecting exotic meson production in baryon exchange reactions rather than in meson exchange reactions. In fact, duality[75, 76, 77] and the absence of exotics are untenable assumptions for baryon-antibaryon scattering.[78] If the duality diagram for baryon-antibaryon scattering is considered (see Fig. 6), it is seen that if the s-channel intermediate state is required to be a $q\bar{q}$ system, then there are two $q\bar{q}$ pairs (an exotic system) in the t-channel intermediate state. Thus, ordinary s-channel resonances are seen to be dual to exotic resonances in the t-channel. On the other hand, there is no theoretical requirement that exotics must couple to a meson-meson vertex as they do to a baryon-antibaryon vertex. In fact, the approximate exchange degeneracy of the ordinary meson trajectories (ρ, f, ω, and A_2) requires that the coupling of the ordinary mesons to exotic mesons is small.[1,79] Therefore, the best place to look for the production of low mass (less than $B\bar{B}$ threshold) exotic mesons is at the baryon-antibaryon vertex in a baryon exchange reaction,[80] as shown in Fig. 7. The produced exotic meson resonances, due to their small couplings to ordinary mesons, will have narrow widths, with the mass of the lowest expected to be above approximately 1 GeV but below 2 GeV. Various theoretical estimates have placed the exotic meson production cross sections in such backward scattering experiments as comparable to the cross sections for ordinary vector or tensor meson production.[81]

2. Experimental evidence

Evidence for exotic mesons can manifest itself in two ways, either as evidence of exotic exchange in the t-channel, or directly in a production

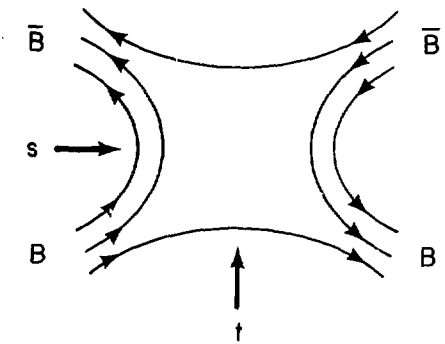

Fig. 6

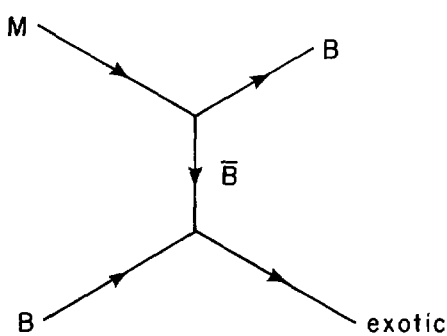

XBL 773-7940

Fig. 7

experiment. In the first case, reactions are analyzed in which the quantum numbers exchanged in the t-channel are exotic. If forward peaking is displayed, this is taken as evidence for the exchange of an exotic. There is ample evidence for this type of behavior. Some typical reactions are

$$\pi^- p \rightarrow K^+ \Sigma^-$$

and

$$\pi^- p \rightarrow K^+ Y^{*-},$$

in which a forward K^+ peak is observed.[82,83,84] The quantum numbers of the exchanged particle (if it is assumed to be a single particle) are Y=1 and I=2 which makes it exotic. (Note that this reaction is accessible in this experiment since K^+ triggers were accepted. However, the analysis of these reactions is not discussed in this thesis.) Also requiring exotic meson exchange are reactions such as

$$\bar{p}p \rightarrow \bar{\Sigma}^- \Sigma^- \quad 85$$

and

$$pn \rightarrow \Delta^- \Delta^{++} \quad 86$$

which have also been observed with forward peaking.

Aside from the obvious explanation of the exchange of a single Regge trajectory corresponding to an exotic meson, there are other possible explanations for this phenomenon. It is well known that at low energies, scattering processes can be well explained by s-channel diagrams. The reactions generally show both forward and backward peaks. (The reason for this is clear when the reaction is described in terms of a Legendre polynomial partial wave expansion.) Calculations based on such an s-channel resonance model predict a very steep falloff of the cross section with s.[87]

The data does show a very steep falloff (as large as s^{-10}) for most of these reactions for $s \lesssim 10$ GeV^2, and thus an explanation is available which does not rely on the existence of exotic mesons. Other kinematic interpretations have also been invoked to explain the peaking in some reactions.[88]

For those reactions in which data is available at higher energies ($s > 10$ GeV^2), the falloff of the cross section with energy is not as steep as at lower energies,

$$\frac{d\sigma}{dt} \sim s^{-4}.$$

It is still possible to explain these results by a process which does not involve the exchange of an exotic Regge trajectory, but rather the exchange of two ordinary Regge poles (a Regge cut). Differentiating between these two models may not be very simple since the cross section dependence on s is very similar for the two models. For a single Regge pole exchange (see Eq. (9))

$$\frac{d\sigma}{dt} \sim s^{2\alpha-2}.$$

It is expected that $\alpha(0)$ for an exotic is less than 0 but probably on the order of -0.5. For a Regge cut

$$\frac{d\sigma}{dt} \sim s^{2\alpha-2} (\ln(s))^{-2},$$

where

$$\alpha(0) = \alpha_1(0) + \alpha_2(0) - 1$$

and α_1 and α_2 are the trajectories of the two Regge poles being exchanged. Inserting typical values for the intercepts of the ordinary meson trajectories gives an s dependence very similar to that of exotic exchange except for the $\ln(s)$ dependence which is extremely difficult to observe over the narrow range of energy for which data can be expected to exist in

the near future. Thus, the evidence for exchange of a single exotic trajectory is far from conclusive.

Many experiments have looked for direct production of exotic mesons, but to date, none have been found. Most experiments in which exotic searches have been made are meson exchange reactions such as

$$\pi^+ p \rightarrow \pi^+ \pi^+ n$$

or

$$\pi^- n \rightarrow \pi^- \pi^- p$$

where structure in the $\pi^+\pi^+$ or $\pi^-\pi^-$ invariant mass is searched for. Some results of exotic searches are summarized in the review articles by Cohen[89] and Brabson.[90] Typical upper limits of 1-10 μb were presented for forward exotic meson production. As discussed earlier, baryon exchange reactions are more suitable for exotic searches, but the experimental effort has not been as great. An experiment utilizing the SLAC 15 in. rapid cycling bubble chamber at 8.4 GeV/c has searched for exotic production[91] in the reaction

$$\pi^+ p \rightarrow X^{++} n,$$

where the neutron is forward and the decay modes of X^{++} which were analyzed were $\pi^+\pi^+$, $\pi^+\pi^+\pi^+\pi^-$, $\pi^+\pi^+\pi^+\pi^+\pi^-\pi^-$, and $\bar{p}\, p\, \pi^+\pi^+$. No evidence for a resonance peak was seen in any channel, and a 4σ upper limit of approximately 1μb was set for the $\pi^+\pi^+$ decay mode for values of the $\pi^+\pi^+$ invariant mass between 0.5 and 3.0 GeV. Similar upper limits were set on the other pion decay modes, but over a more limited region of invariant mass. The limits were based on the assumption that the resonance width was less than 0.10 GeV.

This experiment is not as suitable for an exotic meson search as a $\pi^+ p$ or $\pi^- n$ experiment. As shown in Fig. 8(a), in order to produce a meson

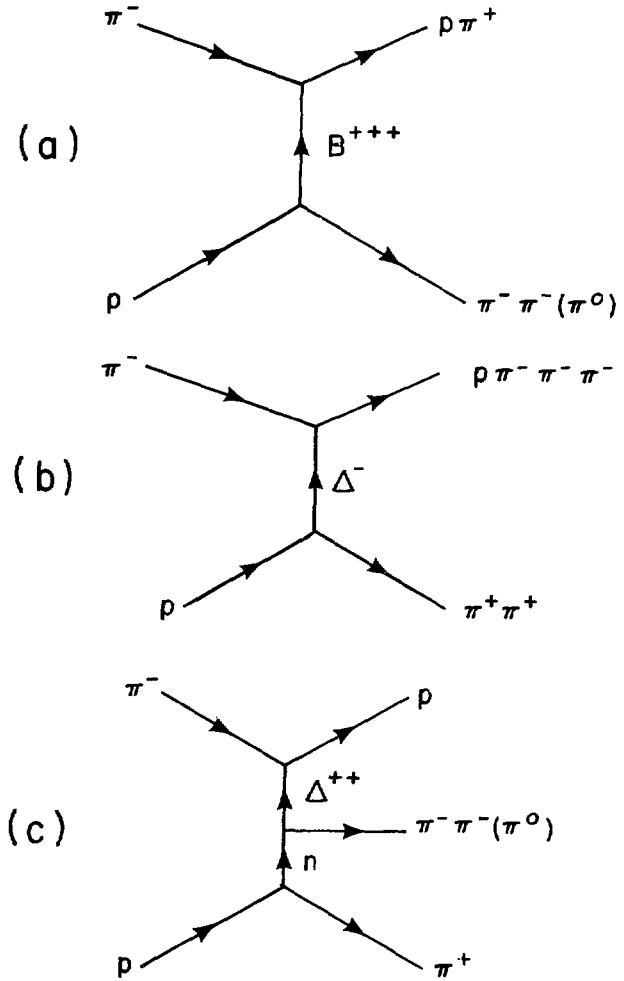

XBL 771 250

Fig. 8

system which has charge -2, it is necessary to exchange an exotic baryon with charge 3 (I=5/2). For this reason, exotic production is not expected to occur in this manner as the coupling at the top vertex is likely to be small. In order to produce a meson system with charge 2 as shown in Fig. 8(b), it is necessary to analyze 6-prong events which are not very prevalent at this energy. These events are not discussed in this thesis. It is possible to construct diagrams in which there are more than two vertices, so that it is possible to have an exotic meson coupled to an ordinary baryon-antibaryon vertex as in Fig. 8(c). Also, it is still possible to produce other members of exotic isospin multiplets which have charge 0 or ±1 by ordinary nucleon or delta exchange in a two vertex interaction. Observation of a new narrow resonance would be an indication of a possible exotic meson.

III. Experimental Layout

The experimental layout of the streamer chamber and spectrometer is shown in Fig. 9. A 4 GeV/c π^- beam passed through two planes of beam defining spark chambers and entered the streamer chamber. Near the upstream end of the streamer chamber was the liquid hydrogen target through which the beam passed. The entire streamer chamber was inside an M5 magnet which provided an approximately constant 13 KG magnetic field throughout the chamber with field perpendicular and into the plane of the diagram.

Downstream of the streamer chamber was the spectrometer system designed to trigger on fast forward protons and K^+'s. The two scintillation counter hodoscopes, H1 and H2, determined when a fast (greater than approximately 1.5 GeV/c), positively charged track had gone through the spectrometer. Between the two counter hodoscopes was a Freon filled Cerenkov counter whose purpose was to reject pion triggers. Just upstream of the front hodoscope (H1), were two spark chamber planes, the spark position data from which were used to improve the determination of the fast forward track parameters.

A. Streamer Chamber

A streamer chamber is much like a bubble chamber in that they both produce visible tracks of charged particles which pass through the chamber, and they are both essentially 4π detectors. In order to produce the visible tracks in the streamer chamber, a short high voltage signal is pulsed across a wide gap containing neon gas. This high voltage pulse initiates avalanche formation along the track where ionization took place resulting from the passage of a charged particle. Due to the shortness

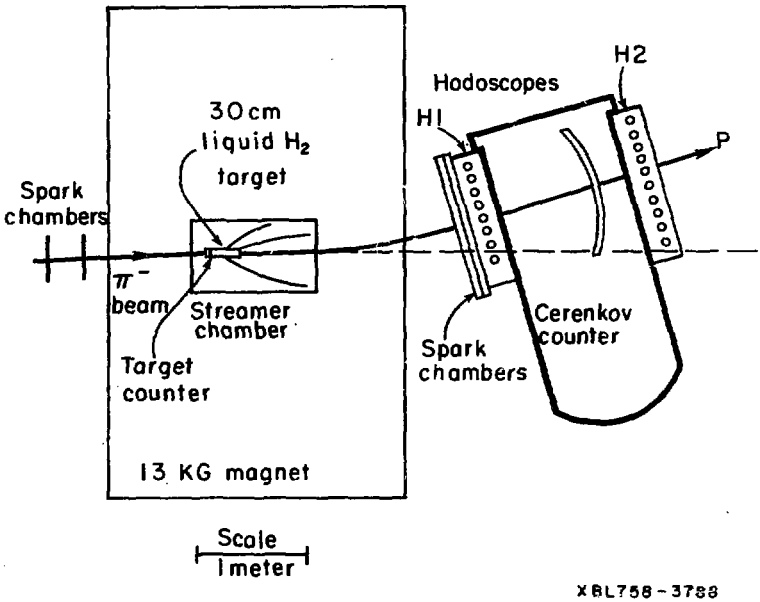
30 cm
liquid H_2
target
Spark
chambers
π^-
beam
Streamer
chamber
Target
counter
13 KG magnet
Hodoscopes
H1
H2
P
Cerenkov
counter
Spark
chambers
Scale
1 meter
XBL758-3788

Fig. 9

of the high voltage pulse, the avalanche formation is halted before the gap sparks across (as in a spark chamber), and one is left with short streamers along the length of the track.

The one tremendous advantage the streamer chamber has over the bubble chamber is that the high voltage is pulsed after the interaction has already taken place. It is thus triggerable, and analysis of the outgoing particles from the interaction can be used to determine whether or not the streamer chamber is to be triggered. The streamer chamber has some inherent disadvantages also. Since the chamber is filled with gas, the target must be contained in an isolated system. Thus, the interaction vertex is hidden from view, along with any tracks which may be in the shadow of the target. In addition, tracks produced with a large relative component of momentum parallel to the electric field become very broad due to increased streamer formation, and are often unmeasurable.

The streamer chamber used in this experiment (similar in design to the UCLA chamber built by Harold Ticho) was a double gap chamber constructed primarily of PVC foam with a mylar front window and mylar windows at the beam entrance and exit locations. The two gaps were each 20 cm and had a common negative high voltage electrode in the center of the chamber. The streamer chamber was 128 cm long by 60 cm high. Fig. 10 shows a diagram of the streamer chamber box and the coordinate system used in the data processing and analysis. In the top view, the central high voltage electrode and the front ground plane are shown as dashed lines. The back ground plane is the backplate of the streamer chamber. The beam line is seen to pass through the target box which projects out from the backplate, nearly to the central electrode. The y-axis is defined to be along the beam

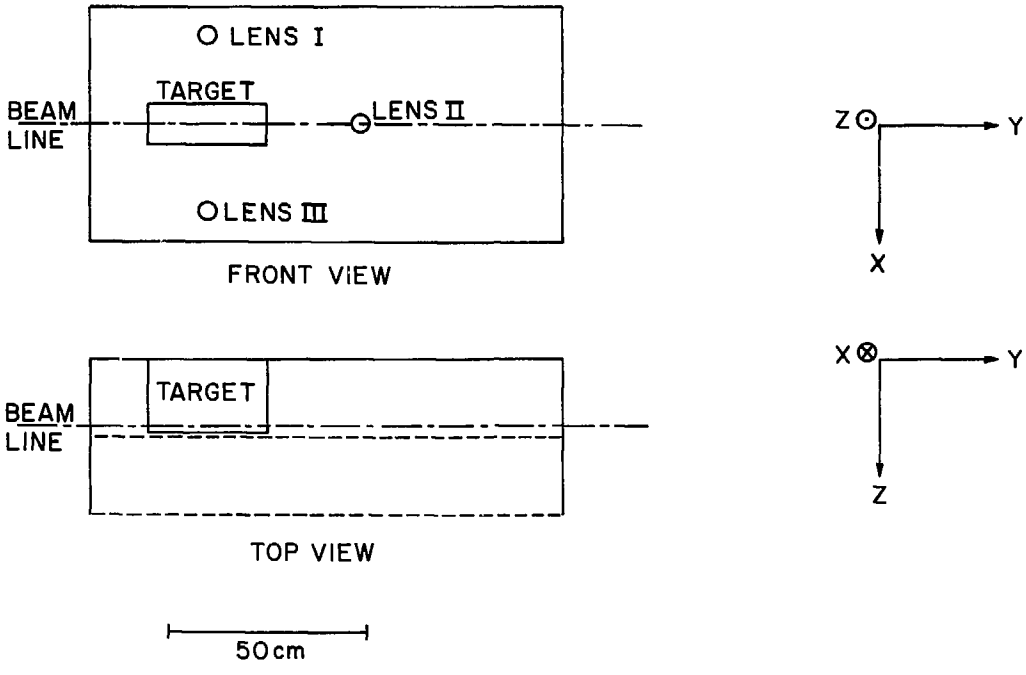

Fig. 12

XBL 7610-4670

direction with origin at the center of the streamer chamber. The z-axis is normal to the backplate with origin at the backplate. The x-axis is constructed to make a right-handed coordinate system and is vertically downwards with origin at the center of the chamber (beam line).

The front ground plane and the central high voltage plane consisted of 0.3 mm wire mesh in a 2 mm grid. The backplate was aluminum plated and contained six fiducials. The four front fiducials and the digits displaying the roll and frame numbers were mounted around the sensitive volume in front of the chamber. In Fig. 11, a photograph of the streamer chamber taken from the front while the chamber was inside the magnet is shown. The front fiducials can be seen near the four corners of the chamber with the roll and frame number digits between the top two fiducials. On the backplate, with the painted grid, can be seen the six back fiducials. In Figs. 12 and 13 are two sample events. The beam entered from the left.

The chamber was filled with standard spark chamber neon which consisted of approximately 90% neon and 10% helium. In addition, a few ppm of SF_6 was added to poison the chamber gas and thereby achieve a memory time of approximately 2 μs. This prevented the pictures from becoming inundated with extra beam tracks. The gas was kept at a slight positive pressure to prevent leakage of outside air into the chamber. The gas was continually recirculated through a purifying system which contained a Linde molecular sieve 13X purifier operated at liquid nitrogen temperature.

B. Camera System

The camera system consisted of three modified flight research cameras

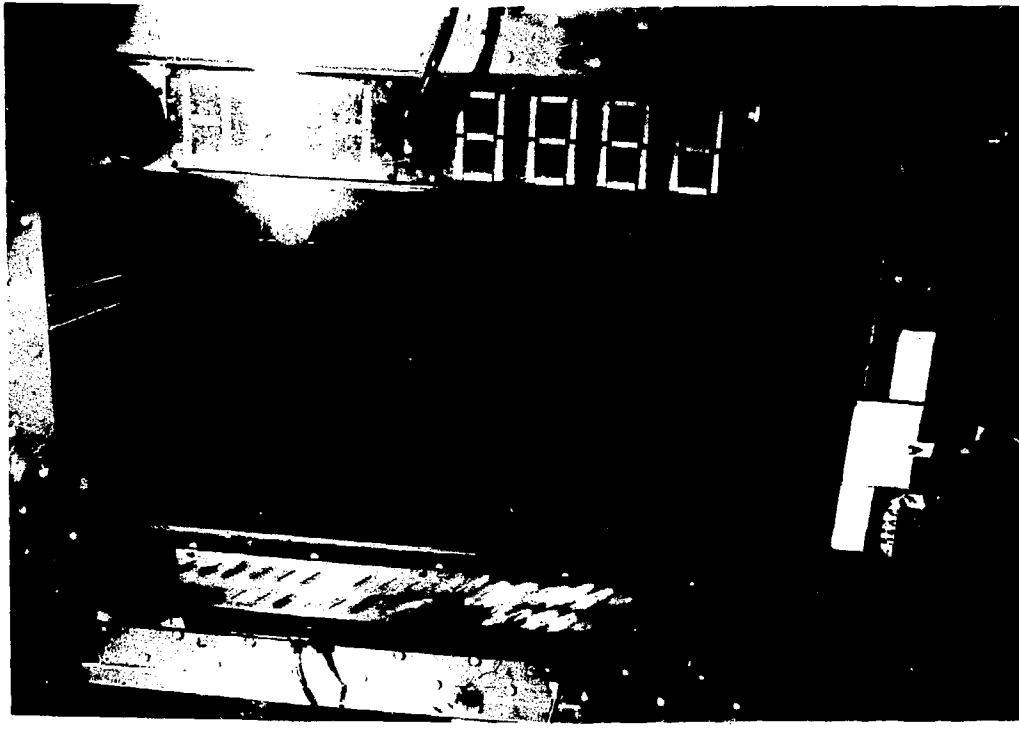

Fig. 11

CBB 7411-8345

XBB 7410-7069

Fig. 12

XBB 7410-7072

Fig. 13

with loop generators, at a distance of 187 cm from the central electrode screen. They were situated as shown in Fig. 10, with one camera at the beam line and downstream of the target, and the other two centered above and below the target. Each camera was separated from the other two by approximately 49.4 cm, yielding a 15^{o} stereo angle between the lenses.

The lenses were f/2 Zeiss Distagon 35 mm lenses which provided a demagnification of about 50X. Vacuum plantens were used, and a mechanism provided by which the vacuum was released while the film was being advanced. High speed film (Kodak SO143) was used in the cameras. This film had a special antihalation backing to help reduce the problem of flares which are generally so common in streamer chamber film.

The orientation of the cameras was modified during the running of the experiment. The camera lens normals were along the z-direction during the exposure of the first 5 (out of a total of 88) rolls of film. For the remainder of the exposure, the camera lens normals were tilted at an angle so as to point towards the center of the streamer chamber. This provided a better overall light acceptance from the outgoing tracks for lenses I and III, and from the beam track for lens I'.

C. Liquid Hydrogen Target

The target consisted of a cylindrical flask 30 cm long by 2.5 cm in diameter which contained liquid hydrogen. The flask was constructed from 3 mil mylar (except the domes on both ends which were 2 mil mylar). The flask was contained inside a box of PVC foam which was 35 cm long by 7.6 cm high and extended to the backplate where it was inserted through the plate. The outside surface of the foam was painted black, thereby reducing reflections of tracks from the surface of the target box.

The liquid hydrogen was cooled by two helium refrigerators in tar... and brought into the flask by means of a fill line. The target pressur... was kept at about 5 P.S.I.G., with just enough refrigeration to liquefy the hydrogen in the flask.

Just upstream of the target flask, but within the foam box, was the hydrogen target counter which was used to define a beam particle entering the target.

D. Pulsing System

The pulsing system consisted of a 24 stage, 12 gap Marx generator followed by a Blumlein pulse forming network. Each stage was charged to approximately ±30 kv with a regulated high voltage power supply. The charging time was about 150 ms. The gaps were triggered by the master trigger amplified to 17 kv by a CX 1157 ceramic tetrode hydrogen thyratron. The final output voltage yielded by the Marx generator was approximately 700 kv.

The purpose of the Blumlein was to shape the pulse and convert it from coaxial to planar geometry. The Blumlein had a built-in trombone, making it possible to adjust the pulse duration from about 7 to 15 ns. The spark gap was a single gap consisting of two 0.375 in. diameter elkonite balls separated by 0.75 in., with SF_6 gas flowing through a hole in one of the balls. The Blumlein was set to output a 500 kv pulse with approximately a 10 ns pulse length.

E. M5 Magnet

The momentum analyzing magnet for the streamer chamber was a modified M5 magnet from which both pole pieces had been removed; one for

photography, and the other to allow the insertion of the hydrogen target assembly. In addition, the two coil packs contained a total of 992 turns rather than the 640 turns with which the M5 magnet is usually equipped in its standard configuration.

The outer dimensions of the magnet steel were 175 in., 110 in., and 101 in. along the x-, y-, and z- axes, respectively. The pole face bore, through which the cameras viewed the chamber, was 63 in. in diameter. The major component of the field was antiparallel with the z-axis, which was the axis of approximate cylindrical symmetry. The streamer chamber was centered on the z-axis, slightly forward of the midplane. This offset allowed the liquid hydrogen target to be centered on the magnet midplane.

All three components of the magnetic field were measured[92] at a magnet current of 5150 amperes, the magnet current used throughout the running of this experiment. The field within the chamber is found to be 13.2 KG with a maximum field variation of 9%. The map for the entire field, both inside and outside the streamer chamber, is contained on a magnetic tape. An interpolation program has been written which can access the magnetic field given the space coordinates.

F. Trigger Hodoscopes

The two trigger hodoscopes, H1 and H', consisted of arrays of scintillation counters oriented longitudinally along the z-axis. Both hodoscopes were mounted on a large frame on either side of the Cerenkov counter; each oriented at an angle of 15.2^{0} from the vertical in order to provide an approximately perpendicular intersection of the particle trajectory with the counter planes. The front hodoscope, H1 (shown in Fig. 14), consisted of 16 scintillation counters, each 36 in. long by 2 in.

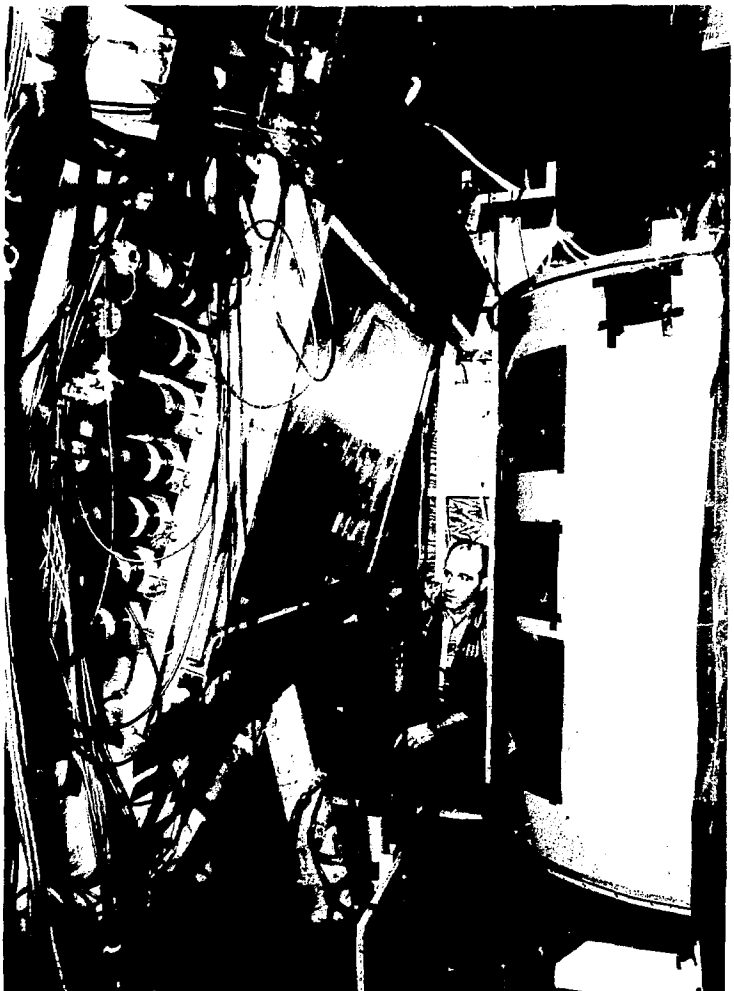

CBB 7411-8153

Fig. 14

wide by 0.375 in. thick. The back hodoscope, H2 (shown in Fig. 15), consisted of 26 counters, each 48 in. by 2 in. by 0.75 in. The high voltages on the counters were set using the end point of the Sr^{90} decay spectrum.

G. Cerenkov Counter

The Cerenkov counter used in this experiment (shown from above in Fig. 16) was cylindrical in shape with an outside diameter of 48.75 in., a height of 114.50 in., and 0.375 in. aluminum walls. Under normal operating conditions, the counter was filled with Freon 12 at 90 P.S.I.G. pressure at a temperature of 110° F. Two coils in the central area and lower flange provided the heat to the counter. The index of refraction of the Freon 12 under these conditions was approximately 1.009.

Radiation produced by the passage of a fast particle through the counter was focused by a 41 in. wide spherical mirror and reflected from a 24 in. wide flat mirror into eight RCA 4522 phototubes. The phototubes required positive high voltage which was supplied through a Zener divider. Calibration of the phototubes was maintained by monitoring the signal from two Ru^{106} sources, cemented between two pairs of phototubes, and a triggerable light pulser, which provided a signal visible to all the phototubes.

The efficiency of the Cerenkov counter was determined by passing the beam through the counter and varying the beam momentum. The pion detection efficiency was found to be close to 0% at 1.05 GeV/c momentum and to reach nearly 100% as the momentum was increased to 1.15 GeV/c. Thus the Cerenkov counter provided separation of pions from kaons and protons for momenta greater than approximately 1.15 GeV/c.

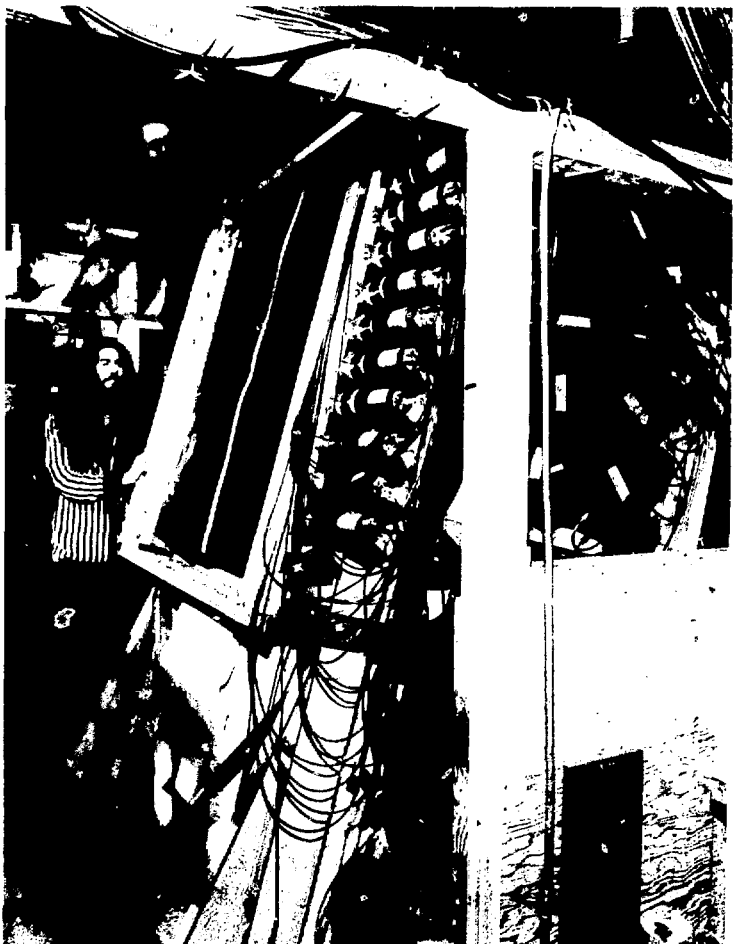

CBB 7411-8155

Fig. 15

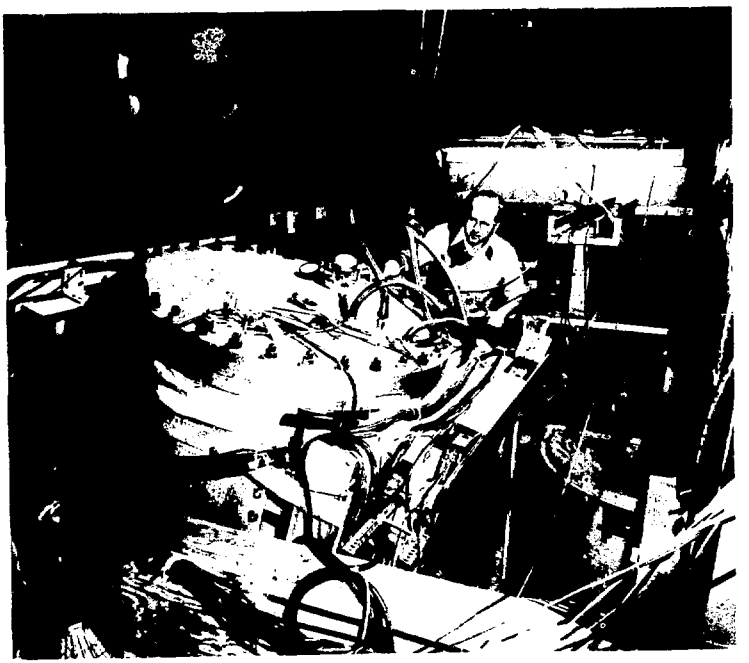

CBB 7411-8151

Fig. 16

H. Spark Chambers

The downstream spark chamber, consisting of two planes of wires, was mounted on the front hodoscope frame, just upstream of the front hodoscope. Each plane contained wires in the z-direction and the tilted x-direction (at an angle of 15.2^{o} from the x-direction in the x-y plane). The wire spacing was 1 mm. The two planes were separated by 0.375 in. and each had an active area of 40.5 in. (in the z-direction) by 29.0 in. (in the tilted x-y direction). Magnetostrictive wands were used for readout, and due to the magnetic field from the M5 magnet in the region of the spark chamber, it was necessary to use iron shielding for the wands oriented along the z-axis. Fiducials were provided at both ends of each wand enabling absolute positions to be determined from the relative spark positions.

Each of the two spark chambers upstream of the streamer chamber contained wires in the z-direction and the x-direction, with 1 mm wire spacing. The two chambers were separated by 32 cm and each had an active area of 30 cm by 30 cm. Due to the magnetic field, iron shielding had to be used on both sides of each magnetostrictive wand. Again, fiducials were provided at both ends of each wand.

The gas used in the spark chambers was spark chamber neon (90% neon and 10% helium, but without the SF_6 used in the streamer chamber). A gas purifying system similar to that used for the streamer chamber was utilized.

I. Beam Line

Beam line 26B, which transported the secondary pion beam to the streamer chamber, is shown in Fig. 17. The extracted internal proton beam (EPBI) was scattered on a copper target 4 in. long by 0.2 in. high by 0.3 in. wide. A secondary beam of pions of momentum 4 GeV/c was produced at an

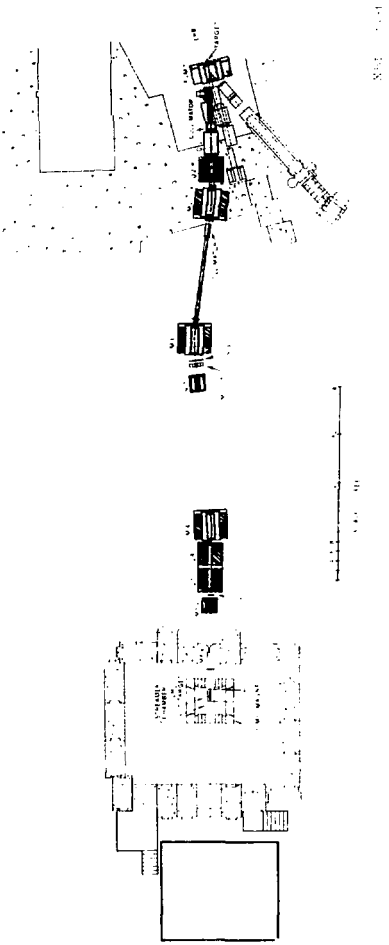

Fig. 17

angle of 5^{0} and deflected by magnet X1M7 into the beam channel. The beam was focused in both the horizontal and vertical directions by the quadrupoles Q1 and Q2 at the location labeled P (the first focus). M2 and M3 were horizontal bending magnets. The quadrupoles Q4 and Q5 focused the beam at the location of the hydrogen target. The horizontal bending magnet M4, and the vertical bending magnets M5V and M6V were used to steer the beam into the hydrogen target. The spread of the beam was determined by the magnet apertures and various adjustable collimators.

To define the beam for the trigger, various scintillation counters distributed along the beam line were used. At the first focus was situated the momentum hodoscope, consisting of five vertically oriented 0.5 in. wide scintillation counters (M1-5) distributed horizontally across the focus. The dispersion of the beam as a function of momentum allowed an accurate determination of the momentum to be made using the hodoscope counter latch information. In addition to the M counters, the P, Q, and H (hydrogen target) counters defined the beam. The H counter was 0.875 in. in diameter and tagged particles entering the 1 in. diameter liquid hydrogen target. Noninteracting beam tracks leaving the streamer chamber were vetoed by a paddle counter, designated BOUT, downstream of the streamer chamber.

The beam flux was approximately 25,000 pions per spill (resulting from approximately 10^{11} protons incident on the primary target). The spill generally lasted slightly longer than one second of the Bevatron's six second cycle, during which time the streamer chamber was triggered twice on the average.

J. Fast Logic and Electronics

Three requirements were necessary in order for a trigger to be initiated. These are shown schematically in Fig. 18. First, a fast forward, positively charged particle, as determined by the coincidence matrix output, was required. The inputs to the coincidence matrix were the 14 output signals from the H1 hodoscope counters, and the 24 output signals from the H2 hodoscope counters. For any given coincidence between a counter in H1 and a counter in H2, the momentum of the track traversing the two counters was crudely determined. The coincidence matrix consisted of a set of hardwired coincidences, designed to give a coincidence only for those combinations which determined that the momentum of the fast, positively charged track was greater than approximately 1.5 GeV/c. The output of the coincidence matrix was the OR of all the allowed (hardwired) coincidences.

The experiment was run with two different trigger conditions, determined by two different wirings of the coincidence matrix. The allowed coincidences are shown in Table VII. In the first column is the H1 hodoscope counter. In the next two columns are the H2 hodoscope counters for the allowed coincidences for the two different coincidence matrix wirings. Matrix 1 refers to the wiring used in the trigger for the exposure of the first 22 rolls of film. Matrix 2 refers to the wiring used for the remainder of the exposure (rolls 23 to 88).

The matrix 1 trigger was the looser of the two, with a trigger rate of approximately 2×10^{-3}. The matrix 2 trigger rate was approximately 10^{-3}. Matrix 1 allowed lower momentum tracks to trigger than did Matrix 2. With this trigger, much of the phase space available to a proton from the decay of a forward Λ or N^* was within the acceptance of the system.

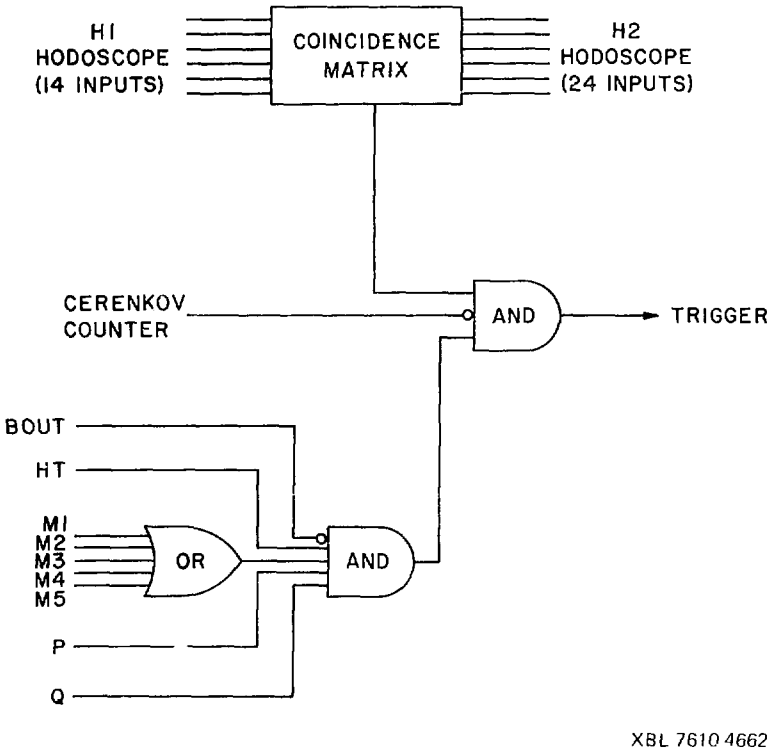
H1
HODOSCOPE
(14 INPUTS)
COINCIDENCE
MATRIX
H2
HODOSCOPE
(24 INPUTS)
CERENKOV
COUNTER
AND
TRIGGER
BOUT
HT
M1
M2
M3
M4
M5
OR
AND
P
Q
XBL 7610 4662

Fig. 18

Table VII. Coincidence matrix combinations.

H1 counter	H2 counter	
	Matrix 1	Matrix 2
1	1,2	1
2	1,2,3	1,2
3	2,3,4,5	3,4
4	3,4,5,6,7	4,5
5	5,6,7,8	6,7
6	7,8,9,10	7,8
7	8,9,10,11	9,10
8	10,11,12,13	10,11,12
9	11,12,13,14,15	12,13
10	13,14,15,16	13,14,15
11	15,16,17,18	15,16
12	16,17,18,19	17,18
13	18,19,20,21	18,19,20
14	20,21,22,23	20,21

With the matrix 2 trigger, a higher proportion of the events accepted corresponded to a relatively low mass meson system recoiling against the forward proton.

The second trigger requirement was that there be no signal from the Cerenkov counter in time with the hodoscope signals. The Freon 12 in the Cerenkov counter was at a pressure such that pions produced Cerenkov radiation on traversing the counter. Thus the fast triggering particle was required to be a proton or a K^+ (with momentum less than approximately 3.5 GeV/c). Removing this requirement (i.e., allowing π^+ triggers) resulted in an increase in the trigger rate by a factor of 2.75.

The final trigger requirement was that a beam particle had entered the target and had either interacted or scatttered before reaching the downstream spectrometer. This requirement, which will be denoted by BIN, is logically defined as

$$BIN = \Sigma M \cdot P \cdot Q \cdot H \cdot \overline{BOUT} ,$$

where ΣM is the OR of the five momentum hodoscope counters, and P, Q, H, and BOUT refer to the respective beam line counters. Note that the BOUT counter is in anticoincidence with the other components of BIN.

The output from the trigger was used to fire the streamer chamber and spark chambers, provide a strobe for the hodoscope counter latches, initiate the data break transfer into the PDP-5, and advance the film in the cameras.

The electronics used in this experiment were fairly standard. Schematic logic diagrams for the scintillation counter output signals, the hodoscope counter output signals, and the Cerenkov counter output signals are shown in Figs. 19-21. Spark chamber output pulses were converted to digital counts by means of a zero-crossing discriminator and a SAC scaler box.

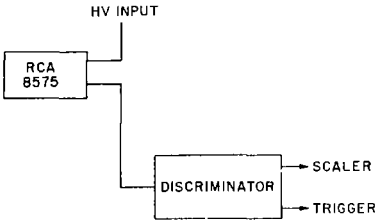

Fig. 19

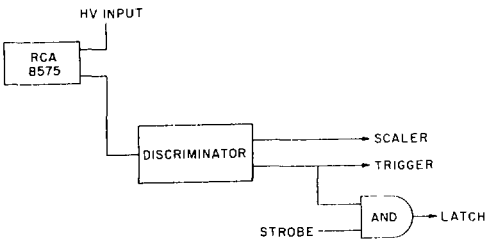

Fig. 20

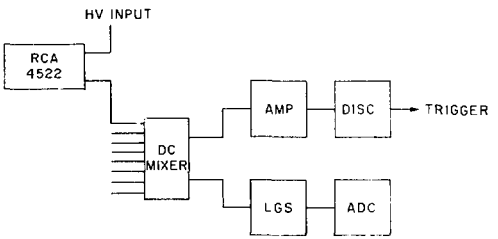

Fig.

K. Slow Logic

The slow logic involved the on-line computer which handled the running of the experiment and the data taking, the interfaces between the Bevatron IPIP signals and the fast logic and the on-line computer, and the NIDBUS (Nuclear Instrumentation Data Bussing System).

The on-line computer was a PDP-5 with 8K 12 bit words of core memory. It was equipped with a D2020 tape drive capable of writing on 7-track tape at a density of 556 BPI. The input-output transfer (IOT) connections were modified for this experiment.

The PDP-5 had a three-fold purpose during the running of the experiment. First, it was aware of the status of the internal proton beam, and gated the electornics off and on so that events were accepted only during the Bevatron beam spill. Second, it recorded all relevant information about each event on magnetic tape for later use in the off-line processing. This information, which was stored in core by means of the DBC (data break control) during the spill, was written onto magnetic tape at the end of the spill, or as soon as four events had been accumulated, if they occurred during a single spill. The information recorded for each event included the roll and frame number of the event, latch information for all three hodoscopes, the Cerenkov counter ADC pulse height, spark counts for all wands, and the M5 magnet shunt voltage. In addition, every 25 spills, the counts on all scalers were recorded. Among the signals scaled were those from the beam line counters and those from various inputs to the trigger logic. Finally, the PDP-5 monitored the hardware and electronics during the running by accumulating and displaying histograms of hodoscope latch counts and spark chamber posi-

tions. A schematic of the interfaces between the Bevatron IPIP signals and the fast logic and the PDP-5 is shown in Fig. 22.

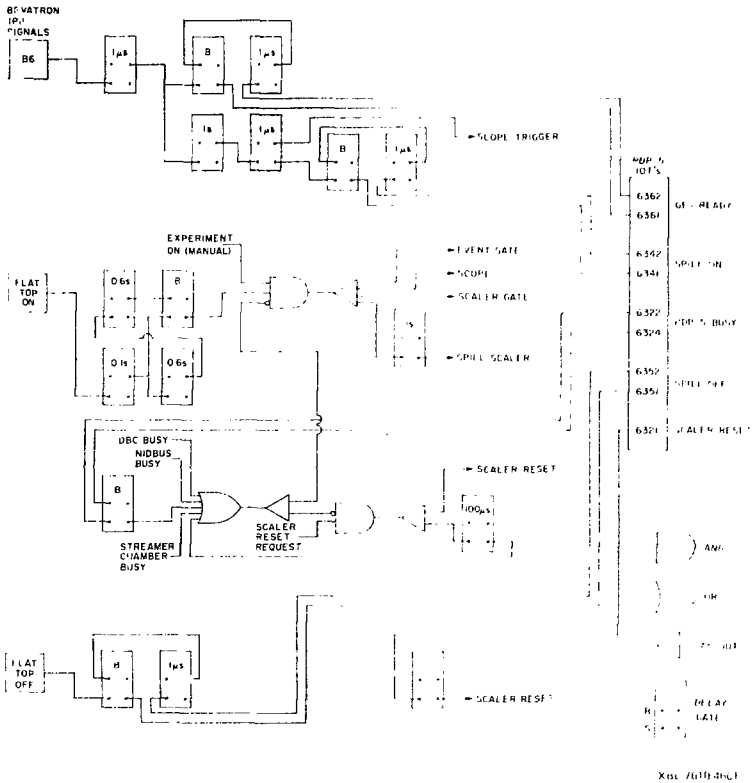
BEVATRON TP.I SIGNALS
B6
1μs
B
SCOPE TRIGGER
1s
EXPERIMENT ON (MANUAL)
FLAT TOP ON
0.6s
EVENT GATE
SCOPE
SCALER GATE
SPILL SCALER
0.1s
DBC BUSY
NIDBUS BUSY
SCALER RESET
100μs
SCALER RESET REQUEST
STREAMER CHAMBER BUSY
FLAT TOP OFF
6362
6361
6342
6341
6322
6324
6352
6351
6321
AND
OR
DELAY GATE

Fig. 22

IV. Data Handling and Processing

In this chapter, I describe the handling and processing of the data. In Fig.23 is a schematic of the data flow. First, the film was scanned to determine the topology of each event. Then selected events were measured on the COBWEB[93] measuring system. The measured tracks were reconstructed using a modified version of TVGP[94] (Three View Geometry Program). Then the reconstructed events were merged with the on-line data from the PDP-5 which was used to make improvements on the track parameters of the beam track, and the fast forward track. The hidden vertex was reconstructed by the program APACHE[95]. Finally, in SQUAW[96], the kinematic fitting was done.

A. Scanning

All of the film was scanned frame-by-frame once, and approximately 10 of the film was scanned twice. The first 15,000 frames of film scanned were done manually on scanning tables which presented all three views of the film to the scanner. For each frame, the event type and other relevant information was coded for later processing to generate the sample of events to be measured. The remainder of the film (about 315,000 frames) was scanned on FSD Roadmaker Tables. These tables presented all three views of the film to the scanner and in addition allowed for digitization of selected points. A reference fiducial and an estimate of the primary vertex position were digitized in one view for later use in event selection for measurement. All relevant information concerning the event was entered through a control panel and written directly onto magnetic tape.

One of the problems encountered in the scanning and measuring of film involved the occurrence of multiple incoming beam tracks in approximately 15% of the events. The finite memory time of the streamer chamber

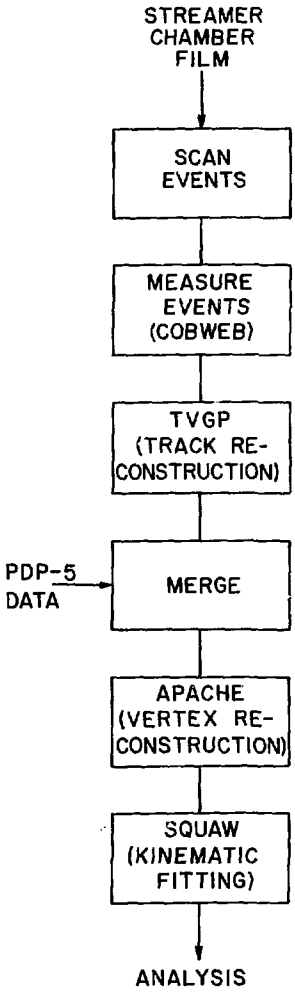
STREAMER CHAMBER FILM
SCAN EVENTS
MEASURE EVENTS (COBWEB)
TVGP (TRACK RE-CONSTRUCTION)
PDP-5 DATA
MERGE
APACHE (VERTEX RE-CONSTRUCTION)
SQUAW (KINEMATIC FITTING)
ANALYSIS
XBL 7610 4671

Fig. 23

was responsible for this. Since the primary vertex is not observable in a streamer chamber event, it was often difficult to determine which beam track interacted. If the scanner could determine the correct beam track, this track was measured. If the correct beam track could not be determined, the event was flagged to indicate that the beam track was not to be measured.

Another problem encountered resulted when a steeply dipping track flared making it impossible to measure, or even to determine the charge of the track. The events were also flagged thus indicating that the topology was incorrectly represented by the event type.

B. Measuring

Events were selected for measurement by the COBWEB measuring system on the basis of the event types determined from the scanning. The event type criteria used were not the same for all of the measuring. For a sample of approximately 18,000 frames, all events that either conserved charge or had net charge ± 1, and in addition had at least one positive track were measured. For the remainder of the film, only three types of events were measured. Nearly all of the events scanned which contained a visible vee were measured. Over two-thirds of the 4-prong single vertex events and over one-half of the 2-prong single vertex events were measured. In Table VIII, the information pertaining to the measurement of these three types of events is summarized. The percent of exposure, given in column III, is the number of frames scanned divided by the total number of measurable frames. The total number of measurable frames was determined from the scan to be 328,046. The entry labeled "other" refers to events from the sample of 18,000 frames which do not fall into any of the three previous categories. A total of 111,538 events were measured.

Table VIII. Event scanning and measuring summary.

Type of event	No. of scanned frames	% of exposure	No. of measured frames
visible vee	308081	.98	6551
4-prong (SC22)	237580	.76	47228
2-prong (SC11)	201082	.64	52399
other			5360

On most of the events measured, an additional requirement was imposed in the event selection. The estimated position of the primary vertex, as determined from the digitized point taken during the scanning, was required to be downstream of the target counter. This requirement eliminated the measurement of a large number of events which would have been eliminated in the analysis anyway, and eliminated very few good events in which the primary vertex was actually in the hydrogen target.

The COBWEB measuring system consists of semiautomatic "Franckenstein" measuring machines (three were used in this experiment) controlled by an IBM 7044 computer. The Franckensteins have track following capabilities, but require operators to do the actual measuring. For each of the three views, five fiducials were measured by the operator. COBWEB insured that the relative positions of these fiducials were within preset tolerances. Then all of the tracks in each view were measured. The operators were instructed to measure the entire length of each track and to skip portions of the track with poor streamer quality or flares. COBWEB made sure that the point scatter for each track was within tolerance, and required re-measurement of any poorly measured track. The digitized fiducial points and track points for each event were output on magnetic tape, and then run through an editing program which formated the data in a form compatible with the track reconstruction program

C. Track Reconstruction

The measured events were input into a modified version of TVGP in which each track was geometrically reconstructed in space. Each track was fit to a helix, modified to take into account variations of the magnetic field

in the streamer chamber and the energy loss (which is small) in the neon. The fitted track was parameterized in terms of the azimuth angle ϕ, the slope $s=\tan(\lambda)$, and the curvature $k = 1/p \cos(\lambda)$. The azimuth is the angle about the z-axis of the track projected onto the x-y plane, with $\phi=0$ along the x-axis. The dip angle, λ, is given by $\sin(\lambda)=p_z/p$. In order to represent the magnetic field of the M5 magnet, a polynomial fit to the measured field values inside the streamer chamber was made. The RMS deviation of the fitted value from the measured value was approximately 10 gauss (less than 0.1%). This fit was used to represent the field in TVGP.

In reconstructing a track generally more than one mass assignment was made to account for the energy loss of different particles. Different mass assignments were made depending on the topology of the event. These mass assignments are listed in Table IX.

A major modification made in TVGP involved the calculation of the position error matrix at the beginning point of all outgoing tracks and at the end point of the beam track. This addition was made rendering it possible to later reconstruct the primary vertex position inside the target.

One measure of the accuracy of the track measurements and the optical constants is the RMS deviation of the measured track points from the fitted track. In Fig.24, a histogram of the film RMS deviation of a sample of tracks consisting of all the outgoing prongs from a sample of 2-prong and 4-prong events is shown. The distribution peaks at about 6μm. Since the lenses provide a demagnification of about 50X in the center of the streamer chamber, this represents a point setting error of about 300 μm in space.

Table IX. TVGP track mass assignments.

Type of track	Mass assignments
beam	π^-
neg. prong	π^-, K^-
pos. prong	π^+, K^+, p
neg. vee prong	π^-
pos. vee prong	π^+, p
neg. prong on kinking track	π^-, K^-, Σ^-
(for NV event type only)	π^-, K^-, Σ^-, Ξ^-
neg. prong after kink	π^-
pos. prong on kinking track	π^+, K^+, p, Σ^+
pos. prong after kink	π^+, p
neutral from primary vertex	K^0, Λ^0
neutral from kink	Λ^0

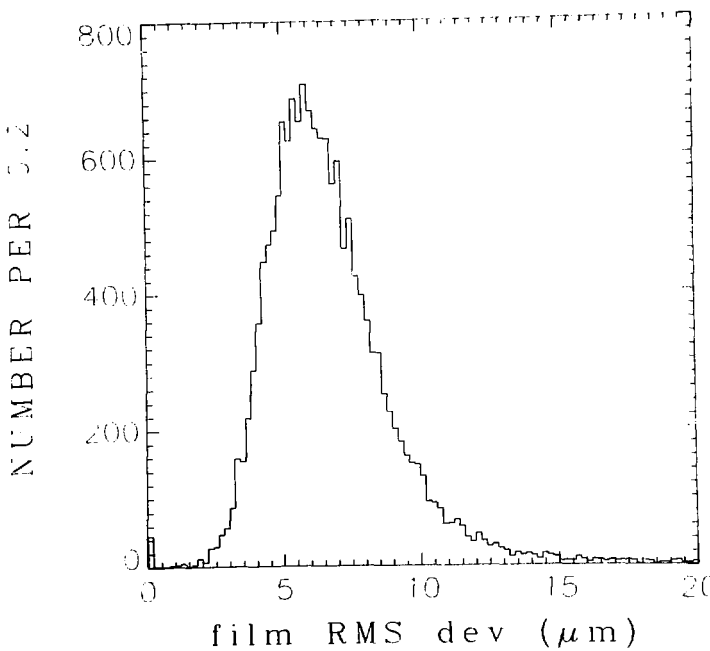

Fig. 24

After processing through TVGP, the reconstructed events were written out onto magnetic tape. This output tape was then input into an intermediate program which had three functions: it merged the TVGP output data with the on-line PDP-5 data written during the running of the experiment; made corrections to the beam parameters and fast forward track parameters using the spark chamber and hodoscope information; and kept track of the performance of the measurers maintaining a constant check on the quality of the measurements.

The information from the PDP-5 on-line data tape which was merged with the reconstructed track information included spark positions for both the beam spark chambers and the downstream spectrometer spark chamber planes; latch information for the beam momentum hodoscope and the downstream trigger hodoscopes; the ADC pulse height output from the Cerenkov counter signal; and the M5 magnet shunt voltage. The spark chamber and latch information was used for correction of track parameters. The Cerenkov counter ADC information was used for later analysis of the efficiency of the Cerenkov counter. The M5 magnet shunt voltage was used to check that the magnetic field in the streamer chamber remained constant.

The beam track was generally a very poorly measured track, resulting from it being a high momentum track with only a short path length visible before it entered the target. In addition, there was often more than one beam track entering the target making it sometimes impossible to determine which track interacted and which track passed through the target. For this reason, the beam track was always corrected, or if none existed, it was added to the track banks and the banks reconstructed so that they were identical in form to events which had a measured beam track.

In order to correct the beam momentum, information from the momentum

hodoscope latches was utilized. There were five counters in the hodoscope. The mean momentum of beam tracks passing through the center counter was 3974 MeV/c. The difference in mean momentum of beam tracks passing through adjacent counters was 37 MeV/c. If a latch for only one of the counters was set, the mean momentum corresponding to that counter was assigned to the beam track, replacing the measured value, if any, with an error of about 27 MeV/c. If the latches for two adjacent counters were set, the average of the mean momenta corresponding to the two counters was assigned to the beam track with the same error as above. Under any other conditions, the nominal value of 3974 MeV/c was assigned to the track with an error of about 79 MeV/c.

Determination of the momentum to be assigned to each counter in the momentum hodoscope was done in two different ways, giving results consistent with each other within errors. The first determination was made by analyzing a special sample of noninteracting beam tracks traversing the length of the chamber. These events were triggered by a coincidence between the beam counters and the BOUT counter with the hodoscope coincidence matrix and the Cerenkov counter eliminated from the trigger. The nominal beam momentum was determined to be about 3950 MeV/c. The second determination was made by assigning the previously determined beam momentum to the beam tracks, and kinematically fitting a sample of 4-prong events in SQUAW. The 4C events resulting from the kinematic fitting were used to correlate fitted beam momentum with beam hodoscope counter. The results from this second determination were used rather than those from the first determination since the statistics were higher and represented an average over all rolls of film, whereas the first determination was based on a sample of triggers all taken near the beginning of the experimental running.

The beam angle parameters (azimuth and dip) were corrected with the help of the positional information obtained from the two upstream spark chamber planes. Since the separation of the two spark chamber planes was only 32 cm, and the extrapolation to the streamer chamber through the fringe fields of the M5 and M6V magnets was difficult, it was difficult to determine the beam angles accurately without additonal information. With the addition of the reconstructed vertex position from APACHE, it was possible to significantly improve the measured beam angles, so the final determination of the beam parameters was made after the vertex was reconstructed and is discussed in the next section. However, until the final determination was made, the measured values of the beam angles were temporarily replaced by the nominal values. These nominal values were determined by examining the fitted values from the sample of 4-prong, 4C events described in the previous paragraph.

The final correction made to the beam track was the correction of the spatial coordinates of the beginning and end points of the track. If the beam track was measured, no change was made either to the coordinates or the coordinate errors as computed by TVGP. If no measurement was made, the beginning and end points of the track were assigned nominal coordinates with errors consistent with the beam spot size. The errors in this case were large enough so that they had essentially no effect on the vertex fitting in APACHE.

Despite the fact that the fast forward track generally had a long track length in the streamer chamber (about 75 cm), its high momentum resulted in a large error in the momentum measurement. The additional points on the track downstream of the streamer chamber, due to the two planes of spark chambers, considerably improved the resolution on this

track. The fast forward track (or each of them if there were two) was swum through the fringe magnetic field to the downstream spectrometer system. If there was at least one spark chamber position coordinate in the vicinity of the extrapolated fast track, a fit was made varying the track parameters (curvature, azimuth, and slope) and the spark chamber position coordinates (up to four coordinates); constraining the extrapolated track to pass through the spark chamber position coordinates. If all four spark chamber position coordinates existed, a 4C fit was attempted. For each missing position coordinate, the constraint class was decreased by one, but the fit was still attempted.

In Fig. 25 is a histogram of the χ^2 confidence level for a sample of fits. The peak at small confidence level is due to scattered or misidentified tracks. For fits with confidence level greater than 0.01, the old track parameters were replaced by the fitted parameters. The fitted relative momentum error, $\Delta p/p$, was about 1% compared to the measured relative momentum error of at least 2-3%. The fitted angular errors were about 0.04^{o} for the azimuth and about 0.03^{o} for the dip compared to measured errors which were greater than 0.1^{o}. In order to demonstrate that the fitted parameters and errors were reasonably assigned, histograms of the pulls (fitted minus measured value of a parameter divided by the square root of the difference of the errors squared) on the fitted track parameters, and histograms of the pulls on the fitted spark chamber position coordinates were constructed. The pull on the azimuth is given in Fig. 26(a), on the slope in Fig. 26(b), and on the curvature in Fig. 26(c). The spark chamber position coordinates are labeled S1-S4 and are given in Figs. 27(a)-(d), respectively. The superimposed curves are Gaussians of unit width, each normalized to the area under the corresponding histogram.

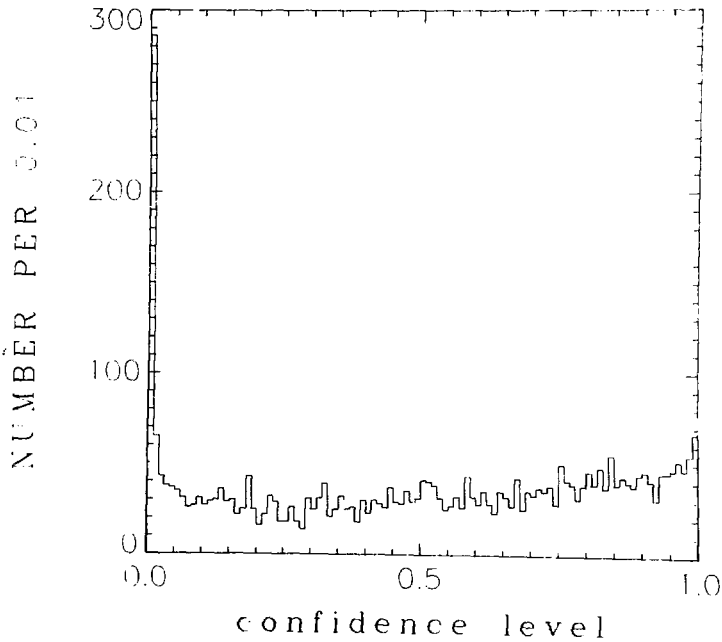

Fig. 25

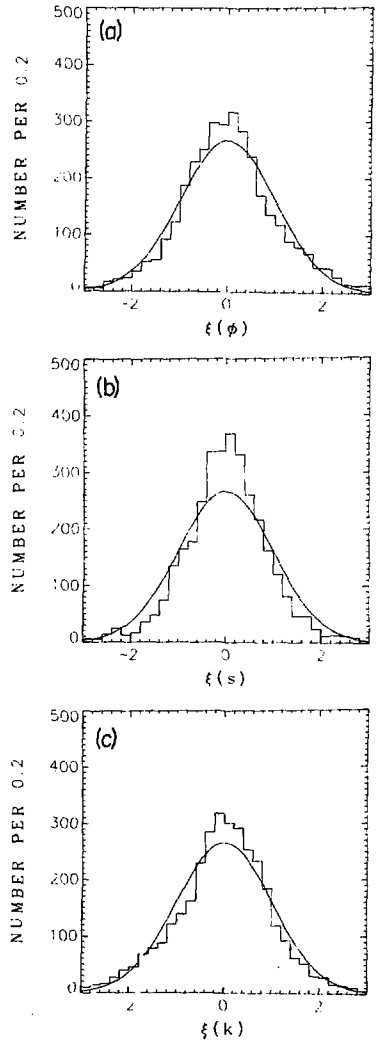
(a)
NUMBER PER 0.2
500
400
300
200
100
0
-2
0
2
ξ(φ)
(b)
NUMBER PER 0.2
500
400
300
200
100
0
-2
0
2
ξ(s)
(c)
NUMBER PER 0.2
500
400
300
200
100
0
-2
0
2
ξ(k)
XBL 7610-4674

Fig. 26

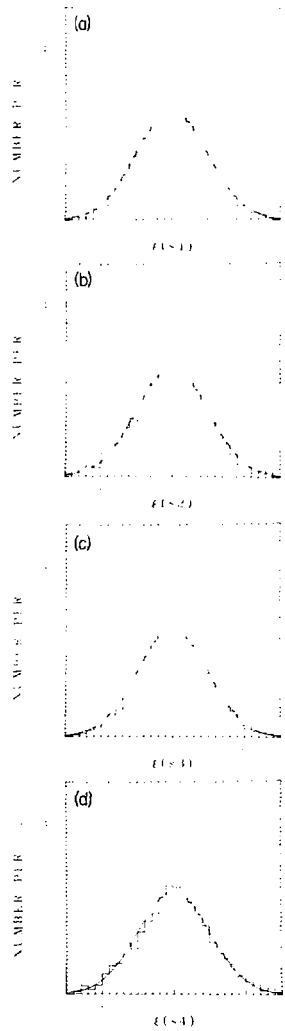

Fig. 27

At this point in the processing, it is convenient to discuss briefly the mass resolution of the reconstructed events. A measure of this resolution was obtained by constructing a histogram of the invariant mass of pairs of tracks which formed visible vees in the streamer chamber. The negative track was assumed to be a π^- and the positive track was assumed to be a proton. This histogram is shown in Fig. 28 for a limited range of invariant mass. The Λ^0 is seen to dominate the histogram. The superimposed curve is a fit (see Appendix A) assuming a Gaussian signal over a small quadratic background. The Λ^0 signal is seen to include larger tails than are provided by the Gaussian used in the fit. This is due to the fact that not all tracks have the same errors, and to reflect reality, instead of a single Gaussian, a sum of Gaussians of varying widths should be used in the fit. This is both impractical and unnecessary, since the simple fit with a single Gaussian will give an accurate estimate of the central mass value and mass resolution of the Λ^0. The values of the parameters obtained in the fit are M=1.1158 ± 0.0001 GeV and σ = 0.0017 GeV.

The mass resolution appears to be quite good, but this is partially due to the low Q-value of the Λ^0 decay. Another measure of the mass resolution is given by the K^0 invariant mass, though there is a slight difference since most of the protons from the Λ^0 decays are the trigger particles and hence go through the downstream spark chambers, whereas few of the π^+'s from the K^0 decays go through the downstream spark chambers. Fig. 29 shows the histogram of the invariant mass of pairs of tracks which formed visible vees, but with the positive track assumed to be a π^+ rather than a proton. The K^0 is seen to dominate the histogram in this case. The curve is a fit similar to that made in the case of the Λ^0 signal. The values of the parameters obtained in the fit are M=0.4976 ± 0.0004 GeV and σ = 0.0049

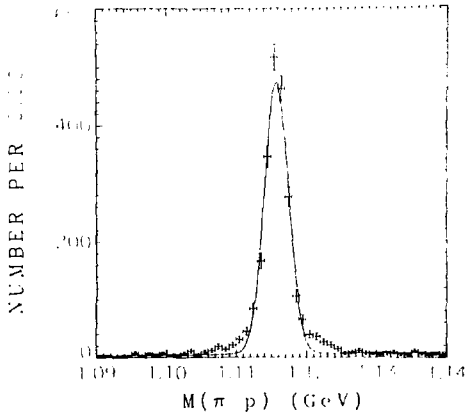
NUMBER PER
200
0
1.09
1.10
1.11
1.14
M(π p) (GeV)

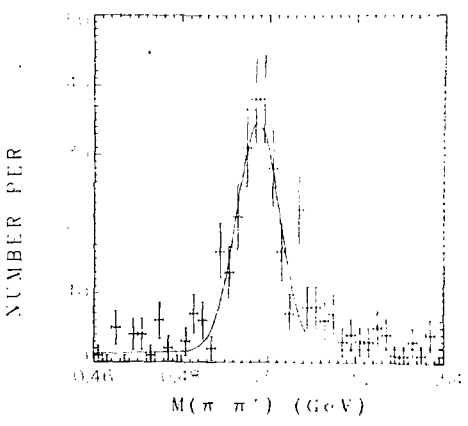
NUMBER PER
0.46
M(π π') (GeV)

GeV. The mass resolution is still seen to be less than 5 MeV.

In order to clean-up the mass distributions shown in Figs. 28 and 29, any vee which was consistent with being a K^0 was eliminated from Fig. 28, and any vee consistent with being a Λ^0 was eliminated from Fig. 29. In addition, any vee consistent with being a Dalitz pair was eliminated. In addition to providing an estimate of the mass resolution, the central value of the mass provides a check on the normalization of the magnetic field used in TVGP. The fitted value of the Λ^0 mass is very close to the world average of 1.1156 GeV, and the fitted value of the K^0 mass is equal within errors to the world average of 0.4977 GeV.

D. Vertex Reconstruction

The reconstruction of the vertex position hidden inside the target box was done in APACHE. This program fit to find the primary vertex location by varying all the track beginning point coordinates (beam end point coordinates), constraining all the tracks, when extrapolated into the target, to intersect at a common point. The number of constraints was 2n-3 where n is the number of tracks involved in the fit. If the χ^2 confidence level of the vertex intersection fit was greater than 0.02, the fit was considered to be good and no further fitting was attempted.

If the confidence level of the fit was less than 0.02, a search was made for a hidden secondary vertex inside the target box. If there were no visible vees with invariant mass consistent with the lambda mass, a search was made for a hidden vee vertex. Pairs of tracks of opposite charge were taken one at a time and fit to hypotheses corresponding to Λ^0 and K^0 decay. If a good fit was found with confidence level greater than 0.01, the primary vertex was again fit without the two charged tracks, but with the reconstructed neutral track, provided that it was unambiguously

a K^0. If the confidence level of this fit was greater than 0.0001, the fit was considered to be good.

If there was a visible vee with invariant mass consistent with the lambda mass, a search was made for a hidden kink consistent with a lambda producing decay. Goodness of fit criteria for both the hidden secondary vertex and the primary vertex were the same as for the search for hidden vees. The details are not important, for no analysis of events of this type was ever made.

If at this point in the program, no good fit had been found, the original confidence level of the primary vertex was reexamined, and if it was greater than 0.0001, the fit was considered to be good. An event without a good fit was given a failure code and no further analysis was done.

After the vertex or vertices were found, all tracks were swum back to their respective vertices. All track parameters and errors were recalculated at the vertex. This calculation took into effect the energy loss and multiple scattering due to the particle traversing the liquid hydrogen in the target, and the foam, mylar, and epoxy of which the target box was made. For those events in which a hidden vertex was found, the event type was changed, and new track banks in the TVGP format were added.

In Fig. 30, a histogram of the confidence level of the primary vertex fit for a sample of 4-prong events is shown. The excess of events at low confidence level is due to poor measurement, and possibly to some scattering of the tracks. The excess of events at high confidence level is due to the fact that for many events, the beam has large errors on its end point coordinates, and thus the beam track has essentially no effect on the fit.

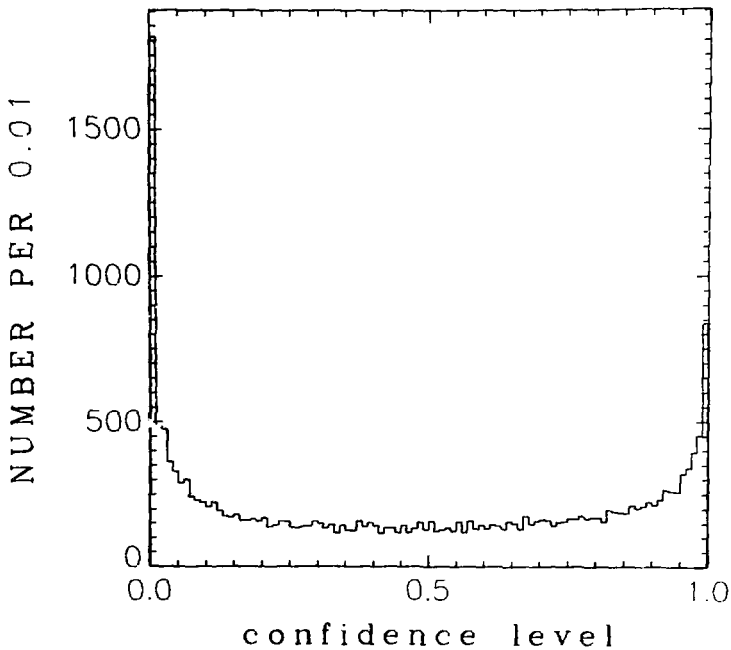

Fig. 30

However, in calculating the confidence level of the fit, the two degrees of freedom associated with the beam were included, thus skewing the distribution to large values of confidence level.

In Fig. 31 is a scatter plot of the reconstructed primary vertex position in y vs r (the radial distance from the beam line) for the same sample of 4-prong events as was included in Fig. 30. The good resolution of the vertex position is indicated by the fact that the structure of the target box is evident in the scatter plot. At both the upstream and downstream ends of the target box, one can see the epoxy which lines the foam box as two vertical bands of heavy density. Also, near $y \approx -30$ cm and at large r, the hydrogen fill line projecting into the target can be seen. The resolution of the vertex position is estimated to be a few mm in the x-y plane and about 0.5 cm in the z-direction, but varies depending on the quality of the measurements and the length of track extrapolated.

After determining the position of the primary vertex, the final corrections to the beam angles were made. The deviation of the beam track from its nominal center position at the upstream spark chambers was known. If there was no scattering of the beam prior to the interaction in the target, the deviation of the beam track from the nominal vertex position was also known. The deviation from nominal of the beam azimuth and dip can be determined analytically by calculating the derivatives of the angle variables with respect to the deviations from nominal of the track position coordinates and the beam momentum. In this manner, the beam angles were corrected. The resulting errors on the angles were less than 0.1^{0} which can be compared to the nominal errors of about 0.4^{0} in azimuth and 0.23^{0} in dip.

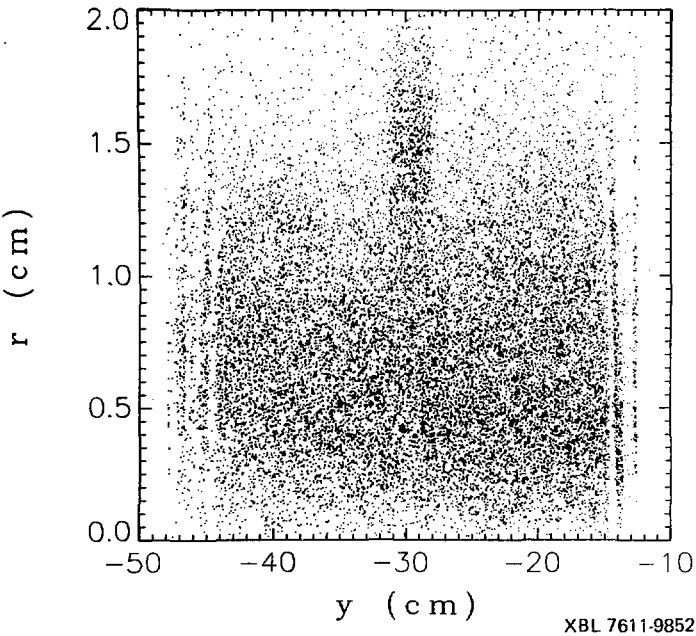

Fig. 31

E. Kinematic Fitting

An event reaching this point in the data processing looked no different than a bubble chamber event, and a standard version of SQUAW was used to do the kinematic fitting. It was necessary to code SQUAW for each reaction or hypothesis for which a fit was desired. This coding involved specifying the vertex structure for a given hypothesis, assigning masses to the reconstructed tracks, and specifying any missing tracks. The fitting was done in SQUAW by varying the kinematic parameters (azimuth, slope, and curvature) of the tracks and imposing the constraints of energy and momentum conservation. In the case of a single vertex event with no missing tracks, the fit was a 4-constraint (4C) fit. When one track was missing, the fit reduced to a 1-constraint (1C) fit. In the case of events with more than one vertex, all vertices were fit simultaneously. In these fits, there were additional constraints imposed requiring the connecting track to intersect both vertices.

Coding of hypotheses was done for many topologies which were never analyzed, so only those hypotheses used in kinematic fitting of event types on which analysis was done will be listed. The hypotheses coded for SC11 events (2-prong, single vertex) are listed in Table X; for SC22 events (4-prong, single vertex) in Table XI; and for SV11 events (2-prong with a vee) in Table XII. The fits which include MM (missing mass) are fits in which there were no energy-momentum constraints at the primary vertex, and the missing mass at that vertex was calculated.

The pulls for a sample of 4-prong, 4C events satisfying the hypothesis

$$\pi^- p \rightarrow \pi^- \pi^- \pi^+ p \qquad (4)$$

Table X. SC11 kinematic fit hypotheses.

$\pi^-p \to \pi^-p$	$\pi^-p \to \pi^-p\pi^0$	$\pi^-p \to \pi^-p$ MM
$\pi^-p \to K^-pK^0$	$\pi^-p \to K^-p$ MM	
$\pi^-p \to \pi^-\pi^+n$	$\pi^-p \to \pi^-\pi^+$ MM	
$\pi^-p \to K^-K^+n$	π^- K^-K^+ MM	
$\pi^-p \to \pi^-K^+\Lambda^0$	$\pi^-p \to \pi^-K^+\Sigma^0$	$\pi^-p \to \pi^-K^+$ MM

Table XI. SC22 kinematic fit hypotheses.

$\pi^-p \to \pi^-\pi^-\pi^+p$	$\pi^-p \to \pi^-\pi^-\pi^+p\pi^0$	$\pi^-p \to \pi^-\pi^-\pi^+p$ MM
$\pi^-p \to \pi^-K^-\pi^+pK^0$	$\pi^-p \to \pi^-K^-\pi^+p$ MM	
$\pi^-p \to \pi^-\pi^-\pi^+\pi^+n$	$\pi^-p \to \pi^-\pi^-\pi^+\pi^+$ MM	
$\pi^-p \to \pi^-K^-\pi^+K^+n$	$\pi^-p \to \pi^-K^-\pi^+K^+$ MM	
$\pi^-p \to \pi^-\pi^-\pi^+K^+\Lambda^0$	$\pi^-p \to \pi^-\pi^-\pi^+K^+\Sigma^0$	$\pi^-p \to \pi^-\pi^-\pi^+K^+$ MM
$\pi^-p \to \pi^-K^-K^+p$	$\pi^-p \to \pi^-K^-K^+p\pi^0$	$\pi^-p \to \pi^-K^-K^+p$ MM
$\pi^-p \to \pi^-\pi^-K^+pK^0$	$\pi^-p \to \pi^-\pi^-K^+p$ MM	

Table XII. SVII kinematic fit hypotheses.

$\pi^- p \rightarrow \pi^- \pi^+ \Lambda^0 K^0$, $\Lambda^0 \rightarrow \pi^- p$
$\pi^- p \rightarrow \pi^- \pi^+ \Lambda^0$ MM , $\Lambda^0 \rightarrow \pi^- p$
$\pi^- p \rightarrow \pi^- K^+ \Lambda^0$, $\Lambda^0 \rightarrow \pi^- p$
$\pi^- p \rightarrow \pi^- K^+ \Sigma^0$, $\Sigma^0 \rightarrow \Lambda^0 \gamma$, $\Lambda^0 \rightarrow \pi^- p$
$\pi^- p \rightarrow \pi^- K^+ \Lambda^0 \pi^0$, $\Lambda^0 \rightarrow \pi^- p$
$\pi^- p \rightarrow \pi^- K^+ \Lambda^0$ MM , $\Lambda^0 \rightarrow \pi^- p$
$\pi^- p \rightarrow \pi^- \pi^+ K^0 \Lambda^0$, $K^0 \rightarrow \pi^- \pi^+$
$\pi^- p \rightarrow \pi^- \pi^+ K^0 \Sigma^0$, $K^0 \rightarrow \pi^- \pi^+$
$\pi^- p \rightarrow \pi^- \pi^+ K^0$ MM , $K^0 \rightarrow \pi^- \pi^+$
$\pi^- p \rightarrow K^- p K^0$, $K^0 \rightarrow \pi^- \pi^+$
$\pi^- p \rightarrow K^- p K^0 \pi^0$, $K^0 \rightarrow \pi^- \pi^+$
$\pi^- p \rightarrow K^- p K^0$ MM , $K^0 \rightarrow \pi^- \pi^+$
$\pi^- p \rightarrow \pi^- p K^0 K^0$, $K^0 \rightarrow \pi^- \pi^+$
$\pi^- p \rightarrow \pi^- p K^0$ MM , $K^0 \rightarrow \pi^- \pi^+$
$\pi^- p \rightarrow \pi^- K^+ K^0 n$, $K^0 \rightarrow \pi^- \pi^+$
$\pi^- p \rightarrow \pi^- K^+ K^0$ MM , $K^0 \rightarrow \pi^- \pi^+$
$\pi^- p \rightarrow K^- \pi^+ K^0 n$, $K^0 \rightarrow \pi^- \pi^+$
$\pi^- p \rightarrow K^- \pi^+ K^0$ MM , $K^0 \rightarrow \pi^- \pi^+$

were calculated. A histogram of the azimuth pull is shown in Fig. 32(a), the slope pull in Fig. 32(b), and the curvature pull in Fig. 32(c) for the beam tracks in this sample. The superimposed curves are Gaussians of unit width, normalized to have the same area as the histogram. The pulls are very good, indicating that the beam parameters and errors are well known. Fig. 33 shows histograms of the pulls for the outgoing tracks from this same sample of events. In this case also, the pulls look very good, indicating an understanding of the system optics and errors.

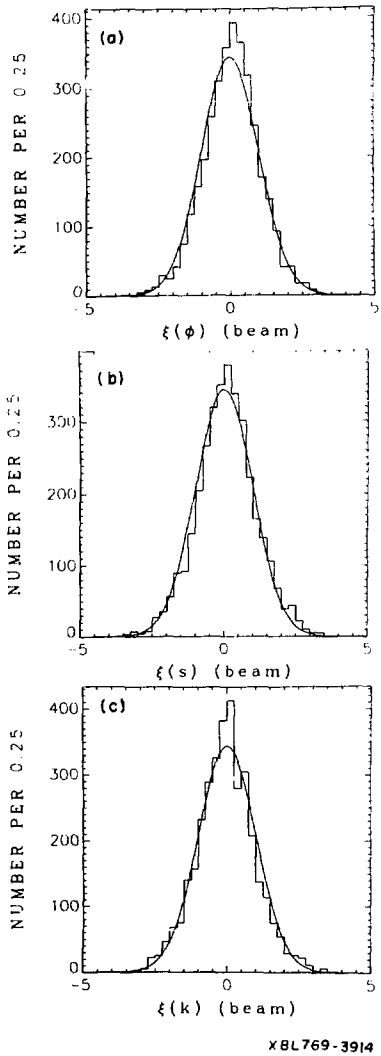
(a)
NUMBER PER 0.25
400
300
200
100
0
-5
0
5
ξ(φ) (beam)
(b)
NUMBER PER 0.25
300
200
100
0
-5
0
5
ξ(s) (beam)
(c)
NUMBER PER 0.25
400
300
200
100
0
-5
0
5
ξ(k) (beam)
XBL769-3914

Fig. 32

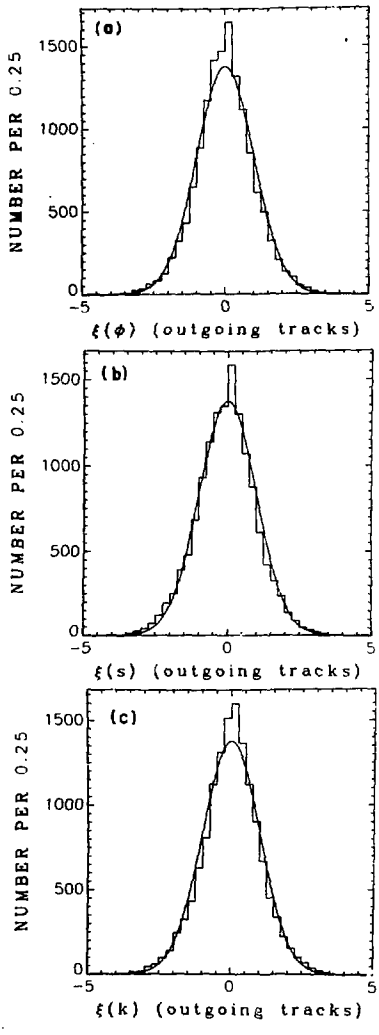
(a)
NUMBER PER 0.25
1500
1000
500
0
-5
0
5
ξ(φ) (outgoing tracks)
(b)
NUMBER PER 0.25
1500
1000
500
0
-5
0
5
ξ(s) (outgoing tracks)
(c)
NUMBER PER 0.25
1500
1000
500
0
-5
0
5
ξ(k) (outgoing tracks)
XBL769-3913

Fig. 33

V. Cross Section Calculation

A. Cross Section

Given a number of events, N_{ev}, for a particular reaction or topology in a certain region of phase space, the cross section to which this number of events corresponds is determined by the equation

$$(1 - N_{ev}/N_{beam}) = e^{-\sigma L \rho N_o/A} , \tag{13}$$

where

N_{beam} = number of beam tracks passing through the hydrogen target

σ = cross section corresponding to N_{ev} events (cm^2)

L = path length of the beam in the hydrogen (cm)

ρ = density of hydrogen (gm/cm^3)

N_o = 6.022×10^{23} $mole^{-1}$

A = atomic weight of hydrogen = 1.008 gm/mole.

To simplify Eq.(13), the exponential is expanded in a series which can be truncated after the linear term. Since the trigger rate in this experiment was small,

$$N_{ev}/N_{beam} \sim 10^{-3},$$

this is an excellent approximation. Eq. (13) then becomes

$$N_{ev}/N_{beam} = \sigma L \rho N_o/A . \tag{14}$$

1. Path Length

The path length of the beam in the liquid hydrogen is very well known since cuts were made in the analysis programs on the primary vertex position of the event. The length of hydrogen in which events were accepted was 28 cm. However, a few small corrections must be made to

this number. There is a small loss of path length due to small perturbations in the assumed cylindrical geometry of the liquid hydrogen flask, such as the domes at the ends of the flask. Calculations indicate that these corrections are very small, on the order of a few tenths of a percent. The exact number depends on the absolute position of the target. A loss in path length also results from the method of event selection for measurement employed. As was described in Ch. IV, events which appeared to originate in the target counter or upstream of it were not measured. To determine the loss of hydrogen events as a result of this cut, a comparison was made of the distributions of the fitted vertex positions between a sample of 4-prong events in which the cut was made and a sample in which no cut was made. The two samples of data were normalized in the region

$$-41 \leq y < -31 \text{ cm},$$

where y is the fitted vertex y-coordinate position, where the cut had no effect. In the region upstream of this normalization region,

$$-44 \leq y < -41 \text{ cm},$$

the loss of events in the sample with the target counter cut was found to require a 3.7% correction to account for the lost events. Thus, when considering the full 28 cm of target length, this amounts to a correction of only 0.4%. This correction diminishes even more when those rolls in which no target counter cut was made are accounted for, resulting in a 0.3% correction. Combining this with an estimated geometrical correction yields a total correction of 0.5% to the target length with an estimated error of roughly the same size. Therefore,

$$L = 27.86 \pm 0.14 \text{ cm},$$

2. Density of liquid hydrogen

The density of the liquid hydrogen in the flask is directly related to the temperature of the liquid hydrogen, which in turn depends upon the pressure. During the running of the experiment, the absolute pressure of the liquid hydrogen was monitored continuously. The pressure never varied by more than ± 2 P.S.I. from the nominal pressure of 20 P.S.I.A. Relating the pressure to the temperature, a value of 21.4 ± 0.4^{0} K. is obtained. Tabulated density measurements[97] determine the density to be

$$\rho = 0.0690 \pm 0.0005 \ gm/cm^3.$$

3. Beam flux

The number of beam particles entering the hydrogen target was determined from the scaler information which was recorded during the running. The quantity which was scaled is logically defined as

$$BEAM = \Sigma M \cdot P \cdot Q \cdot HT,$$

where ΣM is the OR of the five momentum hodoscope counters, and P, Q, and HT refer to the respective beam line counters. This quantity provides only a crude estimate of the actual integrated beam flux through the liquid hydrogen; corrections were made for interactions of the beam in the target and the target box, beam contamination, and beam tracks not traversing the entire length of the liquid hydrogen target.

Beam interactions of concern are only those which occurred in the target counter, the target box, or the liquid hydrogen. Any interaction which occurred prior to the beam reaching the hydrogen target counter can be ignored as negligible.

Prior to entering the target fiducial volume at $y = -44$ cm, the beam

passed through 4 cm of scintillator, foam, epoxy, mylar, and liquid hydrogen. Since it is difficult to determine the exact amounts of various materials in the path of the beam, and the cross sections of pions on these materials, the interaction rate in this region is assumed to be approximately the same as that due to the same thickness of liquid hydrogen. Based on calculations which will be made later in this section, a more accurate estimate of the interaction rate is 1.35 ± 0.15 times that of hydrogen for the same thickness. The total cross section for π^- on protons at 4 GeV/c is approximately 30 mb. Using Eq. (14), the interaction rate in hydrogen is found to be

$$N_{ev}/N_{beam} = 1.23 \times 10^{-3} L, \qquad (15)$$

where L is the thickness of hydrogen through which the beam passes. Using the factor of 1.35 ± 0.15 for the upstream material, Eq. (15) becomes

$$N_{ev}/N_{beam} = (1.66 \pm 0.18) \times 10^{-3} L.$$

In 4 cm of material, the interaction rate is $(6.64 \pm 0.72) \times 10^{-3}$.

The interactions in the liquid hydrogen also led to a decrease in the total beam path length. The interaction rate in the 28 cm length of liquid hydrogen is calculated to be 0.0344 from Eq. (15). The error is negligible. The correction to the number of beam particles is only half this number since an average interacting beam track passes through half the hydrogen before interacting. Combining this loss with the loss due to interactions in the 4 cm of material upstream of the liquid hydrogen gives a 2.4 ± 0.1% loss of beam tracks due to interactions.

Contamination of the beam comes from two sources: pion decay,

$$\pi^- \rightarrow \mu^- \bar{\nu}_\mu,$$

and production of K^- and $\bar{p}$ at the primary target. The muon

contamination in the beam results primarily from pion decays upstream of the target. As a function of distance from the target counter, the percentage of decays producing a muon which hit the target counter was calculated. This acceptance as a function of distance is shown in Fig. 34. The acceptance differs appreciably from zero only downstream of the last horizontal bending magnet in the beam line. The decay rate per inch is 1.14×10^{-4} in.$^{-1}$. Multiplying this by the acceptance integrated over the decay distance (73. in.), gives the expected μ^- contamination, 0.8%. The estimated error on this number is 0.4%.

No definitive study of the beam used in this experiment has ever been made to determine the K^- and $\bar{p}$ contamination, though estimates place the K^- contamination at less than 1%, and the $\bar{p}$ contamination less than this. A study of an earlier, but similar Bevatron secondary beam[98] which produced π^-'s at 4 GeV/c determined the ratio of K^- to π^- production to be $\sim 10^{-4}$. Production of $\bar{p}$ was even smaller. Thus, this contamination can be neglected.

The largest correction to the beam path length is due to those beam particles which passed through the hydrogen target counter, but not through the liquid hydrogen. The misalignment of the hydrogen target counter with respect to the liquid hydrogen flask during much of the running was largely responsible for this effect. In addition, there were also some beam tracks which passed through the target counter and into the flask, but as a result of the angle of the track, they exceeded the radial limits of the flask prior to reaching the end.

In order to determine this correction, the assumption was made that the beam flux outside the target fiducial volume was proportional to the

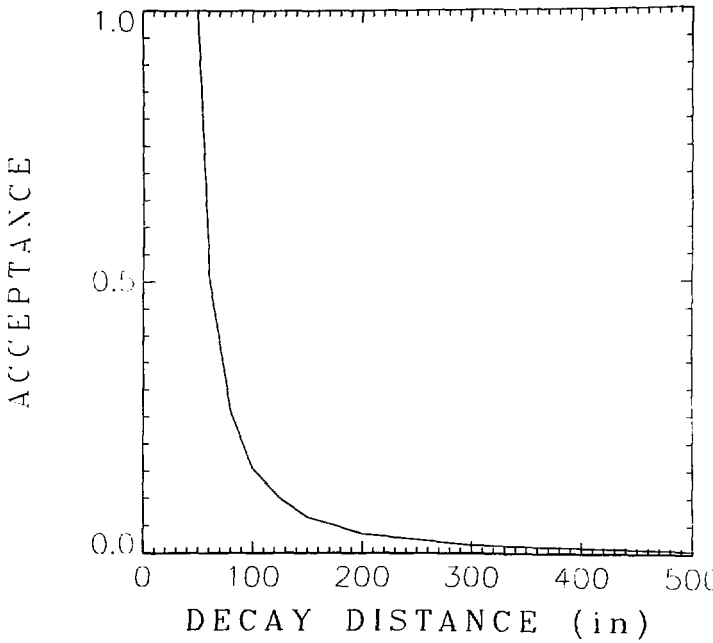

Fig. 34

number of interactions outside the fiducial volume, but within the foam target box. (The number of beam tracks passing outside the target box altogether is negligible.) Implicit in this assumption is the assumption that the target box material is homogeneous. Although this is not strictly true, geometrical arguments set bounds on the correction which are consistent with the determination based on this assumption. Since the pion cross section in the foam (plus epoxy and mylar) is not the same as that in hydrogen, it was necessary to correct the number of interactions in the foam by the ratio of the pion cross section in hydrogen to the cross section in foam. Then the ratio of interactions inside and outside the target fiducial volume was equal to the ratio of the beam flux inside and outside the fiducial volume.

Since this cross section ratio was unknown, it was determined empirically. Vertex intersection coordinate information for a large sample of 4-prong events was utilized. The sample contained only events in which the y-coordinate of the vertex intersection point was within the fiducial volume,

$$-44 \leq y < -16 \text{ cm.}$$

A least squares fit was made to a histogram of the radial distribution of the vertex intersection point with assumed functional form

$$N(r) = Are^{-(r-r_0)^2/2\sigma^2}, \text{ for } r < 1.15 \text{ cm}$$

$$= \alpha Are^{-(r-r_0)^2/2\sigma^2}, \text{ for } r \geq 1.15 \text{ cm},$$

where N(r) is the number of events in a given interval of width Δr around

the radial coordinate r, and r is the distance from the beam line (center line of the target) to the vertex intersection point. The parameters A, r_0, σ, and α were varied in the fit. The histogram of the data and the resulting fit (the solid curve) is shown in Fig. 35. This data included events from all rolls measured. In addition, similar fits were made restricting the events to certain groupings by roll number. Roll group I consists of the first 22 rolls of film (matrix 1 trigger). Roll group II consists of rolls 23 to 53 (matrix 2 trigger). Roll group III consists of rolls after roll 53, and is separated from roll group II since the hydrogen target counter was realigned after roll 53. The resulting values of α determined in these fits are given in Table XIII. Note that α is the desired ratio of the foam cross section to the hydrogen cross section, and is the basis for the correction factor used earlier in this section to calculate the interaction rate of the beam prior to entering the flask.

Since different roll groups reflect different trigger conditions, it is not expected that the ratio α should be the same for different roll groups. However, roll groups II and III had identical triggers, and hence α should be the same for these two roll groups. The weighted average of these two values of α was calculated and is included in Table XIII. Also included is the value of α obtained in the global fit to all roll groups.

With the information in Table XIII, the factor needed to correct for beam tracks not passing through the fiducial volume was calculated,

$$F_{beam} = \frac{N_{in}}{N_{in} + N_{out}/\alpha}, \qquad (16)$$

where

N_{in} = number of interactions inside the target fiducial volume

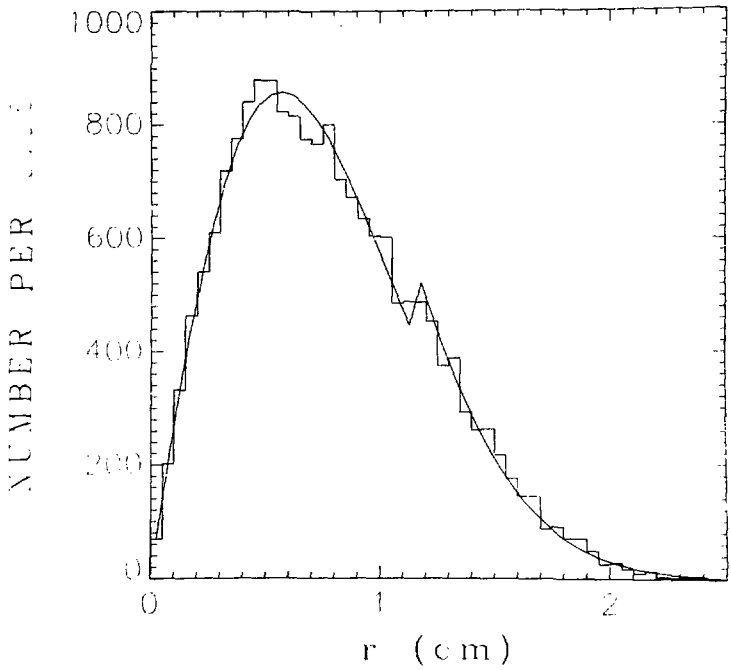

Fig. 35

Table XIII. α as a function of roll group.

Roll group	α
I (1-22)	1.24 ± 0.07
II (23-53)	1.50 ± 0.07
III (54-88)	1.38 ± 0.12
II + III	1.47 ± 0.06
I + II + III	1.31 ± 0.04

Table XIV. F_{beam} as a function of roll group.

Roll group	F_{beam}
I	0.854 ± 0.037
II	0.849 ± 0.038
III	0.963 ± 0.010
I + II	0.851 ± 0.038

Table XV. Cross section correction factors.

Correction factor	Value
L	27.86 ± 0.14 cm
ρ	0.069 ± 0.0005 gm-cm^{-3}
$F_{int.}$	0.976 ± 0.001
F_{decay}	0.992 ± 0.004
F_{beam} (I + II)	0.851 ± 0.038
F_{beam} (III)	0.963 ± 0.010

N_{out} = number of interactions outside the target fiducial volume. The correction factor determined for each of the roll groups is given in Table XIV. The correction factors for roll groups I and II are expected to be the same since the target counter was identically positioned for both roll groups. Thus, the weighted average of the two factors was calculated and is given as the last entry in Table XIV. The errors include contributions due to the uncertainties in the assumptions.

4. Cross section

In Table XV is a compilation of all the factors discussed in this section necessary for the calculation of cross sections. $F_{int.}$ and F_{decay} are the correction factors due to beam interactions and the decay of the beam respectively. Using the values given, Eq. (14) becomes

$$\sigma = (871 \pm 8)\ N_{ev}/N_{beam}\ \text{mb}, \tag{17}$$

where

$$N_{beam} = (0.824 \pm 0.037)\ N'_{beam\ I,II} + (0.932 \pm 0.010) N'_{beam\ III}. \tag{18}$$

$N'_{beam\ I,\ II}$ is the raw number of beam tracks entering the target as determined from scaler information for events in roll groups I and II. $N'_{beam\ III}$ is the similar quantity for events in roll group III. These two quantities are listed in Table XVI, along with N_{beam} as calculated using Eq. (18). The different values of the beam flux for the different topologies was not uniform.

Table XVI. Beam flux as a function of topology.

Beam flux	Topology		
	2-prong	4-prong	Visible vee
$N'_{beam\ I,\ II}$	1.033×10^8	1.079×10^8	1.079×10^8
$N'_{beam\ III}$	0.546×10^8	0.893×10^8	1.612×10^8
N_{beam}	$(1.360 \pm 0.038) \times 10^8$	$(1.721 \pm 0.041) \times 10^8$	$(2.391 \pm 0.043) \times 10^8$

B. Acceptance and Efficiencies

Eq. (17) is based on the expectation that the number of events, N_{ev}, of the desired type is known. If the acceptance of the apparatus for detecting the desired events is not 100%, or there are inefficiencies in the abstraction of the events, a correction must be made to the measured number of events to account for the losses. These corrections fall into two categories. In the first category are geometry dependent acceptances and efficiencies which are corrected for on an event by event basis. These include corrections due to the following:

(1) recoil acceptance - geometric acceptance of the system recoiling against the proton,

(2) trigger acceptance of the fast forward proton, and

(3) Cerenkov counter rejection of events with a fast pion.

In the second category are corrections which are only slightly geometry dependent or are geometry independent. These include corrections due to:

(4) proton interactions upstream of the trigger hodoscopes,

(5) secondary interactions of outgoing tracks in the target box,

(6) Cerenkov counter rejection of fast proton events,

(7) detection efficiency of vees hidden in the target box,

(8) software elimination of events with poor fit χ^2 probabilities,

(9) scanning efficiency, and

(10) measuring efficiency.

Not included in the above list are corrections which were considered, but trivially found to be negligible (e.g., loss of events through software

problems or bad tapes). Also not included is a discussion of the effect of ambiguous kinematic fits on the selection of the event sample. The corrections required by these ambiguities are so highly dependent on the reaction being considered that they are handled separately for each final state. The discussion of these corrections is in Ch. VI.

Since the application of the geometry dependent corrections to the data depends on the analysis procedure, it is pertinent to briefly mention the two different methods of analysis utilized at this time. In the first method of analysis, each real event is assigned a weight equal to the inverse of its acceptance. If the acceptance is below a fixed minimum value, the event is thrown out. After each event is "corrected up" by the assigned weight, the data is binned as a function of some variable (e.g., mass or u). The resulting histogram purports to give the distribution of the actual cross section as a function of the binning variable. This method of analysis is fine as long as all events of interest have a reasonable acceptance. If however, there are some events of interest which have a very small acceptance, or none at all, the second method of analysis provides more reliable results. The procedure in this case involves the generation of Monte Carlo events distributed according to a model hypothesized to reproduce the actual distribution (cross section) of interest. These Monte Carlo events are then "corrected down" by assigning each one a weight equal to the acceptance of the event. No acceptance correction is made to the real events, but if real events of certain configurations are eliminated, the corresponding Monte Carlo events are also eliminated. Then a comparison or fit can be made between the "corrected down" Monte Carlo events and the real events. When the weighted

Monte Carlo distribution reproduces the distribution of the real events, the actual distribution is given by the unweighted Monte Carlo distribution.

1. Recoil acceptance

One of the disadvantages of the streamer chamber is that there are certain event configurations which are unmeasurable, or even unobservable in a streamer chamber, but pose no measurement problem in a bubble chamber. The events included in this category are those in which one or more tracks dips steeply (i.e., has a large relative momentum component along the direction of the applied electric field) so that it flares, becoming very broad and difficult to measure; and those in which one or more outgoing tracks is emitted such that it is obscured from the cameras by the target box.

The regions of poor acceptance were determined by considering the angular distribution of a sample of outgoing prongs. The angle θ was defined to be the polar angle of the outgoing track from the y-axis, and the angle ψ was defined to be the azimuthal angle about the y-axis, with $\psi = 0^{\circ}$ along the x-axis. The distribution of the number of tracks observed as a function of θ showed no depletion of events except in the region $50^{\circ} \lesssim \theta \lesssim 130^{\circ}$. The two conical regions outside of this band will be referred to as region I. Within this band, analysis showed that the depletion was due to the loss of events in the azimuthal regions defined by $60^{\circ} \lesssim \psi \lesssim 120^{\circ}$ (region III), and $240^{\circ} \lesssim \psi \lesssim 300^{\circ}$ (region IV). The region not within these defined ψ bands, but within the θ band, will be referred to as region II. The depletion of tracks in region III is due to target obscuration, and in region IV to flaring.

The correction due to recoil acceptance is made to the event as a whole, but is based on the acceptance of each track considered independently of the others. No correction is made for tracks falling in region I. The trigger proton will always fall in region I due to the requirement that it reach the downstream trigger system. All events with a track falling in either region III or region IV are eliminated. This cut is rather liberal since some good events are eliminated. However, it was found that there were many events measured, in region IV particularly, which because of the nature of the tracks were very poorly measured, and hence it was better to eliminate them. The liberality of this cut insures that the depletion of tracks is contained in regions III and IV. The correction made for tracks in region II is dependent upon the analysis procedure. If the procedure involves correcting up real events, then the event is assigned a weight equal to $(1.5)^n$, where n is the number of tracks failing in region II for the event in question. The number 1.5 is based on the assumption of azimuthal symmetry (the only defined direction in the initial state is the beam direction, and hence there can be no preferred azimuthal orientation), the fact that the eliminated regions (III and IV) encompass $2\pi/3$ of the azimuth, and the assumption that the directions of all the outgoing tracks are uncorrelated. The assumption that the outgoing track directions are uncorrelated is not true, but the effects of the correlation are significant only when the recoil system's invariant mass is close to the sum of the constituent masses making up the system. A correction is made which eliminates the effects of this correlation in the manner in which the proton trigger acceptance is calculated (to be discussed later in this section). If the analysis procedure involves correcting down

Monte Carlo events, then each Monte Carlo event (and each real event) is given unit weight, unless a track falls in region III or IV, in which case it is eliminated. Clearly, the correlation problem does not arise here.

2. Trigger acceptance

The correction for the trigger acceptance is the most important correction made to the data as the trigger requirement eliminates approximately 95% of the cross section. The experiment was run under two different trigger conditions as determined by the two trigger coincidence matrices described in Ch. III. The acceptances for both matrices have been calculated in various manners suitable to different analyses.

As a first approximation, the acceptance can be defined as a function of two variables; the momentum of the proton in the laboratory system (P_{lab}), and the polar angle of the proton from the y-axis (θ_{lab}). As mentioned earlier, the physics should be independent of the azimuthal angle of the proton, whereas the triggering system is not, so the acceptance can be averaged over the azimuthal angle. The determination of this acceptance function was made by establishing a grid of points in momentum and polar angle. The points were separated by 0.25 GeV/c in momentum and spanned the region from 1.25 GeV/c to 4.50 GeV/c. The separation in angle was 2^0 and the points spanned the region from 0^0 to 20^0. For each grid point, 500 tracks were generated with fixed momentum and polar angle, with the azimuthal angle generated randomly to fill 2π radians, and with the beginning points of the tracks generated randomly to fill the liquid hydrogen target volume. Each track was swum through the magnetic field inside the streamer chamber and through the fringe field outside the streamer chamber

to the downstream hodoscope trigger system. The hodoscope counters in H1 and H2 which were intercepted by the track were determined. The acceptance for a given grid point was defined to be the number of tracks which intercepted a pair of counters giving a valid coincidence divided by the number of tracks generated. The acceptance for a given point not on the grid is determined by linear interpolation in two dimensions from the four surrounding grid points.

The resulting acceptances for coincidence matrices 1 and 2 are shown in Figs. 36 and 37 respectively, as contours of constant acceptance in the θ_{lab} - P_{lab} plane. The dashed curves are the acceptance contours, the adjacent numbers representing the value of the acceptance along the contour. The solid curves shown are contours of M_x, the recoil mass from the proton.

For certain regions of proton momentum and angle, this method of acceptance calculation gives a poor estimate of the acceptance. The problem is connected with the recoil acceptance previously discussed, and arises as a result of the correlation between the direction of the proton track and the directions of the other outgoing tracks. The correlation becomes greater as the number of outgoing tracks diminishes, or as the recoil mass from the proton approaches the sum of the masses of the constituents comprising the recoil system. Thus, in the calculation of the trigger acceptance just described, contributions to the acceptance from proton azimuth angles were included which, if the proton were considered as a track in a real event, might have a very small average recoil acceptance.

There are two solutions to this problem, the suitability of each depending upon the analysis procedure. The solution suitable for analysis in which the real events are corrected up by the inverse of the acceptance

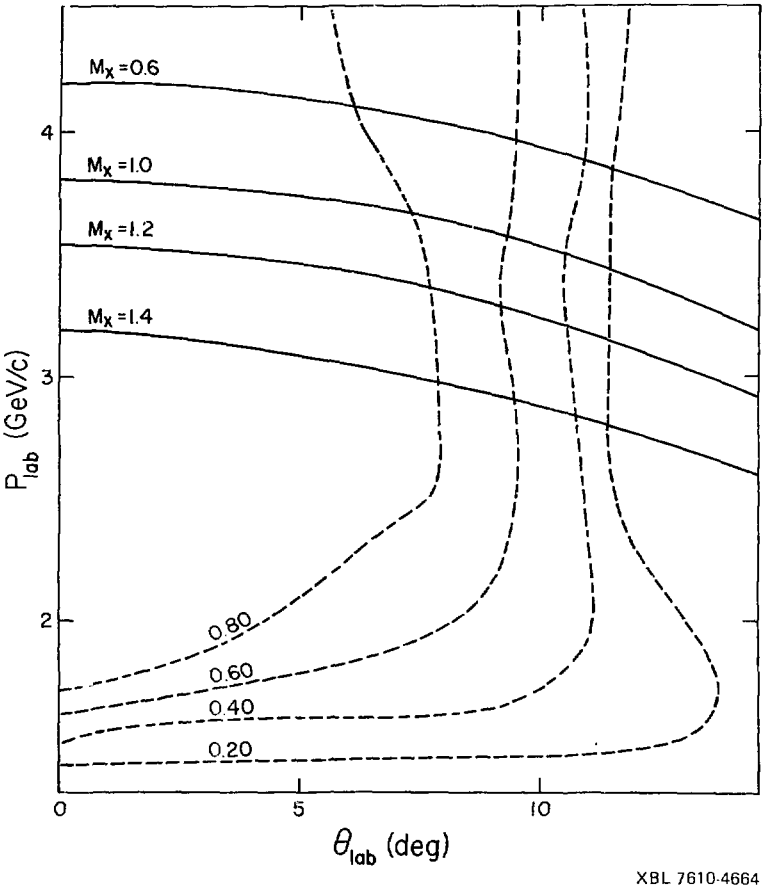
M_X =0.6
M_X =1.0
M_X =1.2
M_X =1.4
0.80
0.60
0.40
0.20
P_{lab} (GeV/c)
θ_{lab} (deg)
0
5
10
2
3
4
XBL 7610-4664

Fig. 36

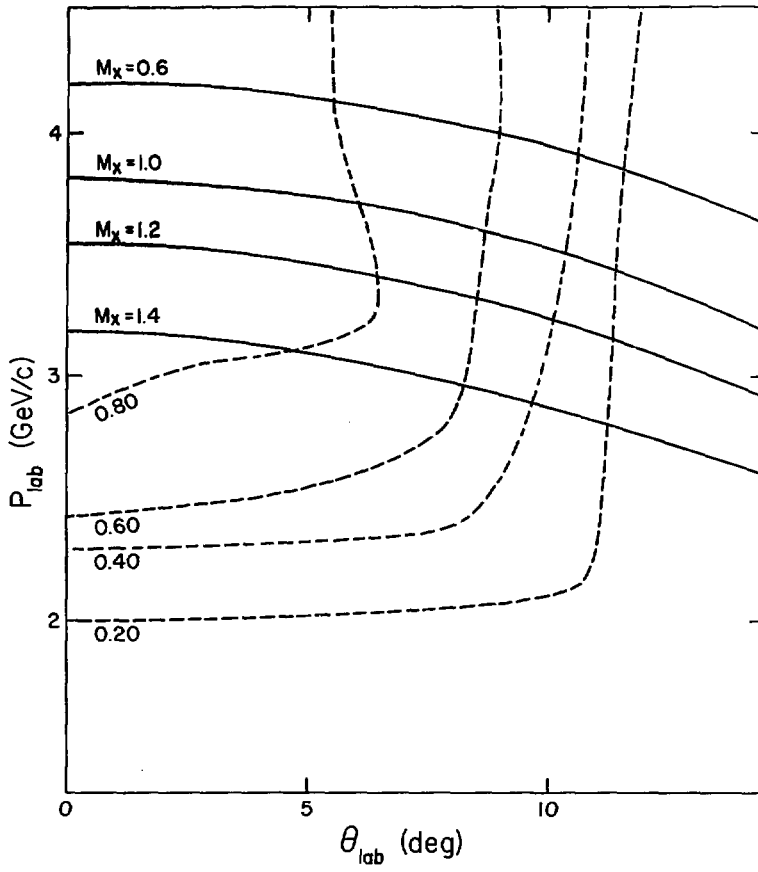

XBL 7610-4666

Fig. 37

involved generation of proton tracks for points in a grid of momentum and polar angle with randomly generated azimuth angle and vertex position, as was previously done. A recoil system, conserving energy and momentum, was generated against the proton. This recoil system was then allowed to decay isotropically in its center of mass into a system of pions. (The Monte Carlo event generation program SAGE[99] was used to generate the n-body recoil system.) The proton was swum through the magnetic field to the trigger system. The acceptance was calculated at each point in the grid by dividing the number of events with valid coincidences (each weighted by the recoil weight) by the number of events generated. The entire procedure was repeated for each recoil topology of interest (one to four pions in the recoil system).

In addition to providing realistic proton acceptances, this method of calculation also eliminates the problem related to track independence in assigning the recoil acceptance weight. To see this, consider an event with three pions recoiling against a proton, with recoil mass just above threshold for three pions. The three pions will then have essentially the same momenta and production angles. If the three tracks all fall in region II, the event will be assigned a recoil weight of $(1.5)^3$, whereas the weight should really be 1.5 since the 3-momenta of the pions are 100% correlated. However, this effect is cancelled out by the trigger acceptance which will have a weight of $(1.5)^3$ for two-thirds of the events generated, and a weight of zero for the other one-third, giving an average weight of $(1.5)^2$. The recoil weight is divided by this factor, yielding a total weight of 1.5 as required.

The one weak point in the method just described is the assumption of

isotropic decay of the recoil system. To produce a really rigorous acceptance, a model of the recoil system obtained from the data should be used to generate the recoil system decay, rather than phase space. This new acceptance, when applied to the data, would yield a more reliable model to be used in the generation of the recoil decay to produce a new acceptance. This procedure would be repeated until a static condition ensued. However, the improvement expected in the acceptances through this procedure is estimated to be minimal compared to the corrections which must be made because so much of phase space has zero acceptance. Therefore, the procedure was not implemented.

In Fig. 38 is shown the acceptance for elastic scattering events as a function of lab momentum (for a fixed beam, there is only one independent variable) for matrix 1 (matrix 2 is similar). The dashed curve is the acceptance as it was originally calculated. The solid curve is the acceptance when the recoil weight is taken into account. There is seen to be a significant difference between the two acceptances. As mentioned earlier, elastic scattering is the worst case, and the difference is not as great for higher multiplicity events except near the threshold of the recoil system.

The solution suitable for analysis in which Monte Carlo events are corrected down by the acceptance is simpler and cleaner than the solution previously described, but, as will be seen, is clearly restricted to this type of analysis. Instead of calculating the acceptance as a function of two variables, it is calculated as a function of all three proton variables; p, θ and ϕ, the azimuthal angle of the proton around the y-axis. A three-dimensional grid was established with 10^{o} separation in azimuth angle. For each point in the grid, a number of proton tracks were

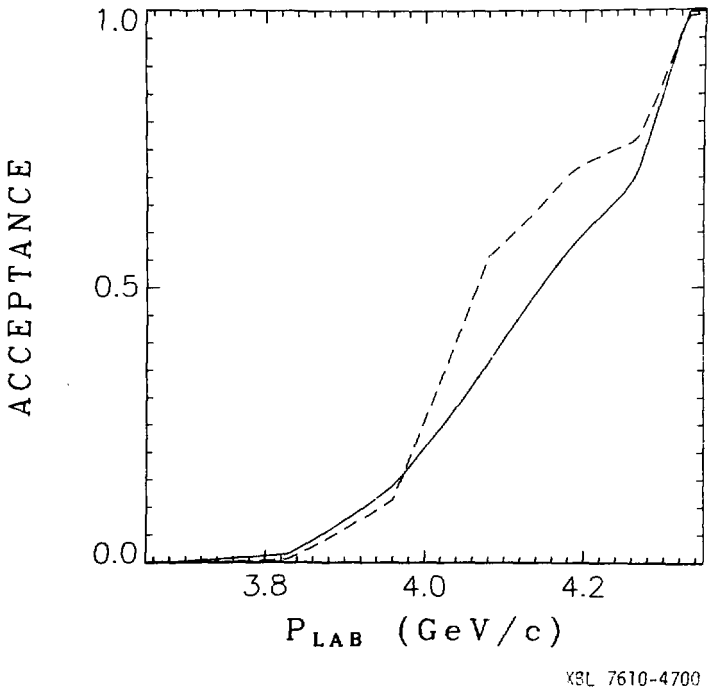

XBL 7610-4700

Fig. 38

generated along the length of the hydrogen target, and swum through the magnetic field to the trigger system. The acceptance was calculated as the number of valid coincidences divided by the number of tracks generated. The three-variable acceptance function solves the problem of correlation between the proton direction and the directions of the recoil particles, which was caused by azimuthal averaging. Acceptances for points not in the grid are calculated by linear interpolation between the eight adjacent grid points.

The acceptance calculations described above apply only to events in which the proton is produced at the primary vertex. The acceptance must be recalculated for events in which a fast Λ^0 is produced at the primary vertex, which then decays into $p\pi^-$, the proton providing the trigger. Since the number of events with a fast Λ^0 was small compared to the number with a fast proton, and the analysis done on these events was not planned to be as extensive as that done on the fast proton events, the acceptance was calculated only as a function of two variables; the Λ^0 momentum and production polar angle with respect to the y-axis. The correlation between the directions of the recoil particles and the direction of the triggering proton is small due to the extra kinematic freedom resulting from the Λ^0 decay. Thus, it was not necessary to extend the lambda acceptance calculation as was done for the proton.

A grid of points in lab momentum and polar angle were established for the lambda production. Tracks were produced with the beginning point randomly generated in the liquid hydrogen and a randomly generated azimuth angle. The lambdas were then allowed to decay downstream of the target in accordance with the known lambda lifetime. The generated decay was

isotropic in the lambda rest frame. The produced proton was swum through the remaining magnetic field to the hodoscopes, and the acceptance calculated.

For each of the two coincidence matrix configurations, three acceptances were calculated. The first acceptance was calculated under the assumption that a lambda decay anywhere upstream of the hodoscopes was acceptable as long as the resulting proton created a coincidence. The second acceptance was calculated with the proviso that only lambdas decaying within the streamer chamber volume were acceptable. This acceptance was used to correct events from those rolls in which both visible vee events and hidden vee events were measured. A hidden vee event is an event which is measured as a single vertex event, but in the vertex fitting routine, it is found that there is a vee decay hidden within the target box. Thus, if one is interested in analyzing 2-prong events with a vee, this acceptance is used for those rolls in which all 2-prong vee events plus all 4-prong events were measured. In the calculation of the third acceptance, only lambdas decaying within the streamer chamber volume but outside the target box were acceptable. This acceptance was used to correct events from those rolls in which only visible vees were measured. (There were no rolls in which only hidden vees were measured.) The first acceptance was used only as a check.

The resulting acceptances are shown in Figs. 39 and 40 for coincidence matrices 1 and 2 respectively as contours of constant acceptance in the θ_{lab} - p_{lab} plane. Note that the kinematic variables refer to the lambda, not the proton. The dashed curves are the contours of the second acceptance function, and the dotted and dashed curves are the contours of the third

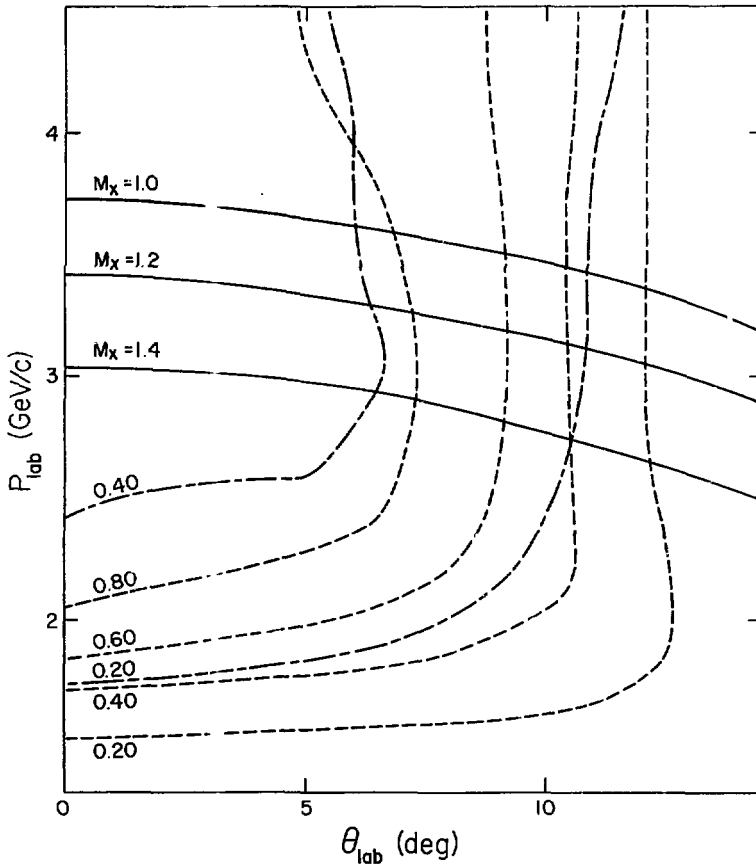

XBL 7610-4665

Fig. 39

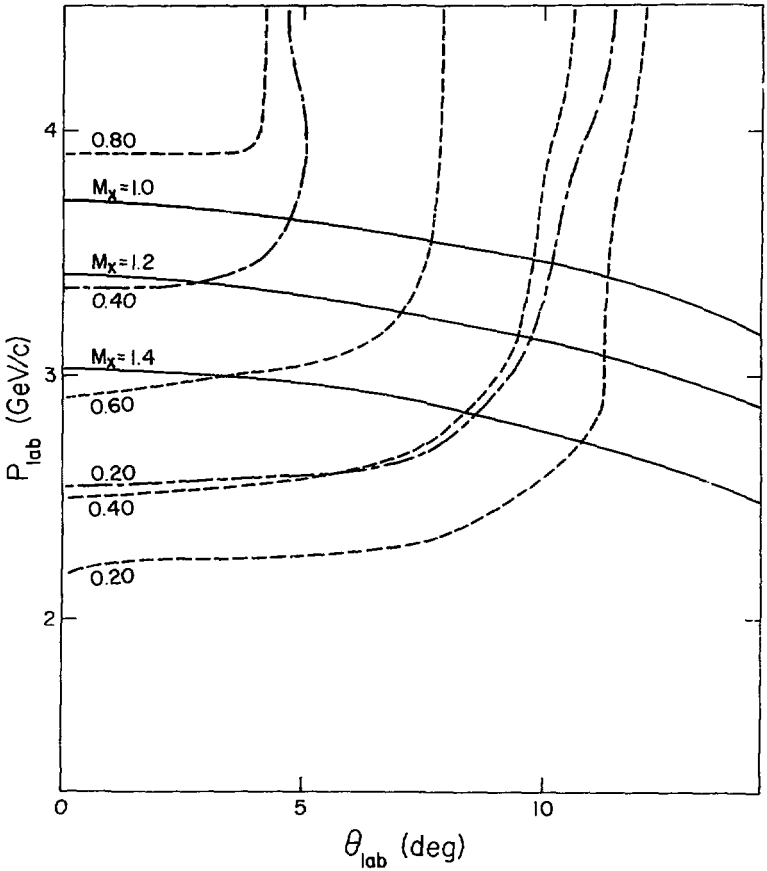

XBL 7610-4663

Fig. 40

acceptance. As can be seen from the relative acceptances, approximately one-half of the fast lambda decays take place within the target box. The solid curves are contours of constant recoil mass from the Λ^0

3. Cerenkov counter pion rejection

It occasionally happened that a good event, with a proton which traversed both hodoscopes and provided a valid coincidence did not trigger as a result of a fast pion which went through the Cerenkov counter and radiated. The correction for this was accomplished simply for analyses involving correcting Monte Carlo events down. An acceptance for pions entering a region in space defined by the Cerenkov counter active region was calculated as a function of three variables; the pion momentum, polar angle, and azimuthal angle. In a manner totally analogous with that used to calculate the proton acceptance, a three-dimensional grid was established, and pions swum out through the magnetic field to the Cerenkov counter. The acceptance was defined as the number of pions passing through the Cerenkov counter active region divided by the number of pions generated. The acceptance calculation was done separately for both positively and negatively charged pions. This acceptance was applied during analysis by eliminating all events (both real and Monte Carlo) with unit acceptance for a pion to pass through the Cerenkov counter. In addition, Monte Carlo events with nonzero acceptance were corrected down by a factor equal to

$$C_3 = 1 - \text{acceptance}.$$

The acceptance to be used in analyses in which real events are corrected up was more difficult to calculate, and less reliable. Fortunately, the correction is small, as will be seen. It was desired to make this correction as a function of proton kinematic variables rather than the pion

variables in order to correct for missing events. To estimate this correction, Monte Carlo events were generated in which a proton was produced recoiling against a system of four pions. The proton was required to be accepted by the hodoscope system. One of the pions was assumed to be positively charged, and its detection efficiency in the Cerenkov counter was evaluated using the function just described. The average pion acceptance was calculated as a function of proton lab momentum and polar angle. It was found to be roughly independent of proton angle and to decrease monotonically with proton momentum. A cutoff was imposed at a proton momentum of 1.25 GeV/c since the proton acceptance was essentially zero below this momentum. The acceptance as a function of proton lab momentum is shown in Table XVII. A similar calculation was done assuming the pion of interest was negatively charged, and the resulting acceptance was found to be 25% of the π^+ acceptance, with the same functional dependence on proton momentum.

The acceptance calculated in this manner is expected to be in error because of the assumption of isotropic decay of the pion system. The principal source of error is the production of fast N^* or Λ resonances, which decay into a proton and one or more pions, resulting in more fast pions than would be expected from the isotropic decay model. In order to obtain a more reliable acceptance, it was necessary to make use of the experimental data.

During the experimental running, a special run was made in which the Cerenkov counter signal was not included in the trigger. This resulted in triggers in which both a proton and a pion traversed the Cerenkov counter in addition to the pion triggered events. From this run, a sample of

Table XVII. Cerenkov counter π^+ acceptance as a function of proton momentum.

Proton momentum (GeV/c)	Acceptance	Scaled acceptance
1.25	0.043	0.113
1.50	0.035	0.092
1.75	0.025	0.066
2.00	0.019	0.050
2.25	0.010	0.026
2.50	0.006	0.016
2.75	0.002	0.005
3.00	0.	0.

4-prong events which satisfied the 4C hypothesis

$$\pi^- p \rightarrow \pi^- \pi^- \pi^+ p \qquad (4)$$

in kinematic fitting, and in which the proton was the fast forward particle, was selected. Only those events in which the proton track, when extrapolated to the hodoscopes, provided a valid coincidence were acceptable. The sample contained 48 events. Of this number, 5 also had a π^+ which reached the region of space defined by the Cerenkov counter.

Another sample of 4-prong, 4C events was chosen, satisfying the same requirements as above except that the Cerenkov counter signal (in anti-coincidence) was included in the trigger. This sample contained 656 events with a fast proton, of which 37 also had a fast π^+ which reached the Cerenkov counter. The existence of any events with fast pions in this sample is due to the inefficiencies in the Cerenkov counter, particularly near the edges of the counter, and the fact that the definition of the region of space assigned to the Cerenkov counter was rather liberal. The information obtained from the comparison of these two samples of data allows a calculation of the average correction factor due to Cerenkov counter pion rejection to be made:

$$C_3 = \left(\frac{a_1}{a_2}\right)\left(\frac{b_2}{b_1}\right), \qquad (19)$$

where

a_1 = number of events with a fast proton but no fast pion with Cerenkov counter in trigger

a_2 = number of events with a fast proton with Cerenkov counter in trigger

b_1 = number of events with a fast proton but no fast pion without Cerenkov counter in trigger

b_2 number of events with a fast proton without Cerenkov counter in trigger.

Inserting the numbers quoted above into Eq. (19) gives a correction factor of $C_3 = 1.053 \pm 0.053$. Unfortunately, the error is large due to the poor statistics of the event sample without the Cerenkov counter in the trigger, but it is the best estimate available from the data.

In order to compare the experimental correction factor with the results from the Monte Carlo, the average acceptance of the Monte Carlo events was calculated by integrating the normalized observed momentum spectrum (over 1.25 GeV/c), weighted by the acceptance, over momentum. The average acceptance was calculated to be 0.019 as compared to the experimentally determined average,

$$\frac{C_3 - 1}{C_3} = 0.050.$$

The experimentally determined average is larger than the average obtained for the Monte Carlo events in accordance with expectations. It is expected that the variation of the acceptance with momentum is fairly well approximated by the Monte Carlo, even if the normalization is not. Thus, an improved estimate of the acceptance as a function of momentum is obtained by scaling up the Monte Carlo acceptance by the ratio of the experimental to Monte Carlo average acceptance,

$$\text{scale factor} = \frac{0.050}{0.019} = 2.63.$$

This scaled acceptance is shown in the last column of Table XVII.

In order to facilitate the application of this correction to the

data, an analytic approximation to the acceptance was obtained by fitting the scaled acceptances in Table XVII to a polynomial in the proton lab momentum. The fit was done in the region of lab momentum between 1.25 GeV/c and 3.00 GeV/c, and a good fit was found to a quadratic. The resulting fit was

$$\text{acceptance} = 0.3128 - 0.1928\ P_{lab} + 0.02948\ P^2_{lab}. \qquad (20)$$

Above 3.00 GeV/c and below 1.25 GeV/c, the acceptance is defined to be zero. The resulting correction applied to the data on an event by event basis is

$$C_3\ (P_{lab}) = 1/(1\text{-acceptance}). \qquad (21)$$

A similar correction is made to correct for π^- rejection by the Cerenkov counter. An acceptance equal to 0.25 of the acceptance defined in Eq. (20) is used and the correction calculated according to Eq. (21). For events with more than one charged pion, the total correction to the event is defined as the product of the individual corrections due to each pion. For events with a fast Λ^0, P_{lab} is the lambda momentum rather than the proton momentum.

4. Proton interactions

Due to the presence of material through which the fast proton must pass before reaching the downstream hodoscopes, there was a loss of triggers due to proton interactions. The correction required because of this loss was estimated by assuming an average proton momentum of 2 to 3 GeV/c, and calculating the interaction rate of the proton with the material between the primary vertex and the back hodoscope. In Table XVIII are listed the materials through which the proton must pass, along with the estimated interaction rate for the given thickness of material, and the correction

Table XVIII. Proton interaction correction factors.

Material	Thickness (in.)	Total interaction rate	Inelastic interaction rate	Correction
Target + box	7	0.033	0.017	1.034
Neon	40	0.001	0.	1.001
Foam	1	0.002	0.001	1.002
Elbow	0.003	0.	0.	1.000
Air	80	0.004	0.001	1.004
Scintillator	0.375	0.019	0.006	1.006
Aluminum	0.375	0.042	0.014	1.014
Freon	40	0.056	0.019	1.000
Aluminum	0.375	0.042	0.014	1.000

which must be applied to the number of measured events. The entry labeled "target + box" gives numbers corresponding to the average thickness of hydrogen plus target box material through which the proton must pass after interaction. The foam refers to the streamer chamber wall material. The elbow is the transmission elbow from the Blumlein to the streamer chamber.

In order to estimate the total interaction rate in the materials of interest, the 20 GeV/c neutron cross section data from the Particle Data Group tables[56] was scaled by a factor of 1.12, which is approximately the ratio of the pp total cross section between 2 and 3 GeV/c to the pp total cross section at 20 GeV/c. Inserting these numbers into Eq.(14) yielded the total interaction rates given in column III of Table XVIII. In the next column is an estimate of the inelastic interaction rate. For hydrogen, the inelastic cross section is slightly more than one-half the total cross section in the relevant momentum range. For heavier materials, an estimate of one-third was used. In the last column is the correction factor to be used to correct for interaction losses in the material.

The calculation of the correction factor for a particular material depended on how far away from the target the material was. For the entire path length from the target interaction point to the front hodoscope, the total interaction rate was assumed to be the relevant quantity, and the correction to the number of events was given by

$$C_4 = 1/(1- \text{interaction rate}). \qquad (22)$$

This is possibly a slight overestimate, since many interactions will produce a fast proton which can trigger the system. However, the largest correction is due to secondary interactions in the target or the target box. These events are likely to fail during kinematic fitting, and hence

be lost from the event sample to be analyzed, even if the proton triggers the system.

Interactions of the proton in the front hodoscope counters or the front Cerenkov counter wall were assumed to result in loss of the trigger only for inelastic interactions. This assumption was based on the fact that most elastic events are small angle scatters, and after having gone through the front hodoscope, the probability of the scattered proton traversing a counter in the back hodoscope yielding a valid coincidence is very high. The correction factor was calculated according to Eq. (22), where the interaction rate applies to the inelastic interaction rate.

No correction was made for interactions of the proton occurring inside the Cerenkov counter volume, or in the back wall of the Cerenkov counter. It was estimated that nearly any kind of interaction would provide a charged particle to pass through an appropriate counter in the back hodoscope, and very few interactions in the Freon would cause a Cerenkov counter veto.

Two comments should be made. The first is in regard to the accuracy of the previous calculations. Since most of the interaction rate comes from the liquid hydrogen which has a well known cross section, the estimates of the other cross sections and the question of whether the total or the inelastic interaction rate is the relevant quantity, is not crucial. The other comment regards events which trigger the system only because of a downstream interaction. For instance, it is possible for a fast pion to interact downstream of the target and produce a proton which causes a trigger to occur. These events have no effect on the cross section because any event with very small acceptance (as determined by the proton

momentum and angles) is not included in the analysis.

Including all the corrections listed in Table XVIII, an overall correction factor due to downstream interactions of the fast proton of $C_4 = 1.06 \pm 0.04$ is calculated. The error quoted is an estimate of the uncertainty in assigning the correct interaction rates. For events in which a forward Λ^o provides the trigger, the proton has a shorter length to travel in the target on the average than protons produced at the primary vertex. Hence, the correction to be applied to these events is $C_4 = 1.04 \pm 0.03$.

5. Secondary track interactions

A similar correction to that made for proton interactions downstream of the primary vertex must be made to account for interactions of the other outgoing tracks in the liquid hydrogen and the target box. There is a large variation in the momentum of the outgoing tracks, but most have momentum less than about 1 Gev/c. Thus, a πp cross section of 40 mb was chosen as a typical value to be used in the correction. The average track length in the hydrogen plus the target box was found by examining a sample of events of 2- and 4- prong topologies, and calculating the length of track from the vertex position to the point where the track left the target box. The average length was found to be 7.6 cm. From Eq.(14), the interaction rate was calculated to be 0.0125 for a single track. To account for the slightly higher cross section of pions in the target box compared to that in the liquid hydrogen, an interaction rate equal to 0.015 was used. The correction to be applid to the number of measured events is thus,

$$C_5 = 1/(1 - \text{interaction rate})^n, \qquad (23)$$

where n is the number of outgoing tracks (excluding the proton) leaving the

primary vertex. For 2-prong events, Eq.(23) gives $C_5 = 1.02 \pm 0.01$. The error is an estimate based on the uncertainty in the cross section. For 4-prong events, $C_5 = 1.05 \pm 0.02$, and for 2-prong events with a Λ^0, $C_5 = 1.03 \pm 0.02$.

5. Cerenkov counter proton rejection

The possibility that some events were lost in which the only particle traversing the Cerenkov counter was a proton is considered here. The mechanism for such a loss would be the generation of noise or some spurious signal which surpassed the threshold level and caused a trigger veto. In order to evaluate this correction, the sample of 4-prong, 4C events from the special run without the Cerenkov counter in the trigger was utilized. Only those events in which there was a single fast positive track reaching the downstream spectrometer were considered. This track was required to be the proton as determined by the kinematic fit. There were 64 such events in the sample.

In addition to pulse height information from the Cerenkov counter, there also existed a latched bit, requiring the coincidence between the Cerenkov counter signal and the strobe, recorded on magnetic tape. Presumably, a Cerenkov counter signal large enough to veto the trigger would also set this latch. Of the 64 events considered, the latch was set in one. This would yield a loss in trigger rate of 0.016 ± 0.016 if the Cerenkov counter was in the trigger and the trigger was vetoed for this one event. To check the validity of this number, a sample of 4-prong, 4C events with the normal trigger was also considered. Out of 660 events in the sample, the latch was set in seven. This yields a background rate of 0.011 ± 0.004 in which the latch was set, but the

trigger was not vetoed. Subtracting this background from the previous rate yields an actual loss in trigger rate of 0.005 ± 0.016. This number is consistent with zero and no correction is made to the data.

7. Hidden vee detection efficiency

For events with a Λ^o, there is a correction which must be made for events in which the secondary (Λ^o decay) vertex is very close to the primary vertex and within the target box. For events in which the secondary vertex is within approximately 1 cm of the primary vertex, APACHE will often obtain a good fit for all tracks being produced at one vertex, and will not attempt a fit with a second vertex. This results not only in the loss of good events with lambdas, but also contaminates the single vertex event samples.

For those rolls in which only visible vee events were measured, the previously described trigger acceptance corrects for all vees with decay vertex hidden inside the target box. However, for those rolls in which both visible vee events and events yielding hidden vees (If 2-prong events with a vee are of interest, then 4-prong events must be measured to obtain those events with hidden vees.) were measured, the trigger acceptance was calculated based on the assumption that all the hidden vee events were in the sample. It is for this sample of events that the correction must be made.

In order to determine this correction, a sample of events satisfying the 7C hypothesis

$$\pi^- p \rightarrow \pi^- K^+ \Lambda^o \qquad (7)$$

were analyzed. Only rolls in which both 2-prong events with visible vees and 4-prong events were measured were included in the sample. The events were weighted by the inverse of the Λ^0 trigger acceptance. The lifetime in the Λ^0 rest frame was calculated for each event:

$$t = L/\beta c\gamma,$$

where

L = distance Λ^0 travels before decay in laboratory system

βc = velocity of the Λ^0 in laboratory frame

$\gamma = 1/(1-\beta^2)^{\frac{1}{2}}$.

A histogram of $c\tau$ is shown in Fig.41. As can be seen, no events with $c\tau \gtrsim 2$ cm are lost. Since $\beta\gamma$ is on the order of 1, no events in which the Λ^0 travels more than approximately 2 cm are lost.

A least squares fit (see Appendix A) of the data, for $c\tau$ between 2 and 20 cm, was made to

$$N = Ae^{-c\tau/(c\tau)_0}, \qquad (24)$$

where

N = number of events observed as a function of $c\tau$

A = normalization factor

$(c\tau)_0$ = mean lifetime

The best fit was obtained for $(c\tau)_0 = 8.3 \pm 1.6$ cm. The fit gave a χ^2 of 7.0 for 7 degrees of freedom, and is shown as the solid line in Fig. 41. The dashed line corresponds to the value $(c\tau)_0 = 7.73$ cm. When this value $(c\tau)_0$ is used in Eq. (24), the resulting χ^2 deviation from the data is 7.1. Thus, the value of the mean lifetime obtained from the data is consistent, within errors, to the world average of 7.73 cm.

To correct for the loss of events with $c\tau < 2$ cm, a correction

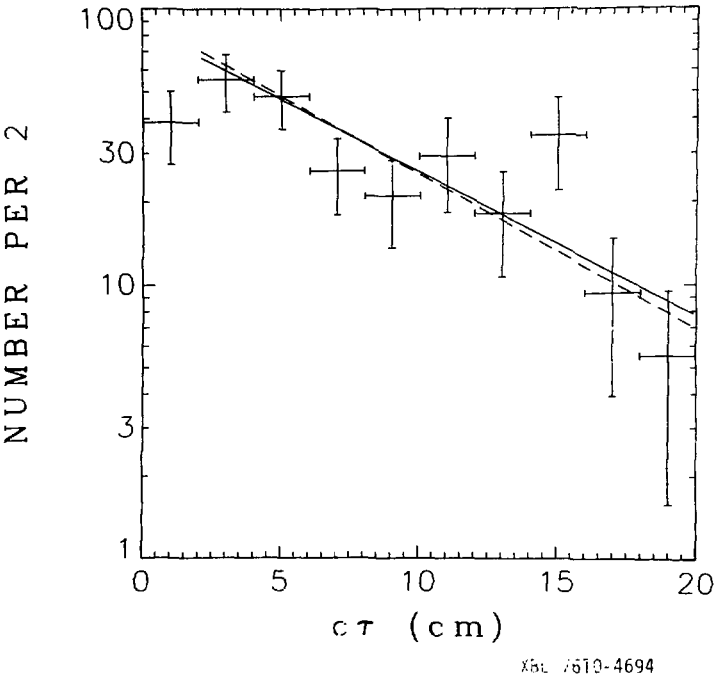

Fig. 41

$$C_7 = 1 + \frac{a_1 - b_1}{b_1 + b_2}, \qquad (25)$$

where

a_1 = fitted number of events according to Eq. (24) with $c\tau < 2$ cm

b_1 = measured number of events with $c\tau < 2$ cm

b_2 = measured number of events with $c\tau \geq 2$ cm,

is made. Using the value $(c\tau)_0 = 7.73$ cm, Eq. (25) gives $C_7 = 1.14 \pm 0.05$. If the value $(c\tau)_0 = 8.3$ cm had been used instead, the correction would have changed only slightly to 1.13.

8. χ^2 probability cuts

In analyzing the various final states, cuts were made on both the vertex χ^2 probability and the kinematic fit χ^2 probability in order to improve the proportion of good events in the data sample. A correction is required to account for the loss of good events eliminated from the sample by these cuts.

The cut made on the primary vertex fit was 0.01 in confidence level for all final states. Events with a secondary vee vertex had an additional confidence level cut of 0.0001 on the vee vertex, but this cut eliminated a negligible number of events. Recalling the vertex fit confidence level histogram in Fig. 30, it is seen that there are a large number of events with fit confidence level less than 0.01. These events fall into two categories. In the first category are those events which fit poorly because one or more tracks scattered in the target box, or there was a secondary interaction involving one of the outgoing tracks. In the second category are those events which are either poorly measured, or just happen to fall in the tail of the χ^2 distribution. Correction for

events in the first category are discussed elsewhere.

If no tracks were poorly measured, and the errors on the track positions were perfectly understood and Gaussian, the correction to be made for loss of events in the second category would be

$$C_{8V} = 1/(1- p), \tag{26}$$

where

$p = \chi^2$ probability cutoff.

With a cutoff of $p = 0.01$, Eq. (26) gives $C_{8V} = 1.01$. However, since both premises are false, it is expected that this correction is an underestimate. In order to better estimate this correction, it is necessary to make use of some of the results of the data analysis. If there exists a reaction in which a histogram of the invariant mass of some combination of the final state particles displays a strong resonance signal above the background, this resonance signal can be used to determine the relative purity of different event samples. The assumption is made that the kinematics for events with good confidence level and for events with poor confidence level is essentially the same. Thus, given two samples of events which purport to satisfy a given hypothesis, the number of bona fide events in each sample which satisfy the hypothesis is proportional to the number of events in the resonance signal. There are some hazards involved in this method of correction, but the corrections are not very large, and the errors are thus expected to be small. The worst error arises due to events that are so poorly measured that the resonance signal becomes smeared and is included in the background. This error is compensated for in the measuring efficiency correction discussed later. Thus, the correction to be applied for loss of events due to a confidence

level cutoff is

$$C_{8V} = 1 + a_1/a_2, \tag{27}$$

where

a_1 = cross section of a resonance signal above background for a sample of events with confidence level below the cutoff value

a_2 = cross section of a resonance signal above background for a sample of events with confidence level above the cutoff value.

In Fig. 129 is shown the $\pi^+\pi^-\pi^0$ invariant mass distribution for a sample of 4-prong events satisfying the 1C hypothesis

$$\pi^- p \to \pi^-\pi^-\pi^+ p\pi^0. \tag{5}$$

An ω^0 signal is clearly evident. In order to estimate the number of events in the signal, a linear background was assumed, and a subtraction made based on the number of events in bins adjacent in mass to the ω^0; both for the sample of events shown in Fig. 129 which have vertex fit confidence levels above the cutoff value of 0.01, and for the sample of events with confidence levels below the cutoff value (figure not shown). The assumption is made that the two cross sections are proportional to the respective number of weighted events corresponding to each signal. Inserting these values into Eq. (27) gives $C_{8V} = 1.05$ which is significantly larger than the naive value of 1.01 obtained from Eq. (26). In Fig. 53 is shown the $\pi^-\pi^0$ invariant mass distribution for a sample of 2-prong events satisfying the 1C hypothesis of

$$\pi^- p \to \pi^- p\pi^0. \tag{2}$$

A similar calculation, assuming a linear background under the ρ^- peak observed here, gives a correction factor of $C_{8V} = 1.04$. Finally, in

Fig. 93 is shown the $\pi^+\pi^-$ invariant mass distribution for a sample of 4-prong events satisfying the 4C hypothesis of Eq. (4). Based on the ρ^0 cross section in this channel, a correction factor of $C_{8V} = 1.08$ is obtained.

The three values for C_{8V} obtained through analysis of the ω^0, ρ^-, and ρ^0 signals are consistent with each other. However, due to the narrowness and the strength of the ω^0 signal compared to the other two, it is believed that the value of C_{8V} based on the ω^0 cross section is the most reliable, and that value will be accepted as the correction factor, $C_{8V} = 1.05 \pm 0.01$. The error is an estimate based partially on the statistics involved in the signals.

As additional evidence that the number of bona fide events per confidence level interval increases as the confidence level decreases, the correction factor was recalculated using the data in a slightly different manner. Again using the ω^0 cross section data, C'_{8V} was defined as

$$C'_{8V} = 1 + \left(\frac{10}{9}\ a_1\right)/a_2,$$

where

a_1 = cross section of the ω^0 signal with $0.01 \leq$ confidence level < 0.10

a_2 = cross section of the ω^0 signal with $0.10 \leq$ confidence level.

The factor 10/9 is an attempt to correct the cross section a_1 to include all events with confidence level less than 0.10. The data yields a value of $C'_{8V} = 1.15$ which is to be compared to the naive estimate of 1.11 from Eq. (26), to correct for a confidence level cutoff of 0.10.

The χ^2 probability cuts imposed on the kinematic fits vary with the

hypothesis under consideration. For hypotheses in which there is a dramatic rise in the number of events per confidence level interval below a certain value, a cutoff is made at this level. For hypotheses in which the distribution does not show a dramatic change, the cutoff is somewhat arbitrary. These cuts are described in more detail in Ch. VI. Confidence level histograms are shown in Fig. 91 for the 4-prong events satisfying the 4C hypothesis of Eq.(4), in Fig. 123 for the 4-prong events satisfying the 1C hypothesis of Eq.(5), and in Fig. 51 for the 2-prong events satisfying the 1C hypothesis of Eq.(2). The lowest bin (confidence level less than 0.01) in each histogram is empty as a result of the requirements imposed during the generation of the data summary tapes, from which most of the analysis was done. All events with confidence level less than 0.01 were eliminated from the data sample for a particular hypothesis.

To correct for loss of events due to the kinematic fit confidence level cutoff, the same procedure was used as described above. The cross sections for ω^o, ρ^-, and ρ^o production for events with confidence level above the cutoff, and for events with confidence level below the cutoff were estimated, and the correction factor calculated. Based on the sample of ω^o events, the correction to be applied to the sample of 4-prong, 1C events with confidence level greater than 0.07 is

$$C_{8K} = 1 + \left(\frac{7}{6}a_1\right)/a_2,$$

where

a_1 = ω^o cross section with $0.01 \leq$ confidence level < 0.07

a_2 = ω^o cross section with $0.07 \leq$ confidence level.

Inserting the estimated cross sections yields $C_{8K} = 1.07$, whereas a

naive estimate based on Eq. (25) is 1.08. From the sample of ρ^- events, the correction to be applied to the 2-prong, 1C events with confidence level greater than 0.04 is

$$C_{8K} = 1 + (-\frac{4}{3} a_1)/a_2,$$

where

a_1 = ρ^- cross section with $0.01 \leq$ confidence level < 0.04

a_2 = ρ^- cross section with $0.04 \leq$ confidence level.

Inserting the ρ^- cross sections gives $C_{8K} = 1.05$, as compared to 1.04 as calculated using Eq. (26). In both cases above, the correction factor calculation based on the cross section information is consistent with the number obtained from Eq. (26); in one case it is 1% larger and in the other case 1% smaller.

A similar calculation based on the ρ^0 signal, intended to provide a correction factor to be applied to the 4-prong, 4C events, resulted in a number which was significantly larger than the number obtained from Eq. (26). The discrepancy results from the fact that many of the events which have poor fits to the 4C hypothesis are actually events with a missing π^0. Since these events are expected to have some resonant ρ^0 production, the original assumption made that the number of bona fide events is proportional to the number of events in some resonance signal is false, and hence, a reliable estimate of the correction factor can not be obtained in this way. On the other hand, the ρ^- and ω^0 decays produce π^0's, and it would be very unlikely if an event satisfying another hypothesis contributed to the resonance signal. Thus, it is expected that the correction estimates based on the ρ^- and ω^0 signals are fairly reliable. Since these estimates correspond so closely

to the naive estimates of Eq. (26), the correction applied to compensate for the kinematic fit confidence level cutoff is calculated by Eq. (26) for all hypotheses.

9. Scanning efficiency

The scanning efficiency was evaluated by scanning a portion of the film twice, and comparing the event types assigned in the two scans. The frames in which there was a discrepancy in the event type assignment were scanned a third time, and an evaluation made to determine the correct event type based on the event itself, and the results of the measurement and fitting of the event. Both 2-prong and 4-prong topologies were examined separately, and the number of events misidentified in a single scan was evaluated. In order for this efficiency to be meaningful, only events which would not be eliminated in the data analysis, assuming they were scanned correctly, were considered in the evaluation of the efficiency. Thus, events with zero recoil acceptance were not considered. These events were misidentified more often in scanning than average events since they often included very short tracks or tracks accompanied by flares.

Also included in the scanning inefficiency were those events which were considered to be of poor track quality or of questionable event type making them essentially unmeasurable. The loss of events due to scanning inefficiency was found to be 2% for both 2-prong and 4-prong events. A similar correction is expected to apply to all topologies, and so an overall correction of $C_9 = 1.02 \pm 0.01$ is applied to correct for scanning inefficiencies.

10. Measuring efficiency

The measuring efficiency was estimated by analyzing a sample of 617 remeasured 4-prong events. These events, on originally being measured, yielded 4-constraint fits to the hypothesis of Eq. (4), all had a fast forward proton with acceptance greater than 15% in the trigger system, and all had nonzero recoil acceptance. In addition, all the events were determined to have the interaction vertex inside the hydrogen target volume, and had greater than 0.01 χ^2 probability for both the vertex fit and the kinematic fit. It was assumed that the percentage of bona fide 4C events which were correctly measured the first time, but produced no good 4C fit the second time due to poor measurement, was equal to the percentage of bona fide 4C events which were not measured correctly the first time. This will be defined as the measuring inefficiency. It was assumed that any event which was pathological enough to always fail in measurement was included in the scanning efficiency correction.

After remeasure, only 414 of the original 617 events produced 4C fits satisfying all the original criteria. However, the measuring efficiency correction should not be naively set to $C_{10} = 617/414 = 1.49$ for two reasons; the first being that some of the loss is included in other corrections previously discussed, and the second that some of the events which originally satisfied the 4C hypothesis of Eq. (4) were not bona fide events, and should not be included in the estimate.

If the events failing during remeasurement are grouped according to the reason for failure, limits can be set on the measuring efficiency correction. (a) of the 617 events measured, only 540 satisfied a 4C hypothesis in the kinematic fitting with a χ^2 probability greater than

10^{-5}. This accounts for a correction factor of 1.14. (b). Of the 540 remaining events, 507 fit with a vertex within the target fiducial volume. This gives a correction of 1.07. Although the number of events in which the interaction takes place inside the target, but is reconstructed by APACHE to be outside the target is approximately equal to the number in which the interaction takes place outside the target, but is reconstructed by APACHE to be inside the target, the events outside the target are primarily reactions on carbon or other heavy nuclei which are not expected to generate bona fide 4C events. (c) This number is reduced to 459 when the requirement is made that the vertex fit confidence level is greater than 0.01. This accounts for a factor of 1.10. However, this correction is partially included in the vertex fit confidence level cut correction of $C_{8V} = 1.05$. Thus, the correction to be included as part of the measuring efficiency correction reduces to 1.05. (d) Finally, when a confidence level cut of 0.01 is applied to the kinematic fit, only 414 events remain. This is a correction of 1.11. However, according to Eq. (26), a correction of 1.01 is already being made. Thus, this correction reduces to 1.10.

In the most severe case, when all the original events were assumed to be bona fide 4C events, the total correction is equal to the product of the four corrections (a-d) listed above, $C_{10} = 1.41$. A minimum correction can be estimated by assuming that only those events lost due to the interaction vertex being outside the target, and those events with a poor vertex fit, contribute to the correction. Loss of events due to a poor kinematic fit are considered to be due to the contamination of the original event sample with events which were not bona fide 4C events. Under these

assumptions, $C_{10} = 1.12$. Thus, the measuring efficiency correction factor is expected to be between the limits of 1.12 and 1.41.

In order to better estimate this number, two additional analyses were performed. The first analysis was to estimate the background in the 4C event sample which were not bona fide events. To do this, a sample of unfitted 4-prong events were considered. Approximate conservation of each of the three components of momentum was required. For the events remaining, the distribution of the energy difference between the initial and final states was considered. There was a peak at $\Delta E = 0$, corresponding to the bona fide 4C events. The background under this peak was estimated to be 15-20% by extrapolating from the region outside the peak to the region under the peak. This gives a lower limit on the correction factor of about 1.12, consistent with the estimate above.

The second analysis involves comparison of the cross section of a resonance signal above the background for both the original sample of events and the sample of remeasured events in much the same way as the corrections for the confidence level cutoffs were estimated. On the basis of this analysis, the correction factor is given by

$$C_{10} = \frac{N_O}{N_R} \left(\frac{a_\rho}{a_T} \right) \Big/ \left(\frac{b_\rho}{b_T} \right), \qquad (28)$$

where

N_O = number of original events submitted for remeasure

N_R = number of accepted 4C events after remeasure

a_ρ = ρ^O cross section for original sample of accepted 4C events

a_T = total cross section for original sample of accepted 4C events

b_ρ = ρ^O cross section for remeasured sample of 4C events

b_T = total cross section for remeasured sample of 4C events.

In Fig. 42(a) is shown the weighted $\pi^+\pi^-$ invariant mass distribution for all

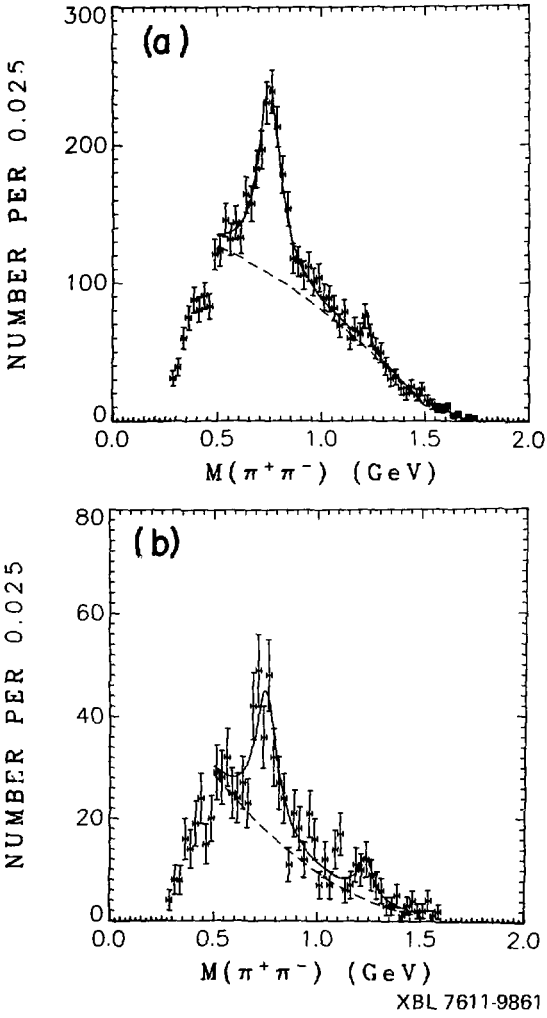
(a)
NUMBER PER 0.025
300
200
100
0
0.0
0.5
1.0
1.5
2.0
M(π⁺π⁻) (GeV)
(b)
NUMBER PER 0.025
80
60
40
20
0
0.0
0.5
1.0
1.5
2.0
M(π⁺π⁻) (GeV)
XBL 7611-9861

Fig. 42

4C events. This weighted distribution is equal to the cross section of accepted events except for an overall multiplicative conversion factor. The solid curve is a least squares fit to the data in the region of the curve. The fit was made to the incoherent sum of ρ^o and f^o Breit-Wigner resonances over a quadratic background. The mass and width of the ρ^o were held fixed and not allowed to vary during the fitting. The dashed curve shows the background. In Fig. 42(b) is the same invariant mass distribution for the sample of remeasured events which gave a satisfactory 4C fit. The mass and width of the ρ^o were fixed at the same values used in the previous least squares fit, and a similar fit was made to this mass distribution. The solid curve shows the overall fit, and the dashed curve is the background. The ρ^o cross sections, a_ρ and b_ρ, were determined from the fits, and the total cross sections, a_T and b_T, from the areas under the respective distributions. Inserting these numbers into Eq.(28) yields a correction factor of $C_{10} = 1.25$. This value is consistent with the previously determined limits, but the error is rather large, approximately 0.10 - 0.20, due to the uncertainty in the background under the resonances.

Evaluation of all the available information leads to an estimate for the measuring efficiency correction factor of $C_{10} = 1.25 \pm 0.10$. Remeasurements were not undertaken for any other sample of events, making it necessary to use this same correction factor for all topologies. There is no reason to believe that the efficiency should differ very much for different topologies, so this number should be acceptable.

11. Summary

The efficiency corrections falling into the second category are summarized in Table XIX. The corrections falling into the first category, since they are corrected for on an event by event basis, are not listed. In addition, the correction factor for loss of events due to the kinematic fit confidence level cutoff is not included since it varies depending on the kinematic hypothesis. Finally, note that the correction factor for loss of hidden vees due to the secondary vertex being too close to the primary vertex is given, but is not included in the total since it is only applied to events in rolls in which both SC22 and SV11 topologies were measured. Note that the error on the total correction factor is approximately 10%. The total systematic error including the corrections in the first category is estimated to be less than 15%. However, relative cross section ratios, and distributions in mass or u, are not expected to be in error by this amount.

Table XIX. Efficiency correction factors.

Correction	Event topology		
	SC11	SC22	SV11
C_4 - proton interaction	1.06 ± 0.04	1.06 ± 0.04	1.04 ± 0.03
C_5 - secondary interaction	1.02 ± 0.01	1.05 ± 0.02	1.03 ± 0.02
C_6 - proton rejects	1.00	1.00	1.00
C_7 - hidden vee	1.00	1.00	1.14 ± 0.05*
C_{8V} - vertex prob. cutoff	1.05 ± 0.01	1.05 ± 0.01	1.05 ± 0.01
C_9 - scanning efficiency	1.02 ± 0.01	1.02 ± 0.01	1.02 ± 0.01
C_{10} - measuring efficiency	1.25 ± 0.10	1.25 ± 0.10	1.25 ± 0.10
Total	1.45 ± 0.13	1.49 ± 0.14	1.43 ± 0.13

*not included in the total since correction applied only to certain events

VI. Data Analysis

A. $\pi^- p \to \pi^- p$

This reaction has been analyzed in the baryon exchange region in many experiments (see Ch. II). The reason for including a discussion of this analysis here is not necessarily to present new information on the reaction, but instead to demonstrate the method of analysis employed in a simple case, and to show by comparison with other analyses of this reaction that the cross section normalization of this experiment has been done correctly.

1. Event sample

The sample of events analyzed consists of 389 2-prong events satisfying the 4C hypothesis of reaction (1). This sample consists only of events in which the confidence level of the vertex fit is greater than or equal to 0.01 and the confidence level of the kinematic fit is greater than or equal to 0.02. A histogram of the kinematic fit confidence level is shown in Fig. 43.

The main source of contamination of this event sample consists of events from another reaction which happen to satisfy this kinematic hypothesis with a reasonable confidence level. Since there are no other 4C hypotheses which a 2-prong event can satisfy, the most likely source of contamination comes from those events with a missing π^0, i.e., events from reaction (12). In Fig. 44 is a histogram of the missing mass squared (the points with error bars). The solid curve is a least squares fit to the data with functional form

$$N = Ae^{-(M^2 - M_0^2)^2/2\sigma^2},$$

where

N = number of events

M^2 = missing mass squared.

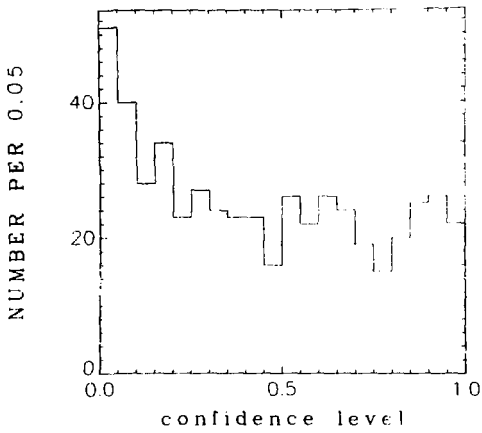
NUMBER PER 0.05
40
20
0
0.0
0.5
1.0
confidence level

Fig. 43

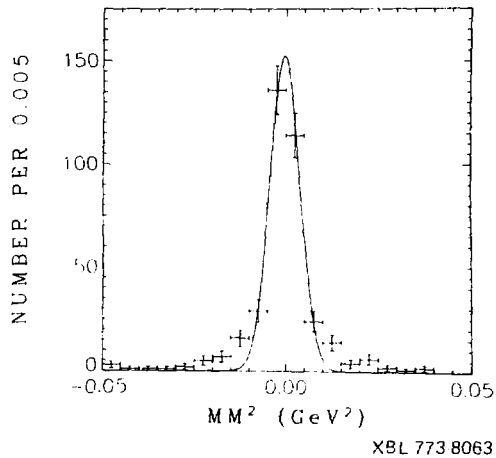
NUMBER PER 0.005
150
100
50
0
-0.05
0.00
0.05
MM² (GeV²)
XBL 773 8063

Fig. 44

A, M_o^2, and σ were parameters varied in the fit. The resulting fit determined the values of the parameters to be $M_o^2 = -0.0003 \pm 0.0002$ GeV^2 and $\sigma = 0.0040 \pm 0.0003$ GeV^2. There is no evidence for any contamination from events with a missing π^o. It is seen that there are larger tails in the data than are given by the Gaussian used in the fit, but this is explained, as for the case of the Λ^o and K^o invariant mass fits described in Ch. IV, as being the result of the variations in the kinematic errors associated with each event. On the other hand, there is no loss of events due to their inclusion in an event sample satisfying another hypothesis, since any event which satisfied the hypothesis for this reaction was included in the event sample, irregardless of whether the event satisfied another hypothesis as well.

2. Cross section

For this reaction, the differential cross section $d\sigma/du$ and the total cross section for the baryon exchange reaction are of interest. The differential cross section for this reaction and others to be discussed later will generally be expressed in terms of u' rather than u.

The analysis of this reaction was done in two ways. The first method of analysis involved binning the events by u' and correcting up each event by the inverse of the proton acceptance. The recoil acceptance was applied as described in Ch. V. All events with proton acceptance less than 0.15 or zero recoil acceptance were eliminated. No correction was made for pions entering the Cerenkov counter since that is kinematically impossible for protons produced at small values of u'. Finally these events were corrected for all other inefficiencies and the cross section for each interval in u' was calculated according to Eq. (17). The results of this

process are shown in Fig. 45 where the differential cross section $d\sigma/du$ is shown. The straight line is a linear least squares fit to the logarithm of the differential cross section,

$$\ln\left(\frac{d\sigma}{du}\right) = a + bu',$$

for the region $-0.35 < u' \leq 0.0$ GeV^2. The slope obtained in the fit is $b = 3.6 \pm 0.7$ GeV^{-2}. The total cross section in the region of the fit is $\sigma = 3.98 \pm 0.25$ μb. If this value of the cross section and slope is used to extrapolate the cross section to include the total backward peak, a cross section $\sigma_T = 5.59 \pm 0.63$ μb is obtained.

If, instead of extrapolating the cross section from the integral over $u' > -0.35$ GeV^2, the cross section is estimated by summing the data over all bins in u' in which data is observed, a value of $\sigma_T = 4.97 \pm 0.31$ μb is obtained. The discrepancy between these two estimates arises as a result of the deviation of the data from the fitted curve in the region where $u' < -0.50$ GeV^2. It is believed that this deviation is not real, but results from the loss of events with proton trigger acceptance less than 0.15. In Fig. 46 is a scatter plot of proton trigger acceptance vs u' for the sample of events analyzed. It is evident from the distribution of points in the plot that the average proton trigger acceptance drops below 0.15 by $u' \sim -0.6$ GeV^2, and hence events are expected to be eliminated. Thus, the low bins in the u' distribution are probably not reliable. However, there appears to be no loss of events for $u' > -0.5$ GeV^2, so the corrected cross section in this region is expected to be reliable.

The second method of analysis involved doing a maximum likelihood fit to the data (as described in Appendix A). The distribution function

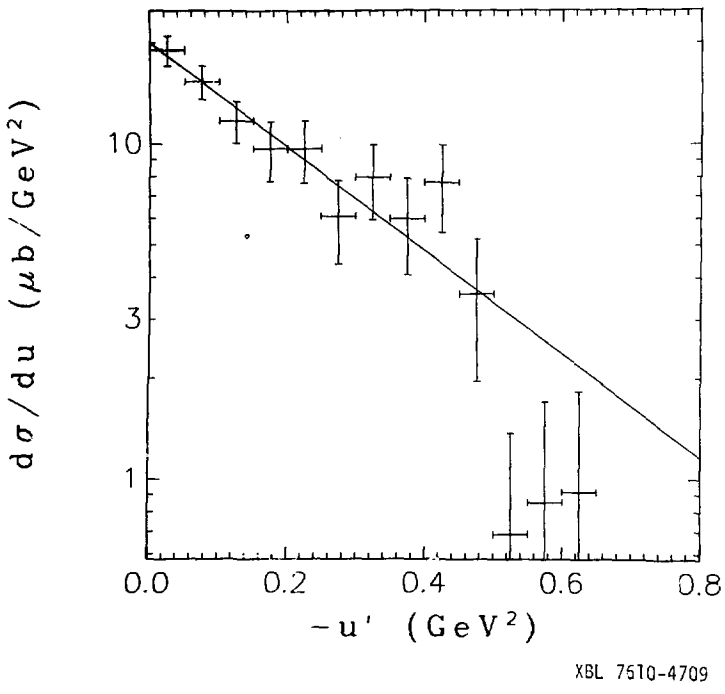

Fig. 45

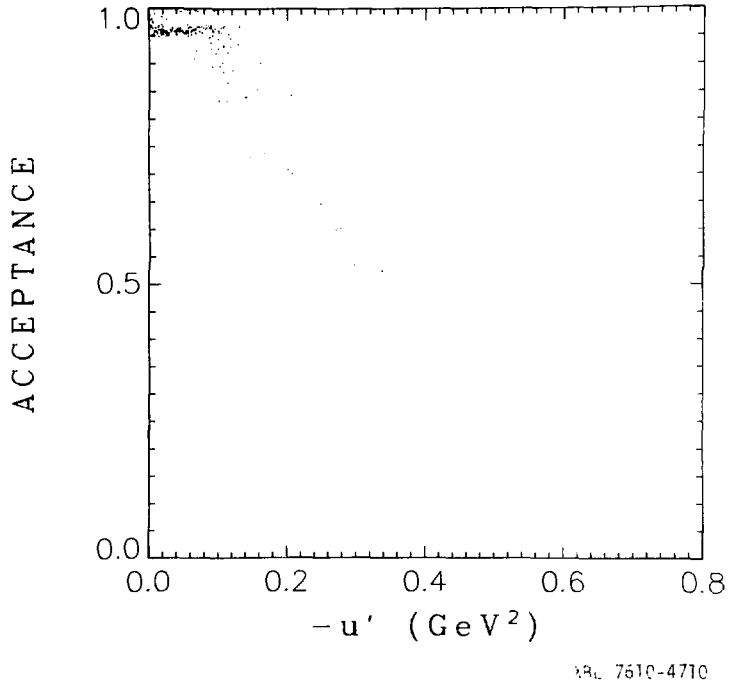

Fig. 46

used in the fit was

$$\frac{d\sigma}{du} = A\, e^{bu'}. \qquad (29)$$

The fit was made to the sample of unweighted real events. In order to numerically integrate the acceptance function, and for comparison with the real event distribution, a sample of Monte Carlo events was generated flat in phase space. Each Monte Carlo event was assigned a weight equal to the proton trigger acceptance (as a function of the three proton kinematic variables). In order to correctly reflect the two trigger matrix conditions, the matrix 1 trigger acceptance was assigned to 17% of the generated Monte Carlo events and matrix 2 to the remaining 83%. These percentages are a reflection of the beam fluxes corresponding to the measured event samples taken under the two matrix conditions. All Monte Carlo events (and real events) with proton acceptance less than 0.15 were eliminated. In addition all events (both real and Monte Carlo) with zero recoil acceptance were eliminated. The results of the maximum likelihood fit are shown in Fig. 47. The points with the error bars are the unweighted real event bin contents. The dashed curve is the weighted Monte Carlo distribution (i.e., each Monte Carlo event is given a weight equal to the proton acceptance mentioned above multiplied by the event probability as given by the distribution function in Eq. (29)). The best value of the slope parameter obtained in the fit was $b=3.77 \pm 0.43\ \text{GeV}^{-2}$, consistent within errors with the value obtained by the other analysis procedure. The total backward elastic cross section obtained from the fit was $\sigma_T = 5.47\ \mu b$. The error on this number is a combination of three separate errors. The error due to the statistics used in the Monte Carlo event

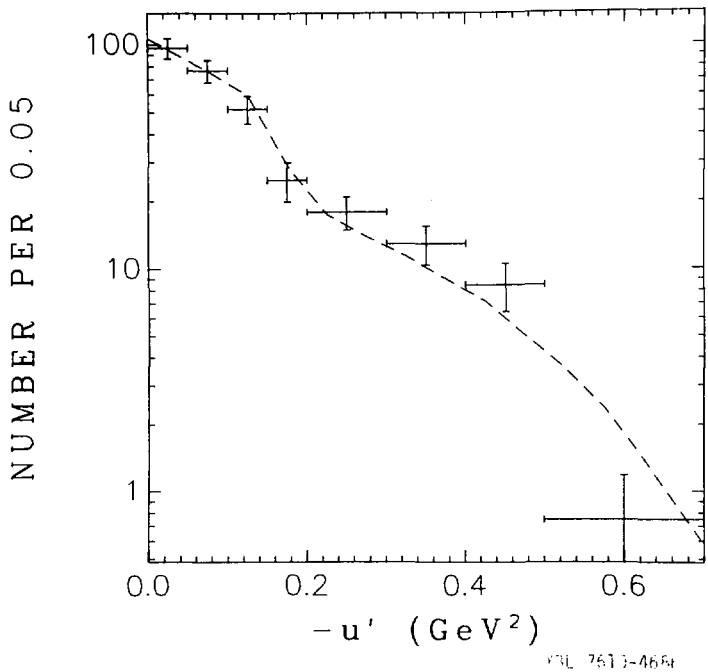

Fig 47

generation was 0.19 μb. The statistical error inherent in the data was 0.31 μb. Normalizing this error to the total cross section gives 0.34 μb. Finally, a systematic error of ± 15% yields 0.82 μb. Combining the three errors in quadrature gives a total error of 0.91 μb.

In Table XX are listed the values of the differential cross section as a function of u'. The errors quoted are statistical only. These values are the results of the weighted histogram shown in Fig. 45. Thus, the quoted cross sections represent the average value of the differential cross section over the domain of width Δu (column II) centered at u' (column I). The total cross section and slope of the differential cross section (based on the assumed form given in Eq. (29)) are given in Table XXI. The values quoted are those obtained from the maximum likelihood fit. These values are expected to be more reliable than those obtained by correcting up the real events since all the data was included in the maximum likelihood fit, rather than just those events with $u' > -0.35$ GeV^2, and the three-parameter acceptance function provides a better estimate of the acceptance of a given event than the two-parameter acceptance function does.

In Fig. 48, the differential cross section for this experiment is shown along with data from some other experiments which have measured the π^-p backward elastic differential cross section. Data from Hoffman et al.[13] is shown at both 3 GeV/c and 5.1 GeV/c incident beam momentum. Data from Brabson et al.[12] is shown at 4 GeV/c. All errors shown are statistical only. The data at 4 GeV/c and 5.1 GeV/c are consistent in structure to the data from this experiment. The data at 3 GeV/c appears to have dip structure and possibly a second maximum, but it is expected that s- and t-channel processes will have more of an effect in the backward region at

Table XX. Differential cross section for $\pi^- p \to \pi^- p$ as a function of u'.

u' (GeV^2)	Δu (GeV^2)	$d\sigma/du$ ($\mu b/GeV^2$)
0.025	0.05	19.1 ± 1.9
0.075	0.05	15.4 ± 1.8
0.125	0.05	11.7 ± 1.7
0.175	0.05	9.7 ± 2.0
0.225	0.05	9.7 ± 2.0
0.275	0.05	6.1 ± 1.7
0.350	0.10	7.0 ± 1.4
0.450	0.10	5.6 ± 1.4

Table XXI. Parameters of fit to differential cross section for $\pi^- p \to \pi^- p$.

σ_T	= 5.47 ± 0.91 μb
b	= 3.77 ± 0.43 GeV^{-2}

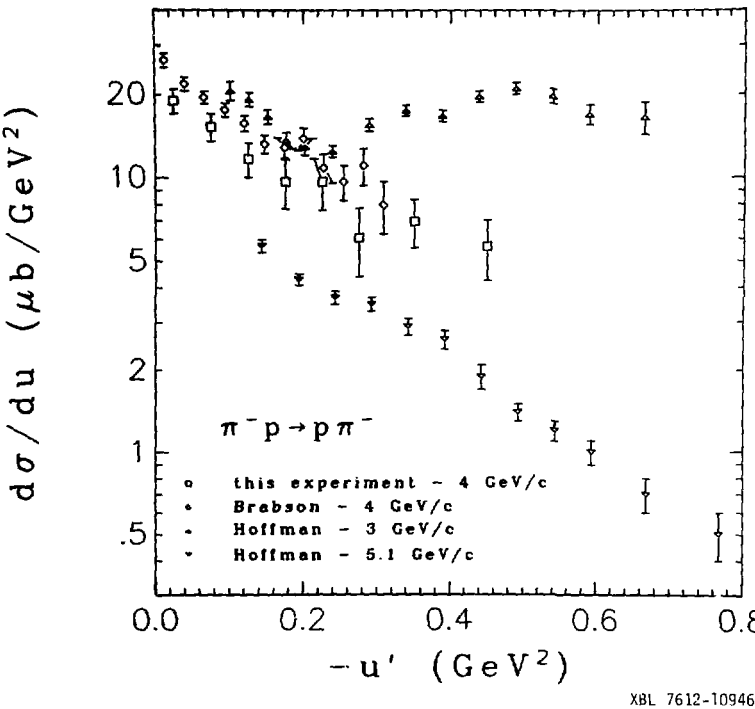
dσ/du (μb/GeV²)
20
10
5
2
1
.5
0.0
0.2
0.4
0.6
0.8
−u' (GeV²)
π⁻p → pπ⁻
this experiment - 4 GeV/c
Brabson - 4 GeV/c
Hoffman - 3 GeV/c
Hoffman - 5.1 GeV/c
XBL 7612-10946

Fig. 48

this energy than at higher energies. The overall normalization of the data from this experiment and the experiment of Brabson et al. appears to be slightly different, but when systematic errors are included, the results are found to be consistent within errors.

In Fig. 49 are shown the extrapolated total backward cross sections measured in this and previous experiments. Included are data from Hoffman et al.[13] at 5.1 GeV/c, Brabson et al.[12] at 4 GeV/c, Owen et al.[26] at 5.9 GeV/c, and Anderson et al.[15] at 8 and 16 GeV/c. Since data is not available for any of these experiments over the entire range of u in the backward region, certain assumptions must be made in order to estimate the total backward cross section. The basic assumption made is that the differential cross section falls off exponentially in u' as described by Eq. (29). Thus, data measured over an interval in u' can be extrapolated to give the total backward cross section which is defined as

$$\sigma_T = \int_{-\infty}^{0} \frac{d\sigma}{du} \, du' = \frac{A}{b} , \qquad (30)$$

where A and b are defined in Eq. (29).

In Brabson et al., a fit of the data to Eq. (29) gives a slope of $b = 3.7 \pm 0.3$ GeV^{-2}. No value for the total cross section is quoted. However, if the assumption made above is valid, an extrapolation of the data from the domain of measurement to all u' can be made. In the region $-0.335 < u' \leq 0.$ GeV^2, the measured cross section is 4.90 ± 0.12 μb, which gives a total cross section of $\sigma_T = 6.89 \pm 0.33$ μb using Eqs. (29) and (30). Brabson et al. claim a systematic error of less than ± 12%. If this 12% systematic error is combined in quadrature with the statistical error, the cross section becomes $\sigma_T = 6.89 \pm 0.89$ μb. The cross section of Brabson et al. (at 4 GeV/c) is seen to be consistent with the cross section from

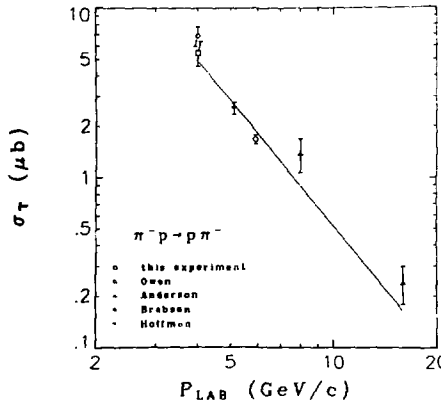
10
5
2
1
.5
.2
.1
σ_T (μb)
$\pi^- p \to p \pi^-$
this experiment
Owen
Anderson
Brabson
Hoffman
2
5
10
20
P_{LAB} (GeV/c)

Fig. 49

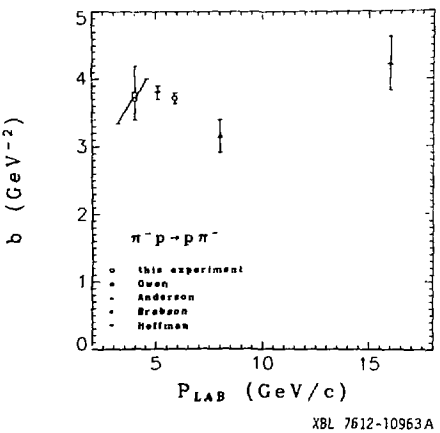
5
4
3
2
1
0
b (GeV^{-2})
$\pi^- p \to p \pi^-$
this experiment
Owen
Anderson
Brabson
Hoffman
5
10
15
P_{LAB} (GeV/c)
XBL 7612-10963A

Fig. 50

this experiment as given in Table XXI.

A similar calculation was made using the data of Hoffman et al. at 5.1 GeV/c. The fitted value of the slope is quoted to be $b = 3.8 \pm 0.1$ GeV^{-2}. The measured cross section in the region $-0.818 \leq u' \leq -0.118$ GeV^2 is $\sigma = 1.53 \pm 0.03$ μb. Extrapolating and integrating over u' yields $\sigma_T = 2.58 \pm 0.06$ μb. A systematic error of less than 8% is quoted which if combined in quadrature with the statistical error gives a total cross section of $\sigma_T = 2.58 \pm 0.21$ μb.

Owen et al. quote parameters of a fit to the differential cross section over the region $|u| < 0.8$ GeV^2. Integration of the differential cross section gives $\sigma_T = 1.68 \pm 0.05$ μb. If the quoted systematic error of 5% is included, $\sigma_T = 1.68 \pm 0.10$ μb.

Anderson et al. quote parameters of fits to the differential cross section over the region $|u| \leq 0.42$ GeV^2 at both 8 GeV/c and 16 GeV/c. Including the quoted 20% systematic error, the total cross sections are $\sigma_T = 1.38 \pm 0.31$ μb at 8 GeV/c and $\sigma_T = 0.25 \pm 0.06$ μb at 16 GeV/c.

The curve in Fig. 49 is a linear least squares fit to the data in log-log space. The functional dependence of the total backward cross section with P_{LAB} as determined by the fit is

$$\sigma_T \propto P_{LAB}^{-2.45 \pm 0.17} .$$

This is consistent with the s dependence expected by Regge theory for delta exchange processes.

In Fig. 50 are the fitted values of the slope parameter b for this experiment and the experiments just discussed in regard to Fig. 49. The value of the slope determined in this experiment is seen to be quite consistent with the results of other experiments.

B. $\pi^- p \to \pi^- p \pi^0$

The results presented here for this reaction provide new information on the baryon exchange reaction. The basic goal of the analysis was to separate the various quasi two-body final states of interest from the background and from each other in order to determine the production characteristics of the various resonances. The particular quasi two-body reactions which were considered are:

$$\pi^- p \to p \rho^- \tag{31}$$

$$\pi^- p \to \Delta^0 \pi^0 \tag{32}$$

$$\pi^- p \to N^{*0} \pi^0 \tag{33}$$

$$\pi^- p \to \Delta^+ \pi^- \tag{34}$$

$$\pi^- p \to N^{*+} \pi^- \quad . \tag{35}$$

The references to Δ^0 and Δ^+ in Eqs. (32) and (34) refer to the $\Delta(1232)$ resonance. The references to N^{*0} and N^{*+} in Eqs. (33) and (35) refer to higher mass baryon resonances in general. Note that only those interactions in which the baryon resonance decays into $p\pi$ are accessible in this channel. Also note that in reactions (32)-(35), the domain of interest is that in which u from the beam to the baryon resonance is small. Finally, the trigger acceptance is a function of the proton momentum, not the resonance momentum, and analysis of these reactions requires assumptions to be made concerning the resonance angular decay distribution.

1. Event sample

The sample of events which was analyzed consisted of 4230 2-prong events satisfying the 1C hypothesis

$$\pi^- p \rightarrow \pi^- p \pi^0 \quad . \qquad 2)$$

The sample consisted only of events in which the χ^2 probability o the vertex intersection fit was greater than or equal to 0.01, and the χ^2 probability of the kinematic fit was greater than or equal to 0.04. A histogram of the kinematic fit confidence level is shown in Fig. 51. t is seen that the elimination of events with confidence level less than 0.04 still leaves a significant background, but eliminating most of the background would also eliminate a large fraction of the bona fide events.

The contamination of this reaction by events from other reactions is considerably worse than either the 4C events discussed in the previous section, or the 4-prong events to be discussed in later sections. This results from the fact that there is only one kinematic constraint and the fact that the momenta of the outgoing prongs are higher on the average than for 4-prong events. The higher track momenta result in poorer momentum resolution, and greater overlap between kinematic hypotheses. (For instance, the replacement of a pion mass by a kaon mass for a high momentum track has a much smaller effect on the energy of the track than it would have for a low momentum track.)

Since the elimination of all events in which alternate hypotheses were satisfied with reasonable probability would have reduced the event sample to 2450 events, the data analysis included all ambiguous events.

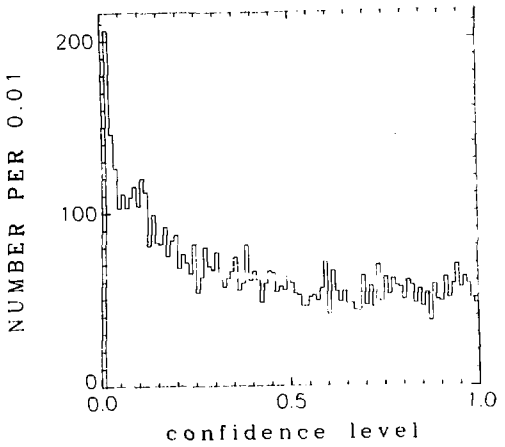
NUMBER PER 0.01
200
100
0
0.0
0.5
1.0
confidence level

Fig. 51

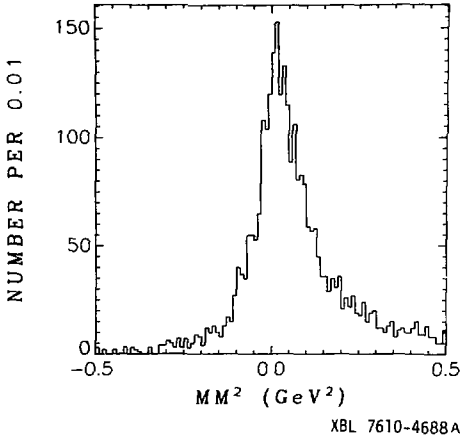
NUMBER PER 0.01
150
100
50
0
−0.5
0.0
0.5
MM² (GeV²)
XBL 7610-4688A

Fig. 52

In addition, since the ambiguous events tend to populate certain kinematic regions, the analysis of certain final states would be impossible if these events were not included in the event sample. Analysis of the ambiguous events indicated that events satisfying other hypotheses did not get confused with resonance production in this channel, but rather provided a smooth background. The only ambiguous events eliminated from the sample were those in which a 4C hypothesis was satisfied and those in which an alternate 1C hypothesis had a χ^2 kinematic fit probability greater than ten times the χ^2 probability for the fit to this hypothesis.

An estimate of the contamination in the event sample can be made by considering the missing mass squared from the charged tracks. As seen in Fig. 52, the distribution peaks near m_π^2, but it is not symmetric due to contamination for positive missing mass squared. Imposing a symmetry constraint indicates that slightly over 50% of the ambiguous events are contamination (i.e., not bona fide events), and hence approximately 25% of all events in the sample are contamination. This estimate is consistent with that obtained by extrapolating the high end of the confidence level histogram in Fig. 51 to all values of the confidence level, and making the assumption that the events above this extrapolated level are not bona fide events.

2. General features

A survey of the data in this channel is made here so that an overall picture of the data is presented in one place. Later, topics of interest will be discussed in more detail. The data is not corrected for acceptance, but events in which the two-parameter trigger acceptance is less than 0.15, the recoil acceptance is 0., or the π^- traversed the

Cerenkov counter, are eliminated from the histogram or scatter plot.

Of primary interest are the invariant mass distributions. Figure 53(a) shows a histogram of the invariant mass of the $\pi^-\pi^0$ system. Figure 53(b) is a histogram of the same data with the additional requirement that

$$\cos \theta^*_{\pi^-\to p} \geq 0.8,$$

where θ^* is the center of mass scattering angle. The subscripts on the scattering angle indicate which particles define the angle. (In this case, it is the angle between the beam and the fast proton.) A comparison of the two histograms shows that nearly all events accepted by the trigger are within this angular cut. The only structure of significance is the ρ^- peak with mass of approximately 0.75 GeV. The broad enhancement at high mass (greater than 1.0 GeV) is primarily due to contamination from other hypotheses. There is essentially no contamination below 1.0 GeV.

In Fig. 54(a) is a histogram of the $p\pi^-$ invariant mass, and in Fig. 54(b) is the same histogram with the additional requirement that

$$\cos \theta^*_{\pi^-\to p\pi^-} \geq 0.8.$$

The most significant structure in this mass distribution is the peak near 1.6 GeV. A signal due to the $\Delta^0(1232)$ is also observable.

The $p\pi^0$ invariant mass distribution is shown in Fig. 55(a). There does not appear to be any significant structure in that distribution. In Fig. 55(b), all events with $\pi^-\pi^0$ invariant mass in the region of the ρ^- peak and events with $p\pi^-$ invariant mass in the region of the

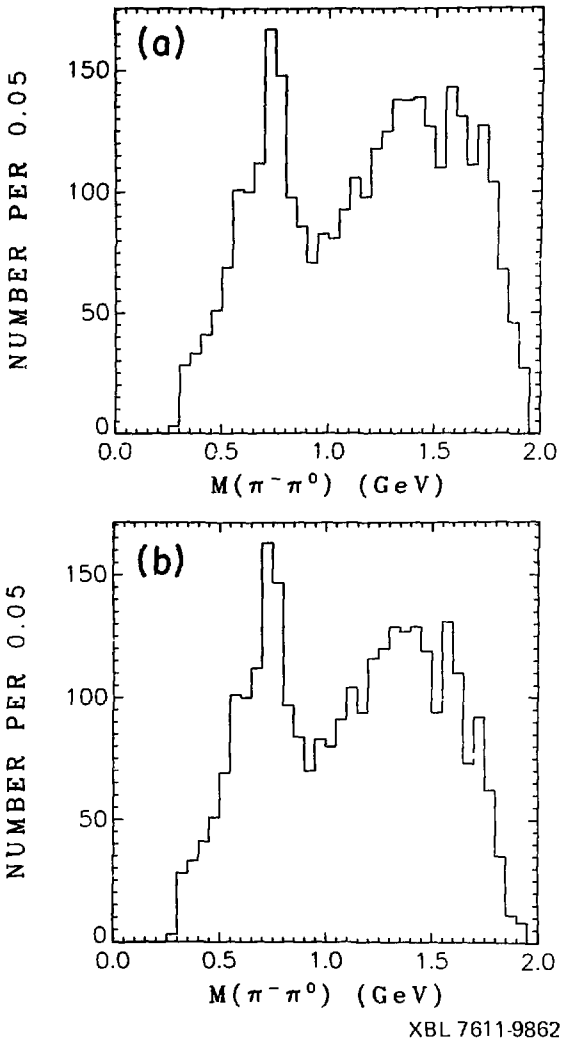
(a)
NUMBER PER 0.05
150
100
50
0
0.0
0.5
1.0
1.5
2.0
M(π⁻π⁰) (GeV)
(b)
NUMBER PER 0.05
150
100
50
0
0.0
0.5
1.0
1.5
2.0
M(π⁻π⁰) (GeV)
XBL 7611-9862

Fig. 53

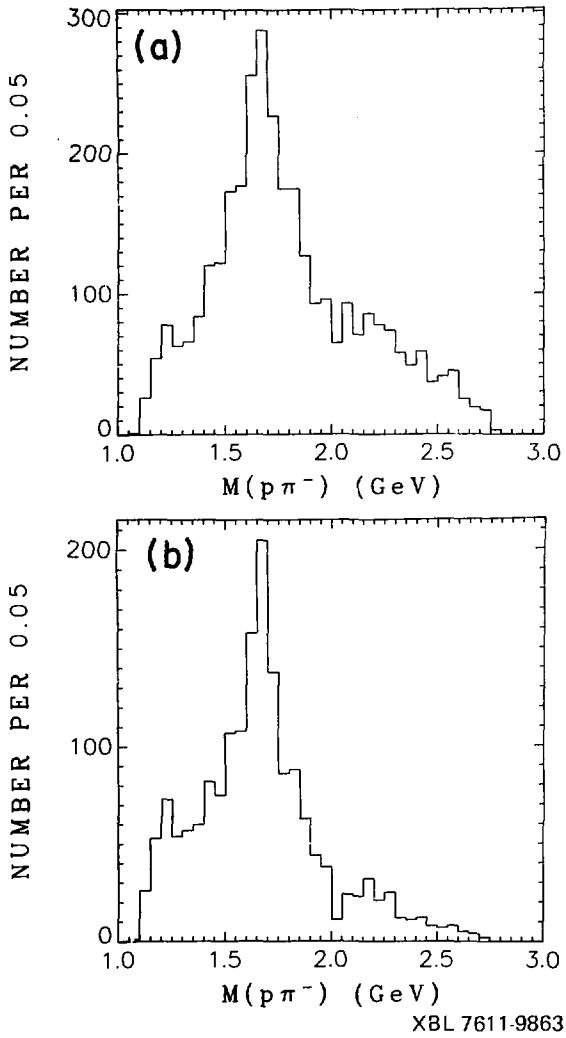
(a)
NUMBER PER 0.05
300
200
100
0
1.0
1.5
2.0
2.5
3.0
M(pπ⁻) (GeV)
(b)
NUMBER PER 0.05
200
100
0
1.0
1.5
2.0
2.5
3.0
M(pπ⁻) (GeV)
XBL 7611-9863

Fig. 54

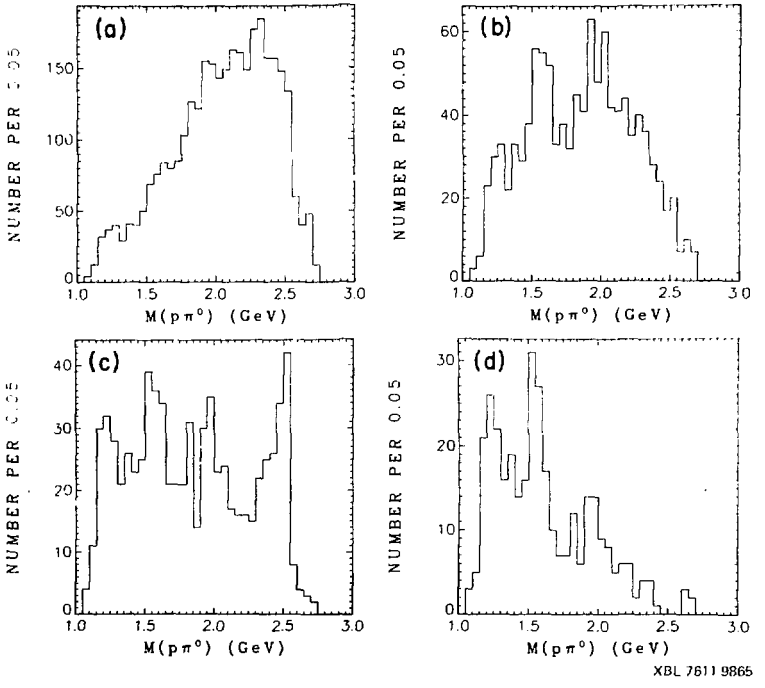

Fig. 55

$\Delta^0(1232)$ or the peak near 1.6 GeV are eliminated. A peak near 1.55 GeV becomes clear and there is the possibility of other structure as well. Fig. 55(c) is similar to Fig. 55(a) with the additional requirement that

$$\cos \theta^*_{\pi^- p \to p\pi^0} \geq 0.8 .$$

In addition to the peak near 1.55 GeV, there is evidence for the $\Delta^+(1232)$ and there is a strong peak near 2.5 GeV. This peak results from the reflection of the ρ^- and the $p\pi^-$ peak near 1.6 GeV into this mass distribution. In Fig. 55(d), the requirements imposed in both Figs. 55(b) and (c) are imposed. The $\Delta^+(1232)$ peak and the peak near 1.55 GeV both become cleaner. In addition, there is a hint of a peak just below 2.0 GeV.

A Dalitz plot of the $\pi^-\pi^0$ invariant mass squared vs the $p\pi^-$ invariant mass squared is shown in Fig.56. Bands due to the ρ^- and the $p\pi^-$ peak near 1.6 GeV can be clearly distinguished. In Fig. 57 is the Chew-Low plot of the $\pi^-\pi^0$ invariant mass squared vs u from the beam to the forward proton. The data is seen to cluster near small values of $-u$, but this is due more to acceptance than to dynamics. The ρ^- appears to be more strongly peaked backwards than the nearby background. In Fig. 58 is the Chew-Low plot of the $p\pi^-$ invariant mass squared vs u from the target proton to the π^0. Clear evidence of backward peaking is seen for the events produced near 1.6 GeV in mass, and some evidence is seen for backward peaking of the $\Delta^0(1232)$. In Fig. 59 is the Chew-Low plot of the invariant mass squared of the $p\pi^0$ system vs u from the target proton to the π^-. There appears to be backward peaking in the low mass region corresponding to the $\Delta^+(1232)$ and the peak near 1.55 GeV, but the statistics are rather poor. The solid curves in

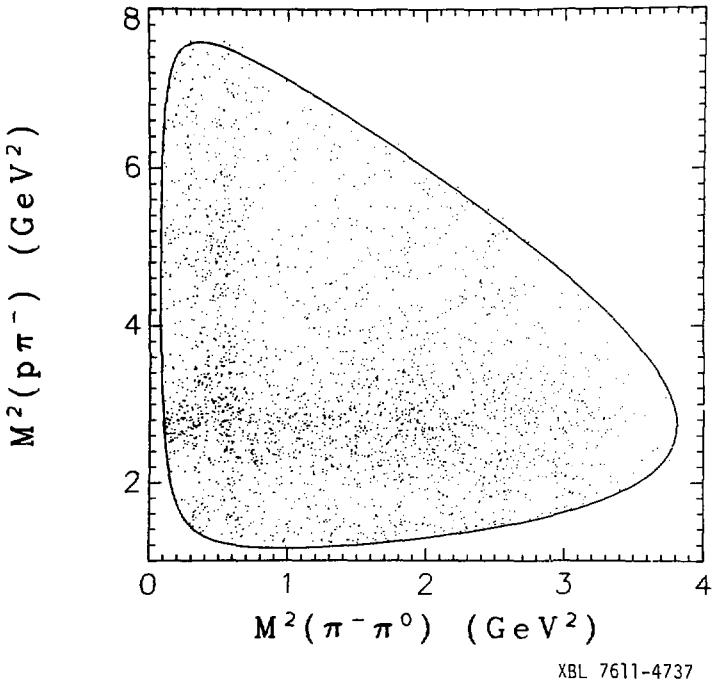

XBL 7611-4737

Fig. 56

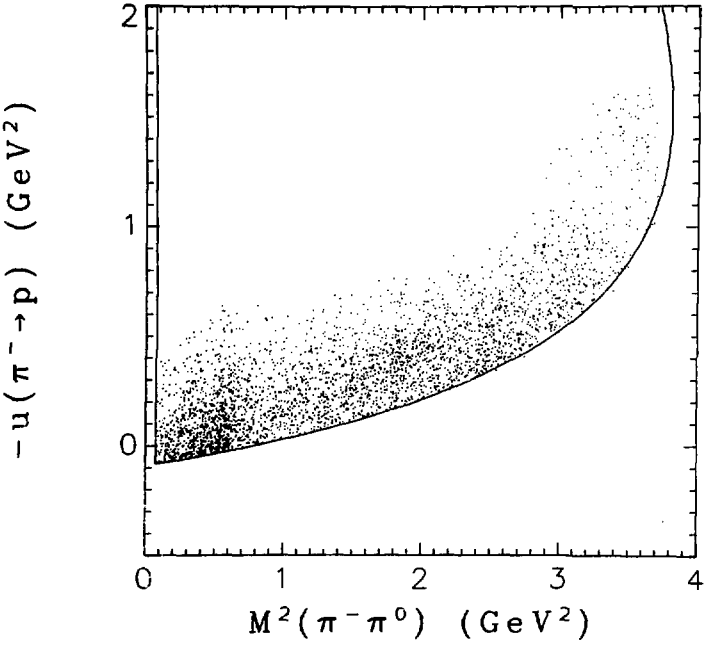

Fig. 57

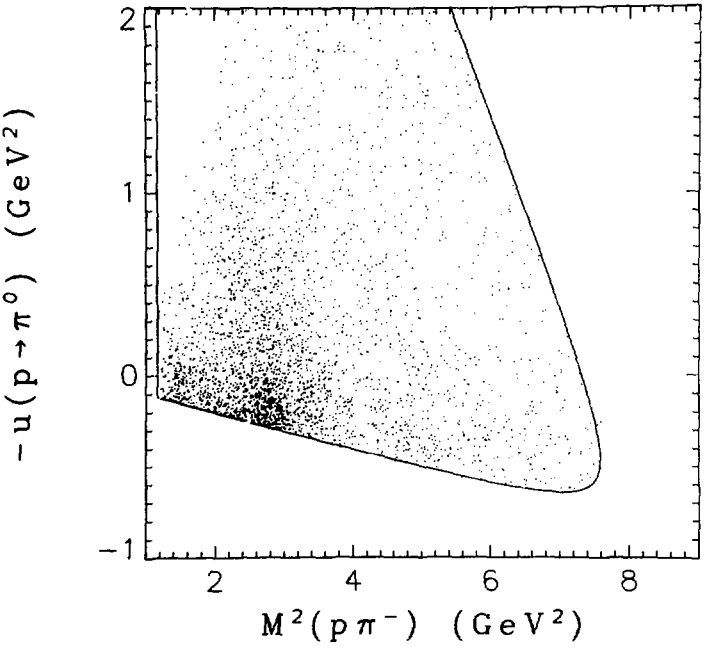

XBL 7611-4733

Fig. 58

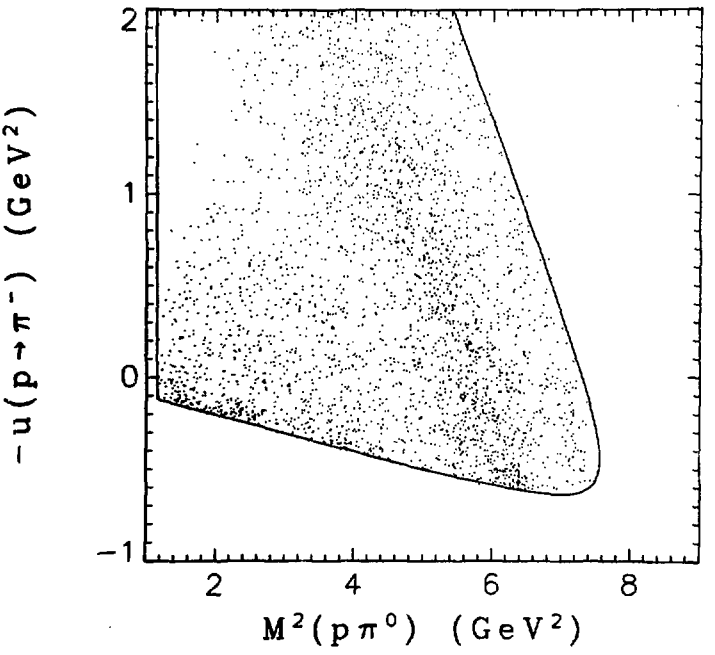

XBL 7611-4734

Fig. 59

Figs. 56-59 are the kinematic limits at the mean beam energy.

In Fig 60 are shown the center-of-mass production angles; from the beam to the proton in Fig. 60(a), from the beam to the $p\pi^-$ system in Fig. 60(b), and from the beam to the $p\pi^0$ system in Fig. 60(c). The events in these plots are corrected up by assigning each event a weight equal to the inverse of the acceptance and eliminating all events with trigger acceptance less than 0.15. A correction factor is then applied which converts the number of events to cross section. The peaking which is observed in the backward region ($\cos\theta^* \approx 1.$) in these three distributions is partially due to an actual falloff of the cross section with production angle and partially due to the elimination of events with small or zero acceptance.

A scatter plot of the trigger acceptance vs the center-of-mass production angle of the proton with respect to the beam is shown in Fig. 61. Only events with trigger acceptance greater than 0.15 are included in the plot. The observed structure results from the two coincidence matrix configurations employed in the trigger. The sharper peak reflects the matrix 2 trigger which was utilized for the majority of the exposure. In Fig. 62 is a scatter plot of the acceptance as a function of the $\pi^-\pi^0$ invariant mass (or equivalently the recoil mass from the proton). Again structure resulting from the two trigger configurations is evident. Acceptances plotted as a function of any other variable show little illuminating structure.

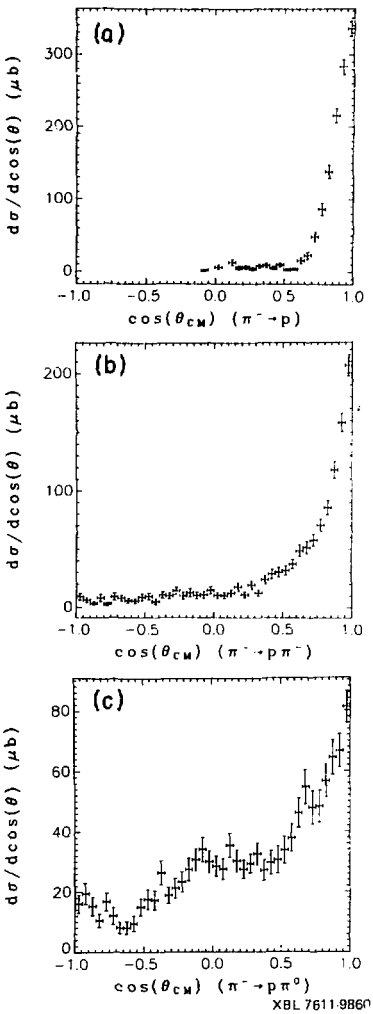
(a)
dσ/dcos(θ) (μb)
300
200
100
0
-1.0
-0.5
0.0
0.5
1.0
cos(θ_CM) (π⁻→p)
(b)
dσ/dcos(θ) (μb)
200
100
0
-1.0
-0.5
0.0
0.5
1.0
cos(θ_CM) (π⁻→pπ⁻)
(c)
dσ/dcos(θ) (μb)
80
60
40
20
0
-1.0
-0.5
0.0
0.5
1.0
cos(θ_CM) (π⁻→pπ⁰)
XBL 7611-9860

Fig. 60

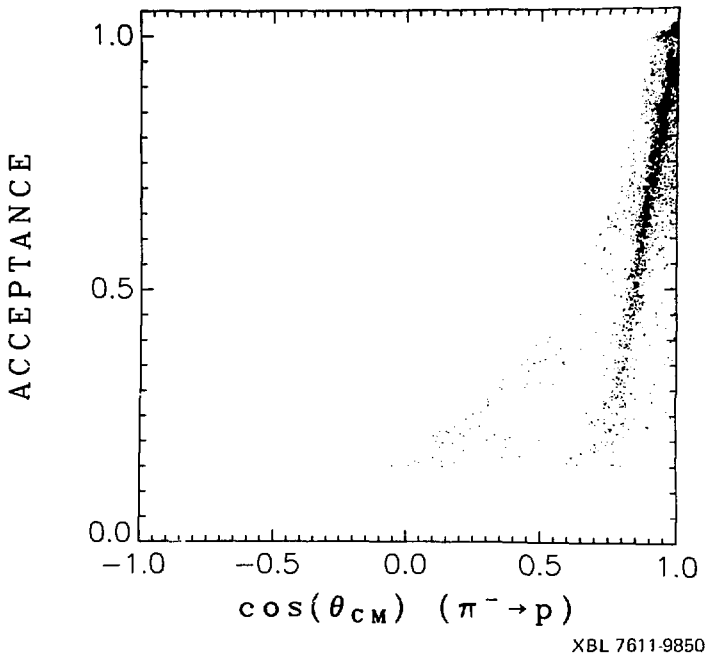

Fig. 61

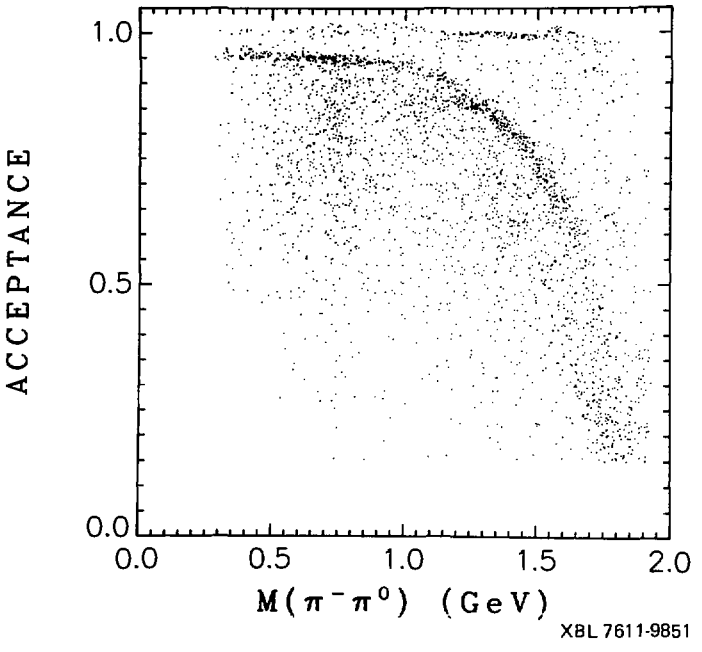

Fig. 62

3. ρ^- production

As seen in Fig. 53, there is evidence for reaction (31) in this channel. It is of interest to determine the differential cross section and the ρ^- density matrix for this reaction as a function of u'. The method of analysis used in determining these distributions involved a background subtraction in the region of the ρ^- peak in conjunction with a Monte Carlo simulation to account for acceptance losses. It appears that the ρ^- peak is shifted in mass from its nominal value. Thus, in order to do an accurate background subtraction, it was necessary to determine the mass and width of the observed ρ^- resonance and the shape of the background under it.

In Fig. 63 is a histogram of the $\pi^-\pi^0$ invariant mass with each event corrected up by the inverse of the trigger acceptance. An additional, constant factor is included so that the number of counts in a bin is equal to the cross section in that bin. However, since all events with acceptance less than 0.15 (as determined by the two-parameter acceptance) are eliminated, this is the cross section only of those events with acceptance greater than 0.15. The solid curve in Fig. 63 is a least squares fit (see Appendix A) to the data assuming a Breit-Wigner resonance above a background. The dashed curve represents the background only. The resulting fit yields a narrow ρ^-, rather low in mass:

$$M_\rho = 0.733 \pm 0.007 \text{ GeV}$$

$$\Gamma_\rho = 0.082 \pm 0.025 \text{ GeV}.$$

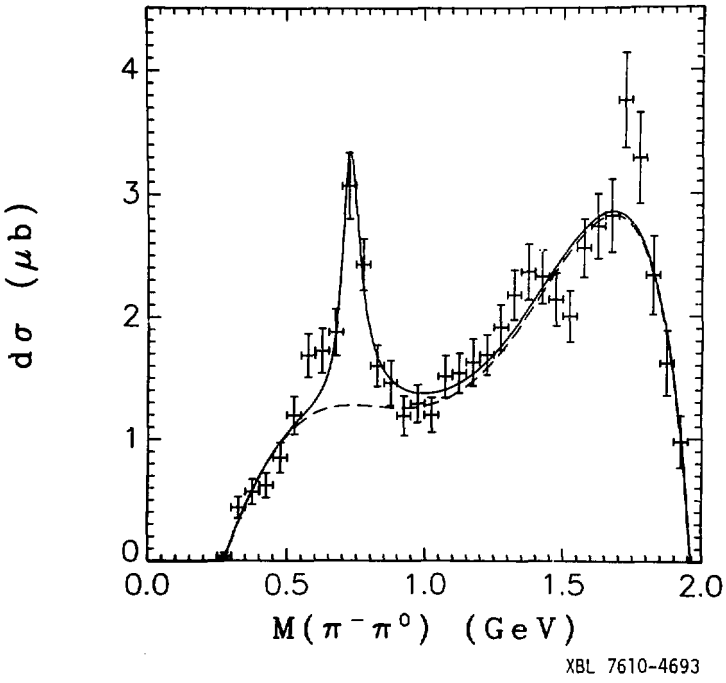

Fig. 63

These parameters, in conjunction with the peculiar shape of the background, indicate the possiblity of ρ^- interference with the background. The interference appears to be destructive on the high mass side of the ρ^-. The apparent sharp peak near 1.75 GeV in mass results from the fact that at high mass the acceptance becomes small (as can be seen in Fig. 62). A small background in the event sample due to events which should not have provided a trigger, but did as a result of a downstream proton interaction or small errors in the acceptance, will produce large effects at high mass due to the large weights assigned to the events.

Since this type of fit is used in much of the analysis described in this chapter, a few comments will be made regarding the fitting procedure. The functional form used in the least squares fit to the data is

$$\sigma = \sigma_{background} + \sigma_1 + \sigma_2 + \cdots,$$

where the total cross section is the incoherent sum of a background term and one or more Breit-Wigner resonance terms. Each term is expressed as a function of the invariant mass M. The background term is represented by

$$\sigma_{background} = (M - M_{min})^{\beta_1}(M_{max} - M)^{\beta_2}(\alpha_1 + \alpha_2 M + \alpha_3 M^2 + \cdots),$$

where

M_{min} = minimum possible mass available (i.e., the sum of the constituent masses)

M_{max} = maximum possible mass available (i.e., the center-of-mass energy minus the sum of the recoil constituent masses).

The exponents β_1 and β_2 are small (less than 5) positive numbers which force the mass distribution to zero at the kinematic limits. The cross section is defined to be zero outside the kinematic limits. The polynomial coefficients $\alpha_1, \alpha_2, \cdots$ are generally small in number to keep the background simple. The Breit-Wigner cross sections are given by

$$\sigma = A \frac{\Gamma}{2\pi} \frac{1}{(M - M_0)^2 + \Gamma^2/4} ,$$

where

A = cross sectional area under the resonance

M_0 = mass of resonance

Γ = width of resonance .

Generally the parameters A, M_0, and Γ are varied in the fit, unless the signal is small or difficult to isolate, in which case M_0 and Γ are held fixed at the nominal values and only A is varied. Various attempts were made to use more accurate parameterizations of the Breit-Wigner cross section. These variations included phase space factors, energy dependent widths, and the inclusion of barrier factors. Since the changes had little effect on the fits, the pure Breit-Wigner line shape with a kinematic limit cutoff was used.

After fitting the invariant mass distribution, it is possible to do the background subtraction. An interval in mass centered near the mass of the resonance is designated as the signal region. The width of this region is arbitrary, but is generally chosen to be larger than the

full width of the resonance. The cross sectional area of the background in the signal region is then calculated by numerically integrating the expression obtained for $\sigma_{background}$ in the fit. Equal width bands on either side of the signal region are constructed such that the sum of the cross sectional areas of the backgrounds in these two bands is equal to the cross sectional area of the background in the signal region. These two bands are designated the background region. The assumption is made that the background events in the background region are similar (in terms of u-distribution, decay distribution, recoil distribution, etc.) to the background events in the signal region. Thus, it is expected that a simple subtraction (i.e., all events associated with the signal region are assigned a positive weight and those associated with the background region are assigned a negative weight) will yield a sample of events with characteristics similar to those which would be obtained from a pure resonance signal without background. Finally, a correction factor is applied to correct for loss of the Breit-Wigner tails. This factor is given by

$$C = \frac{\sigma_{total}}{\sigma_S - \sigma_B} ,$$

where

σ_{total} = total Breit-Wigner cross sectional area

σ_S = Breit-Wigner cross sectional area in signal region

σ_B = Breit-Wigner cross sectional area in background region.

For the ρ^-, the signal region included events with $\pi^-\pi^0$ invariant mass between 0.55 and 0.90 GeV.

At this point, another component of the analysis procedure is introduced. As many events of interest are produced with little or no trigger acceptance, a simple weighting procedure is not sufficient to correct for the loss of all events of interest. For this reason, a Monte Carlo simulation of the reaction of interest is generated for comparison with the actual data distributions. For ρ^- production, a three-body final state event sample was generated in which the probability of generating an event with $\pi^-\pi^0$ invariant mass equal to M was proportional to the ρ^- Breit-Wigner cross section at M. The generated events were distributed in u' according to Eq. (29), where A and b are arbitrary at this point. Each Monte Carlo event is given a weight proportional to the three-parameter trigger acceptance for that event. Any events which would not be observed if they were real (i.e., events in which the two-parameter trigger acceptance is less than 0.15, events in which a fast pion traverses the Cerenkov counter, and events in which the recoil acceptance is zero) are eliminated from the event sample. Histograms of the resulting weighted Monte Carlo events can then be compared with the unweighted real event histograms. The parameters of the Monte Carlo distribution function (e.g., A and b in the case of ρ^- production) can be varied until reasonable agreement between the real data and the corrected down Monte Carlo data is obtained.

As the density matrix for the ρ^- was of interest, the decay angular distribution of the Monte Carlo events was also generated to roughly duplicate the real angular distribution after correction. The

decay angular distribution was assumed to be independent of u'. It was found, not only for the ρ^- but also for the other meson systems analyzed, that the s-channel helicity frame seemed to be a better frame than the u-channel helicity frame for describing the decay. The density matrix elements appeared to vary less as a function of u' in the s-channel frame than in the u-channel frame. On the other hand, a better description of the decays of baryon systems was obtained in the u-channel helicity frame. (The coordinate systems used in specifying helicity frames are discussed in Appendix B. The relationship between the resonance decay angular distribution and the production density matrix elements is discussed in Appendix C.)

In Fig. 64 is the differential cross section for ρ^- production. The real events have all been corrected up by the inverse of the acceptance, and the cross section averaged over intervals in u' is shown with error bars. The dotted curve represents the Monte Carlo simulation of the differential cross section without corrections or event elimination. The dashed curve is the Monte Carlo distribution after being corrected down as described above, and then corrected up in the same manner as the real data (i.e., by weighting each event by the inverse of the trigger acceptance). The dashed curve is seen to represent the data fairly well.

In Fig. 65 are shown the ρ^- decay distributions in the s-channel helicity frame. The angles refer to the direction of the π^- in the ρ^- rest frame. The dotted and dashed curves are as described above. In both the real and Monte Carlo event samples, only events with $u' > -0.4$ GeV^2 are included.

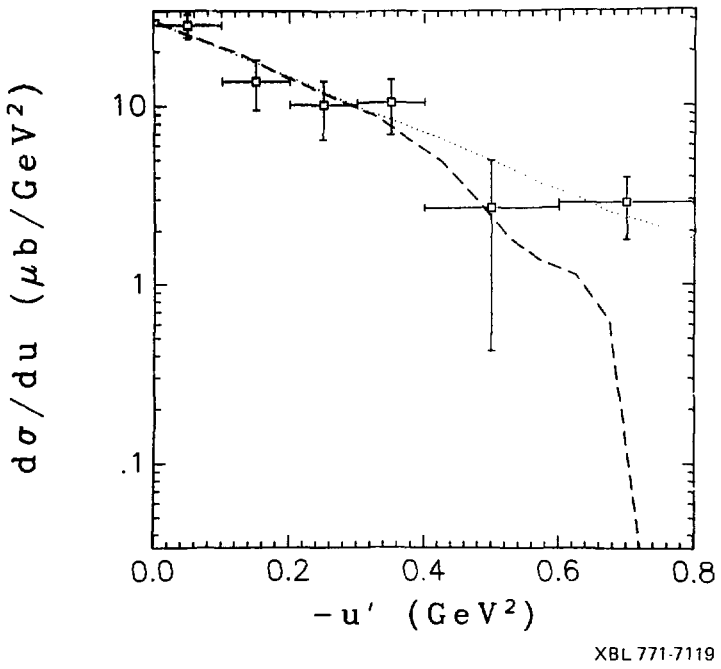

Fig. 64

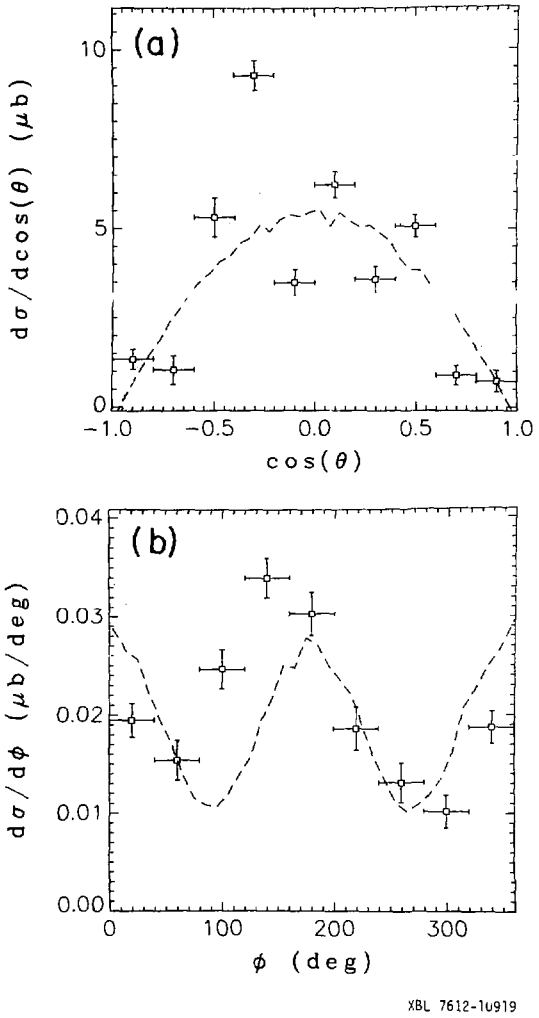
(a)
10
5
0
−1.0
−0.5
0.0
0.5
1.0
dσ/dcos(θ) (μb)
cos(θ)
(b)
0.04
0.03
0.02
0.01
0.00
0
100
200
300
dσ/dφ (μb/deg)
φ (deg)
XBL 7612-1u919

Fig. 65

In Fig. 66 are comparisons of the real and Monte Carlo density matrix elements in the s-channel helicity frame. The density matrix elements as a function of u' are determined by calculating combinations of expectation values of the spherical harmonics over intervals of u', as described in Appendix C. The density matrix elements are fairly constant for $u' > -0.4$ GeV^2. Outside of this interval, the errors become large. In Table XXII are the corrected density matrix elements averaged over the interval $u' > -0.4$ GeV^2. The measured values are corrected for the loss of events with trigger acceptance less than 0.15 by adding the difference between the density matrix elements of the generated Monte Carlo events (given by the dotted curves) and the matrix elements of the corrected Monte Carlo events (given by the dashed curves) to the measured averages. The density matrix elements satisfy the positivity constraints within errors. Parity conservation in the production reaction requires the imaginary parts of the density matrix elements to be zero. This requirement is obeyed for $Im(\rho_{10} - \rho_{0,-1})/2$ but not for $Im(\rho_{1,-1})$. This violation indicates the existence of processes other than the quasi two-body reaction of Eq. (31) in the subtracted event sample.

A variation of the Stodolsky-Sakurai model (see Appendix D) makes predictions for the ρ^- density matrix elements based on the assumption that the ρ^- behaves like an M1 photon transition between the exchanged delta and the target proton. The predictions in the u-channel helicity frame are:

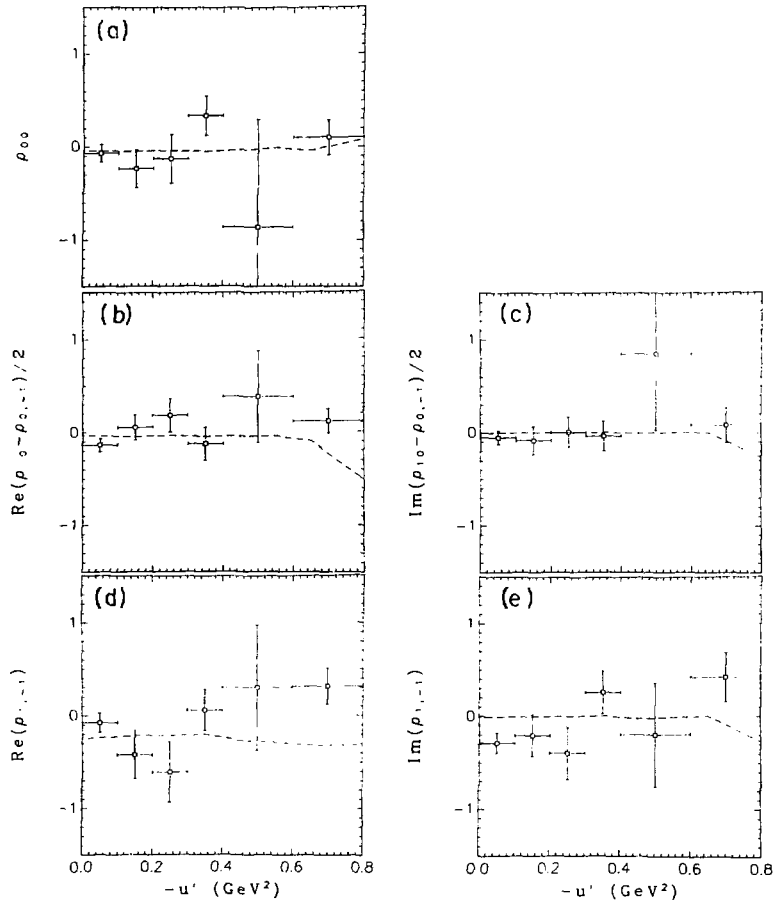
(a)
(b)
(c)
(d)
(e)
ρ_{00}
$\mathrm{Re}(\rho_{1,0}-\rho_{0,-1})/2$
$\mathrm{Im}(\rho_{1,0}-\rho_{0,-1})/2$
$\mathrm{Re}(\rho_{1,-1})$
$\mathrm{Im}(\rho_{1,-1})$
1
0
-1
0.0
0.2
0.4
0.6
0.8
$-u'$ (GeV^2)
XBL 7612-10921

Fig. 66

Table XXII. Average ρ^- density matrix elements in the s-channel helicity frame.

ρ_{00}	=	-0.04 ± 0.08
$\mathrm{Re}(\rho_{10} - \rho_{0,-1})/2$	=	-0.04 ± 0.06
$\mathrm{Im}(\rho_{10} - \rho_{0,-1})/2$	=	-0.05 ± 0.06
$\mathrm{Re}(\rho_{1,-1})$	=	-0.22 ± 0.09
$\mathrm{Im}(\rho_{1,-1})$	=	-0.19 ± 0.09

$$\rho_{00} = 0$$

$$(\rho_{10} - \rho_{0,-1})/2 = 0$$

$$\rho_{1,-1} = -\sqrt{3/4} \doteq -0.43.$$

These predictions can be compared with the data in Table XXIII. Both the u-channel and s-channel helicity frame density matrix elements are given as functions of u' and also averaged over the interval $u' > -0.4$ GeV^2. The u-channel data compares poorly with the prediction while the s-channel data is consistent with the predictions for ρ_{00} and $(\rho_{10} - \rho_{0,-1})/2$, and qualitatively consistent with the prediction for $\rho_{1,-1}$. There is no apparent reason for this effect.

In Fig. 67 is the fully corrected ρ^- differential cross section as a function of u'. The data points presented in the figure are listed in Table XXIV. Each data point includes a correction factor equal to the Monte Carlo cross section (averaged over the bin in u') divided by the Monte Carlo acceptance corrected cross section (also averaged over the bin in u') in order to account for events with trigger acceptance less than 0.15. A least squares fit of the differential cross section over the interval $u' > -0.6$ GeV^2 was made to the form

$$\frac{d\sigma}{du} = \sigma_T b e^{bu'},$$

where

σ_T = total backward cross section

b = slope of the backward peak.

Table XXIII. Real parts of the ρ^- density matrix elements as functions of u' in the u- and s-channel helicity frames.

u'	ρ_{00}		$Re(\rho_{10},\rho_{0,-1})/2$		$Re\ \rho_{1,-1}$	
	UHF	SHF	UHF	SHF	UHF	SHF
0.0 - 0.1	0.00 ± 0.11	-0.06 ± 0.09	.31 ± 0.08	-0.13 ± 0.07	-0.05 ± 0.10	-0.08 ± 0.10
0.1 - 0.2	0.28 ± 0.23	-0.23 ± 0.20	0.52 ± 0.19	0.06 ± 0.14	-0.17 ± 0.21	-0.32 ± 0.26
0.2 - 0.3	0.75 ± 0.30	-0.12 ± 0.26	0.26 ± 0.17	0.18 ± 0.18	-0.18 ± 0.24	-0.61 ± 0.33
0.3 - 0.4	0.16 ± 0.29	0.34 ± 0.21	0.08 ± 0.15	-0.12 ± 0.18	-0.04 ± 0.20	0.05 ± 0.22
0.0 - 0.4	0.21 ± 0.10	-0.04 ± 0.18	0.31 ± 0.06	-0.04 ± 0.06	-0.09 ± 0.08	-0.22 ± 0.09

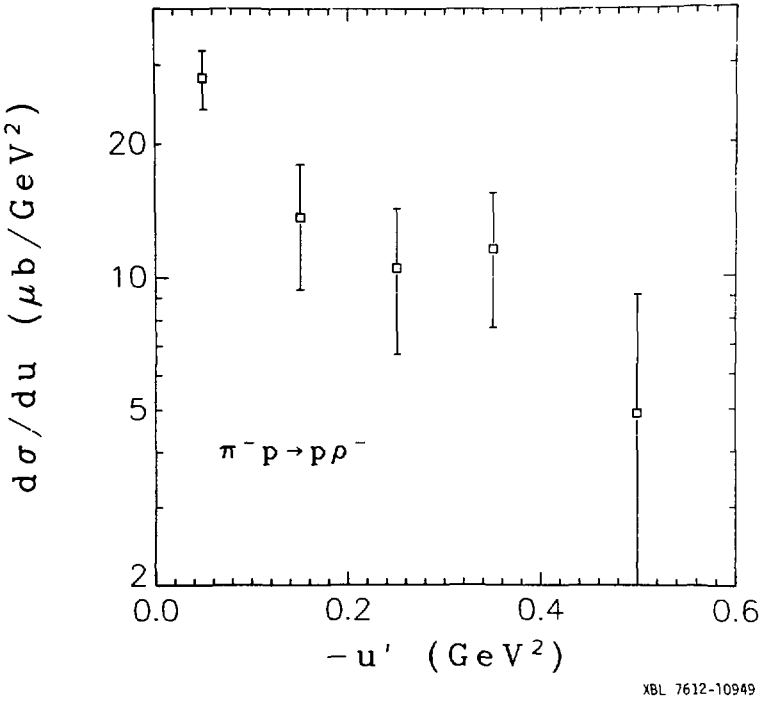

Fig. 67

Table XXIV. Differential cross section for $\pi^- p \to p\rho^-$ as a function of u'.

$-u'$ (GeV^2)	Δu (GeV^2)	$\frac{d\sigma}{du}$ ($\mu b/GeV^2$)
0.05	0.10	28.1 ± 4.2
0.15	0.10	13.7 ± 4.3
0.25	0.10	10.5 ± 3.8
0.35	0.10	11.6 ± 3.9
0.50	0.20	4.9 ± 4.2

The values of the parameters obtained in the fit were $\sigma_T = 8.2 \pm 1.5$ μb and $b = 3.9 \pm 1.2$ GeV^{-2}. If the estimated ±15% systematic error is included in the error assigned to the total cross section, then $\sigma_T = 8.2 \pm 1.9$ μb. There are other possible sources of error which are not included in this estimate. These include the errors associated with the parameters of the ρ^- resonance (mass and width), the shape of the background, the extrapolation of the differential cross section to all values of u', and the assumption of incoherence of the resonant and background cross sections.

In Fig. 68 is a plot of the total cross section as a function of lab momentum for this experiment and the experiment of Anderson et al.[40] at 8 and 16 GeV/c. All data points include systematic errors. The straight line represents a linear least squares fit to the three data points in log-log space. The functional dependence of the total backward cross section with lab momentum as determined by the fit is

$$\sigma_T \propto P_{LAB}^{-2.33 \pm 0.28},$$

where P_{LAB} is the incident beam momentum. The value of the exponent is consistent with the value of 2.45 ± 0.17 obtained in the backward elastic scattering case. Both reactions require delta exchange.

In Fig. 69, the slope parameter b is shown as a function of lab momentum. The slope obtained in this experiment is consistent with the slopes at 8 and 16 GeV/c obtained by Anderson et al.

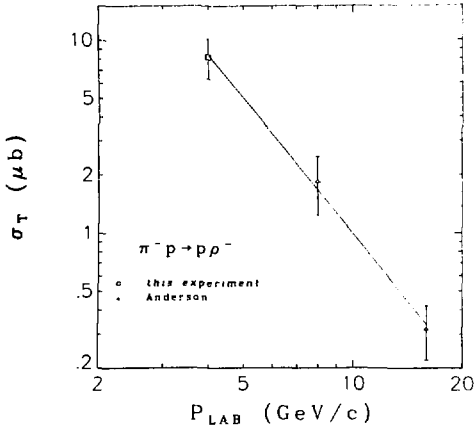
σ_T (μb)
10
5
2
1
.5
.2
$\pi^- p \to p\rho^-$
o this experiment
• Anderson
2
5
10
20
P_{LAB} (GeV/c)

Fig. 68

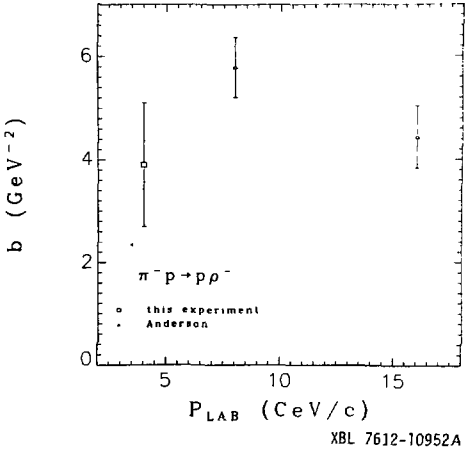
b (GeV^{-2})
6
4
2
0
$\pi^- p \to p\rho^-$
o this experiment
• Anderson
5
10
15
P_{LAB} (GeV/c)
XBL 7612-10952A

Fig. 69

4. $\Delta^0(1232)$ and N^{*0} production

As can be seen in Fig. 54, there is evidence for the processes described by reactions (32) and (33). The procedure used to analyze the Δ^0 and N^{*0} final states was similar to that used in the ρ^- production analysis. In Fig. 70(a) is the weighted $p\pi^-$ invariant mass distribution for all events with trigger acceptance greater than or equal to 0.15. The bin contents are corrected to display cross section. A least squares fit consisting of Breit-Wigner resonance contributions for the $\Delta^0(1232)$, $N^{*0}(1520)$, and $N^{*0}(1670)$ over a background was made to the distribution. Although there is little evidence in this mass distribution for more than one resonance in the neighborhood of 1.6 GeV, data in the 4- and 5-body final states (to be discussed in later sections) indicate the presence of more than one N^* in this region. The identity of the N^*'s is unknown and the selection of the $N^{*0}(1520)$ and the $N^{*0}(1670)$ to represent the enhancement was purely arbitrary. No results are dependent on this selection. The masses and widths of the resonances were fixed in the fitting and only the cross sectional areas allowed to vary. The nominal values given in the Particle Data Group Tables[56] were used:

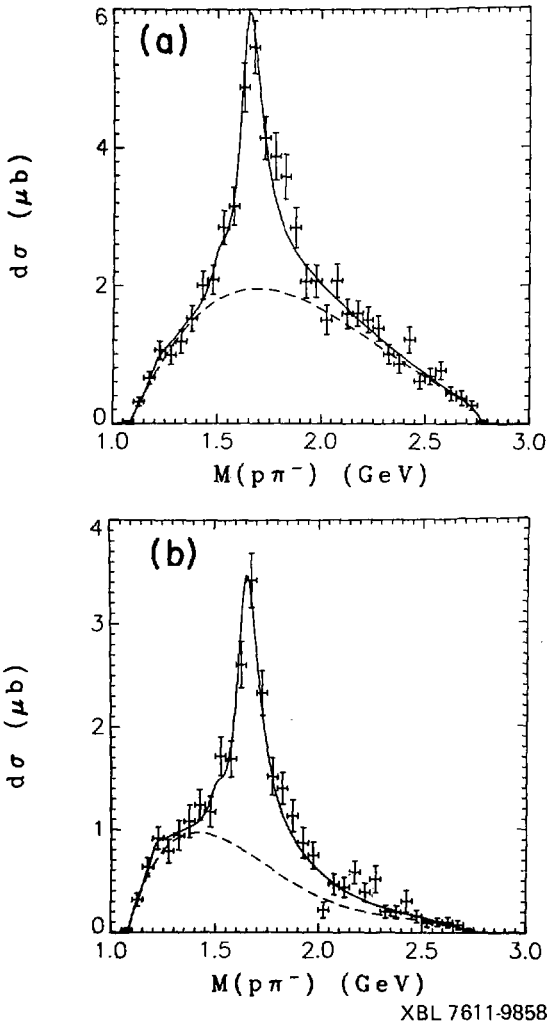

Fig. 70

$$M_{\Delta^0(1232)} = 1.232 \text{ GeV}$$

$$\Gamma_{\Delta^0(1232)} = 0.115 \text{ GeV}$$

$$M_{N^{*0}(1520)} = 1.52 \text{ GeV}$$

$$\Gamma_{N^{*0}(1520)} = 0.125 \text{ GeV}$$

$$M_{N^{*0}(1670)} = 1.67 \text{ GeV}$$

$$\Gamma_{N^{*0}(1670)} = 0.155 \text{ GeV} .$$

The solid curve in Fig. 70(a) represents the results of the fit. The dashed curve is the background. In Fig. 70(b) is a similar mass distribution in which the requirement is imposed that

$$\cos \theta^*_{\pi^- \to p\pi^-} \leq 0.8 .$$

The background determined in the fit was used in the subtraction procedure.

In Fig. 71 is shown the background subtracted differential cross section for $\Delta^0(1232)$ production in this channel. The data points are uncorrected for acceptance but are corrected for the loss of the Breit-Wigner tails . The signal region used in the subtraction

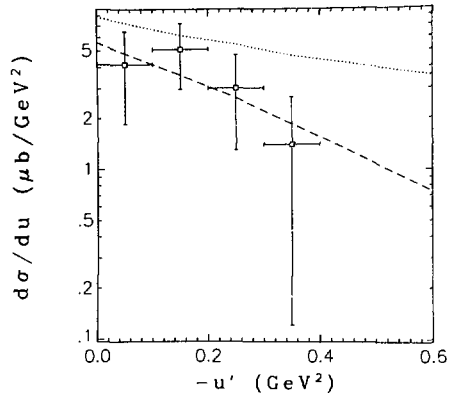
dσ/du (μb/GeV²)
5
2
1
.5
.2
.1
0.0
0.2
0.4
0.6
-u' (GeV²)

Fig. 71

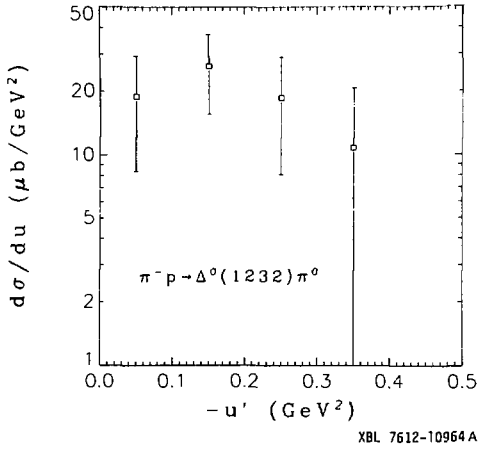
dσ/du (μb/GeV²)
50
20
10
5
2
1
π⁻p→Δ⁰(1232)π⁰
0.0
0.1
0.2
0.3
0.4
0.5
-u' (GeV²)
XBL 7612-10964A

Fig. 72

was $1.15 \leq M_{p\pi^-} < 1.30$ GeV. The dotted line is a simulated Monte Carlo differential cross section and the dashed line is the resulting cross section after weighting each event by the three-parameter acceptance and eliminating those events which are eliminated in the real data sample.

In Fig. 72 is the corrected differential cross section for Δ^0 production. The Monte Carlo has been used to correct for trigger acceptance. In addition, a correction has been included to account for the other decays of the Δ^0 (a factor of 3 due to the isotopic spin Clebsch-Gordan coefficient). The data presented in the figure is listed in Table XXV. There is evidence for peaking in the backward region, but there is an indication of a dip at $u' = 0$. There are no known previous analyses of this reaction with adequate statistics to determine the shape of the backward cross section. However, the reaction

$$\pi^- p \rightarrow \Delta^- \pi^+$$

with forward Δ^- production has been analyzed.[35,36] The cross section is found to dip at $u' = 0$ in this reaction and thus is qualitatively consistent with the Δ^0 production cross section found in this experiment. The total cross section in the interval $u' > -0.4$ GeV^2 is $\sigma = 7.5 \pm 2.1$ μb. When the ±15% systematic error is added in quadrature, $\sigma = 7.5 \pm 2.4$ μb. The inclusion of errors due to the background subtraction will increase the error still more.

Table XXV. Differential cross section for $\pi^- p \to \Delta^0(1232)\,\pi^0$ as a function of u'.

$-u'$ (GeV^2)	Δu (GeV^2)	$\frac{d\sigma}{du}$ ($\mu b/GeV^2$)
0.05	0.10	18.9 ± 10.5
0.15	0.10	26.4 ± 10.8
0.25	0.10	18.6 ± 10.5
0.35	0.10	10.8 ± 9.9

Table XXVI. Differential cross section for $\pi^- p \to N^{*0}(1600)\pi^0$ as a function of u'.

$-u'$ (GeV^2)	Δu (GeV^2)	$\frac{d\sigma}{du}$ ($\mu b/GeV^2$)
0.05	0.10	145.8 ± 19.8
0.15	0.10	99.6 ± 20.0
0.25	0.10	60.9 ± 19.6
0.35	0.10	48.2 ± 14.2
0.50	0.20	49.8 ± 10.2
0.70	0.20	54.0 ± 11.4
0.90	0.20	46.5 ± 11.6

The density matrix of the Δ^0 is not well determined; $\rho_{\frac{1}{2}\frac{1}{2}} = 0.30 \pm 0.16$. The other density matrix elements are consistent with zero within errors of approximately the same magnitude.

The higher mass N^{*0} region will be analyzed as a single enhancement, referred to as the $N^{*0}(1600)$, since separation of the individual resonance contributions is impossible. The analysis procedure is similar to that for the ρ^- and $\Delta^0(1232)$. The signal region includes the interval $1.45 \leq M_{p\pi^-} < 1.85$ GeV, and the Breit-Wigner tail corrections are made based on the $N^{*0}(1520)$ and $N^{*0}(1670)$ cross sections obtained in the least squares fit to the invariant mass distribution. The background subtracted data is shown in Fig. 73 (corrected up by the inverse of the trigger acceptance) along with Monte Carlo simulation curves. The dashed curve is to be compared directly with the data. It appears to describe the data fairly well in the interval $u' > -0.4$ GeV^2, but after this point the data deviates considerably from the Monte Carlo curve. If the real data points are corrected for lost events in the standard manner, the differential cross section appears as in Fig. 74 . In this figure, an isospin Clebsch-Gordan coefficient correction was made based on the assumption that $I = \frac{1}{2}$. Since the identities of the resonant states have not been established, no correction can be made for decay modes other than $N\pi$. The data points represented in Fig. 74 are given in Table XXVI.

The differential cross section appears to have a sharp backward peak superimposed on a flat background. The sharp backward peak is presumably the result of a baryon exchange reaction, but the isotropic component is possibly due to s- or t-channel processes. A least squares fit of the data was made to the expression

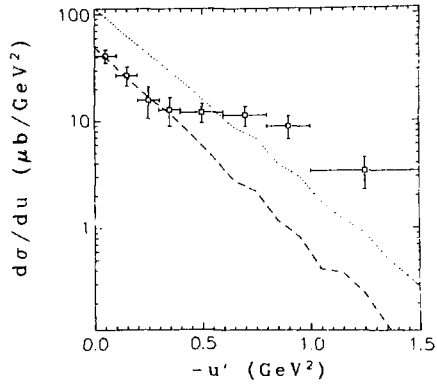
100
10
1
0.0
0.5
1.0
1.5
dσ/du (μb/GeV²)
-u' (GeV²)

Fig. 73

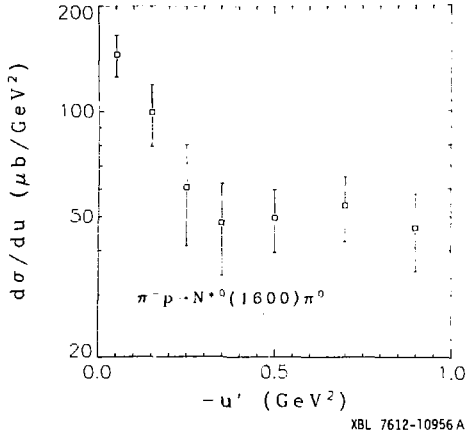
200
100
50
20
0.0
0.5
1.0
dσ/du (μb/GeV²)
π⁻p→N*⁰(1600)π⁰
-u' (GeV²)
XBL 7612-10956A

Fig. 74

$$\frac{d\sigma}{du} = \sigma_{peak}\, b\, e^{bu'} + \left(\frac{d\sigma}{du}\right)_{flat},$$

where

σ_{peak} = total cross section of backward peak

b = exponential slope of backward peak

$\left(\frac{d\sigma}{du}\right)_{flat}$ = cross section of isotropic background .

σ, b, and $\left(\frac{d\sigma}{du}\right)_{flat}$ were varied in the fit and the resulting parameters are

$\sigma_{peak} = 17.6 \pm 5.1$ μb

$b = 8.9 \pm 3.7$ GeV^{-2}

$\left(\frac{d\sigma}{du}\right)_{flat} = 48.2 \pm 6.8$ μb/GeV^2 .

These errors reflect only the statistical errors and the errors associated with the fit.

The decay angular distribution of the $N^{*0}(1600)$ was also examined in the analysis. Figure 75 shows the decay angular distributions as a function of $\cos(\theta)$ and ϕ, where the angles refer to the proton direction relative to the u-channel helicity frame axes in the N^* rest frame. The data is qualitatively consistent with the Monte Carlo distributions (dashed curves). If the assumption is made that the $N^{*0}(1600)$ is a $J = \frac{5}{2}$ resonance (a valid assumption for any $N^{*0}(1670)$

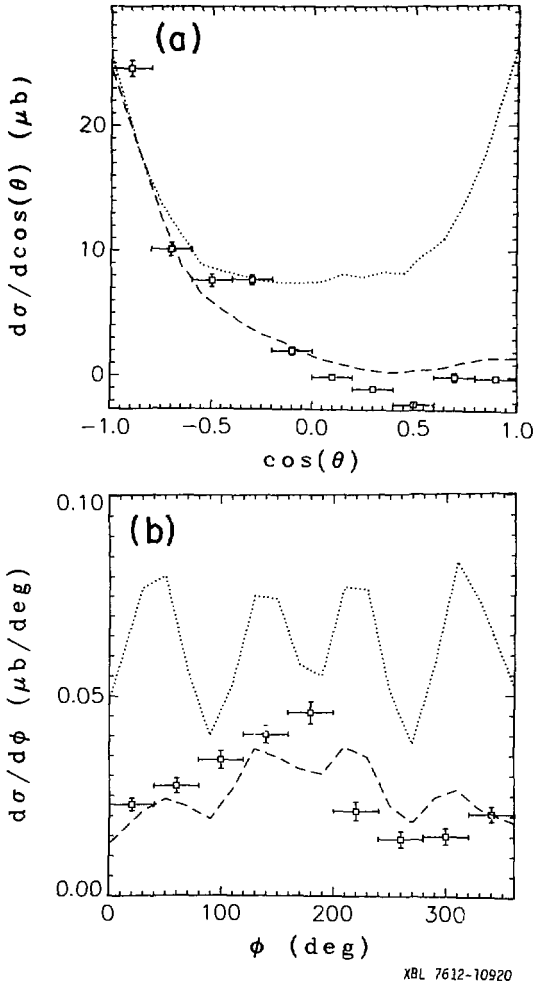
(a)
dσ/dcos(θ) (μb)
20
10
0
−1.0
−0.5
0.0
0.5
1.0
cos(θ)
(b)
dσ/dφ (μb/deg)
0.10
0.05
0.00
0
100
200
300
φ (deg)
XBL 7612-10920

Fig. 75

or $N^{*0}(1688)$ which might be in the enhancement, but not for any $N^{*0}(1520)$), estimates of the density matrix elements can be made. The value determined for $\rho_{1\frac{1}{2}\frac{1}{2}}$ is

$$\rho_{1\frac{1}{2}\frac{1}{2}} = 0.38 \pm 0.08 ,$$

though the statistical error quoted might not be a reliable estimate of the error. The rest of the matrix elements are not well determined but are all fairly close to zero.

5. $\Delta^{+}(1232)$ and N^{*+} production

As can be seen in Fig. 55, there is evidence for reactions (34) and (35). A comparison of these invariant mass distributions with the $p\pi^{-}$ invariant mass distributions reveals that the structure in N^{*+} production is somewhat different than the structure in N^{*0} production. Whereas the predominant N^{*0} state is in the region of the $N^{*}(1670)$, there is no evidence for the production of this high mass state in the $p\pi^{0}$ mass spectrum. Instead, there is an enhancement in the region of the $N^{*}(1520)$. One possible explanation of this effect depends upon the assumption that $p\pi^{-}$ final states are produced by nucleon exchange whereas $p\pi^{0}$ final states are produced by delta exchange. Thus, it would appear that the higher mass state has a small branching fraction into $\Delta\pi$ and the lower mass state has a significant branching fraction into $\Delta\pi$. In Table XXVII are listed the baryon resonances in the mass region of interest from the Particle Data Group Tables, along with the $N\pi$ and $\Delta\pi$ branching fractions. It is seen that the $N^{*}(1520)$ has a relatively large branching fraction into $\Delta\pi$ as does the $N^{*}(1670)$, but the $N^{*}(1688)$

Table XXVII. $N\pi$ and $\Delta\pi$ branching fractions for some baryon resonances.

Resonance	J^P	Fraction $N\pi$ (%)	Fraction $\Delta\pi$ (%)
$N^*(1520)$	$\frac{3}{2}^-$	55	25
$N^*(1535)$	$\frac{1}{2}^-$	30	1
$N^*(1670)$	$\frac{5}{2}^-$	45	50
$N^*(1688)$	$\frac{5}{2}^+$	60	11
$N^*(1700)$	$\frac{1}{2}^-$	55	4
$\Delta(1650)$	$\frac{1}{2}^-$	35	50
$\Delta(1670)$	$\frac{3}{2}^-$	15	45

has a considerably smaller branching fraction. This indicates that the higher mass state is to be identified with the $N^*(1688)$ rather than the $N^*(1670)$, but the evidence is not conclusive either way considering how far off the mass shell the exchanged Δ is.

In Fig. 76 are the $p\pi^0$ invariant mass distributions after correction for events with trigger acceptance greater than or equal to 0.15. Events with trigger acceptance less than 0.15 are eliminated. The four figures have the same requirements imposed as in Fig.55. The solid curves are least squares fits to the mass distributions which consist of Breit-Wigner resonance contributions from the $\Delta^+(1232)$ and the $N^{*+}(1520)$ plus a background term. The masses and widths of the baryon resonances were fixed at the nominal values. The dashed curves represent the background. The fits were poor in many cases due to structure not incorporated into the model.

In Fig.77 is shown the $\Delta^+(1232)$ differential cross section as a function of u'. The data is not weighted by the inverse of the trigger acceptance, but is corrected to be in units of cross section. The Monte Carlo distributions show that the distribution is consistent with isotropy (i.e., there is no backward peaking). In Fig.78 is shown the $N^{*+}(1520)$ differential cross section, also unweighted. Although there is some evidence for backward peaking, the errors are large and the distribution is also consistent with isotropy.

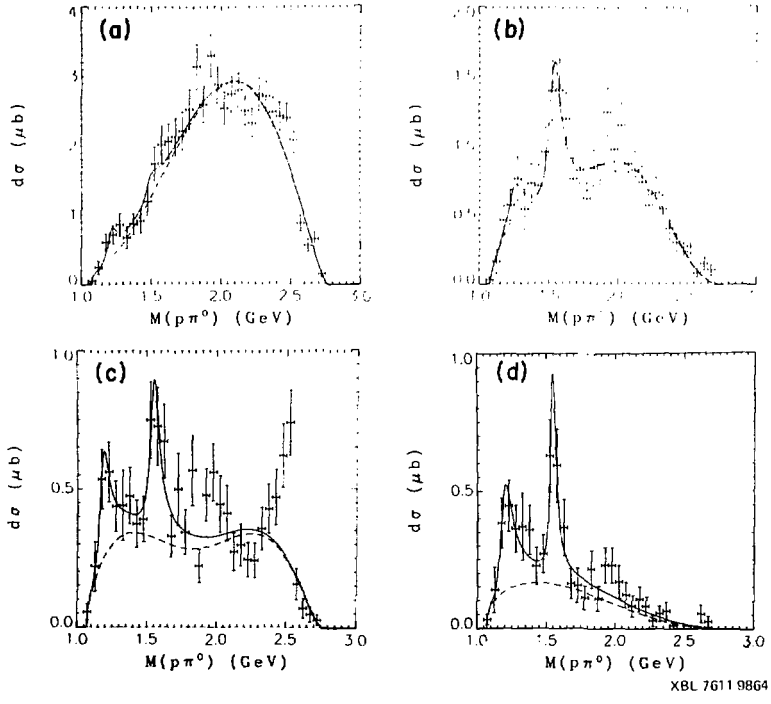

Fig. 76

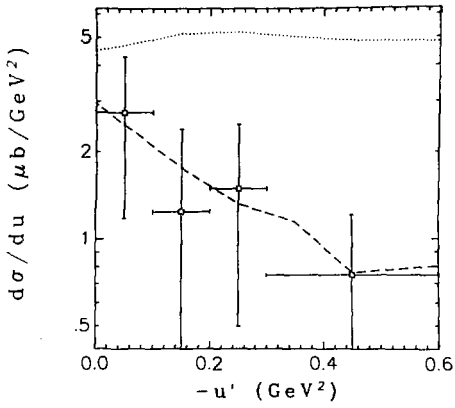
dσ/du (μb/GeV²)
5
2
1
.5
0.0
0.2
0.4
0.6
-u' (GeV²)

Fig. 77

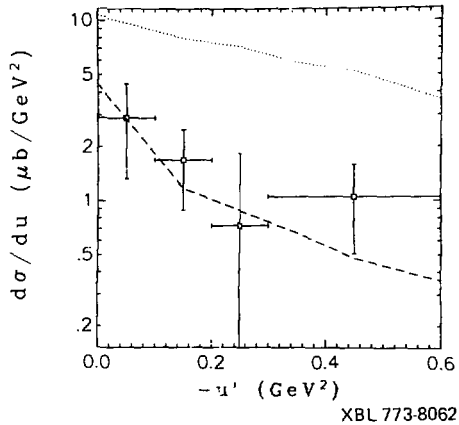
dσ/du (μb/GeV²)
10
5
2
1
.5
.2
0.0
0.2
0.4
0.6
-u' (GeV²)
XBL 773-8062

Fig. 78

6. Maximum likelihood channel fit

A totally independent analysis of the 3-body final state was done which involved a maximum likelihood fit of the data to a distribution function representing the incoherent sum of a set of quasi two-body reaction cross sections. The reactions included in the fit are given in Table XXVIII. The distribution function can be represented by

$$d\sigma = \sum_i \alpha_i BW_i(M)\, W_i(\theta,\phi) e^{b_i u'} R_3 \quad ,$$

where the summation is over the processes included in the fit. The Breit-Wigner factor is given by

$$BW(M) = \frac{\Gamma}{2\pi} \frac{1}{(M - M_0)^2 + \Gamma^2/4} \quad ,$$

where

M = invariant mass of the two-body system

M_0 = resonance mass

Γ = resonance width .

The resonance parameters were not varied in the fit but were either taken as the nominal values or were taken from the results of the analyses discussed previously in this section (e.g., for the ρ^-). For the term describing ρ^- production, M refers to the $\pi^-\pi^0$ invariant mass. The decay angular distribution factor, $W(\theta,\phi)$, is discussed in Appendix C. The density matrix elements, which determine

Table XXVIII. Reactions included in maximum likelihood channel fit. Slopes refer to exponential falloff in u' distribution.

Reaction	Slope (GeV^{-2})
$\pi^- p \rightarrow p\rho^-$	3.6
$\pi^- p \rightarrow \Delta^0(1232)\pi^0$	2.0
$\pi^- p \rightarrow N^{*0}(1520)\pi^0$	3.9
$\pi^- p \rightarrow N^{*0}(1670)\pi^0$	3.9
$\pi^- p \rightarrow \Delta^+(1232)\pi^-$	2.0
$\pi^- p \rightarrow (\pi^- p)\pi^0$	0.0

Table XXIX. Cross sections determined in maximum likelihood channel fit.

Reaction	$\sigma_T(\mu b)$
$p\rho^-$	7.6 ± 0.7
$\Delta^0\pi^0$	1.9 ± 0.6
$N^*(1520)\pi^0$	2.2 ± 1.0
$N^*(1670)\pi^0$	30.2 ± 2.4
$\Delta^+\pi^-$	1.7 ± 0.5

the angular distribution, were varied in the fit. These density matrix elements were assumed to be independent of u', however. For the ρ^-, the s-channel helicity frame was defined as the coordinate system, and θ and ϕ refer to the decay angles of the π^- in the ρ^- rest frame. For the baryon resonances, the u-channel helicity frame was used, and θ and ϕ refer to the proton decay angles. The exponential factor is a function of u' from the target (beam) to the ρ^- (baryon resonance). The slope factors were not varied in the fit, but were taken from the previous analyses of the ρ^- and N^{*0} resonances. For Δ^0 and Δ^+ production, an assumed slope of 2.0 GeV^{-2} was used as the data did not provide reliable estimates for these reactions. (It was decided not to duplicate the complicated u' distributions evident in the data, but rather to make approximations in order to obtain a qualitative description of the 3-body final state.) The factor α_i is related to the cross section for the process in question and is varied in the fit. R_3 represents 3-body phase space. Two final comments should be made concerning the processes included in the fit. The last entry in Table XXVIII represents an isotropic $p\pi^-$ system in which there is no Breit-Wigner term, no u' dependence, and a decay distribution of the form

$$W(\theta,\phi) = 1 + B \cos^2 \theta .$$

There was, in addition, a term intended to duplicate the effect of events which actually satisfied a different hypothesis but were included in the event sample.

A description of the fitting procedure is given in Appendix A. The real events were unweighted. The generated Monte Carlo events were given weights equal to the three-parameter trigger acceptance. Both real events and Monte Carlo events with trigger acceptance less than 0.15 or with zero recoil acceptance, and events in which a charged pion traversed the Cerenkov counter, were eliminated.

The results of the fit are shown in Table XXIX. The reported cross sections represent the total production cross sections uncorrected for unobserved decay modes. The errors (1 s.d.) result from the fit and do not include systematic errors. The ρ^- and N^{*0} cross sections compare well with the results of the previous analyses. The Λ^0 and Λ^+ production cross sections are expected to differ from the previous results due to the assumptions made regarding the u distribution.

In order to evaluate how well the fit represents the data, it is useful to compare projections of the data onto one dimension with the corresponding Monte Carlo projections. In Fig.79 is the unweighted $\pi^-\pi^0$ invariant mass distribution for all events with trigger acceptance greater than 0.15. The histogram represents the real data and the dashed curve represents the Monte Carlo simulation of the fit. The major discrepancy between the data and the simulation is in the region just above the ρ^- in mass. Many variations were included in the fit, but none reproduced the low region in the data. This low region in the invariant mass distribution, along with the narrow width and low mass of the ρ^- resonance, indicates the possibility of interference between the resonance and the background. This possiblity will be discussed

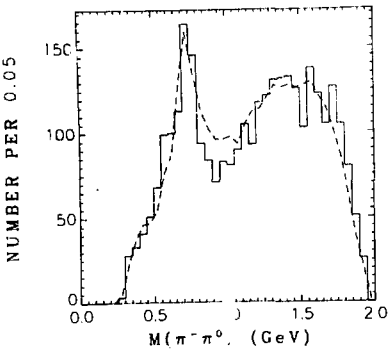

Fig. 79

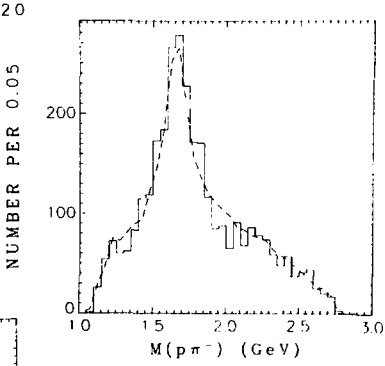

Fig. 80

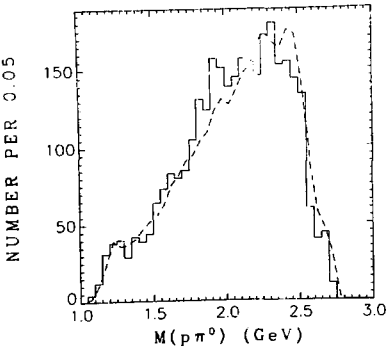

Fig. 81

XBL 7610-4719A

later when ρ^0 production in the 4-body final state (where there is also evidence for interference effects) is discussed.

In Fig. 80 is the π^-p invariant mass distribution. The fit appears to deviate from the data in the region of the $\Delta^0(1232)$, resulting in a smaller value of the cross section than might be expected. The large background in this mass region results from reflections of other channels, and could not be significantly reduced. The fit also appears to deviate from the data in the region near 2.0 GeV. There is no reason to believe that this dip is anything but a statistical fluctuation, though.

In Fig. 81 is the $p\pi^0$ invariant mass distribution. Except for the $\Delta^+(1232)$, the remainder of the mass distribution is the result of reflections from other channels. There is evidence for an excess in the data which is not duplicated by the Monte Carlo simulation just below 2.0 GeV in mass.

The momentum transfer distributions and decay angular distributions are well represented by the fit. In Fig. 82 are histograms of u' from the beam to the p, $p\pi^-$, and $p\pi^0$ systems. In Fig. 83 are the expectation values of some of the spherical harmonics, where the $\pi^-\pi^0$ system decay angles are defined in the s-channel helicity frame, as a function of $\pi^-\pi^0$ invariant mass. The Monte Carlo simulation is seen to deviate somewhat from the data at low invariant mass, but above the ρ mass, the data is well reproduced by the Monte Carlo. In Fig. 84 are expectation values of some of the spherical harmonics, in the u-channel helicity frame, as a function of $p\pi^-$ invariant mass. The

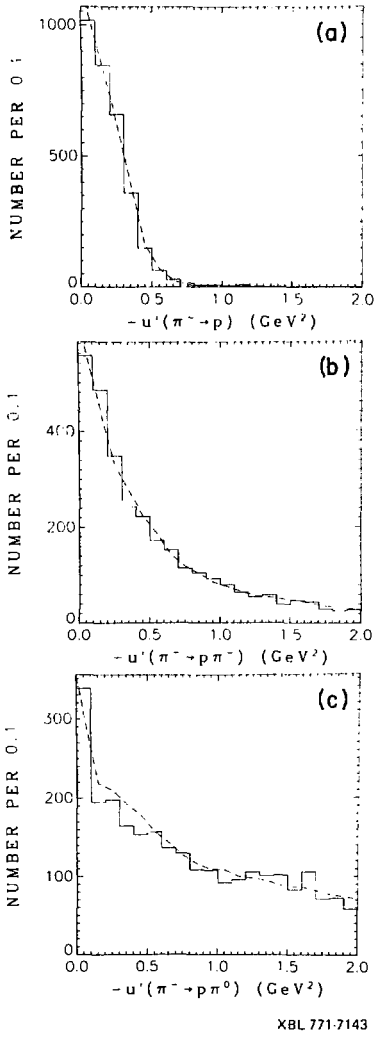
(a)
NUMBER PER 0.1
1000
500
0
0.0
0.5
1.0
1.5
2.0
$-u'(\pi^- \to p)$ (GeV^2)
(b)
NUMBER PER 0.1
400
200
0
0.0
0.5
1.0
1.5
2.0
$-u'(\pi^- \to p\pi^-)$ (GeV^2)
(c)
NUMBER PER 0.1
300
200
100
0
0.0
0.5
1.0
1.5
2.0
$-u'(\pi^- \to p\pi^0)$ (GeV^2)
XBL 771-7143

Fig. 82

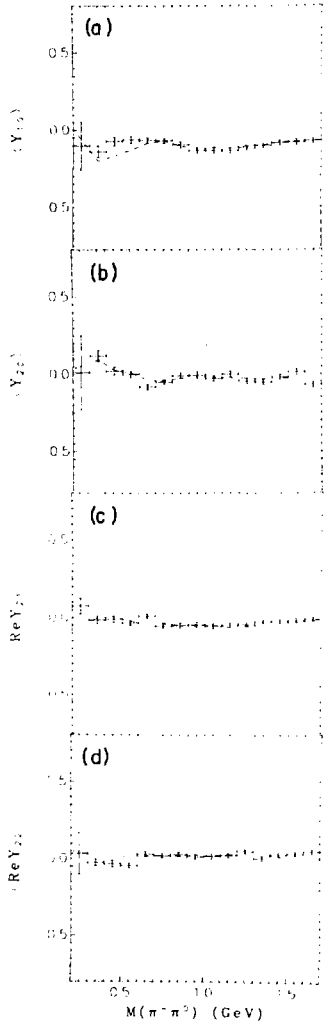

Fig. 83

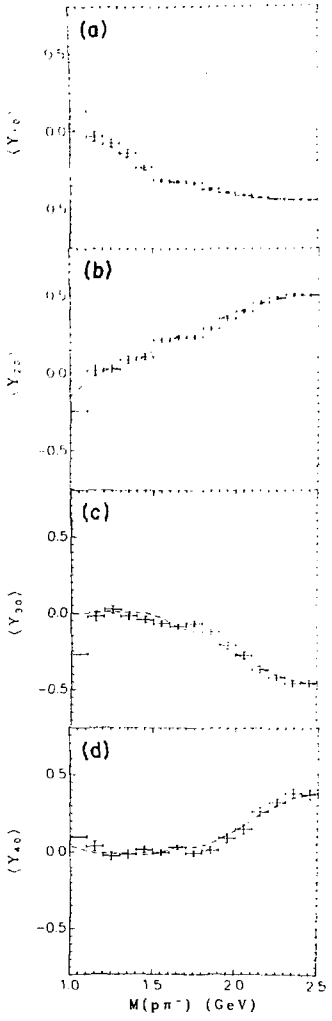
(a)
(b)
(c)
(d)
$\langle Y_{00} \rangle$
$\langle Y_{20} \rangle$
$\langle Y_{30} \rangle$
$\langle Y_{40} \rangle$
0.5
0.0
-0.5
1.0
1.5
2.0
2.5
M(pπ⁻) (GeV)
XBL 771 7141

Fig. 84

four plots shown are the ones which display the most structure as a function of mass. The other expectation values vary only slightly with mass. In Fig. 85 are two samples of the expectation values of the spherical harmonics, in the u-channel helicity frame, as a function of $p\pi^o$ invariant mass.

As the resonance density matrix elements were also varied in the fit, estimates of these are available. For ρ^- production $\rho_{00} = 0.03 \pm 0.04$. This value is a result of a fit to the angular distribution, not a calculation involving the spherical harmonics. The error is the error calculated by the fit. This value is consistent with the results of the previous analysis. For $N^{*o}(1670)$ production, the fit determined $\rho_{1\frac{1}{2}\frac{1}{2}} = 0.51 \pm 0.04$, also consistent with the previous results.

Although this multi-channel maximum likelihood analysis was originally intended to provide a complete description of the 3-body final state, it later became evident that only an approximate description was possible. One of the main problems was related to the production angular distributions which could not be expressed simply in terms of exponential falloffs for most cases. The end result of the analysis was to indicate the channels which provided a significant part of the 3-body final state and the approximate cross sections associated with these channels, and to provide a background which could be used as a basis for examining possibly significant structure in the data.

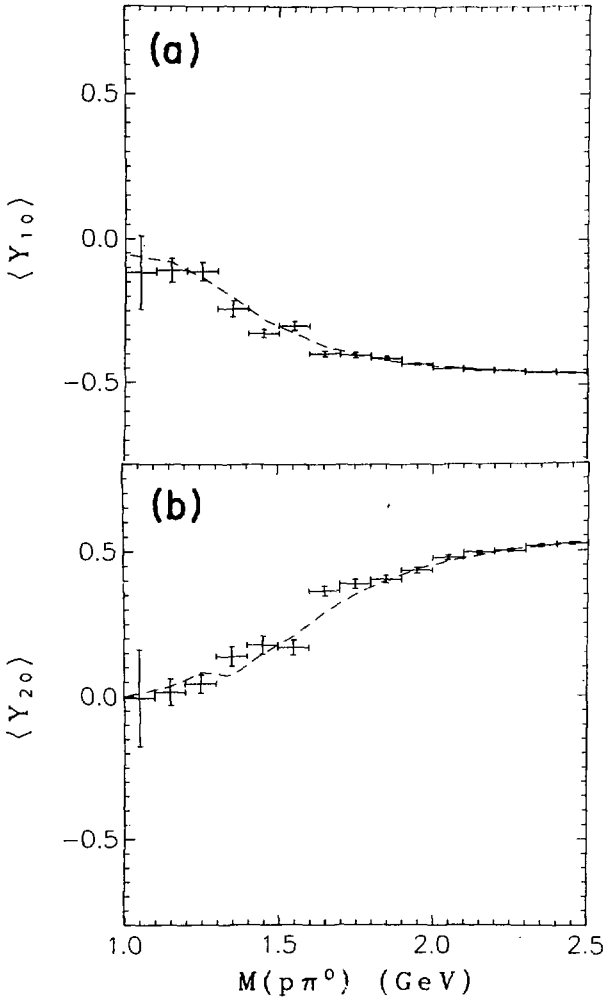

Fig. 85

C. $\pi^- p \rightarrow K^- p K^0$

The analysis of events satisfying this 1C hypothesis was minimal, although a preliminary investigation was carried out to look for evidence of significant structure in the data. There are 3521 2-prong events which satisfy this hypothesis with a kinematic fit χ^2 probability greater than or equal to 0.20, although the majority of the events satisfy at least one other kinematic hypothesis. Events in which the vertex fit χ^2 probability is less than 0.01 and events in which the primary vertex position is not within the liquid hydrogen, are not included in this event sample. In Fig. 86 is a histogram of the kinematic fit confidence level. It is seen that there is a large background consisting of events which are not bona fide events satisfying the hypothesis, even above 0.20 in confidence level. In Fig. 87 is a histogram of the missing mass squared from the charged tracks. The proton mass is assigned to the positive track and the K^- mass is assigned to the negative track. The peak in the distribution is near the square of the K^0 mass.

In Fig. 88 is a histogram of the $K^- K^0$ invariant mass. The events are unweighted, but events with trigger acceptance less than 0.15 are eliminated from the event sample. There appears to be a strong signal near threshold in the $K^- K^0$ invariant mass. However, this peak is consistent with Δ^- production in the reaction

$$\pi^- p \rightarrow \pi^- \pi^+ n ,$$

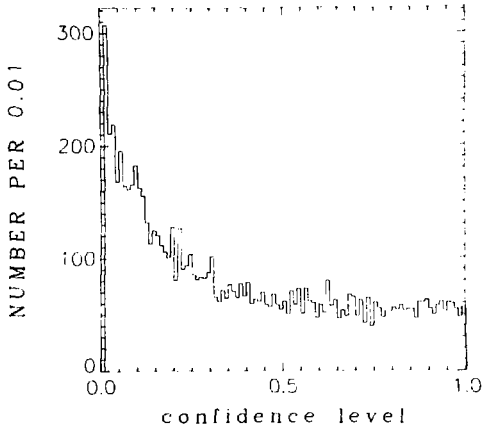
NUMBER PER 0.01
300
200
100
0
0.0
0.5
1.0
confidence level

Fig. 86

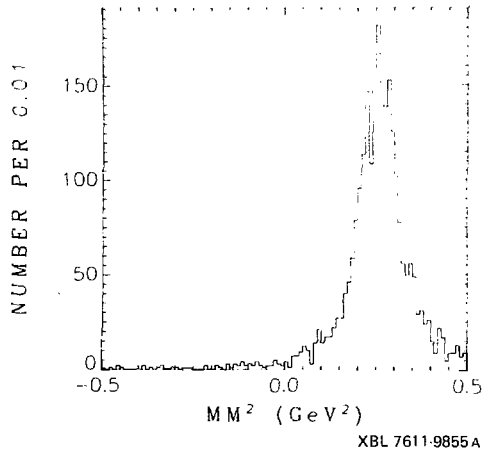
NUMBER PER 0.01
150
100
50
0
-0.5
0.0
0.5
MM² (GeV²)
XBL 7611-9855A

Fig. 87

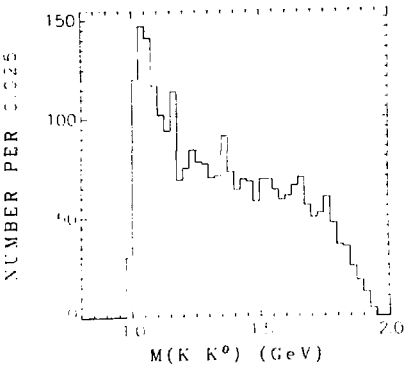

Fig. 88

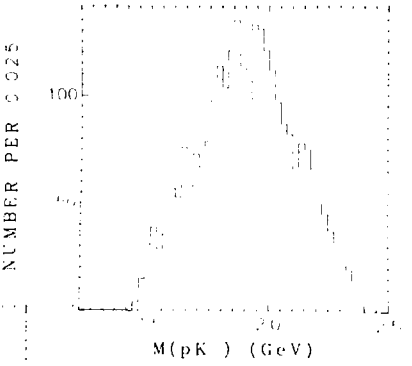

Fig. 89

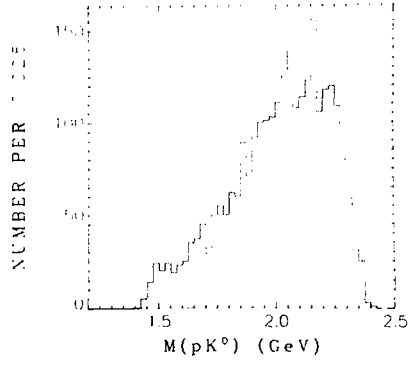

XBL 7611-9857A

Fig. 90

where the π^+ was misidentified as a proton, and the π^- and n were misidentified as a K^- and a K^0. Events with fast π^+'s occur due to Cerenkov counter inefficiencies. In Fig. 89 is the pK^- invariant mass distribution. There is no evidence for Y^* production. In Fig. 90 is the pK^0 invariant mass distribution. There is no evidence for structure in this exotic channel.

D. $\pi^- p \to \pi^- \pi^- \pi^+ p$

In this reaction, emphasis is placed on the analysis of meson production in the final state. Of particular interest is A_1^- and A_2^- production in the reactions:

$$\pi^- p \to p A_1^- \tag{36}$$

$$\pi^- p \to p A_2^- \ . \tag{37}$$

In both reactions (36) and (37), the proton is assumed to be produced at the pion vertex (via delta exchange) recoiling against the 3π system at the other vertex. Neutral meson production is seen in the $\pi^+\pi^-$ invariant mass distribution. Evidence is presented for the reactions

$$\pi^- p \to \pi^- p \rho^0 \tag{38}$$

$$\pi^- p \to \pi^- p f^0 \ . \tag{39}$$

There is no detailed analysis of baryon resonance production discussed, although Δ^{++} production is briefly considered. Finally, upper limits for the production of exotics in the reaction

$$\pi^- p \to \pi^+ p X^{--} \tag{40}$$

are presented.

1. Event sample

A sample of 3565 events satisfies this 4C hypothesis with both vertex fit χ^2 probability and kinematic fit χ^2 probability greater than or equal to 0.01. A histogram of the kinematic fit confidence level is shown in Fig. 91. The distribution shows some deviation from flatness, but analysis of the fits satisfying ambiguous hypotheses indicates that the background due to other 4C hypotheses is less than 1% in the event sample. This deviation partially results from imperfect understanding of the errors. Fig. 92 shows a histogram of the missing mass squared. There is no evidence for any background due to events with a missing π^0. The event sample is thus assumed to be uncontaminated.

2. General features

In Fig. 93 is a histogram of the $\pi^+\pi^-$ invariant mass (combinations per event). The events are not corrected for acceptance, but events with proton trigger acceptance less than 0.15 or zero recoil acceptance, and events with a fast pion which traverses the Cerenkov counter, are eliminated from the event sample. A strong ρ^0 signal, and evidence for an f^0 signal, is seen. It is possible to enhance the f^0 signal by making cuts on the production angular distribution of the events. In Fig. 94 is the $\pi^-\pi^-$ invariant mass distribution. There is no evidence for an exotic peak in this distribution. Fig. 95 shows the $\pi^+\pi^-\pi^-$ invariant mass distribution. There is no evidence for structure in this distribution either.

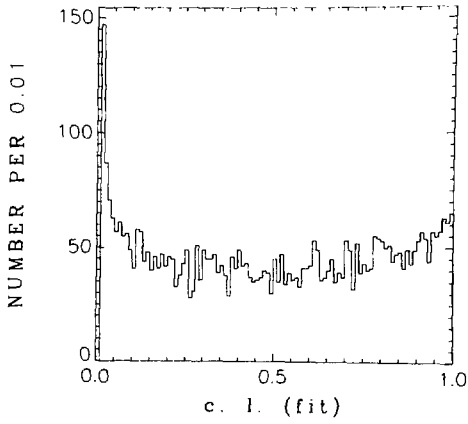
NUMBER PER 0.01
150
100
50
0
0.0
0.5
1.0
c. l. (fit)

Fig. 91

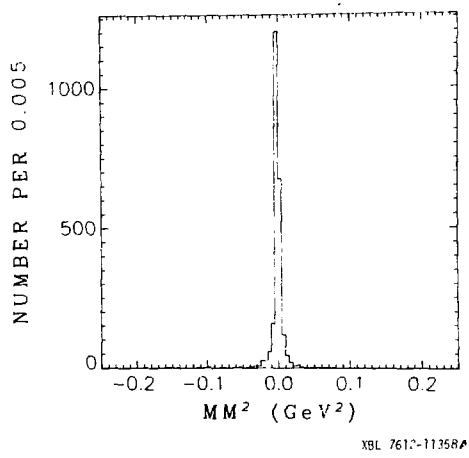
NUMBER PER 0.005
1000
500
0
−0.2
−0.1
0.0
0.1
0.2
MM² (GeV²)
XBL 761?-11358A

Fig. 92

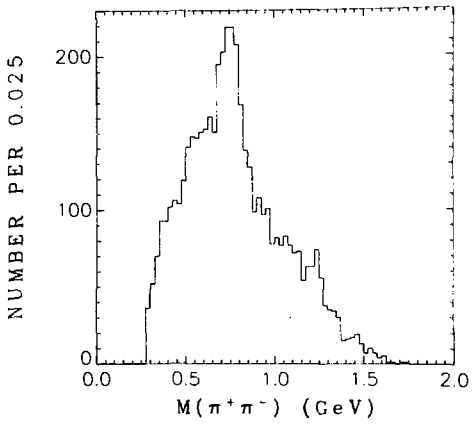

Fig. 93

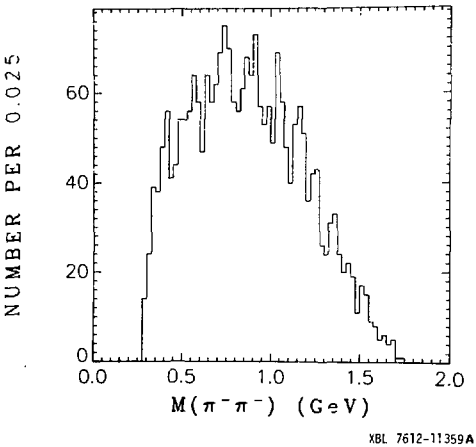

XBL 7612-11359A

Fig. 94

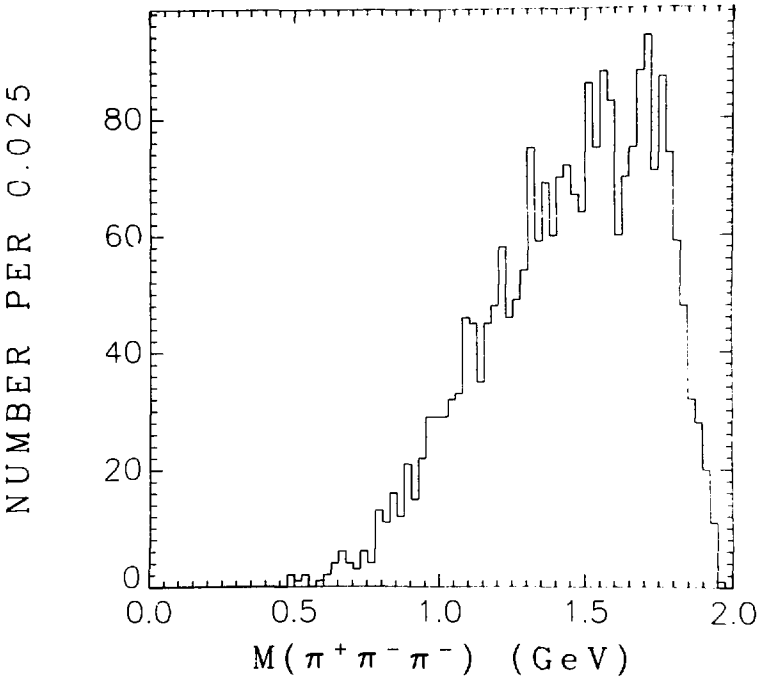

XBL 771 7226

Fig. 95

The invariant mass histograms for the baryon mass combinations are shown in Figs.96-99. A strong Δ^{++} signal is seen in the $p\pi^+$ invariant mass distribution. In the $p\pi^-$ mass distribution (2 combinations per event), there is evidence for two peaks in the high mass N^{*0} region; one near 1.50 GeV and the other near 1.65 GeV. As in the case of the 3-body final state, unambiguous identification of these two states cannot be made. There is also evidence for peaking in the $\Delta^0(1232)$ mass region, although it is hard to estimate the background under the peak. The enhancement in this region appears to be slightly higher in mass and wider than the nominal Δ^0, but when the requirement is imposed that $\cos\theta^*_{\pi^-\to p\pi^-} \geq 0.8$ (shaded region of histogram), a sharp Δ^0 signal is seen at the correct mass, above a broader enhancement. There is no significant structure in either the $p\pi^+\pi^-$ invariant mass distribution (2 combinations per event) or the $p\pi^-\pi^-$ invariant mass distribution.

In Fig. 100 is a Chew-Low plot showing the invariant mass squared of the $\pi^+\pi^-$ system vs u from the target to the $\pi^+\pi^-$ system. ρ^0 production at relatively small values of -u is evident. There also appears to be a low mass enhancement produced at small values of -u, just below the ρ^0 in mass. The curve represents the kinematic limit at the average center-of-mass energy. In Fig.101 is a Chew-Low plot showing the $p\pi^+$ invariant mass squared vs u from the beam to the $p\pi^+$ system. It is seen that the Δ^{++} production is not peaked at the kinematic limit. This has implications which will be discussed later.

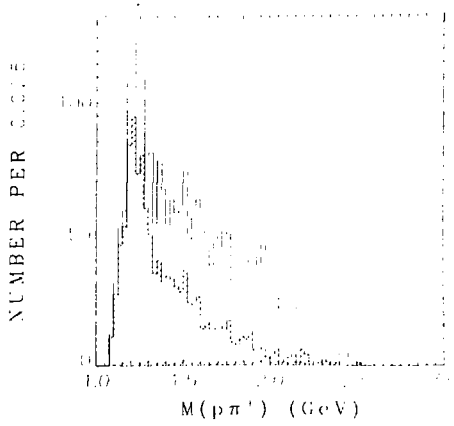

Fig. 96

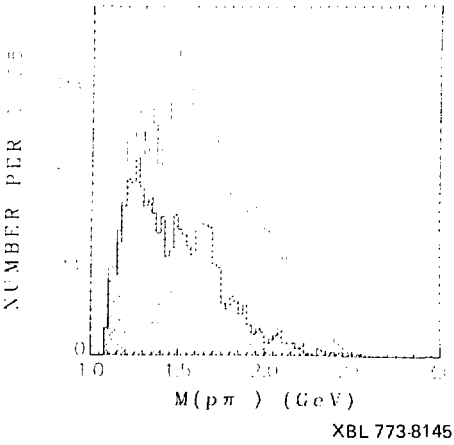

Fig. 97

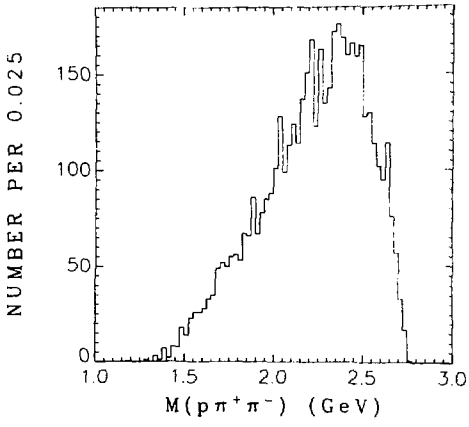
NUMBER PER 0.025
150
100
50
0
1.0
1.5
2.0
2.5
3.0
M(pπ⁺π⁻) (GeV)

Fig. 98

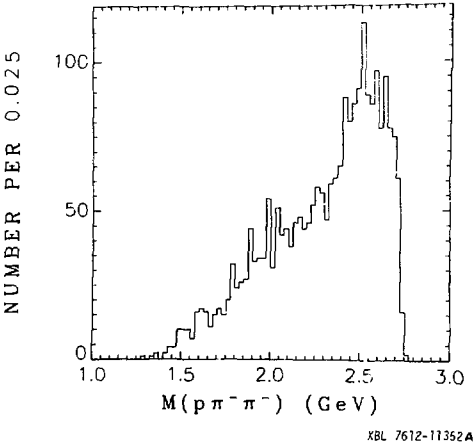
NUMBER PER 0.025
100
50
0
1.0
1.5
2.0
2.5
3.0
M(pπ⁻π⁻) (GeV)
XBL 7612-11352A

Fig. 99

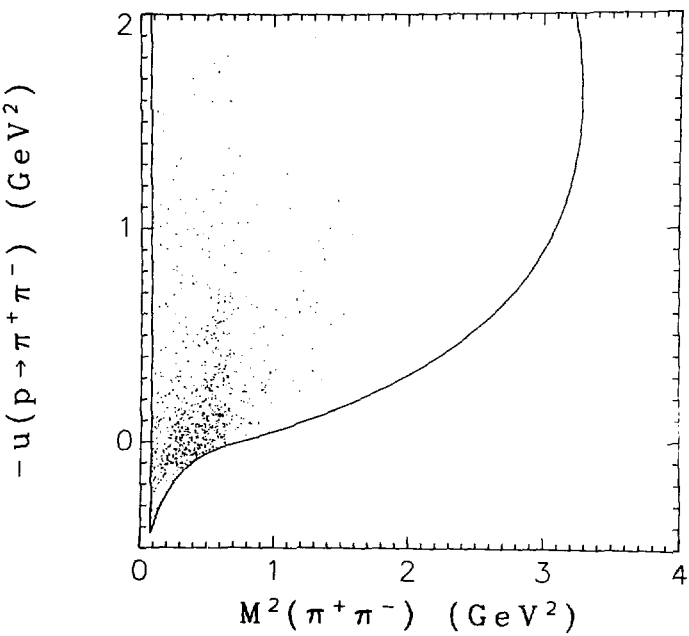

XBL 7612-11394

Fig. 100

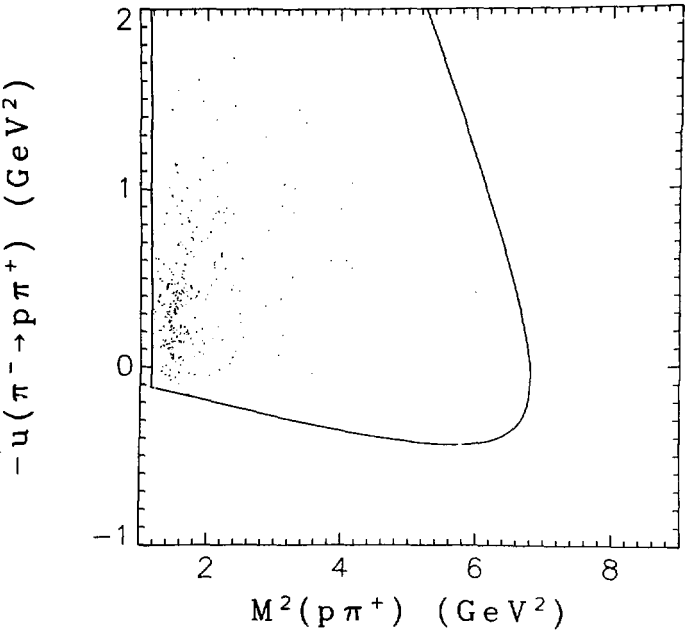

XBL 7612-11395

Fig. 101

3. A^- production

As discussed in Ch. II, one of the primary motivations for this experiment was the search for A_1 production via baryon exchange. As can be seen in Fig.95, there is no evidence for either A_1^- production or A_2^- production (which is expected to be produced in the same channel).

In Fig. 102(a) is a histogram of the $\pi^+\pi^-\pi^-$ invariant mass in which each event has been corrected up for the trigger acceptance, and an overall factor included so that the distribution represents cross section. All events with trigger acceptance less than 0.15 have been eliminated. The dashed curve is the result of a Monte Carlo simulation based on a maximum likelihood fit to the 4-body final state. (This maximum likelihood fit is very similar in concept to that discussed in regard to the 3-body final state.) There is no evidence for relatively narrow structure in either the A_1^- mass region (1.10 GeV) or the A_2^- mass region (1.31 GeV) above the Monte Carlo distribution. In Fig. 102(b) is the same data with the additional requirement that at least one of the $\pi^+\pi^-$ invariant mass combinations is in the ρ^0 mass region (0.675-0.825 GeV). Again, no evidence for A_1^- or A_2^- production is seen. In Fig.102(c), the requirement is imposed that $\cos\theta^*_{\pi^-\to\rho} \geq 0.8$, but no ρ^0 cut is required. Although there appears to be an overall deviation of the data from the Monte Carlo simulation for masses below 1.5 GeV (a result of inaccuracies in the fit), there is no evidence for structure. Finally, in Fig.102(d), the cuts required in both Figs. 102(b) and (c) are imposed. Again, there is no significant structure.

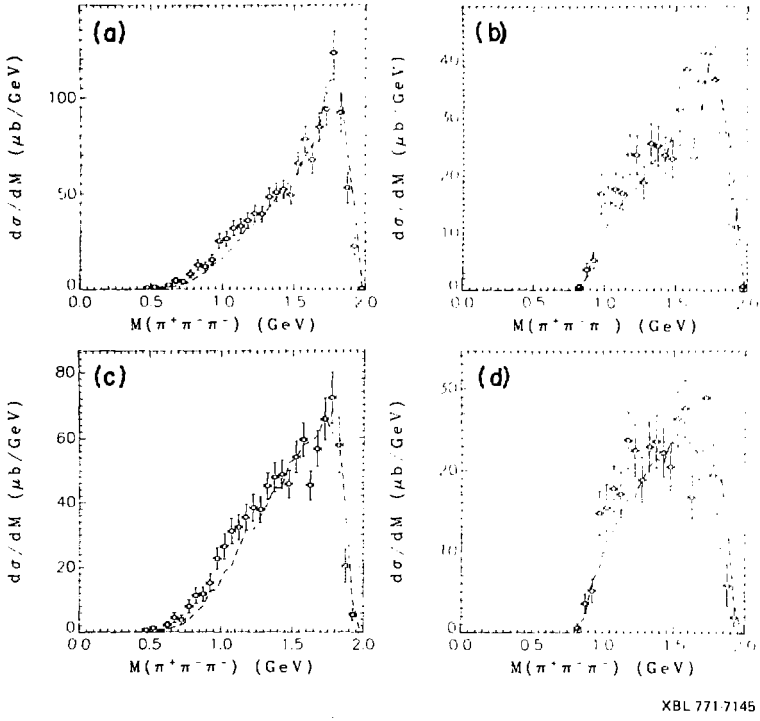

Fig. 102

In order to calculate upper limit cross sections for reactions (36) and (37), the data in Fig. 102(c) was fit to the expression

$$\frac{d\sigma}{dM} = \left(\frac{d\sigma}{dM}\right)_{\text{background}} + \left(\frac{d\sigma}{dM}\right)_{BW} ,$$

where

$$\left(\frac{d\sigma}{dM}\right)_{\text{background}} = \alpha_1 + \alpha_2 M + \alpha_3 M^2$$

and $(d\sigma/dM)_{BW}$ represents the Breit-Wigner resonance contribution for either the A_1^- or the A_2^-. The fit included the region in mass from 0.8 to 1.5 GeV, where the background could be fit well with a quadratic expression. Fits involving the A_1^- and the A_2^- were made separately, and the resonance cross sectional area, α_1, α_2, and α_3 were varied in the least squares fitting procedure. An additional constraint was imposed requiring that the total cross sectional areas represented by the fit and the data were equal. The values of the resonance parameters utilized in the fits are

$$M_{A_1} = 1.100 \text{ GeV}$$

$$\Gamma_{A_1} = 0.100 \text{ GeV}$$

$$M_{A_2} = 1.310 \text{ GeV}$$

$$\Gamma_{A_2} = 0.102 \text{ GeV} .$$

The results of the fits (where the errors are two standard deviation errors) are

$$\sigma_{A_1^-} = 0.64 \pm 1.59 \ \mu b$$

$$\sigma_{A_2^-} = 0.15 \pm 1.59 \ \mu b \ .$$

Thus, the two standard deviation (95% confidence level) cross section upper limits as determined by the fits are $\sigma_{A_1^-} < 2.23 \ \mu b$ and $\sigma_{A_2^-} < 1.74 \ \mu b$.

There are three corrections which must be made to these upper limit values. First, a correction must be made to account for those events which are eliminated with trigger acceptance less than 0.15. This correction is evaluated by generating events according to the model prescribed by the results of the maximum likelihood fit, and calculating the fraction of events which would be lost by this trigger cut (subject to invariant mass constraints and production angle constraints so as to be consistent with the real event sample). Secondly, a correction is applied to provide an estimate of the total backward cross section integrated to all values of u, assuming that the differential cross section falls off exponentially as e^{3u}. Finally, a correction is applied to account for the unobserved decay modes. The A_1^- is assumed to decay only into $\rho\pi$, so a factor of 2.0 is required to correct for the $\rho^-\pi^0$ final state. The A_2^- is assumed to have a branching fraction

of 0.71 into $p\pi$. The final corrected estimates for the two standard deviation (95% confidence level) upper limits are

$$\sigma_{A_1^-} < 6.6 \ \mu b$$

$$\sigma_{A_2^-} < 7.6 \ \mu b \ .$$

Due to the fact that the mass, width, and decay modes of the A_1 are unknown, there is considerable uncertainty in the upper limit assigned to the A_1^- cross section. If the width of the A_1 is varied, the resulting cross section is roughly proportional to the width. A similar fit in which the A_1 was assumed to have a width of 0.300 GeV gave an upper limit of $\sigma_{A_1^-} < 30. \ \mu b$. If the mass of the A_1 is assumed to be higher (up to approximately 1.35 GeV), the cross section does not vary significantly. For masses greater than 1.40 GeV, it becomes difficult to reliably determine a cross section with the data from this experiment.

In Fig. 103 is a plot showing the total backward cross section for reaction (36) as a function of incident beam momentum. The data point at 4 GeV/c is the 95% confidence level upper limit from this experiment. The data point at 8 GeV/c is the 95% confidence level upper limit from the experiment of Abashian et al.[42] The 16 GeV/c data point is the observed cross section (less than a 1.5 standard deviation effect) determined in the missing mass experiment of Anderson et al.[41] The solid curve satisfies the equation

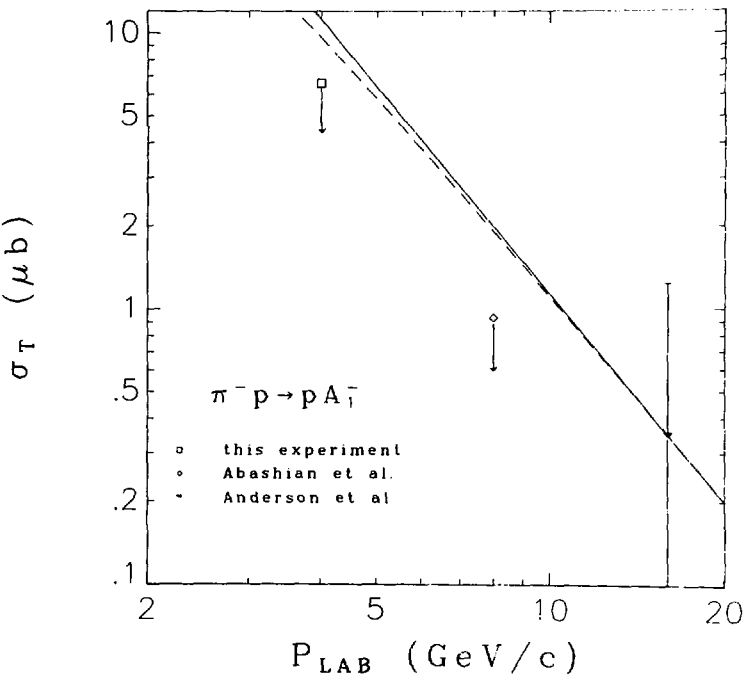
10
5
2
1
.5
.2
.1
σ_T (μb)
$\pi^- p \to p A_1^-$
this experiment
Abashian et al.
Anderson et al
2
5
10
20
P_{LAB} (GeV/c)
XBL 773-7943

Fig. 103

$$\sigma_T = a\, P_{LAB}^{-2.5} ,$$

where a is determined by the constraint that the curve must pass through the 16 GeV/c data point. If it is believed that the total cross section can be described in this manner (which is consistent with expectations for a reaction involving delta exchange), then this curve represents the extrapolation of the 16 GeV/c data point to other values of lab momentum. It is seen that the 95% confidence level upper limits determined at 4 and 8 GeV/c are below this curve by approximately a factor of 2. If one takes into account the variation of u_{max} ($u_{max} = u$ at $u' = 0$) with energy, and makes the assumptions that

$$\left.\frac{d\sigma}{du}\right|_{u=0} = a'\, P_{LAB}^{-2.5}$$

and

$$\frac{u\sigma}{du} \propto e^{3u}$$

at fixed s, then the total cross section extrapolated from the 16 GeV/c data point is represented by the dashed curve. This curve is still approximately a factor of 2 greater than the upper limits at 4 and 8 GeV/c. Various other modifications can be made in the model (such as assuming that the cross section varies as s rather than P_{LAB}), but the results are essentially the same.

In Fig. 104 is a similar plot showing the total backward cross section for reaction (37) as a function of lab momentum. Data from the same three experiments is shown, and the curves represent the extrapolated

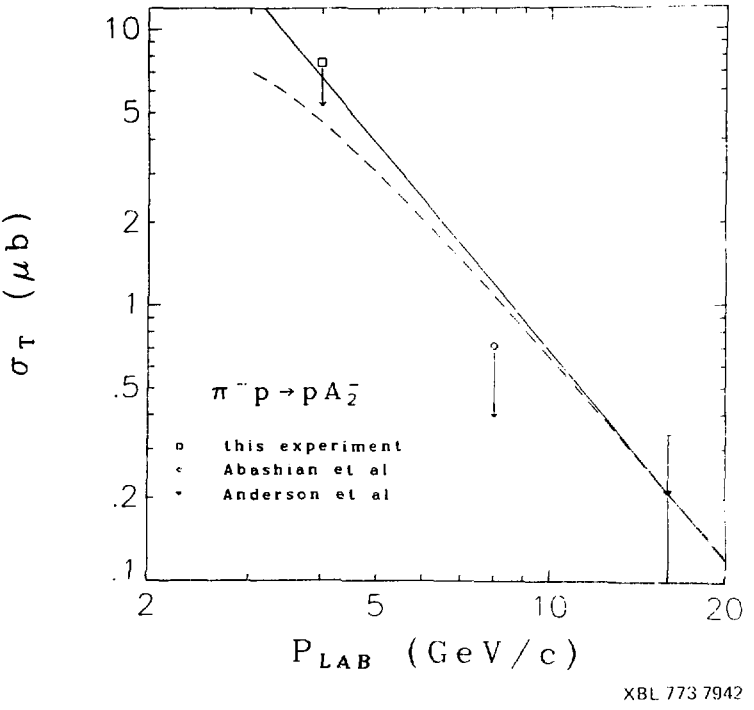
10
5
2
1
.5
.2
.1
σ_T (μb)
$\pi^- p \to p A_2^-$
this experiment
Abashian et al
Anderson et al
2
5
10
20
P_{LAB} (GeV/c)
XBL 773 7942

Fig. 104

cross sections, calculated as for the case of the A_1^-. The discrepancy between the extrapolated cross sections and the calculated upper limits is not as great as for reaction (35), particularly at 4 GeV/c.

4. ρ^0 production

In Fig. 105 is an acceptance corrected histogram of the $\pi^+\pi^-$ invariant mass distribution. Each event is corrected up by the inverse of the trigger acceptance, and events with acceptance less than 0.15 are eliminated. The solid curve represents a least squares fit to the data with ρ^0 and f^0 Breit-Wigner resonance terms above an incoherent background. The resonance parameters obtained in the fit are

$$M_{\rho^0} = 0.754 \pm 0.008 \text{ GeV}$$

$$\Gamma_{\rho^0} = 0.105 \pm 0.015 \text{ GeV}$$

$$M_{f^0} = 1.242 \pm 0.008 \text{ GeV}$$

$$\Gamma_{f^0} = 0.060 \pm 0.028 \text{ GeV} .$$

The ρ^0 is seen to be slightly low in mass, with a narrow width, symptoms similar to those observed for the ρ^- in the 3-body final state. The f^0 is also low in mass and extremely narrow. The dashed curve represents the background.

The method of analysis was very similar to that employed for analysis of the 3-body final state reactions. A background subtraction was made based on the results of the fit. (A signal region from 0.675-0.825 GeV is assumed.) The differential cross section (corrected up by the inverse of the trigger acceptance) is shown in Fig. 106. The dotted

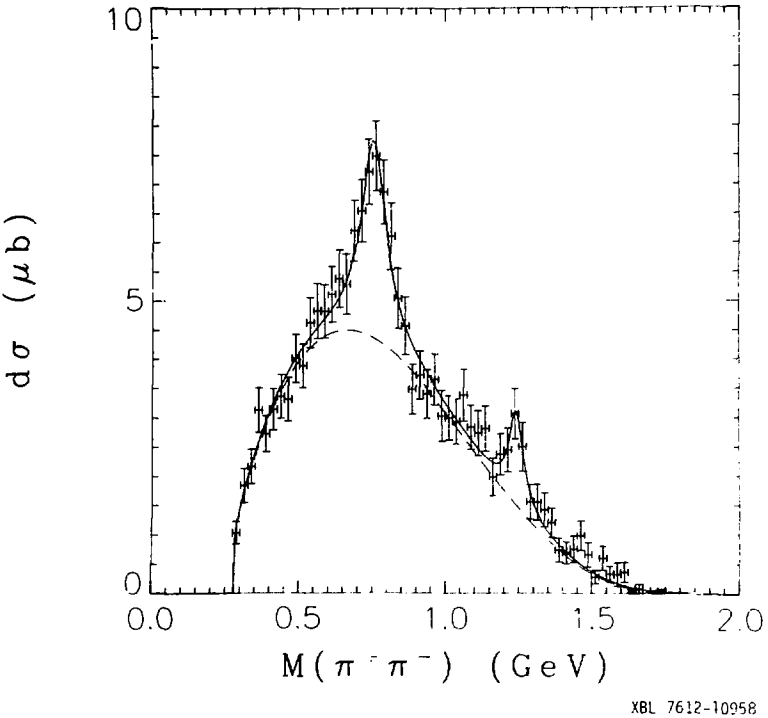

Fig. 105

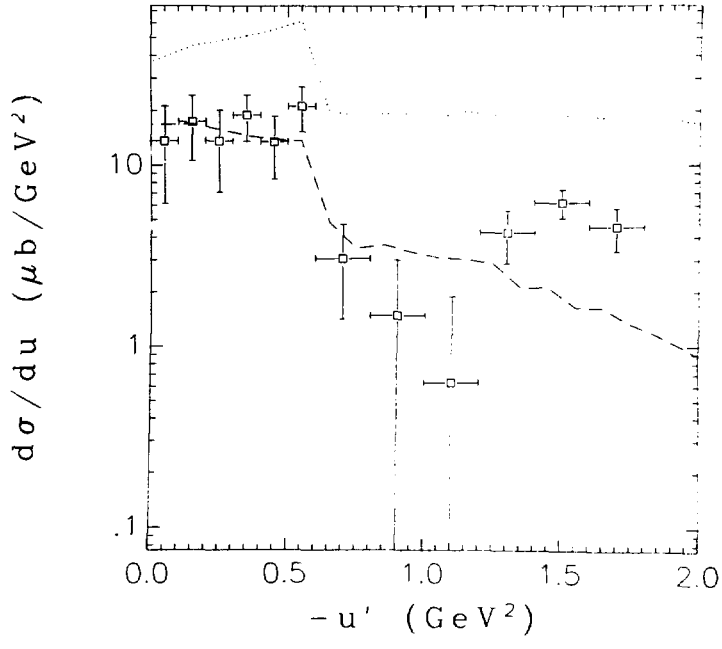

Fig. 106

curve is the Monte Carlo distribution generated according to a model in which the $p\pi^-$ system is produced at the top (pion) vertex, recoiling against the ρ^0 at the bottom vertex. The peculiar distribution of the Monte Carlo as a function of u' was the result of an effort to qualitatively duplicate the real data distribution. The $p\pi^-$ recoil mass distribution was also generated to roughly duplicate the actual recoil distribution. All $p\pi^-$ decays were assumed to be isotropic (in rough agreement with the experimental results), and the ρ^0 decay angular distribution was simulated by the Monte Carlo. The dashed curve is the resulting Monte Carlo distribution after correction. (The Monte Carlo events were first corrected down by the three-parameter trigger acceptance function, and then corrected up by the two-parameter trigger acceptance, eliminating events which were eliminated from the real event sample.)

The model utilized to describe ρ^0 production is somewhat arbitrary. It is also possible to describe ρ^0 production by a model in which the proton is produced at the top vertex recoiling against the $\rho^0\pi^-$ system at the other vertex. The differential cross section for this reaction would be displayed as a function of u' from the beam to the proton. In Fig. 107(a) is the differential cross section as a function of u' from the beam to the proton. The Monte Carlo curves represent the original model, also distributed as a function of this variable. The dashed curve is seen to represent the data well. Similarly, it is possible to describe ρ^0 production by a model in which the $p\rho^0$ system is produced at the top vertex recoiling against a π^-.

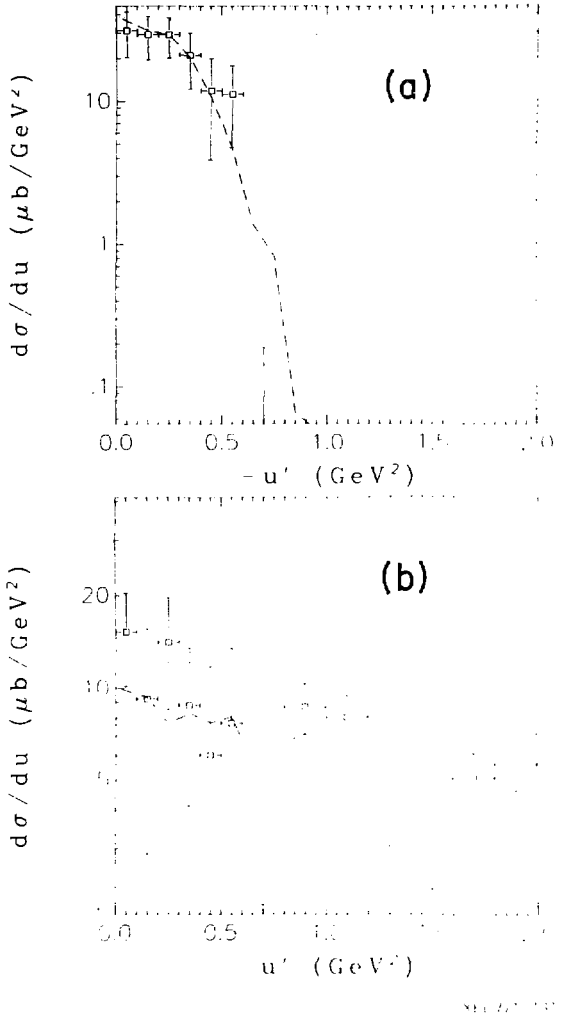
(a)
dσ/du (μb/GeV²)
10
1
.1
0.0
0.5
1.0
-u' (GeV²)
(b)
dσ/du (μb/GeV²)
20
10
0.0
0.5
u' (GeV²)

Fig. 107

Fig. 107(b) displays the differential cross section in terms of u' from the beam to the $p\rho^0$ system. Again, the original model appears to describe the data well.

An attempt was made to simulate the data by generating Monte Carlo events according to a model in which the proton was produced at the top vertex and the $p^0\pi^-$ system was produced at the bottom vertex. The events were generated to simulate the differential cross section in terms of u' from the beam to the proton. The $p^0\pi^-$ system was assumed to decay isotropically. When the Monte Carlo distributions were compared to the real distributions in terms of u' from the beam to the $p\pi^-$ system and u' from the beam to the $p\rho^0$ system, they were found to be totally inconsistent with the data. Similarly, Monte Carlo generation of events according to a model in which the pp^0 system was produced at the top vertex recoiling against the π^- failed to satisfactorily reproduce all three u' distributions. It is possible to reproduce the data well by either of these two models, but it requires the use of unrealistic decay angular distributions of the $p^0\pi^-$ system or the pp^0 system. Thus, it will be assumed that ρ^0 production is described by the original model. Note that nucleon exchange is allowed if the reaction is described by the original model, whereas delta exchange is required by both of the other two models. This is consistent with previous evidence for the suppression of delta exchange relative to nucleon exchange. There is also the possibility that the reaction is better described by a model assuming three vertices (the p, π^-, and ρ^0 each produced at a different vertex), or an s-channel model. The limited data available does not provide enough

information to differentiate between these various models. Thus, the relevance of the results of this analysis must be considered in terms of the relevance of the two-vertex, baryon exchange model assumed in the analysis.

After correction by the Monte Carlo for the loss of events with poor acceptance, the resulting ρ^0 differential cross section as a function of u' from the beam to the $p\pi^-$ system is shown in Fig. 108. The data points represented in the plot are given in Table XXX. Although there is evidence for peaking in the backward region, the cross section does not display a typical exponential falloff. Thus, it is difficult to quantitatively describe the cross section.

It is believed that the reason for the peculiar ρ^0 differential cross section, and the fact that the fitted ρ^0 resonance parameters are significantly different from the nominal parameters, is that there is interference between the ρ^0 signal and the background. In Fig.93, it is observed that there is an enhancement in the $\pi^+\pi^-$ invariant mass distribution below the ρ^0 signal. This enhancement cannot be explained by reflections from other channels. In Fig.100, it is seen that this low mass enhancement is concentrated at small values of $-u$ ($u' \leq -0.5$ GeV^2). This enhancement, in conjunction with the fact that the ρ^0 is narrow and peaks low in mass, is evidence for constructive interference in the low mass tail of the ρ^0 and destructive interference in the high mass tail. This interference explains the peculiar shape of the differential cross section. At small values of $-u'$, the interference is stronger and the effect of the low mass enhancement is to produce a seemingly low ρ^0 cross section after subtraction. At larger values of $-u'$,

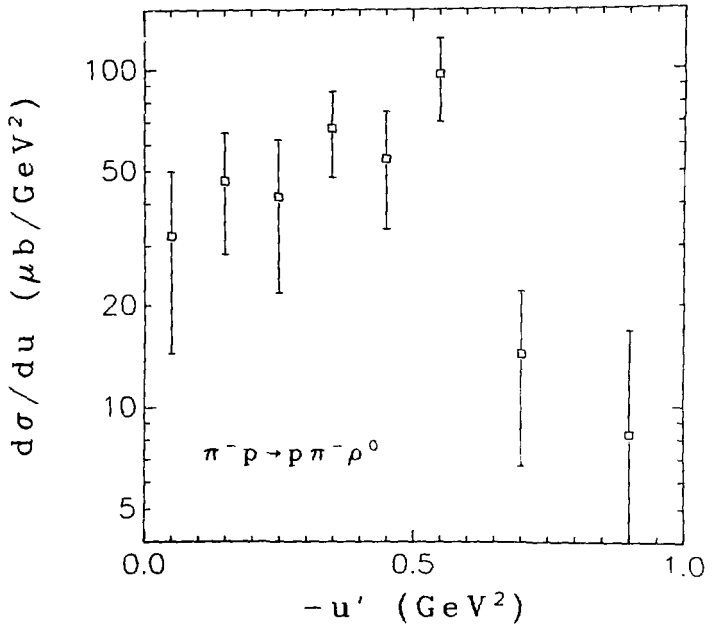

XBL 7612-11331

Fig. 108

Table XXX. Differential cross section for $\pi^- p \to p\pi^- \rho^0$ as a function of u' from the beam to the $p\pi^-$ system.

$-u'$ (GeV^2)	Δu (GeV^2)	$\frac{d\sigma}{du}$ ($\mu b/GeV^2$)
0.05	0.10	32.2 ± 17.7
0.15	0.10	46.8 ± 18.3
0.25	0.10	42.1 ± 20.1
0.35	0.10	67.2 ± 19.1
0.45	0.10	54.5 ± 20.7
0.55	0.10	96.8 ± 26.6
0.70	0.20	14.4 ± 7.7
0.90	0.20	8.3 ± 8.5

Table XXXI. Average ρ^0 density matrix elements in the s-channel helicity frame.

$\rho_{00} = 0.51 \pm 0.14$

$Re(\rho_{10} - \rho_{0,-1})/2 = 0.04 \pm 0.09$

$Im(\rho_{10} - \rho_{0,-1})/2 = 0.07 \pm 0.07$

$Re\ \rho_{1,-1} = -0.04 \pm 0.15$

$Im\ \rho_{1,-1} = -0.07 \pm 0.10$

the low mass enhancement is not as significant, and more realistic values of the cross section are provided by the subtraction. Thus, the assumption of incoherence is a poor assumption, and it is possible that in the absence of interference effects, the ρ^0 cross section would display a more typical differential cross section peaked at $u' = 0$.

In Fig. 109 is an expanded view of the $\pi^+\pi^-$ invariant mass distribution (in 0.01 GeV bins) in the mass region near the ρ^0. The events are corrected up by the inverse of the acceptance, and are scaled to yield cross section. The requirement is imposed that $\cos\theta^*_{\pi^-\to\rho\pi^-} \geq 0.8$, where the π^- associated with the proton is not the π^- in the $\pi^+\pi^-$ combination. The ρ^0 peak is clearly asymmetric and there is evidence for destructive interference on the high mass side. Attempts to fit the distribution based on a ρ^0-ω^0 interference model failed. However, by assuming that the ρ^0 amplitude was interfering with a constant background term, and fitting the data between 0.4 and 1.1 GeV to the expression

$$d\sigma = \left|A_{BW} + A_{flat}\, e^{i\phi}\right|^2 + \sigma_{background} \quad ,$$

where

$$A_{BW} = A_0 \left(\frac{\Gamma}{2\pi}\right)^{\frac{1}{2}} \frac{1}{M_0 - M - i\Gamma/2} \quad ,$$

a reasonable fit was obtained. M_0 and Γ were set to the nominal mass (0.773 GeV) and width (0.152 GeV) of the ρ meson. A_0, A_{flat}, and ϕ were varied in the least squares fitting procedure. The parameters defining $\sigma_{background}$ (a modified polynomial) were also varied in the

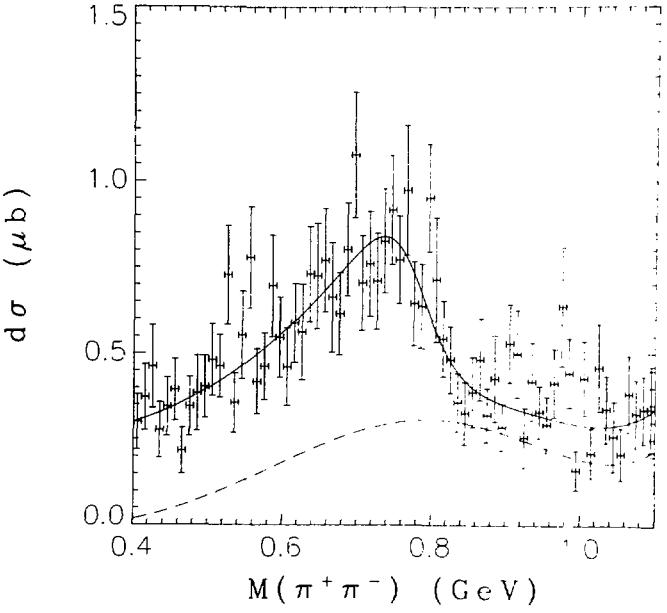

Fig. 109

fit. The solid curve in Fig. 109 represents the results of the fit and the dashed curve represents the incoherent background term. The fitted value of the phase angle between the Breit-Wigner amplitude and the flat background amplitude is $\phi = 6^{\circ} \pm 21^{\circ}$. Although this model is very simple, and a more complicated model could undoubtedly be constructed to explain all of the details of the data quite well, the low mass enhancement, the displacement of the ρ^0 peak position, and the narrow width of the ρ^0 can all be explained by this model. A similar interference effect is presumably the cause of the abnormal ρ^- resonance line shape in the 3-body final state. This interference naturally affects the results of the cross section analyses for both ρ^0 and ρ^- production, which must be taken into consideration in applications or comparisons utilizing these results.

In Fig. 110(a) is the ρ^0 decay angular distribution in the s-channel helicity frame as a function of $\cos(\theta)$. In Fig. 110(b) is the angular distribution as a function of ϕ. The Monte Carlo approximates the data reasonably well. The data represented in these figures is corrected up for trigger acceptance and only includes data in the interval $u' > -0.5$ GeV^2. In Fig. 111 are shown the density matrix elements in the s-channel helicity frame as a function of u', evaluated by calculating combinations of expectation values of spherical harmonics (as described in Appendix C). The average values of the density matrix elements (over the interval $u' > -0.5$ GeV^2) are given in Table XXXI. The only density matrix element whose average deviates significantly from zero is ρ_{00}. There is an indication of structure in $\rho_{1,-1}$ at small values of $-u'$. This structure results from the

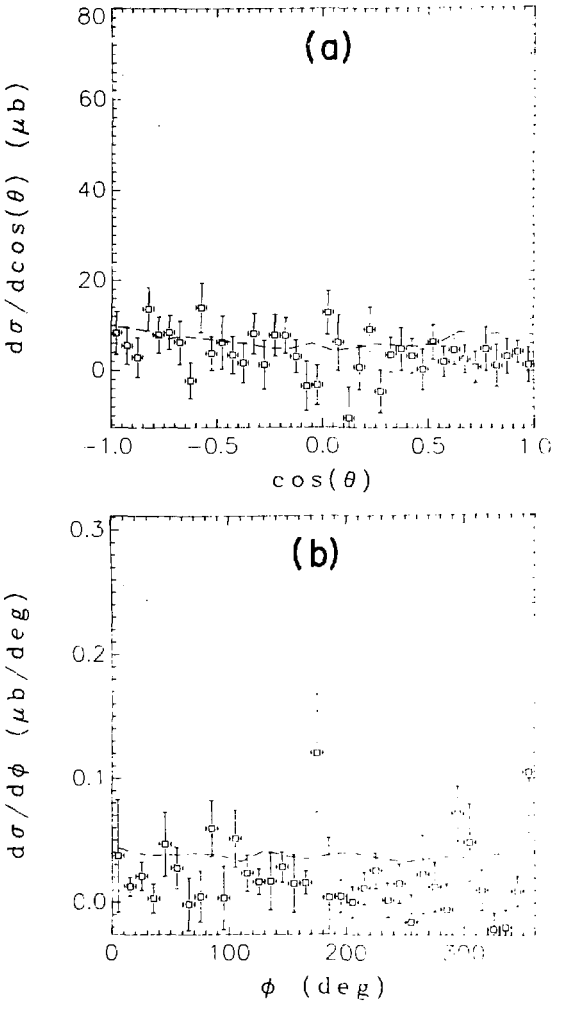
(a)
80
60
40
20
0
-1.0
-0.5
0.0
0.5
1.0
dσ/dcos(θ) (μb)
cos(θ)
(b)
0.3
0.2
0.1
0.0
0
100
200
300
dσ/dφ (μb/deg)
φ (deg)

Fig. 110

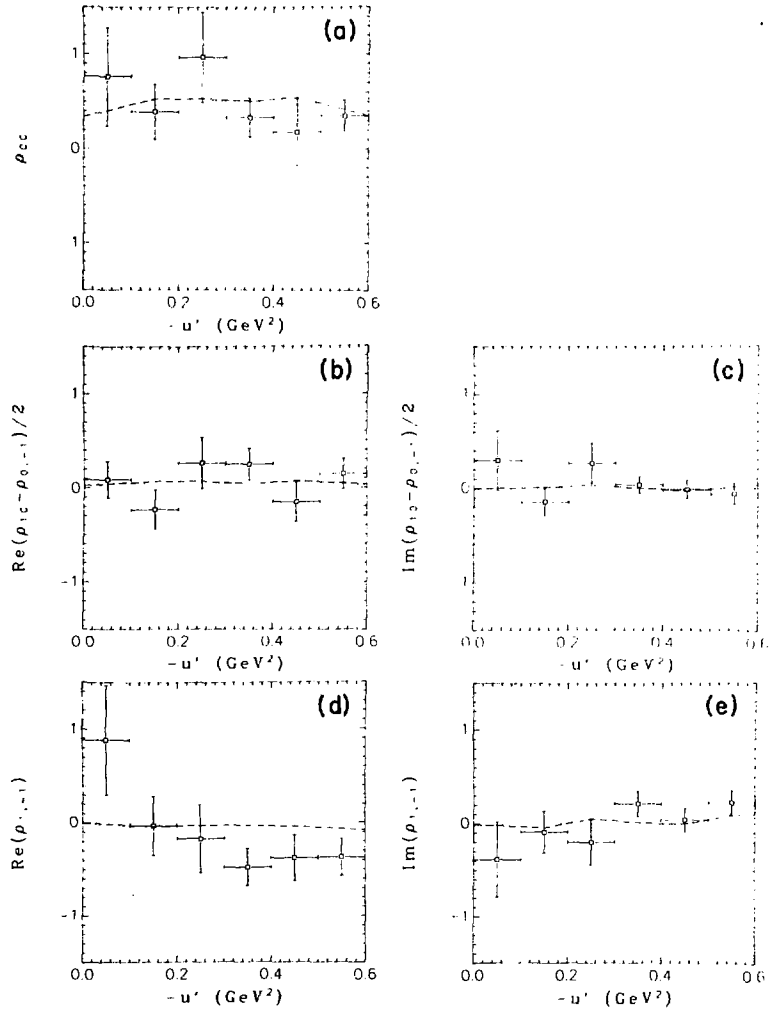
(a)
ρ_{cc}
(b)
$Re(\rho_{1c}-\rho_{0,-1})/2$
(c)
$Im(\rho_{1c}-\rho_{0,-1})/2$
(d)
$Re(\rho_{1,-1})$
(e)
$Im(\rho_{1,-1})$
$-u'$ (GeV^2)
XBL 771 7142

Fig. 111

narrow peaks in the decay distribution as a function of ϕ at $0^{0}(360^{0})$ and 180^{0}. This effect occurs only at small $-u'$, and the decay angles are such that these deviations occur when the ρ^{0} decay products are in the production plane. Thus, it is possible that this structu · in the decay distribution (if it is real) is related to the interfere ice effect previously defined.

In Fig. 112(a) is the uncorrected $p\pi^{-}$ recoil spectrum for events in which the opposing $\pi^{+}\pi^{-}$ system is within the ρ^{0} signal region. It is also required that $\cos\theta^{*}_{\pi^{+}\rightarrow\rho\pi^{+}} \geq 0.8$. In Fig. 112(b) is the same data after events in the ρ^{0} background region have been subtracted from the distribution. (A Breit-Wigner tail correction is also included.) There is evidence for a peak near 1.60 GeV in mass in the recoil spectrum, and possibly evidence for the $\Delta^{0}(1232)$.

In Fig. 113(a) is the $\rho^{0}\pi^{-}$ invariant mass distribution for events in the ρ^{0} signal region. No production angle requirement is imposed on the data. In Fig. 113(b) is the same data after background subtraction and correction for the Breit-Wigner tail. There is no evidence for structure in the $\rho^{0}\pi^{-}$ mass distribution. In Figs. 114(a) (ρ^{0} signal region) and 114(b) (after background subtraction and correction) are the $p\rho^{0}$ invariant mass distributions. There is no evidence of structure.

5. f^{0} production

The f^{0} analysis was done in a manner identical to the ρ^{0} analysis. In Fig. 115 is the f^{0} differential cross section as a function of u' from the beam to the $p\pi^{-}$ system. The background subtracted (signal region is 1.175-1.325 GeV), corrected up data points are shown with the error bars. The Monte Carlo simulation

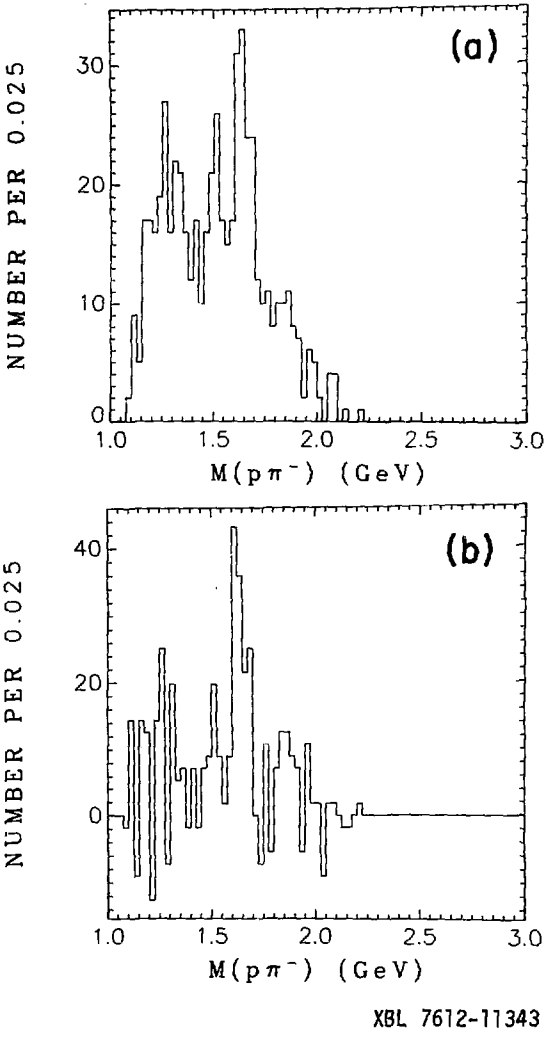
(a)
NUMBER PER 0.025
30
20
10
0
1.0
1.5
2.0
2.5
3.0
M(pπ⁻) (GeV)
(b)
NUMBER PER 0.025
40
20
0
1.0
1.5
2.0
2.5
3.0
M(pπ⁻) (GeV)
XBL 7612-11343

Fig. 112

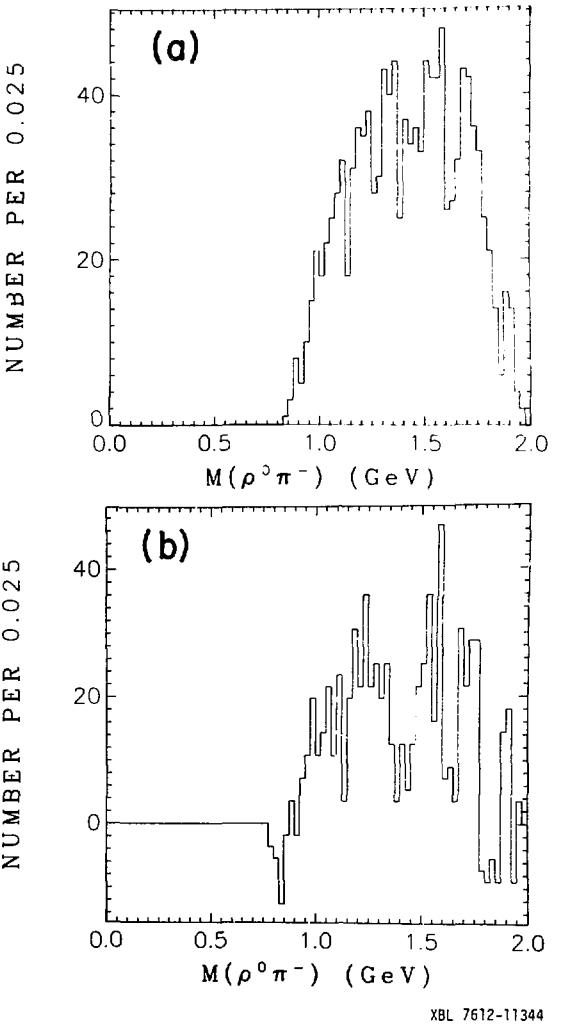
(a)
NUMBER PER 0.025
40
20
0
0.0
0.5
1.0
1.5
2.0
M(ρ⁰π⁻) (GeV)
(b)
NUMBER PER 0.025
40
20
0
0.0
0.5
1.0
1.5
2.0
M(ρ⁰π⁻) (GeV)
XBL 7612-11344

Fig. 113

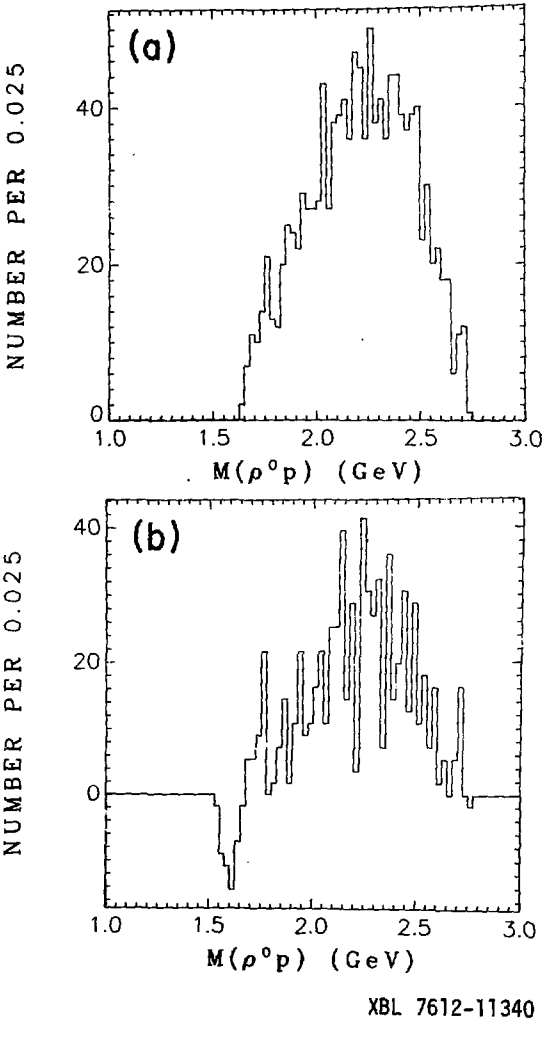
(a)
NUMBER PER 0.025
40
20
0
1.0
1.5
2.0
2.5
3.0
M(ρ°p) (GeV)
(b)
NUMBER PER 0.025
40
20
0
1.0
1.5
2.0
2.5
3.0
M(ρ°p) (GeV)
XBL 7612-11340

Fig. 114

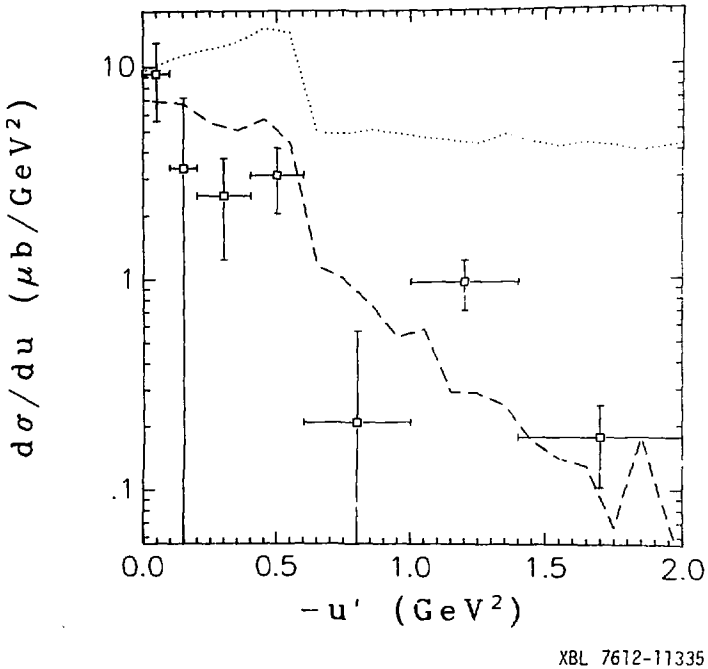

Fig. 115

(similar to that for the ρ^0 analysis) is given by the dotted curve (dashed curve after corrections). The Monte Carlo simulation was also compared with the data distributed as a function of u' from the beam to the proton (see Fig. 116(a)) and as a function of u' from the beam to the pf^0 system (see Fig. 116(b)), and was found to describe the data well. The resulting corrected differential cross section, including corrections for other decay modes (the $\pi\pi$ branching fraction was assumed to be 0.81), is given in Fig. 117. The data points represented in this figure are listed in Table XXXII. There appears to be a backward peak at small values of $-u'$.

Only the diagonal elements of the f^0 density matrix were calculated. The results (integrated over the interval $u' > -0.5$ GeV^2) are given in Table XXXIII for both the s-channel and the u-channel helicity frames. If it is assumed that the reaction is mediated by nucleon exchange (note that delta exchange is not allowed by isospin conservation), then $\rho_{22} = 0$ in the u-channel helicity frame by angular momentum conservation. This is observed to be true within the rather poor statistics available.

In Fig. 118(a) is the uncorrected $p\pi^-$ recoil spectrum for events in which the opposing $\pi^+\pi^-$ combination is within the f^0 signal region and $\cos\theta^*_{\pi^-\to p\pi^-} \geq 0.8$. In Fig. 118(b) is the background subtracted distribution (with correction for Breit-Wigner tails). There is a strong $\Delta^0(1232)$ signal in the recoil spectrum.

In Fig. 119(a) is the uncorrected $f^0\pi^-$ invariant mass distribution. Fig. 119(b) is the background subtracted distribution.

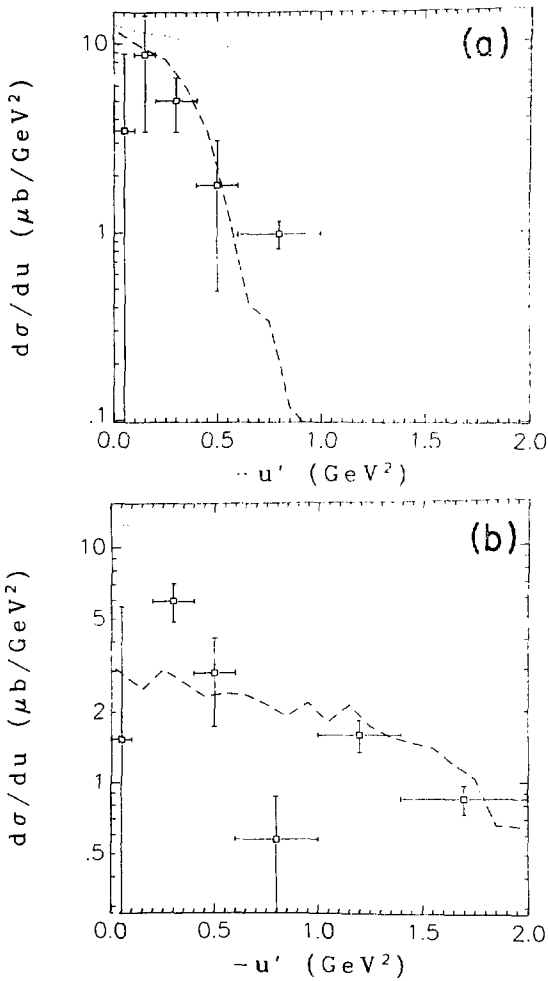

XBL 7612-11334

Fig. 116

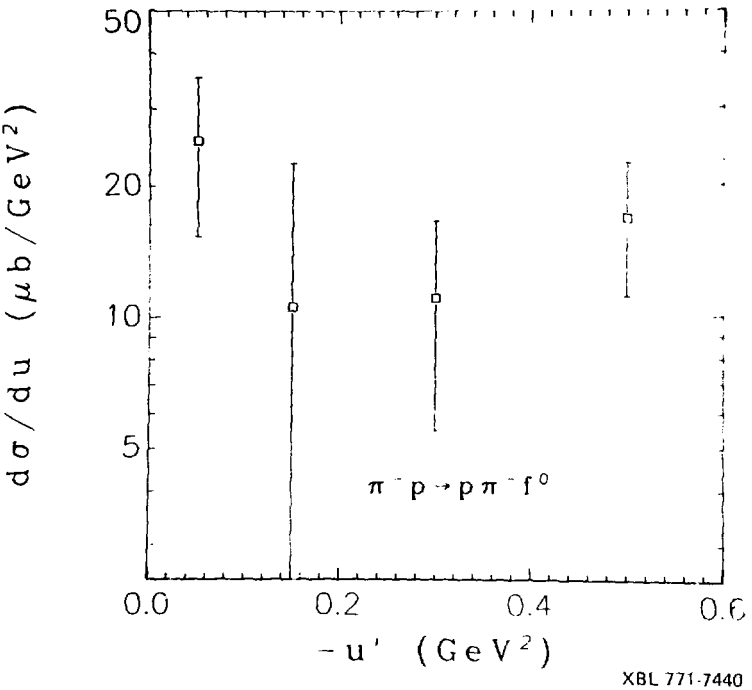

Fig. 117

Table XXXII. Differential cross section for $\pi^- p \to p\pi^- f^0$ as a function of u' from the beam to the $p\pi^-$ system.

$-u'$ (GeV^2)	Δu (GeV^2)	$\frac{d\sigma}{du}$ ($\mu b/GeV^2$)
0.05	0.10	25.4 ± 10.0
0.15	0.10	10.6 ± 12.0
0.30	0.20	11.1 ± 5.6
0.50	0.20	16.9 ± 5.7

Table XXXIII. Average f^0 density matrix elements in the s-channel and u-channel helicity frames.

ρ_{mm}	UHF	SHF
ρ_{00}	0.27 ± 0.24	0.43 ± 0.28
ρ_{11}	0.34 ± 0.16	-0.11 ± 0.18
ρ_{22}	0.02 ± 0.16	0.40 ± 0.18

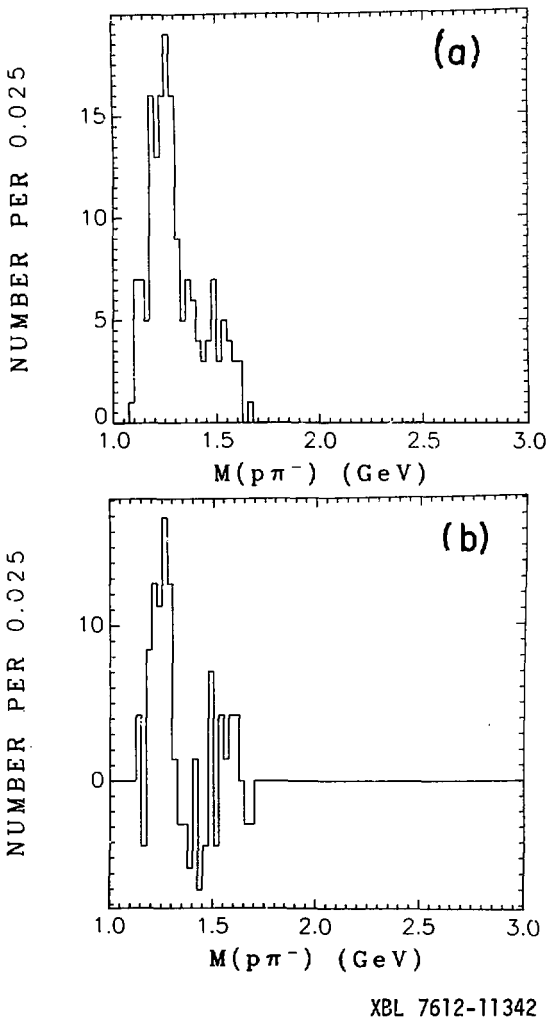
(a)
NUMBER PER 0.025
15
10
5
0
1.0
1.5
2.0
2.5
3.0
M(pπ⁻) (GeV)
(b)
NUMBER PER 0.025
10
0
1.0
1.5
2.0
2.5
3.0
M(pπ⁻) (GeV)
XBL 7612-11342

Fig. 118

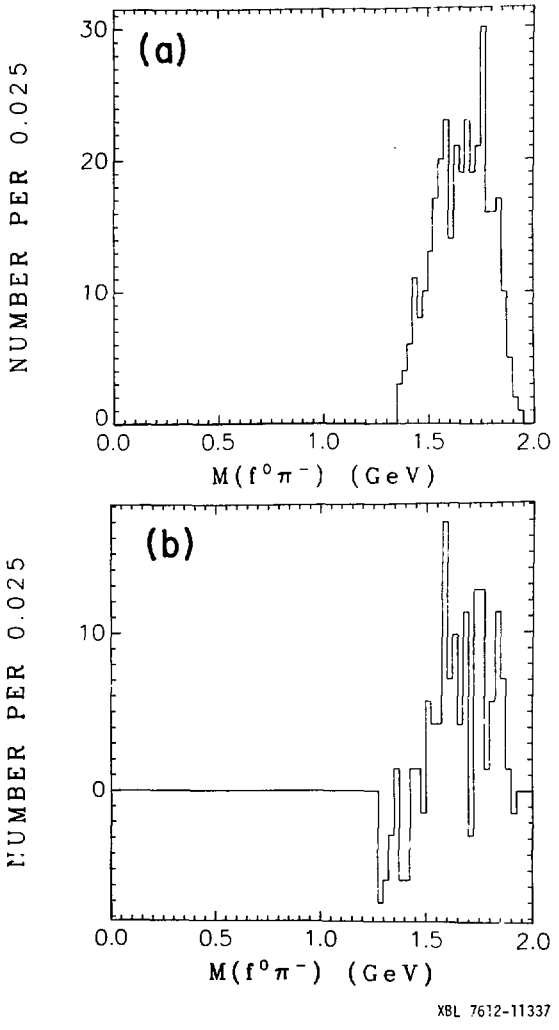
(a)
NUMBER PER 0.025
30
20
10
0
0.0
0.5
1.0
1.5
2.0
M(f°π⁻) (GeV)
(b)
NUMBER PER 0.025
10
0
0.0
0.5
1.0
1.5
2.0
M(f°π⁻) (GeV)
XBL 7612-11337

Fig. 119

Fig. 120(a) shows the uncorrected f^0p invariant mass distribution with the background subtracted distribution in Fig. 120(b). There is no evidence of structure in the $f^0\pi^-$ or f^0p mass distributions.

6. *Δ^{++} production*

As seen in Fig.96, there is significant Δ^{++} production. If it is assumed that the Δ^{++} is produced alone at the pion vertex, then the exchange of an exotic (I = 5/2) baryon is required. It is seen in Fig.101 that the Δ^{++} signal is not peaked at $u' = 0$. Thus, it is possible that a baryon resonance which decays into $\Delta^{++}\pi^-$ is produced at the top vertex. In Fig. 121(a) is a histogram of the uncorrected $p\pi^+\pi^-$ invariant mass distribution. The hatched region of the histogram includes those events in which the $p\pi^+$ invariant mass is between 1.15 and 1.31 GeV (i.e., in the Δ^{++} region). There is no evidence for the cascade decay of a high mass resonance into $\Delta^{++}\pi^-$. Fig. 121(b) shows the same data with the additional requirement that $\cos\theta^*_{\pi^-\to p\pi^+\pi^-} \geq 0.8$. Again, there is no evidence for baryon resonance production.

There are three possible models (in addition to the model requiring the exchange of an exotic baryon) which might explain the large amount of Δ^{++} production. The first model explains the Δ^{++} production in terms of nonresonant $\Delta^{++}\pi^-$ production at the pion vertex. The second model explains it in terms of an s-channel (or possibly t-channel) process rather than a baryon exchange u-channel process. The third model describes the interaction in terms of a three-vertex diagram in which the Δ^{++} and the π^-'s are each produced

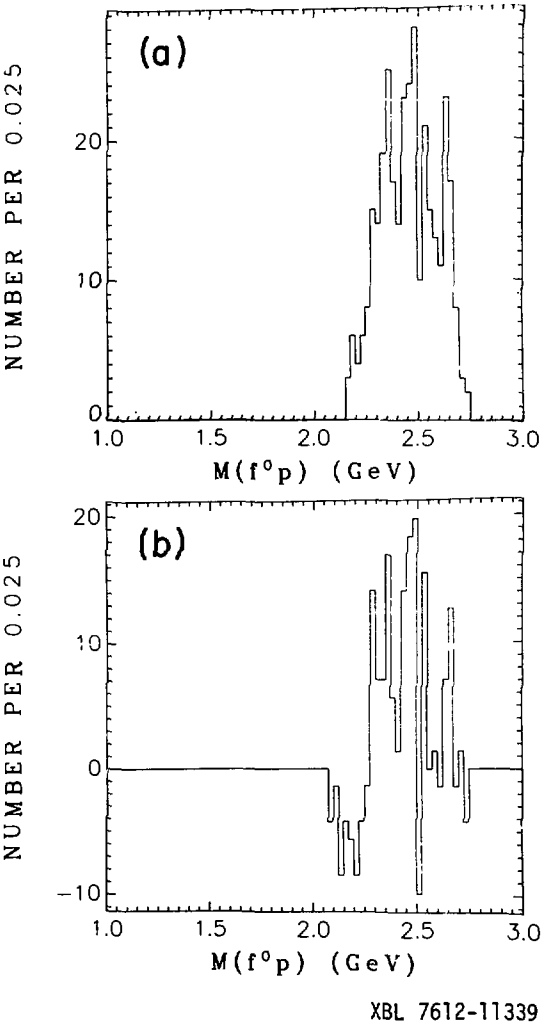
(a)
NUMBER PER 0.025
20
10
0
1.0
1.5
2.0
2.5
3.0
M(f°p) (GeV)
(b)
NUMBER PER 0.025
20
10
0
−10
1.0
1.5
2.0
2.5
3.0
M(f°p) (GeV)
XBL 7612-11339

Fig. 120

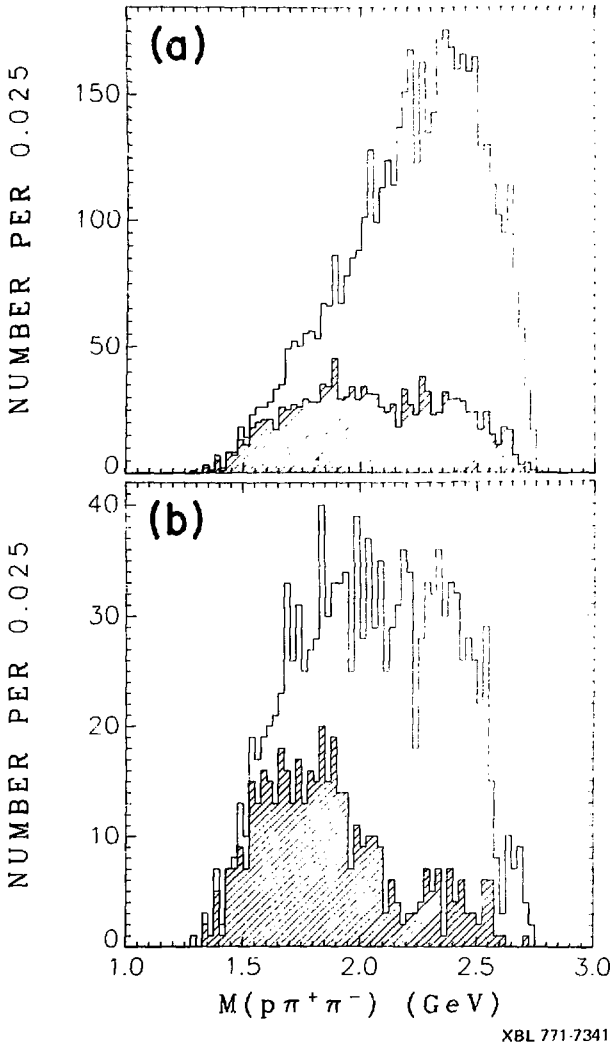
(a)
(b)
NUMBER PER 0.025
NUMBER PER 0.025
150
100
50
0
40
30
20
10
0
1.0
1.5
2.0
2.5
3.0
M(pπ⁺π⁻) (GeV)
XBL 771-7341

Fig. 121

at a different vertex. It is not possible to make a choice between the different models based on the available data.

7. Exotic meson production

As seen in Fig.94, there is no evidence for resonant production in the one inherently exotic channel available in this final state. In order to obtain limits on exotic production, fits were made to the $\pi^-\pi^-$ invariant mass distributions. In Fig. 122(a) is the $\pi^-\pi^-$ invariant mass distribution, corrected up by the inverse of the trigger acceptance. All events with trigger acceptance less than 0.15 are eliminated from the histogram. The bin contents are scaled to display cross section. In Fig. 122(b) is the same data with the requirement that $\cos\theta^*_{\pi^-\to\rho\pi^+} \geq 0.8$. The solid curves represent least squares fits to the mass distributions. There is no evidence of a narrow peak in the mass region between 0.4 and 1.5 GeV. In order to calculate the two standard deviation (95% confidence level) upper limit for exotic production in this channel, all significant positive deviations of the data from the fit (integrated over 0.05 GeV in width) were considered. A Monte Carlo simulation of the entire channel (based on the results of the maximum likelihood fit discussed earlier) was generated, and a calculation of the fraction of events lost due to poor trigger acceptance was made for each of the positive deviations considered. It was assumed in the calculations that the exotic differential cross was of the form

$$\frac{d\sigma}{du} \propto e^{3u'} .$$

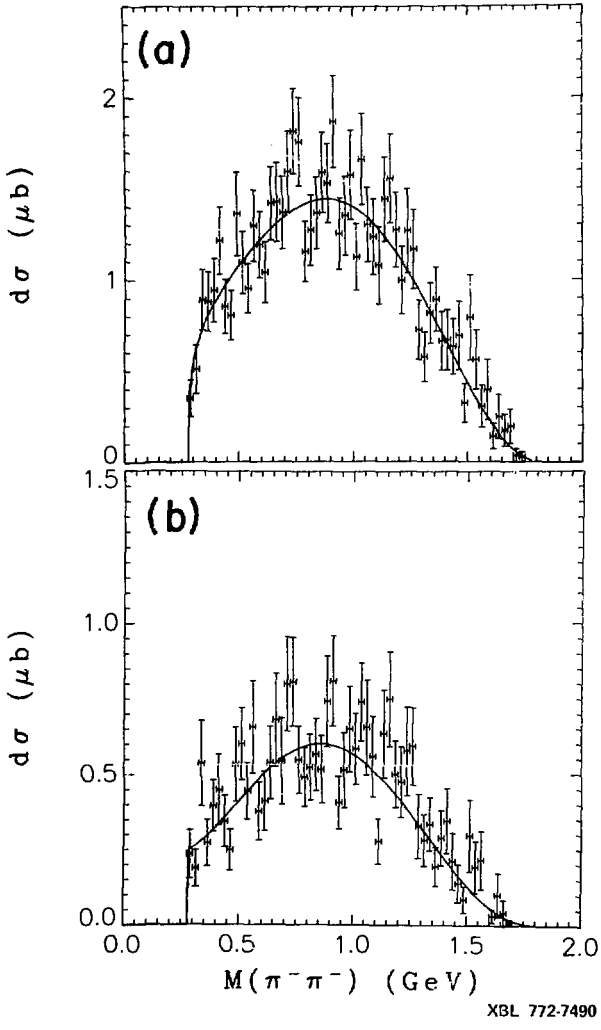

Fig. 122

The largest deviation found was in the mass interval between 0.725 and 0.775 GeV. The deviation had a cross section (with all corrections) of $\sigma = 2.65 \pm 1.14$ μb. Thus, the 95% confidence level upper limit for the cross section times branching ratio of an exotic meson in this channel is

$$\sigma \times \text{B.R.} < 4.9 \text{ μb.}$$

As was discussed in Ch. II, this channel requires exotic exchange if the $\pi^-\pi^-$ system is produced at the bottom vertex recoiling against a $p\pi^+$ system at the other vertex. (Cuts on Δ^{++} in the recoil spectrum did not produce a peak in the $\pi^-\pi^-$ invariant mass spectrum.) However, various other models can provide exotic production without exotic exchange. Examples are three-vertex models, and models in which a higher mass exotic (but with charge -1) decays into $X^{--}\pi^+$. For models such as these, the assumption made regarding the exponential falloff of the differential cross section is probably a poor assumption.

There is also the possibility of exotic production within the framework of a two-vertex model in which only the singly charged or neutral member of the multiplet is produced in this reaction. However, there is no evidence of narrow structure in the $\pi^+\pi^-$ or the $\pi^+\pi^-\pi^-$ invariant mass distributions. Thus, there is no evidence for exotic production of any kind in this reaction.

E. $\pi^- p \rightarrow \pi^-\pi^-\pi^+ p\pi^0$

This reaction is discussed in a manner quite similar to the 4-body final state in the previous section. Neutral meson production is studied in the following reactions:

$$\pi^- p \rightarrow \pi^- p\omega^0 \tag{41}$$

$$\pi^- p \rightarrow \pi^- p\eta^0 , \tag{42}$$

where observation of the $\pi^+\pi^-\pi^0$ decay modes of the ω^0 and η^0 are made. Neutral A_1 and A_2 production is briefly discussed. A cross section upper limit for the reaction

$$\pi^- p \rightarrow pB^- \tag{43}$$

is given. ρ production is observed, but no definitive results can be obtained as a result of the large number of particles in the final state, and the resulting ambiguity in the analysis. Δ^{++} production and limits on the production of exotic mesons are briefly considered.

1. Event sample

A sample of 6904 events satisfies this 1C hypothesis with vertex fit χ^2 probability greater than or equal to 0.01 and kinematic fit χ^2 probability greater than or equal to 0.07. A histogram of the kinematic fit confidence level is shown in Fig.123. The cut at 0.07 is seen to eliminate the majority of the contamination in the event sample. The sample of events utilized in the analysis contained no events which had good fits to other 1C hypotheses. Analysis of a sample of events with ambiguous fits (based on ω^0 cross sections in various samples

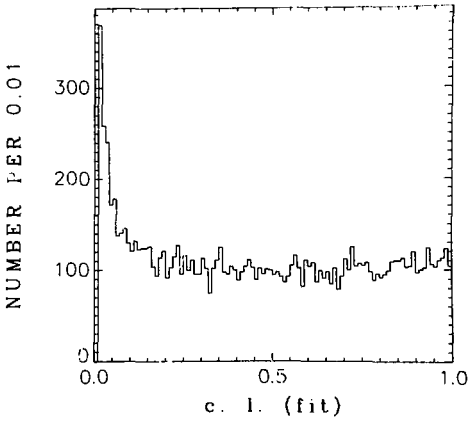

Fig. 123

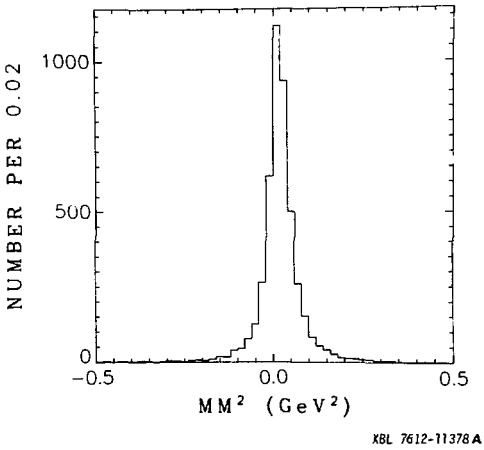

XBL 7612-11378A

Fig. 124

of events analyzed in the manner employed in Ch. V) indicates that 0.01 of the bona fide events are lost by this cut. A correction is made to the cross section to account for this loss. Fig. 124 shows a histogram of the missing mass squared. The distribution is consistent with that expected for a sample of events with a missing π^0.

2. General features

In Fig. 125 is a histogram of the $\pi^+\pi^-$ invariant mass distribution (2 combinations per event). The events are not corrected for acceptance, but events with proton trigger acceptance less than 0.15 or zero recoil acceptance, and events with a fast, charged pion which traverses the Cerenkov counter, are eliminated from the event sample. Evidence for ρ^0 production is seen. In Figs. 126 and 127 are histograms of the $\pi^+\pi^0$ invariant mass and the $\pi^-\pi^0$ invariant mass (2 combinations per event). There is evidence for both charged states of the ρ, but the ρ^- signal appears stronger than the ρ^+ signal. The $\pi^-\pi^-$ invariant mass distribution is shown in Fig. 128. There is no evidence for exotic production.

In Fig. 129 is the neutral $3\pi(\pi^+\pi^-\pi^0)$ invariant mass distribution (2 combinations per event). There is a strong ω^0 signal, evidence for an η^0 signal (it becomes more significant if cuts are made on the center-of-mass production angle from the target proton to the η^0), but no evidence for A_1^0 or A_2^0 production. In Fig. 130 is a histogram of the $\pi^+\pi^-\pi^-$ invariant mass. There is no evidence for resonance production in this channel. Fig. 131 shows the 3-body exotic channel $(\pi^-\pi^-\pi^0)$, but there is no evidence for exotic production. The $\pi^+\pi^-\pi^-\pi^0$ invariant mass distribution shown in Fig. 132 gives no evidence for B^- production.

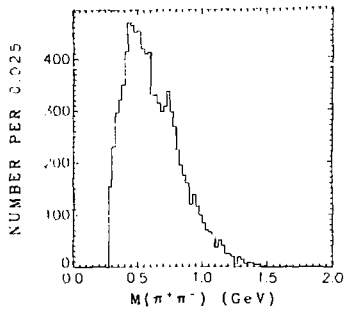

Fig. 126

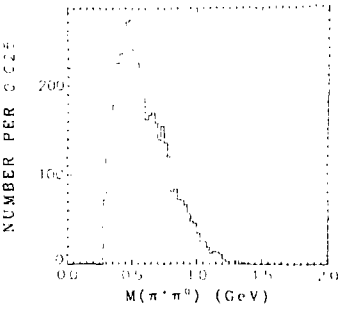

Fig. 126

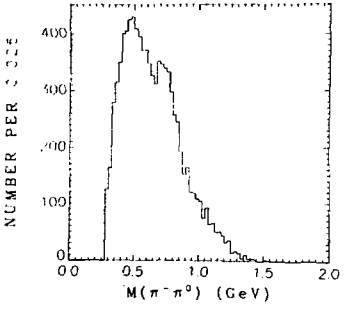

Fig. 127

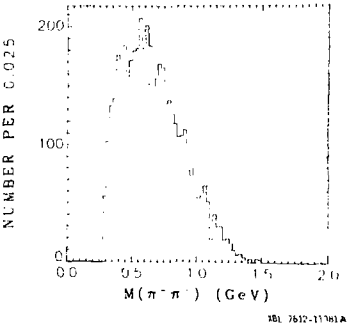

XBL 7612-11761A

Fig. 127

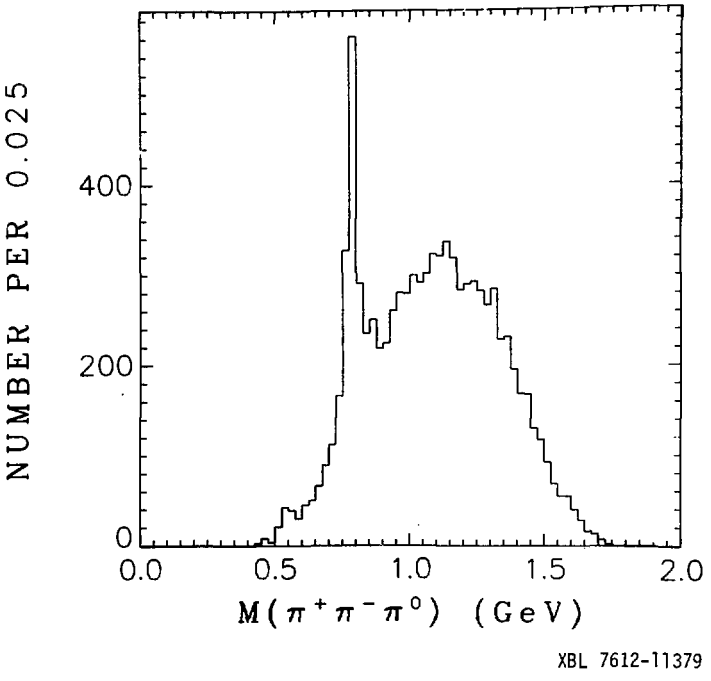
NUMBER PER 0.025
400
200
0
0.0
0.5
1.0
1.5
2.0
M(π⁺π⁻π⁰) (GeV)
XBL 7612-11379

Fig. 129

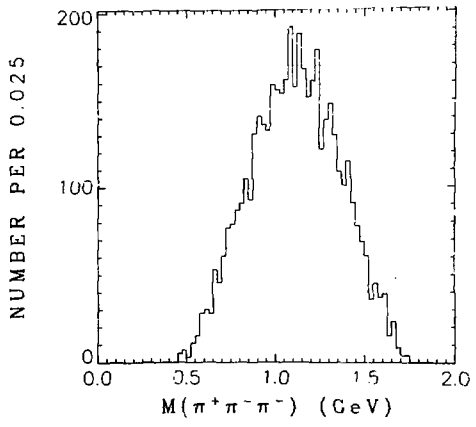

Fig. 130

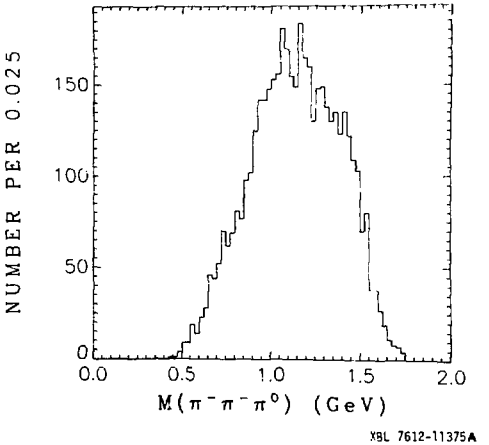

Fig. 131

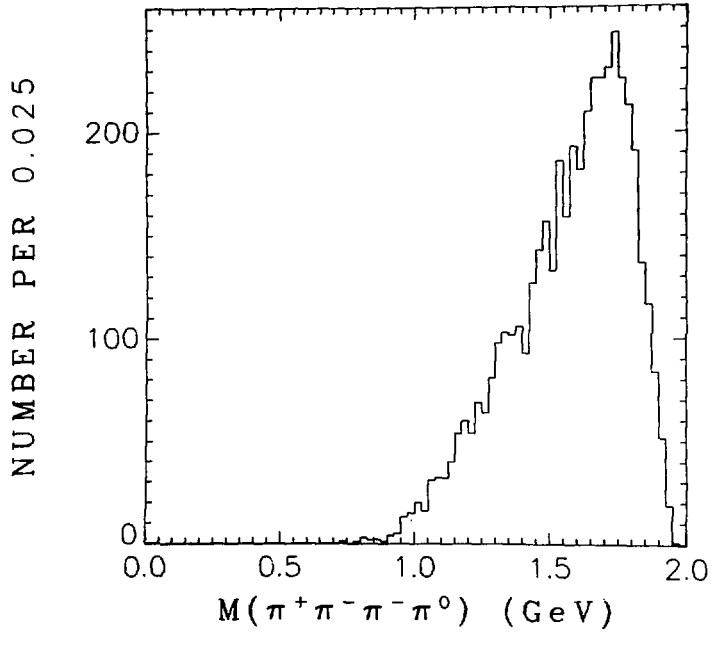
NUMBER PER 0.025
200
100
0
0.0
0.5
1.0
1.5
2.0
M(π⁺π⁻π⁻π⁰) (GeV)
XBL 7612-11377

Fig. 132

In Figs. 133-135 are the 2-body baryon invariant mass distributions. The $p\pi^+$ channel shows a strong $\Delta^{++}(1232)$ signal. The $p\pi^-$ channel (2 combinations per event) appears to have a $\Delta^0(1232)$ signal, although the resonance line shape is rather peculiar. There is also evidence for N^{*0} resonance production near 1.50 GeV. The $p\pi^0$ distribution shows evidence for $\Delta^+(1232)$ production, and possibly evidence for higher mass N^{*+} production, but the uncertainty in the background makes the effect difficult to establish.

In Figs. 136-142 are the 3-body and 4-body baryon invariant mass distributions. There is no evidence of significant resonance production in any of these channels.

In Fig. 143 is a Chew-Low plot of the $\pi^+\pi^-\pi^0$ invariant mass squared vs u from the target proton to the $\pi^+\pi^-\pi^0$ system. (The solid curve represents the kinematic limit calculated for the mean center-of-mass energy of the experiment.) A strong ω^0 signal is seen extending over the entire observed range of u. In Fig. 144 is a Chew-Low plot of the $p\pi^+$ invariant mass squared vs u from the beam to the $p\pi^+$ system. As in the 4-body final state discussed previously, the Δ^{++} production does not peak at the kinematic boundary.

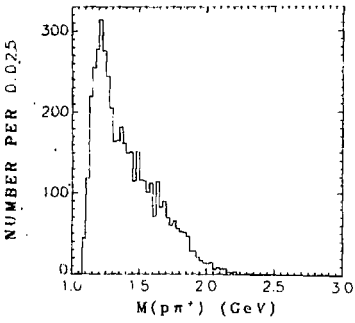

Fig. 133

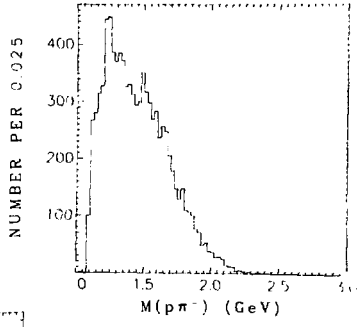

Fig. 134

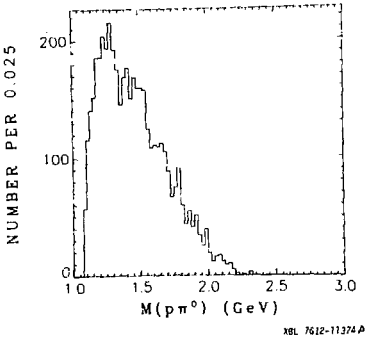

Fig. 135

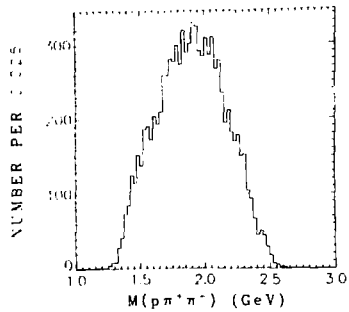
NUMBER PER
300
200
100
0
1.0
1.5
2.0
2.5
3.0
M(pπ⁺π⁻) (GeV)

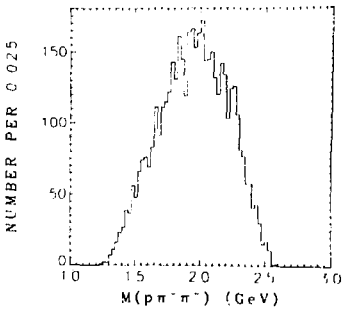
NUMBER PER 0.025
150
100
50
0
1.0
1.5
2.0
2.5
3.0
M(pπ⁻π⁻) (GeV)

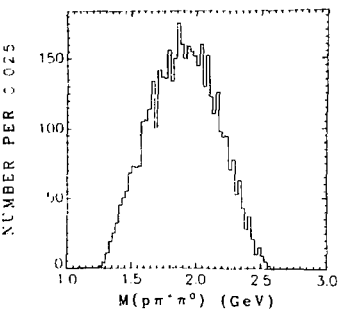
NUMBER PER 0.025
150
100
50
0
1.0
1.5
2.0
2.5
3.0
M(pπ⁺π⁰) (GeV)

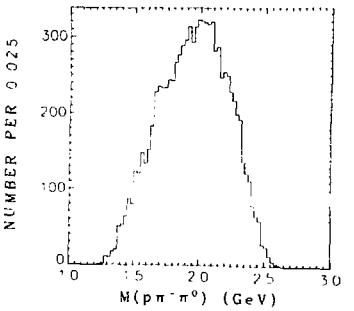
NUMBER PER 0.025
300
200
100
0
1.0
1.5
2.0
2.5
3.0
M(pπ⁻π⁰) (GeV)

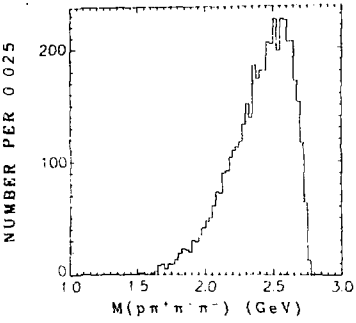

Fig. 13

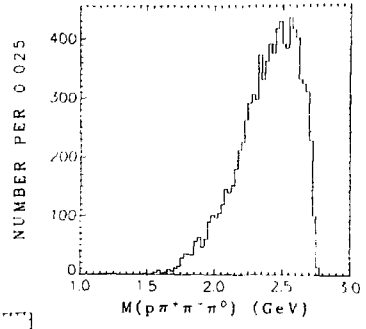

Fig. 141

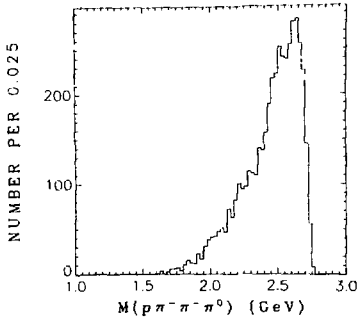

XBL 7612-11368 A

Fig. 142

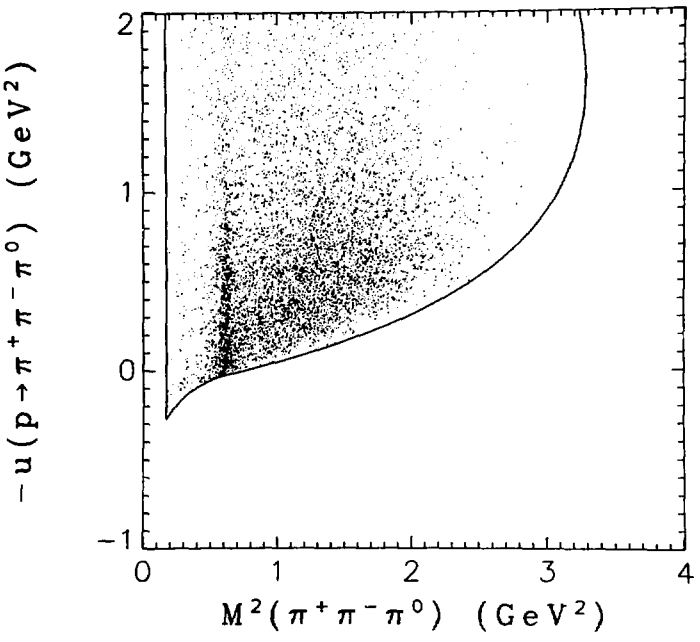

XBL 7612-11393

Fig. 143

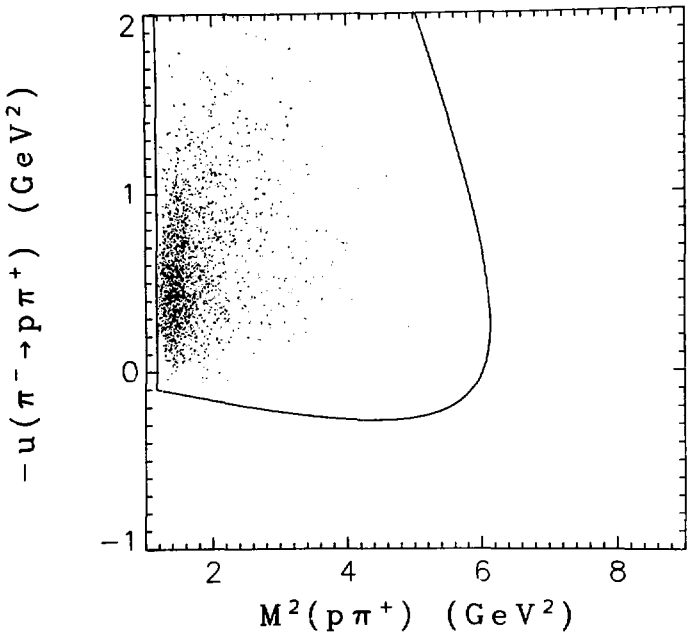

XBL 7612-11392

Fig. 144

3. ω^0 production

The analysis of reaction (41) parallels the ρ^0 analysis of the previous section. A least squares fit was made to the $\pi^+\pi^-\pi^0$ invariant mass distribution shown in Fig. 145. All events are corrected up by the inverse of the acceptance and events with trigger acceptance less than 0.15 are eliminated. The solid curve represents the results of the fit. The distribution function assumed in the fitting procedure consisted of Breit-Wigner resonance terms for the ω^0 and η^0 over an incoherent background term (represented by the dashed curve in the figure). Breit-Wigner resonance terms were used rather than Gaussian resonance terms as they appeared to fit the data better. The resolution distribution has wide tails which are not well represented by a Gaussian distribution (as discussed previously). The parameters obtained in the fit are

$$M_{\omega^0} = 0.783 \text{ GeV}$$
$$\Gamma_{\omega^0} = 0.026 \text{ GeV}$$
$$M_{\eta^0} = 0.547 \text{ GeV}$$
$$\Gamma_{\eta^0} = 0.028 \text{ GeV} \quad .$$

The fitted values of the masses agree quite well with the nominal values. The widths have no relevance to the natural resonance widths, but provide an indication of the 3π mass resolution.

In Fig. 146 is the background subtracted differential cross section for ω^0 production as a function of u' from the beam to the recoiling $p\pi^-$ system. (The signal region used in the background subtraction

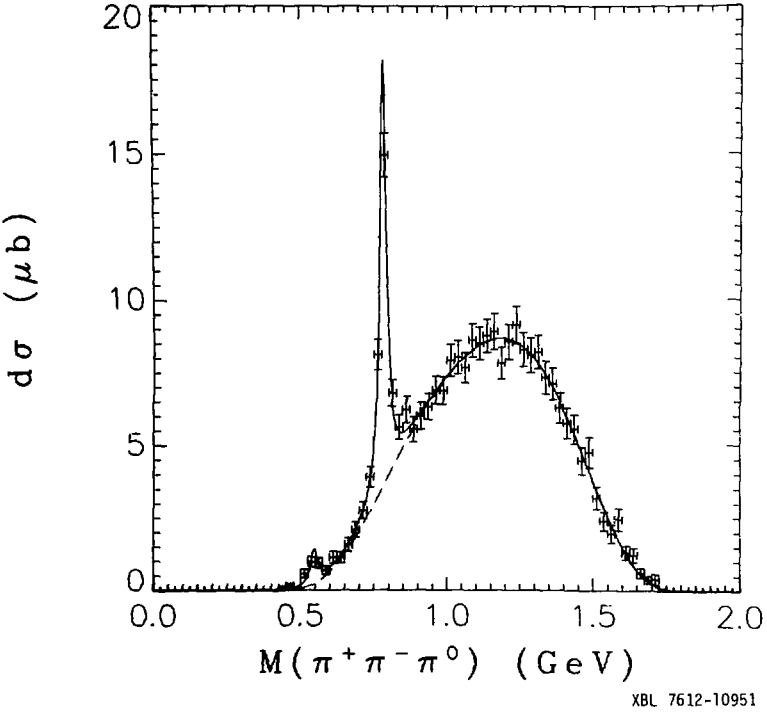

Fig. 145

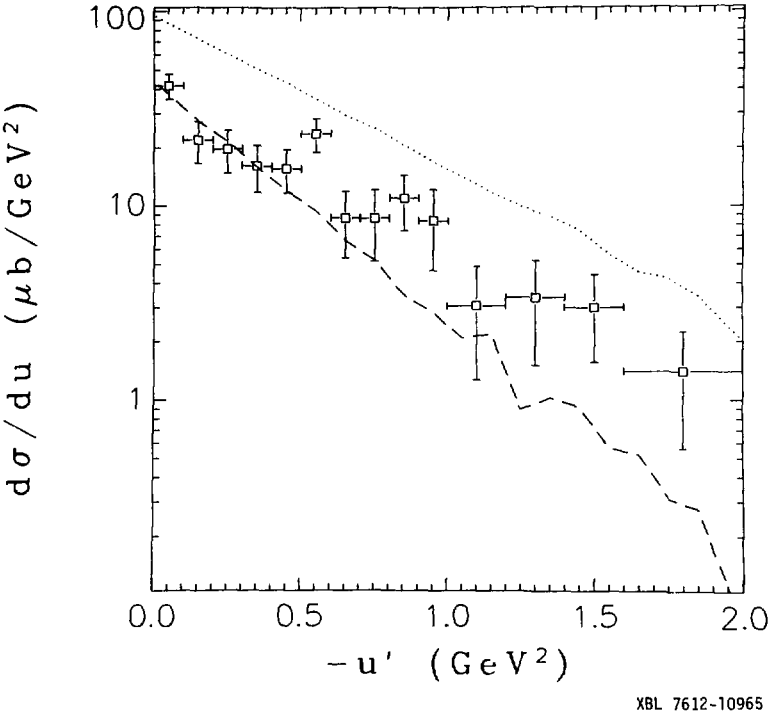

Fig. 146

included the mass interval from 0.735 to 0.835 GeV.) The real data points are given with error bars and have been corrected up for the trigger acceptance. The dotted curve represents a Monte Carlo simulation of ω^0 production. The dashed curve represents the Monte Carlo distribution after correcting down by the three-parameter acceptance function, and then correcting up in the same manner as the real events.

In Fig. 147 is the differential cross section after correction for events lost by the trigger. The data points represented in the plot are listed in Table XXXIV. The data points have been corrected for unobserved decay modes (assuming the branching fraction for $\omega^0 \to \pi^+\pi^-\pi^0$ is 0.899). The differential cross section is observed to have a very sharp, backward peak above a relatively flat distribution. The cross section over the interval $u' > -0.5$ GeV^2 can be described as

$$\frac{d\sigma}{du} = \left(\frac{d\sigma}{du}\right)_{flat} + \sigma_{peak} ,$$

where $\left(\frac{d\sigma}{du}\right)_{flat} = 61.3 \pm 7.4$ μb/GeV^2, and σ_{peak} integrated over the interval $u' > -0.05$ GeV^2 is 4.8 ± 1.1 μb.

In Fig.148(a) is the uncorrected $p\pi^-$ recoil spectrum for events in the ω^0 signal region. Fig.148(b) shows the same distribution after background subtraction and correction for Breit-Wigner tails. The requirement is imposed that $\cos\theta^*_{\pi^-\to p\pi^-} \geq 0.8$ in both distributions. There appears to be a peak near 1.65 GeV, and possible evidence for $\Delta^0(1232)$ production, in the recoil spectrum. However, the Δ^0 appears

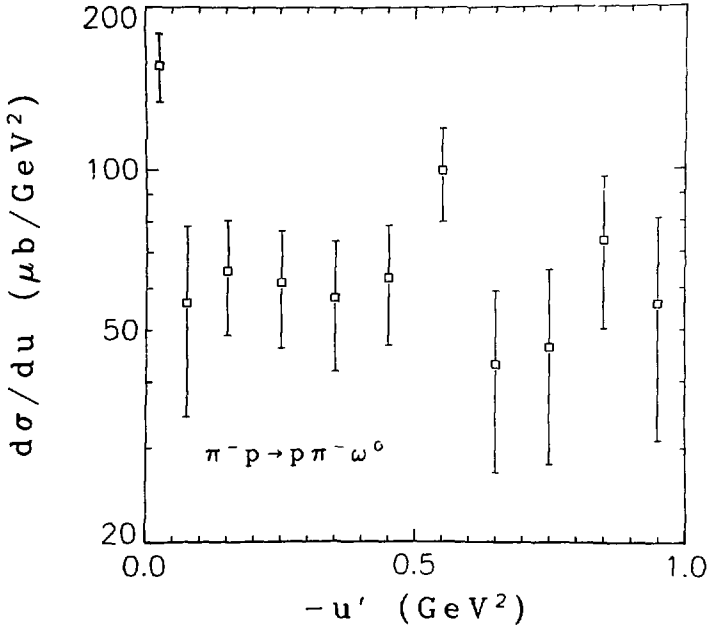

XBL 7612-11385

Fig. 147

Table XXXIV. Differential cross section for $\pi^- p \to p\pi^- \omega^0$ as a function of u'.

$-u'$ (GeV^2)	Δu (GeV^2)	$d\sigma/du$ ($\mu b/GeV^2$)
0.025	0.05	156. ± 22.
0.075	0.05	56. ± 22.
0.15	0.10	65. ± 16.
0.25	0.10	62. ± 15.
0.35	0.10	58. ± 16.
0.45	0.10	63. ± 16.
0.55	0.10	100. ± 20.
0.65	0.10	43. ± 16.
0.75	0.10	46. ± 18.
0.85	0.10	74. ± 23.
0.95	0.10	56. ± 25.

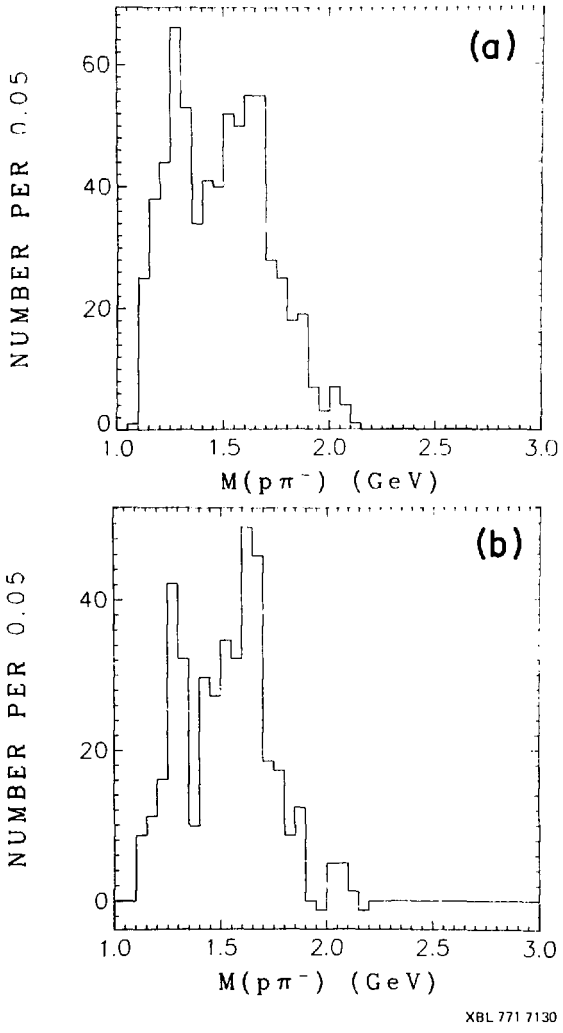
(a)
NUMBER PER 0.05
60
40
20
0
1.0
1.5
2.0
2.5
3.0
M(pπ⁻) (GeV)
(b)
NUMBER PER 0.05
40
20
0
1.0
1.5
2.0
2.5
3.0
M(pπ⁻) (GeV)
XBL 771 7130

Fig. 148

shifted in mass from the nominal value, and there is some question regarding the validity of this interpretation. An examination of the differential cross section as a function of recoil mass was made. The results of various recoil mass cuts are shown in Fig. 149(a) ($1.15 \leq M(p\pi^-) < 1.31$ GeV), in Fig. 149(b) ($1.44 \leq M(p\pi^-) < 1.60$ GeV), and in Fig. 149(c) ($1.61 \leq M(p\pi^-) < 1.77$ GeV). Within the rather large errors involved, the data within each mass region appears similar to the overall differential cross section.

In Fig. 150(a) is the uncorrected $\omega^0\pi^-$ invariant mass distribution for all events in the ω^0 signal region. In Fig. 150(b) is the distribution after background subtraction and correction for the Breit-Wigner tails. No resonance production (e.g., B^-) is observed. In Fig. 151(a) is the uncorrected $\omega^0 p$ invariant mass distribution for events in the ω^0 signal region. The distribution resulting after background subtraction and correction for tails is shown in Fig. 151(b). There is an indication of structure near threshold. A Monte Carlo simulation based on a maximum likelihood fit to the 5-body final state shows no indication of structure near threshold. Verification of this effect must await a higher statistics data sample.

The ω^0 density matrix elements in the s-channel helicity frame are shown in Fig. 152 as a function of u' from the beam to the $p\pi^-$ recoil system. In Table XXXV are the values averaged over the interval $u' > -0.4$ GeV^2. There is no significant structure in the density matrix

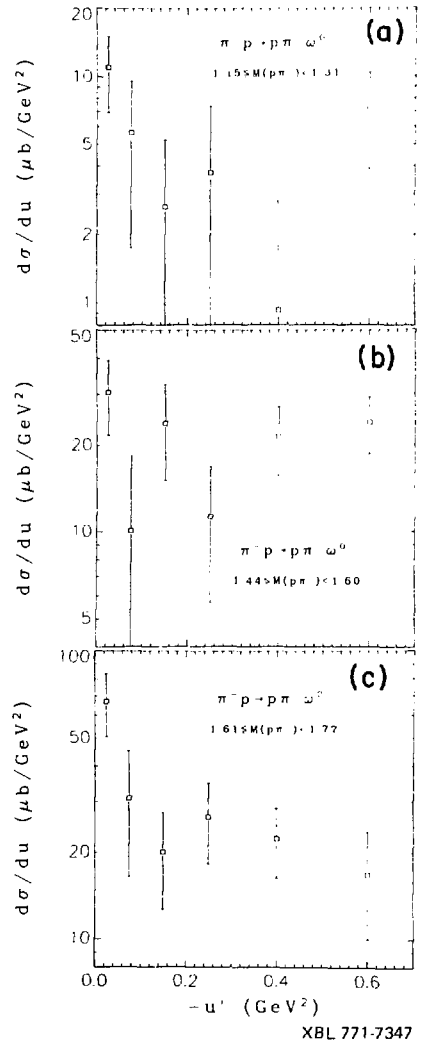

Fig. 149

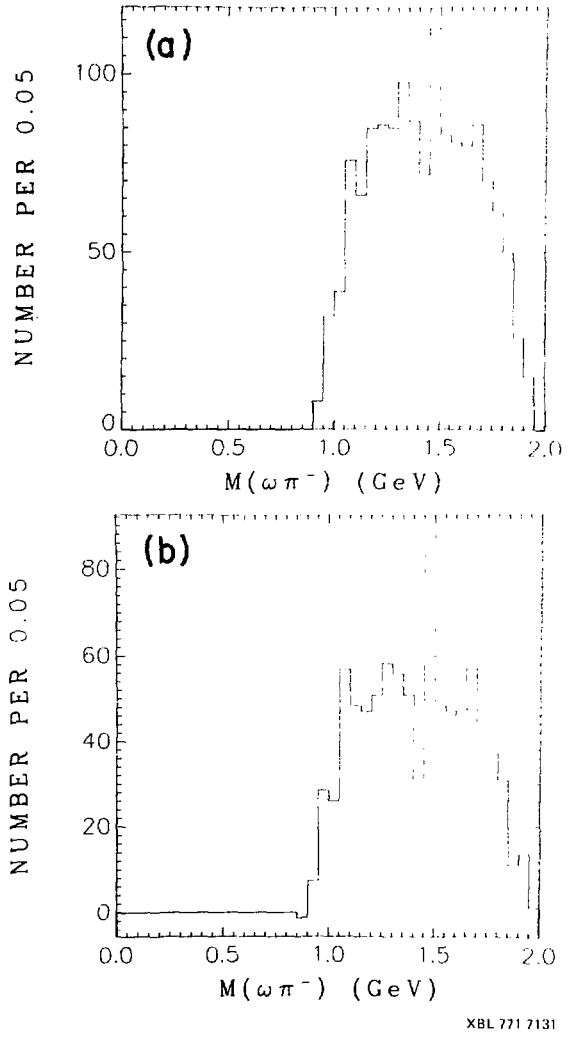
(a)
NUMBER PER 0.05
100
50
0
0.0
0.5
1.0
1.5
2.0
M(ωπ⁻) (GeV)
(b)
NUMBER PER 0.05
80
60
40
20
0
0.0
0.5
1.0
1.5
2.0
M(ωπ⁻) (GeV)
XBL 771 7131

Fig. 150

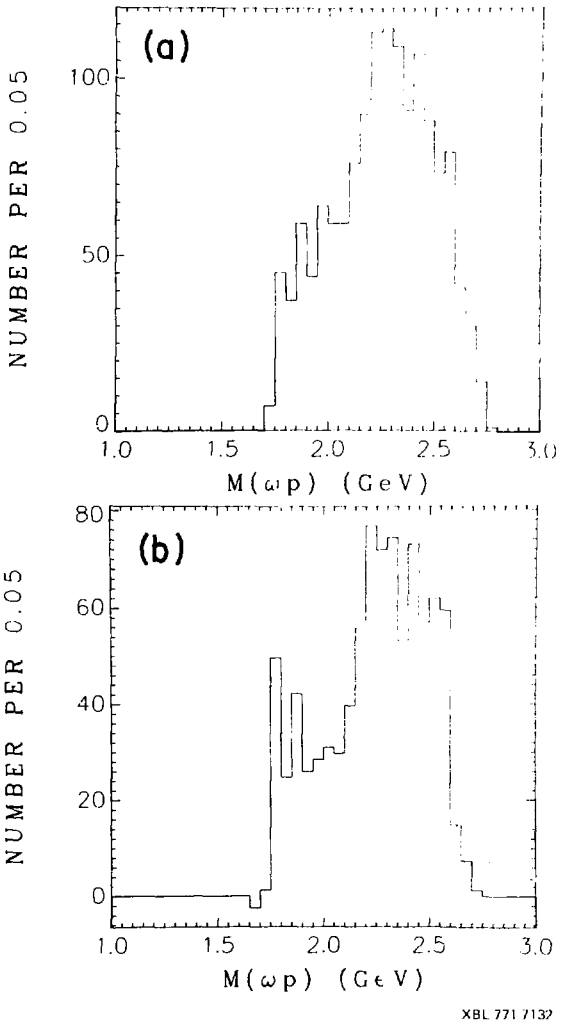
(a)
NUMBER PER 0.05
100
50
0
1.0
1.5
2.0
2.5
3.0
M(ωp) (GeV)
(b)
NUMBER PER 0.05
80
60
40
20
0
1.0
1.5
2.0
2.5
3.0
M(ωp) (GeV)
XBL 771 7137

Fig. 151

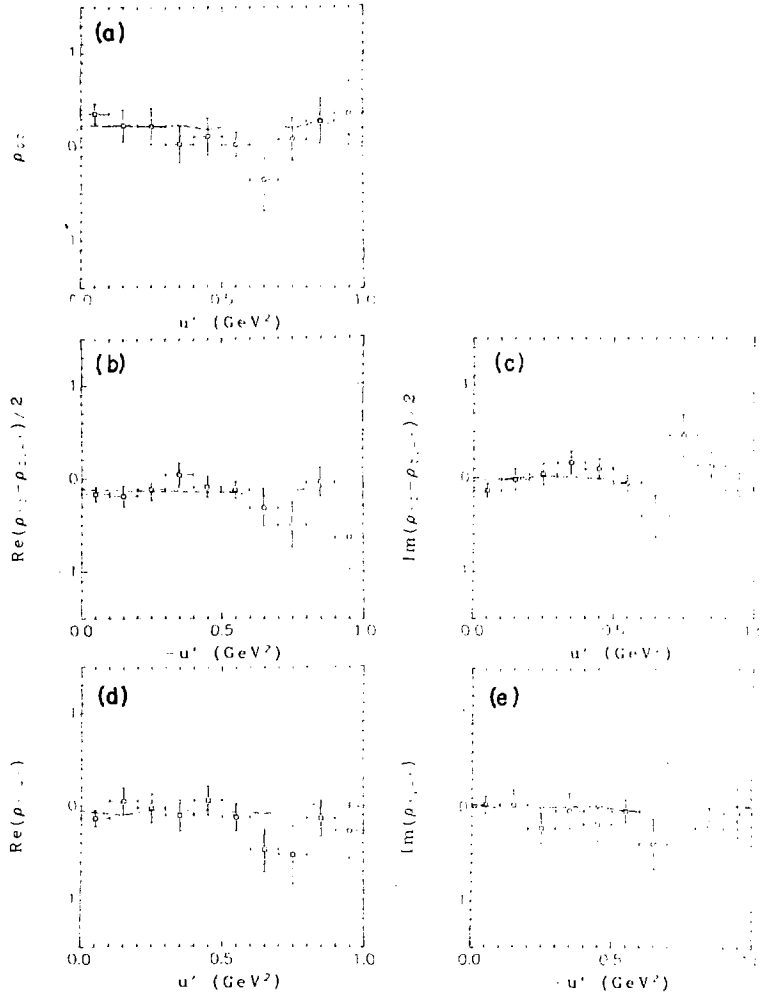

XBL 7612-10968

Fig. 152

Table XXXV. Average ω^0 density matrix elements in the s-channel helicity frame.

ρ_{00}	=	0.25 ± 0.08
$\mathrm{Re}(\rho_{10} + \rho_{0,-1})/2$	=	-0.14 ± 0.05
$\mathrm{Im}(\rho_{10} + \rho_{0,-1})/2$	=	-0.02 ± 0.05
$\mathrm{Re}(\rho_{1,-1})$	=	-0.08 ± 0.06
$\mathrm{Im}(\rho_{1,-1})$	=	-0.03 ± 0.07

elements, and they are not very different from the results expected for an isotropic decay.

4. η^0 production

The analysis of η^0 production was done in the same manner as the ω^0 analysis. In Fig. 153 is the background subtracted (with signal region from 0.505 to 0.585 GeV) differential cross section as a function of u' from the beam to the $p\pi^-$ recoil spectrum. All events are corrected up for trigger acceptance. The curves represent the Monte Carlo simulation. After correction for the loss of events with trigger acceptance less than 0.15, and correction for unobserved decay modes, the differential cross section is given in Fig.154. The data points represented in this plot are listed in Table XXXVI. It was assumed in the correction for the unobserved decay modes that both the $\pi^+\pi^-\pi^0$ and the $\pi^+\pi^-\gamma$ decay modes were included in this event sample. Thus, an observed branching fraction of 0.285 was assumed. A least squares fit of the data to the expression

$$\frac{d\sigma}{du} = b\ \sigma_{backward}\ e^{bu'} ,$$

was made over the interval $u' > -0.5$ GeV^2. The results of the fit are

$$\sigma_{backward} = 8.0 \pm 2.5\ \mu b$$
$$b = 5.0 \pm 3.2\ \text{GeV}^{-2}.$$

There is no evidence of structure in either the $p\pi^-$ recoil spectrum from the η^0, or the $\eta^0\pi^-$ invariant mass distribution. The $\eta^0 p$ invariant mass distribution (shown in Fig. 155(a) for events in the η^0 signal region and in Fig. 155(b) after background subtraction and tail

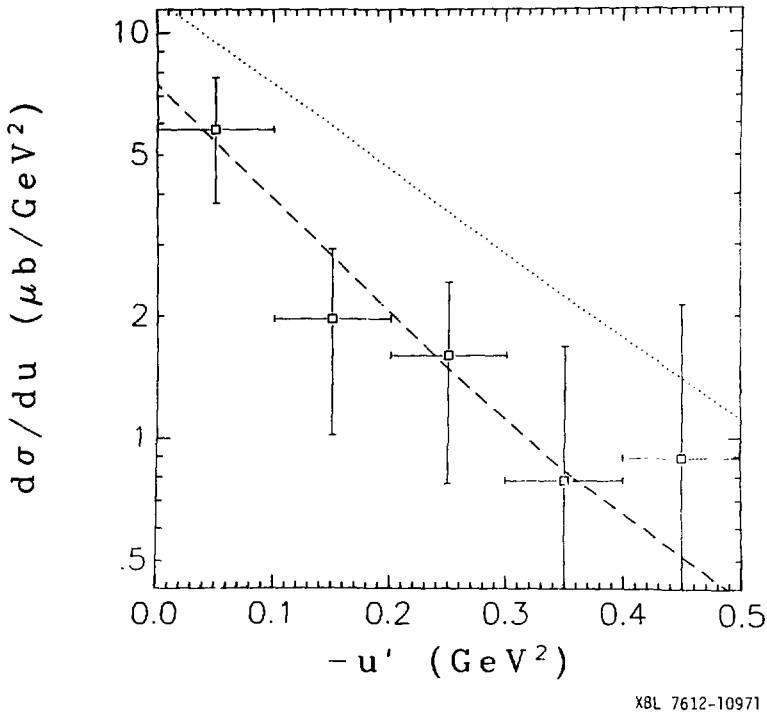

Fig. 153

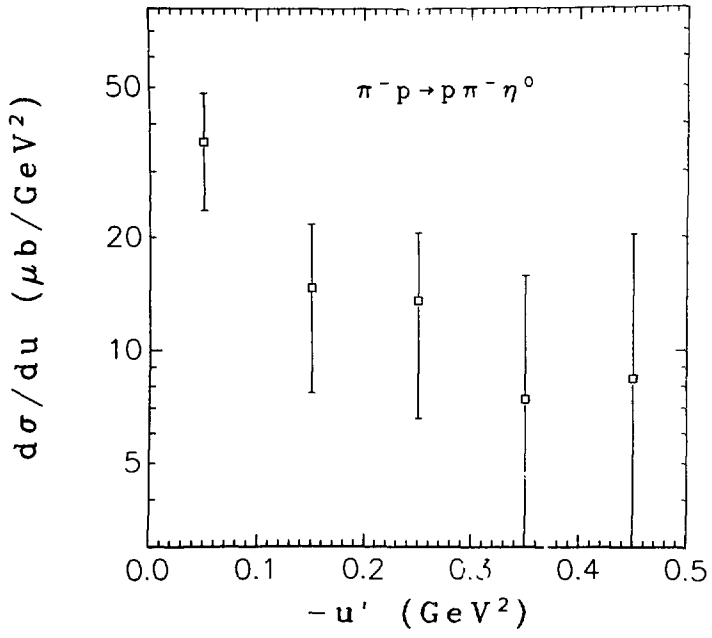

XBL 7612-11386

Fig. 154

Table XXXVI. Differential cross section for $\pi^- p \to p\pi^- \eta^0$ as a function of u'.

$-u'$ (GeV^2)	Δu (GeV^2)	$d\sigma/du$ ($\mu b/GeV^2$)
0.05	0.10	36.0 ± 12.3
0.15	0.10	14.7 ± 7.0
0.25	0.10	13.6 ± 7.0
0.35	0.10	7.4 ± 8.4
0.45	0.10	8.4 ± 11.9

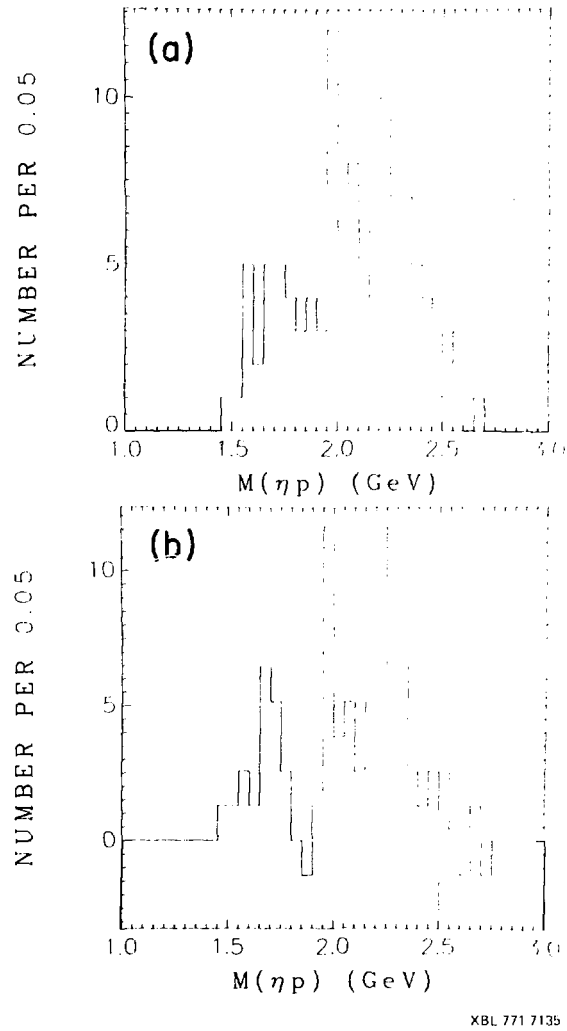
(a)
(b)
NUMBER PER 0.05
NUMBER PER 0.05
10
5
0
1.0
1.5
2.0
2.5
M(ηp) (GeV)
XBL 771 7135

Fig. 155

correction) displays a peak (of minor significance) at approximately the same mass as the $\omega^0\rho$ peak near threshold.

5. A production

This final state allows for production of both the neutral and the negatively charged A_1 and A_2. The neutral 3π channel is shown in Fig. 129 and the charged 3π channel is shown in Fig. 130. In both channels, it is observed that the peak of the mass distribution is at approximately 1.1 GeV. This makes observation of an A_1 signal difficult, and no reasonable upper limits can be placed on the production cross sections. There is no indication of an A_2 signal in either distribution. It is expected that an A_2^0 signal is more likely to be observed than an A_2^- signal, because the A_2^0 is expected to be produced by nucleon exchange whereas the A_2^- requires delta exchange. Also, one-half of the $\rho\pi$ decay made of the A_2^- is unobservable.

A least squares fit to the invariant mass distribution (after correction for trigger acceptance) over the mass interval from 0.9 to 1.5 GeV was made. The fit assumed a Breit-Wigner resonance over a quadratic background. (See the discussion on the A_2^- in the previous section for a more detailed description.) A Monte Carlo simulation was utilized to correct for events with trigger acceptance less than 0.15, based on the assumption that the differential cross section falls off exponentially as $e^{3u'}$. Finally a correction for unobserved decay modes was made. The resulting 95% confidence level upper limit for the cross section is

$$\sigma_{A_2^0} < 32 \ \mu b \ .$$

Unfortunately, this limit does not provide much of a constraint for models.

6. B^- production

In Fig. 132 is the 4π invariant mass distribution. There is no evidence for B^- production in this distribution, or the distribution which results when an $\omega^0\pi^-$ decay is required (see Fig. 150). A comparison of the experimental data distribution with a Monte Carlo simulation (Based on the 5-body maximum likelihood fit) showed no evidence of an excess in the region of the B^-. A least squares fit to the corrected experimental distribution over the mass interval from 0.8 to 1.5 GeV was made, assuming a Breit-Wigner resonance above a quadratic background. The resonance parameters were

$$M_B = 1.228 \text{ GeV}$$

$$\Gamma_B = 0.125 \text{ GeV} \quad .$$

The resulting 2 standard deviation (95% confidence level) cross section upper limit is

$$\sigma_{B^-} < 4.6 \ \mu b \ .$$

This upper limit includes all corrections for unobserved decay modes and lost triggers (assuming a falloff of the differential cross section like $e^{3u'}$).

7. Δ^{++} production

As in the 4-body final state, there is substantial Δ^{++} production. The Δ^{++} is not expected to be produced alone at the top vertex

because of isospin considerations. Fig. 144 gives evidence supporting this expectation. In Figs. 156-159 are shown the 3- and 4-body baryon mass distributions which include both a p and a π^+. (a) includes all events with trigger acceptance greater than 0.15, and (b) has the additional requirement that $\cos\theta^*_{\pi^-\to\text{baryon}} \geq 0.8$. The hatched regions include only those events in which the $p\pi^+$ invariant mass is within the interval 1.15 - 1.31 GeV. There is no evidence for any cascade decay of a high mass N^* resonance into $\Delta^{++}\pi$ or $\Delta^{++}\pi\pi$. Therefore, the same conclusions apply to this final state as were discussed in connection with the 4-body final state in the last section.

8. Exotic meson production

Analysis of the exotic channels was done in the same manner as for the 4-body final state. In Fig. 160(a) is the $\pi^-\pi^-$ invariant mass distribution (corrected up for acceptance). Fig. 160(b) has the additional requirement that $\cos\theta^*_{\pi^-\to p\pi^+\pi^0} > 0.8$. The curves represent least squares fits to the distributions. Significant positive deviations of the data from the fit in the mass interval between 0.4 and 1.2 GeV were considered, and corrections were applied to correct for lost triggers based on the assumption that the differential cross section falls off as $e^{3u'}$. The most significant deviation (within a mass interval of 0.050 Gev) was in the mass interval 1.050 - 1.100 GeV. The 95% confidence level cross section upper limit is $\sigma < 9.5$ μb.

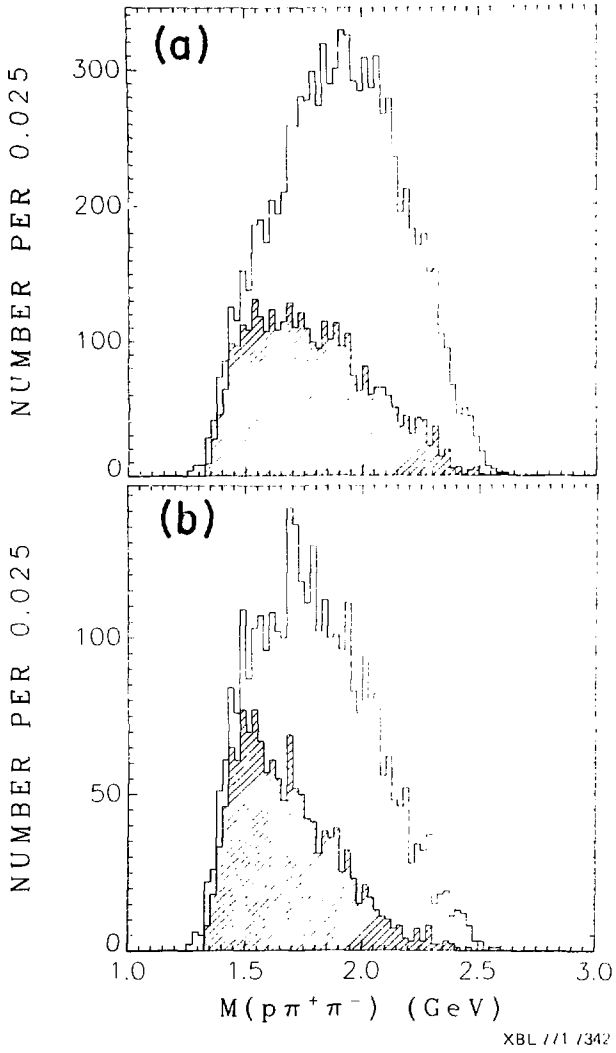
(a)
(b)
NUMBER PER 0.025
NUMBER PER 0.025
300
200
100
0
100
50
0
1.0
1.5
2.0
2.5
3.0
M(pπ⁺π⁻) (GeV)
XBL 771 7342

Fig. 156

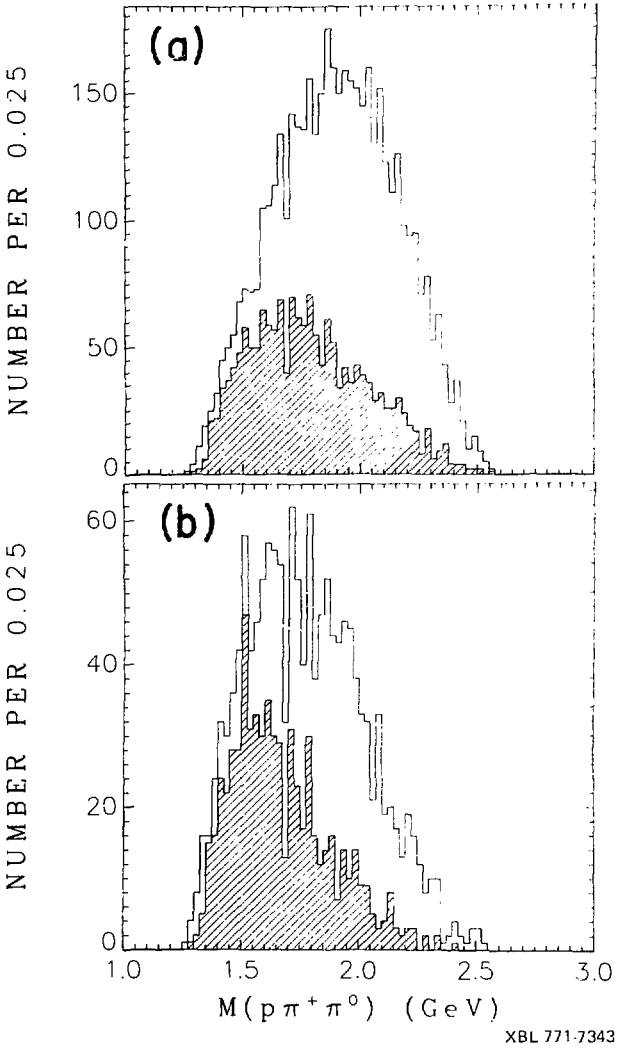
(a)
(b)
NUMBER PER 0.025
NUMBER PER 0.025
150
100
50
0
60
40
20
0
1.0
1.5
2.0
2.5
3.0
M(pπ⁺π⁰) (GeV)
XBL 771-7343

Fig. 157

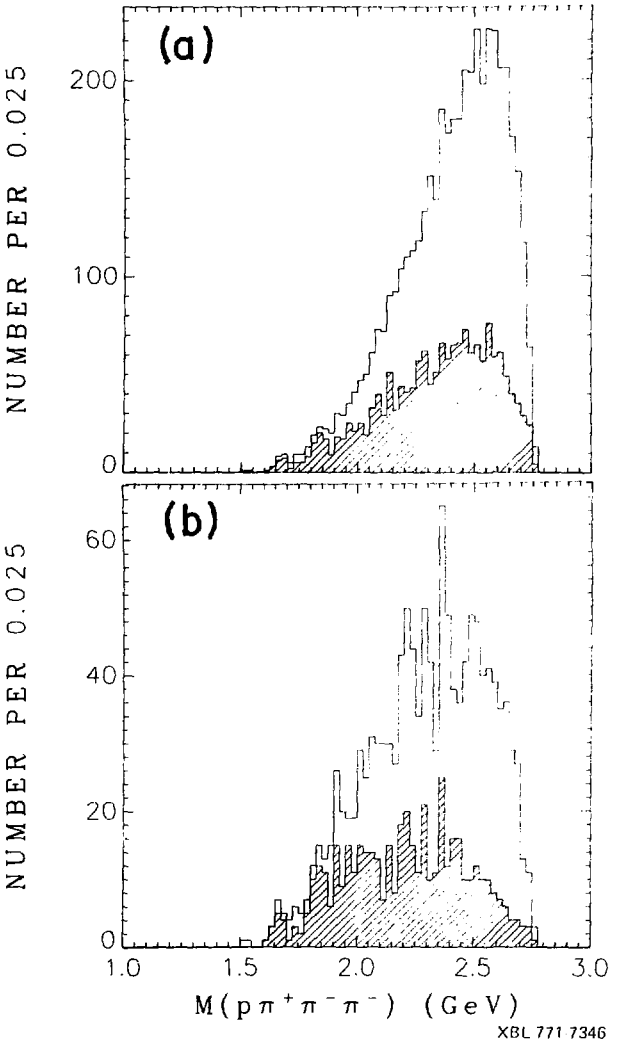
(a)
(b)
NUMBER PER 0.025
NUMBER PER 0.025
200
100
0
60
40
20
0
1.0
1.5
2.0
2.5
3.0
M(pπ⁺π⁻π⁻) (GeV)
XBL 771 7346

Fig. 158

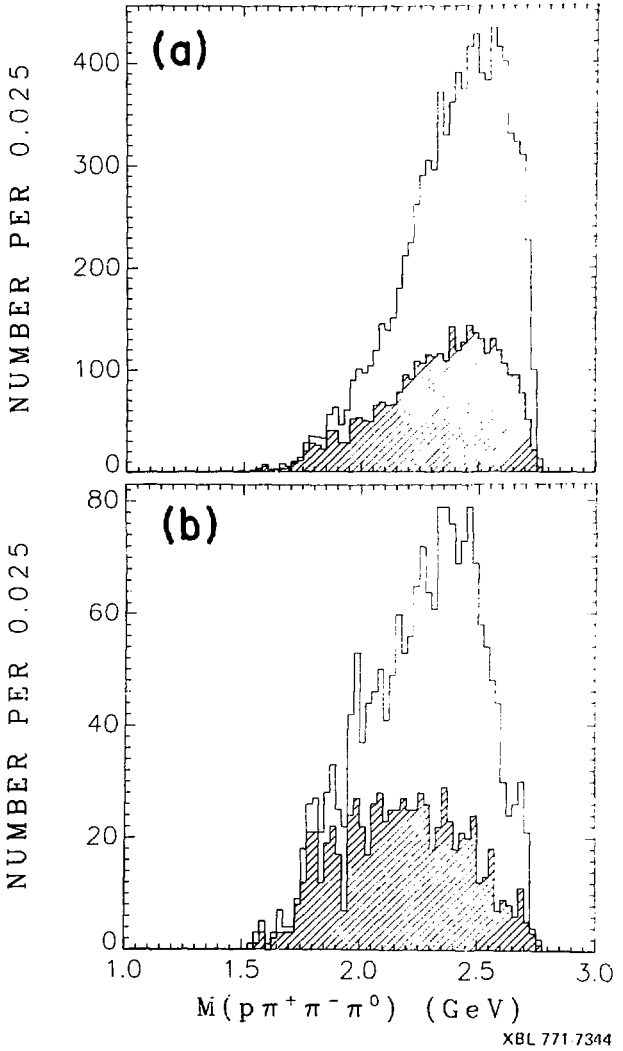
(a)
(b)
NUMBER PER 0.025
NUMBER PER 0.025
400
300
200
100
0
80
60
40
20
0
1.0
1.5
2.0
2.5
3.0
M(pπ⁺π⁻π⁰) (GeV)
XBL 771-7344

Fig. 159

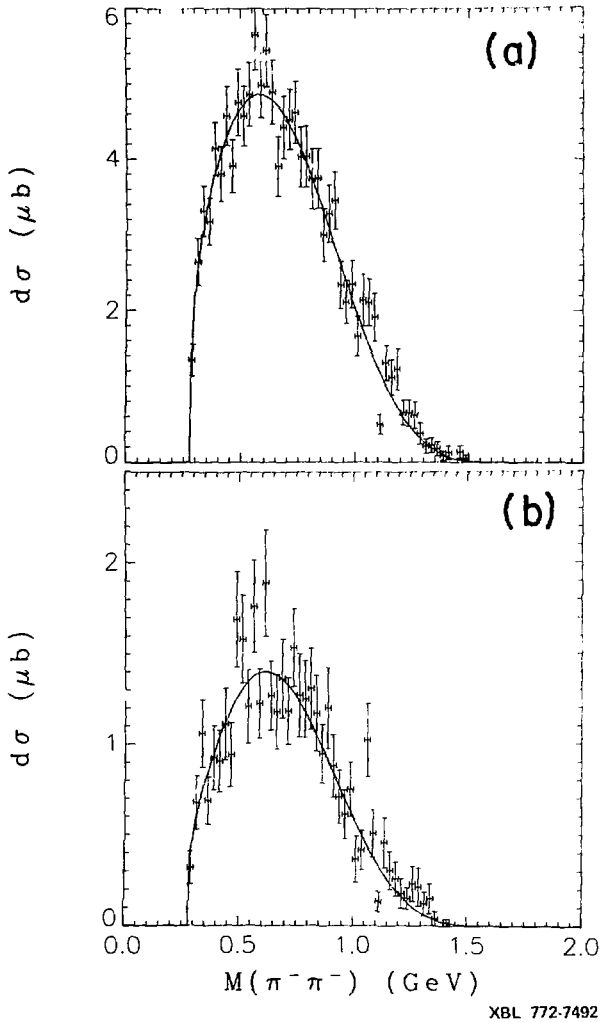

Fig. 160

In Fig. 161(a) is the $\pi^-\pi^-\pi^0$ invariant mass distribution, with the resulting distribution after the imposition of the requirement $\cos\theta^*_{\pi^- \to p\pi^+} \geq 0.8$ shown in Fig. 161(b). The curves represent least squares fits. Within the mass range from 0.6 to 1.4 GeV, the most significant deviation was in the mass interval 1.025-1.075 GeV. A 95% confidence level upper limit of $\sigma < 5.6$ μb is obtained for this channel.

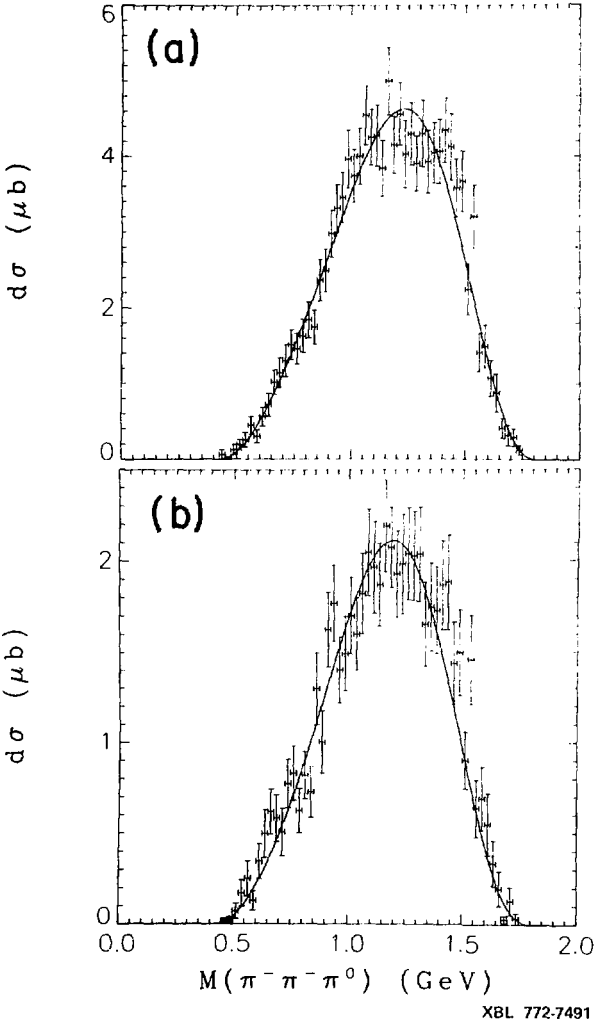

Fig. 161

F. $\pi^- p \to \pi^- K^- K^+ p$

The analysis of events satisfying the 4C hypothesis

$$\pi^- p \to \pi^- K^- K^+ p, \tag{6}$$

was minimal, although a preliminary investigation was carried out to look for structure in the data. There are 825 4-prong events which satisfy this hypothesis with a kinematic fit χ^2 probability greater than or equal to 0.09, and with a vertex fit χ^2 probability greater than or equal to 0.01. This sample includes events with ambiguous fits to other 4C hypotheses, and events in which the K^+ provided the trigger rather than the proton. In Fig. 162 is a histogram of the kinematic fit confidence level. There is evidence for significant contamination in the data sample.

In Fig. 163(a) is a histogram (uncorrected for trigger acceptance) of the $K^- K^+$ invariant mass. In Fig. 163(b) is the same data with the additional requirement that $\cos\theta^*_{\pi^- \to p\pi^-} \geq 0.8$. There appears to be an extremely sharp peak near threshold which might be naively associated with S* or ϕ production. However, this peak can be explained by contamination from

$$\pi^- p \to \pi^- K^+ \Lambda^0, \tag{7}$$

where the Λ^0 decays very near the primary interaction vertex, and the K^+ provides the trigger. In the fitting procedure to the hypothesis of reaction (6), the K^+ was misidentified as a proton, and the π^- and p from the Λ^0 decay were misidentified as a K^- and a K^+. Since the Λ^0 decay vertex is very close to the primary vertex, a reasonable vertex fit was obtained assuming only one vertex. A sample of Monte Carlo events was generated according to reaction (7). For those generated events which also satisfy the hypothesis of reaction (6) after misidentification

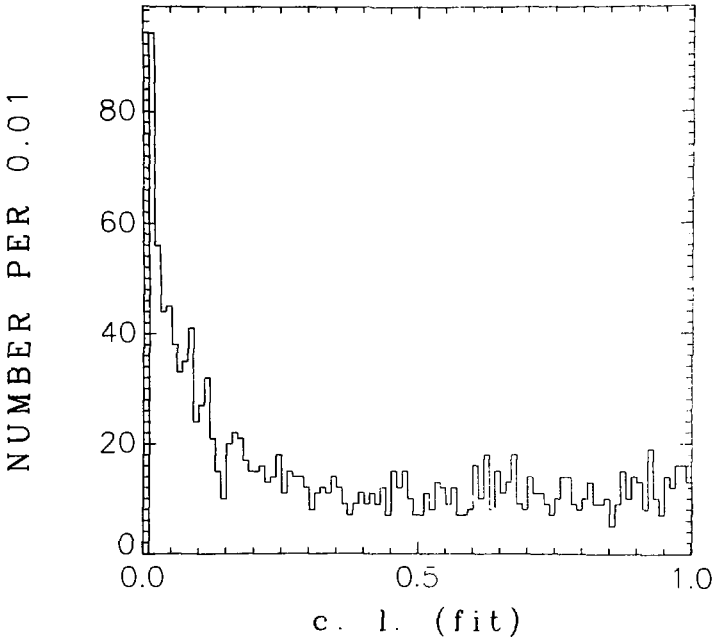

Fig. 162

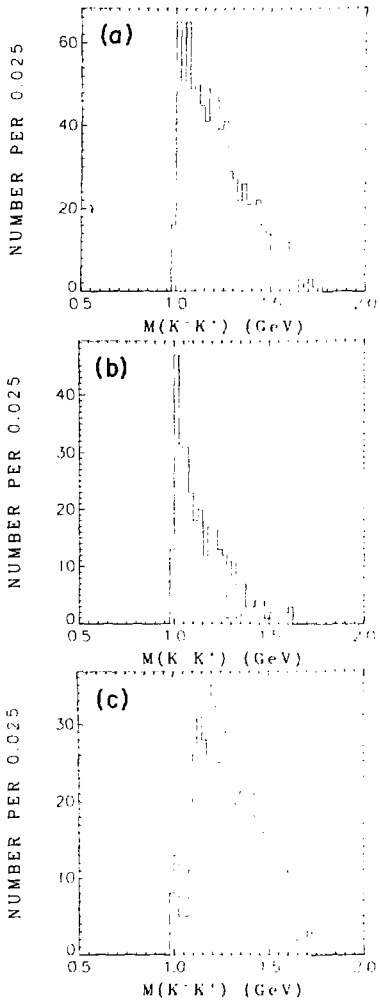

Fig. 163

of the tracks, the K^-K^+ invariant mass (corresponding to the misidentified π^-p mass from the Λ^0 decay) is shown in Fig. 164(a). This distribution is observed to peak near threshold and explains the sharp peak in the data well. There is also evidence in the data for contamination from

$$\pi^- p \rightarrow K^- p K^0, \tag{3}$$

where the K^0 decay vertex is very close to the primary vertex, the K^- is misidentified as a π^-, and the π^- and π^+ from the K^0 decay are misidentified as a K^- and a K^+. A sample of Monte Carlo events was generated according to reaction (3). For those generated events which also satisfy the hypothesis of reaction (6) after misidentification of the tracks, the K^-K^+ invariant mass is shown in Fig. 164(b). It also produces a sharp peak, slightly higher in mass. After elimination of events from the original sample which are consistent with satisfying the hypothesis of reaction (7) or (3), the resulting K^-K^+ invariant mass distribution is shown in Fig. 163(c). There is no evidence for structure in the resulting distribution. No comment can be made regarding ϕ production due to the large kinematic overlap.

In Fig. 165(a) is the π^-K^+ invariant mass distribution, with the resulting distribution after the elimination of events consistent with satisfying reaction (7) or (3) shown in Fig. 165(b). (All of the remaining figures in this section will display first (a) all events in the sample, and then (b) the distribution resulting from the elimination.) There is evidence for a strong K^{*0} signal, but most of the K* production results from meson exchange, where the trigger is provided by the K^+.

In Fig. 166 is the π^-K^- mass distribution (an exotic channel).

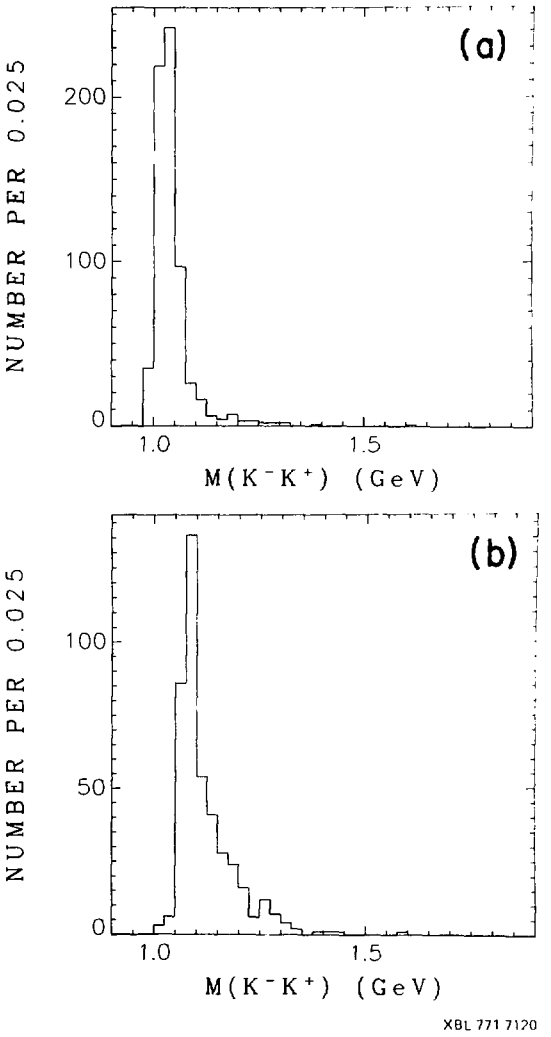
(a)
NUMBER PER 0.025
200
100
0
1.0
1.5
M(K⁻K⁺) (GeV)
(b)
NUMBER PER 0.025
100
50
0
1.0
1.5
M(K⁻K⁺) (GeV)
XBL 771 7120

Fig. 164

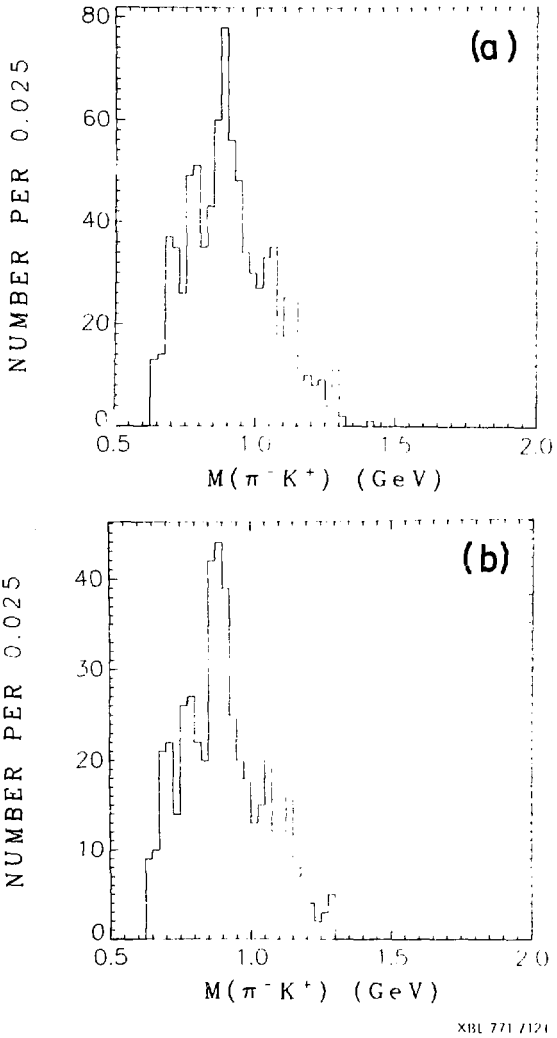
(a)
NUMBER PER 0.025
80
60
40
20
0
0.5
1.0
1.5
2.0
M(π⁻K⁺) (GeV)
(b)
NUMBER PER 0.025
40
30
20
10
0
0.5
1.0
1.5
2.0
M(π⁻K⁺) (GeV)
XBL 771 7121

Fig. 165

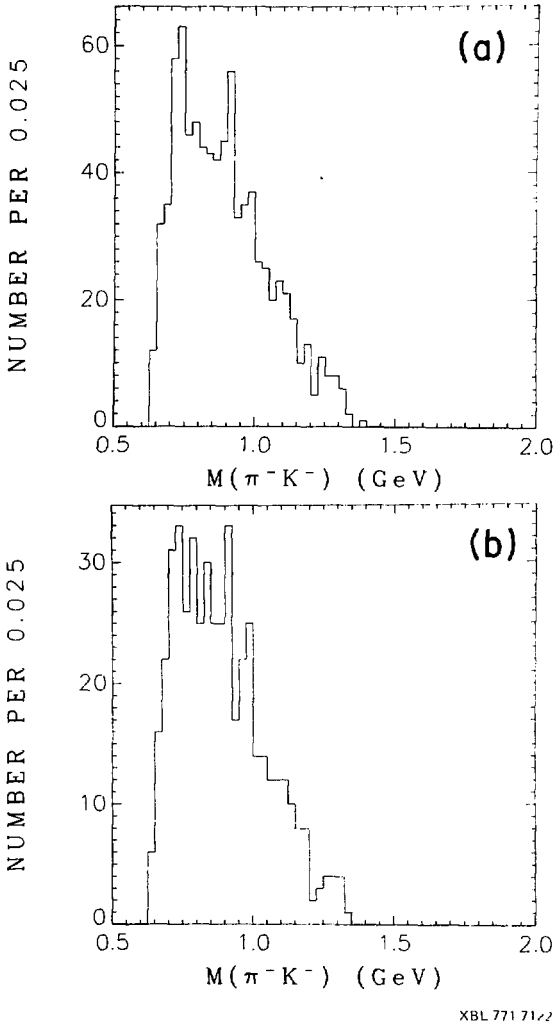
(a)
NUMBER PER 0.025
60
40
20
0
0.5
1.0
1.5
2.0
M(π⁻K⁻) (GeV)
(b)
NUMBER PER 0.025
30
20
10
0
0.5
1.0
1.5
2.0
M(π⁻K⁻) (GeV)
XBL 771 7122

Fig. 166

Evidence for structure is observed in the total event sample, but vanishes when the Λ^0 and K^0 events are eliminated. There is no explanation for this apparent structure. Fig. 167 shows the $\pi^-K^-K^+$ invariant mass distribution, in which there is no evidence for structure

In Fig. 168 is the $p\pi^-$ invariant mass histogram. There is evidence for $\Delta^0(1232)$ production in this channel, but it is mostly produced backwards (i.e., by meson exchange). There is, however, an enhancement in this channel when the requirement is imposed that $\cos \theta^*_{p\pi^-} \geq 0.8$, but this enhancement is slightly high in mass ($\sim$ 1.3 GeV). This is very similar to observations made in the 4- and 5-body (nonstrange) final states. In Fig. 169 is the pK^- invariant mass distribution. There is evidence for a sharp peak near threshold which is possibly evidence for $\Lambda^0(1520)$ production, but is more likely to be Λ^0 production in which the decay π^- was misidentified as a K^-. (These events were not eliminated from the sample.) The events in this peak appear to be due to a K^+ trigger, and the recoiling π^-K^+ invariant mass appears to show some structure in the $K^{*0}(892)$ mass region. This is consistent with either interpretation. In Fig. 170 is the pK^+ channel, in which no significant evidence for resonance production is observed.

In Figs. 171-173 are the 3-body baryon resonances. The only distribution with any evidence of structure is the $p\pi^-K^+$ invariant mass distribution, which is exotic. If this peak results from Λ^0 misidentification, it would represent a Λ^0K^+ resonance. There is not expected to be an N^{*+} or a Δ^+ resonance which would yield such a large signal. If the peak results from K^0 misidentification, it is exotic (pK^0). Finally, there

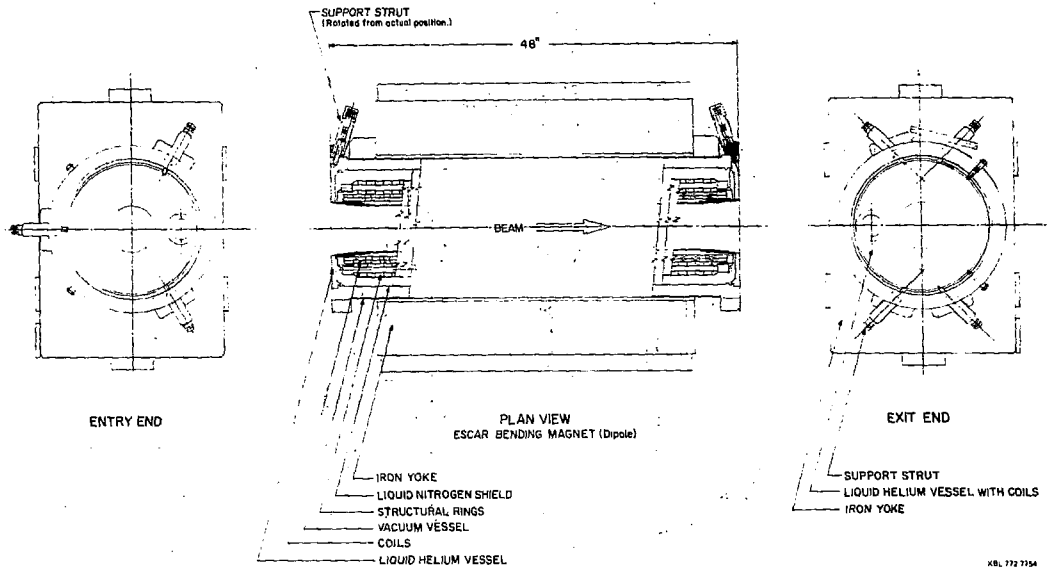

Figure 2. Escar bending magnet.

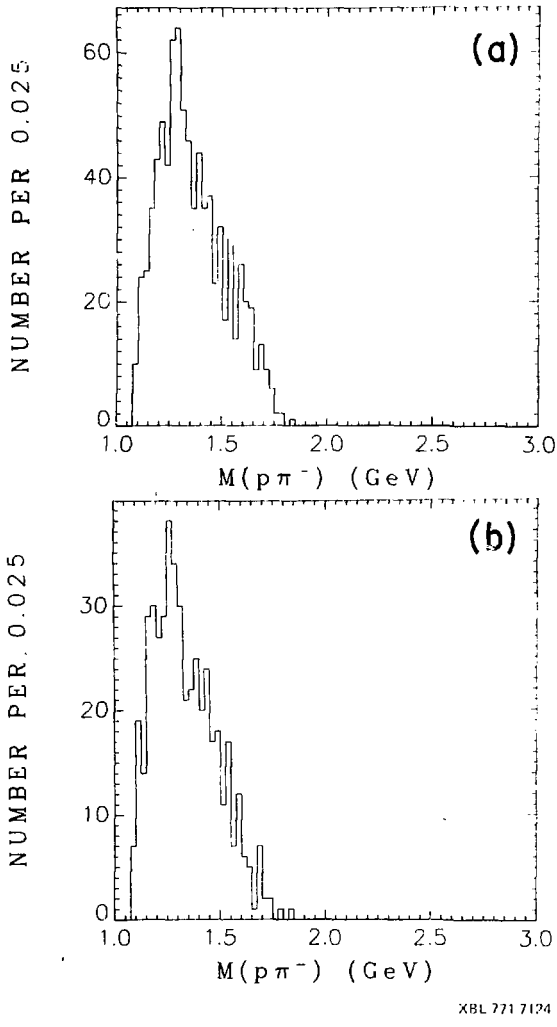
(a)
NUMBER PER 0.025
60
40
20
0
1.0
1.5
2.0
2.5
3.0
M(pπ⁻) (GeV)
(b)
NUMBER PER 0.025
30
20
10
0
1.0
1.5
2.0
2.5
3.0
M(pπ⁻) (GeV)
XBL 721 7124

Fig. 168

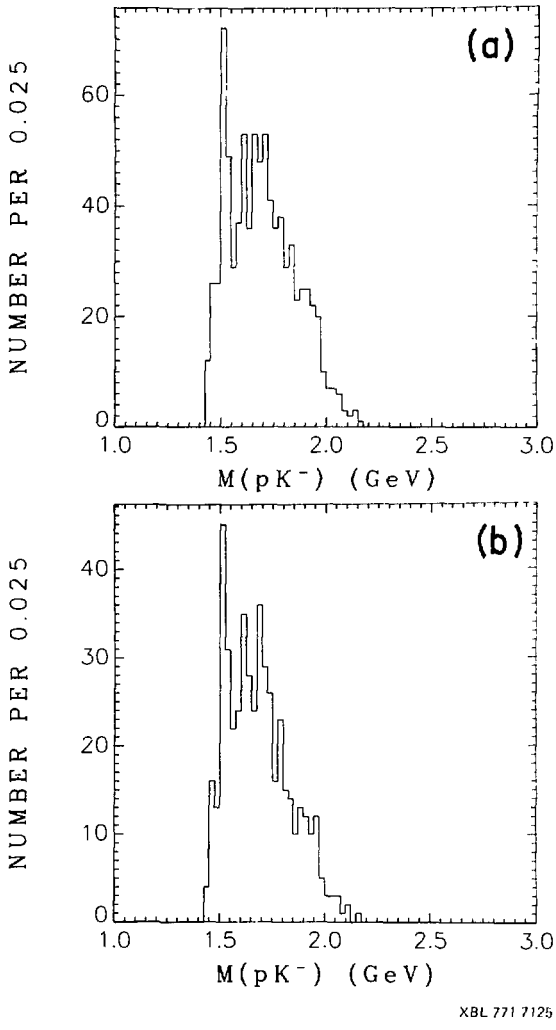
(a)
NUMBER PER 0.025
60
40
20
0
1.0
1.5
2.0
2.5
3.0
M(pK⁻) (GeV)
(b)
NUMBER PER 0.025
40
30
20
10
0
1.0
1.5
2.0
2.5
3.0
M(pK⁻) (GeV)
XBL 771 7125

Fig. 169

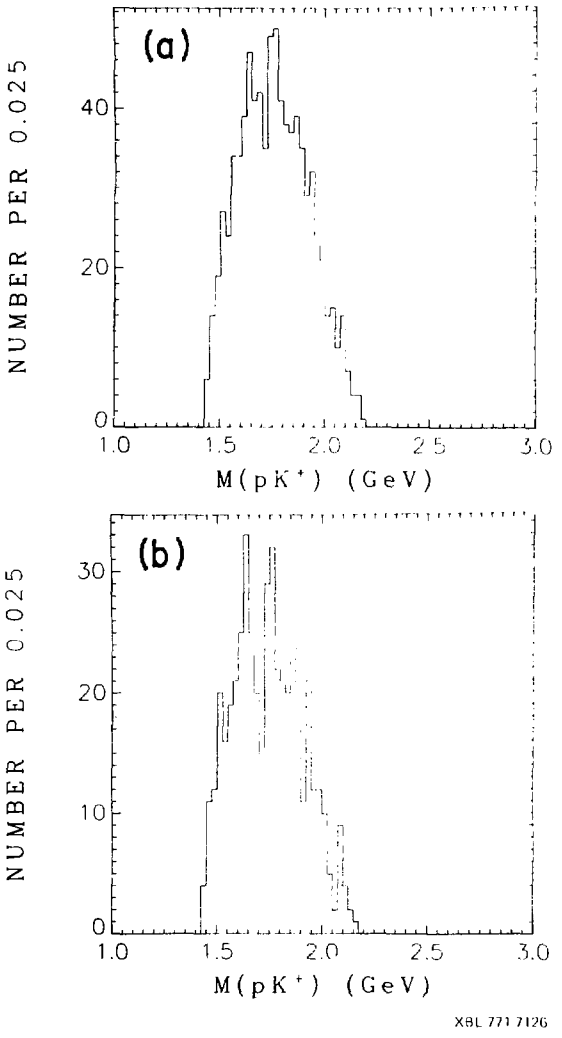
(a)
NUMBER PER 0.025
40
20
0
1.0
1.5
2.0
2.5
3.0
M(pK⁺) (GeV)
(b)
NUMBER PER 0.025
30
20
10
0
1.0
1.5
2.0
2.5
3.0
M(pK⁺) (GeV)
XBL 771 7126

Fig. 170

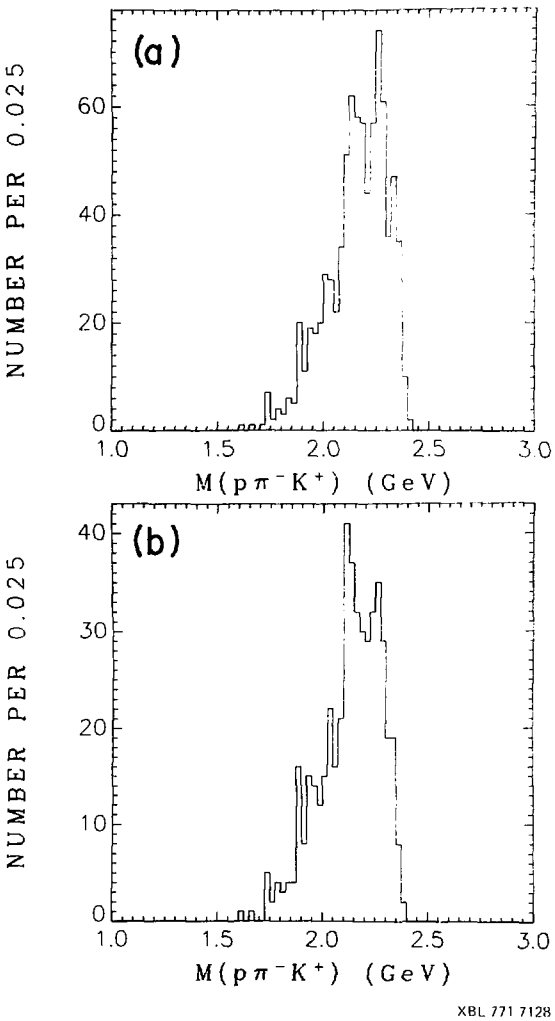
(a)
NUMBER PER 0.025
60
40
20
0
1.0
1.5
2.0
2.5
3.0
M(pπ⁻K⁺) (GeV)
(b)
NUMBER PER 0.025
40
30
20
10
0
1.0
1.5
2.0
2.5
3.0
M(pπ⁻K⁺) (GeV)
XBL 771 7128

Fig. 171

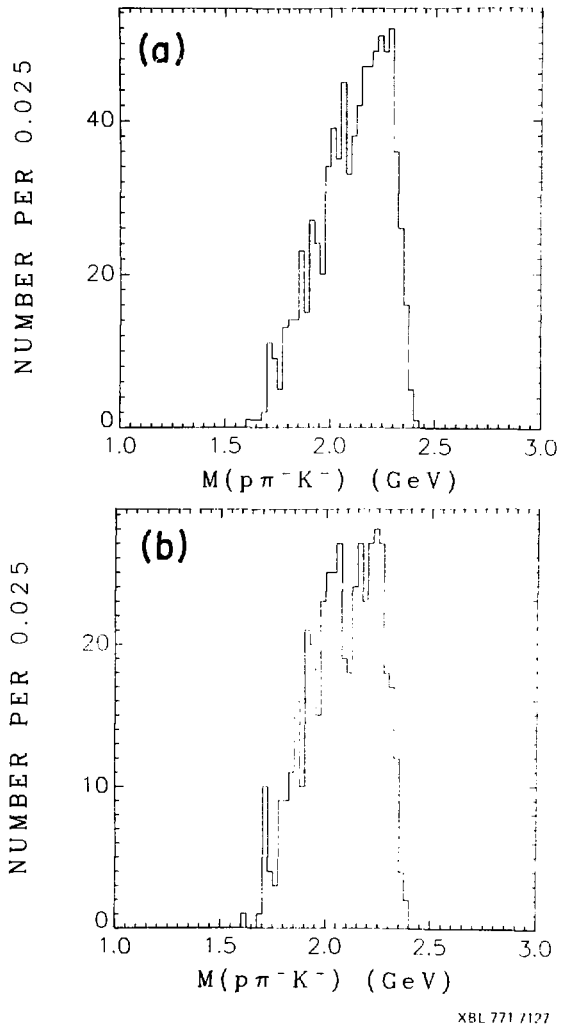
(a)
NUMBER PER 0.025
40
20
0
1.0
1.5
2.0
2.5
3.0
M(pπ⁻K⁻) (GeV)
(b)
NUMBER PER 0.025
20
10
0
1.0
1.5
2.0
2.5
3.0
M(pπ⁻K⁻) (GeV)
XBL 771 7127

Fig. 172

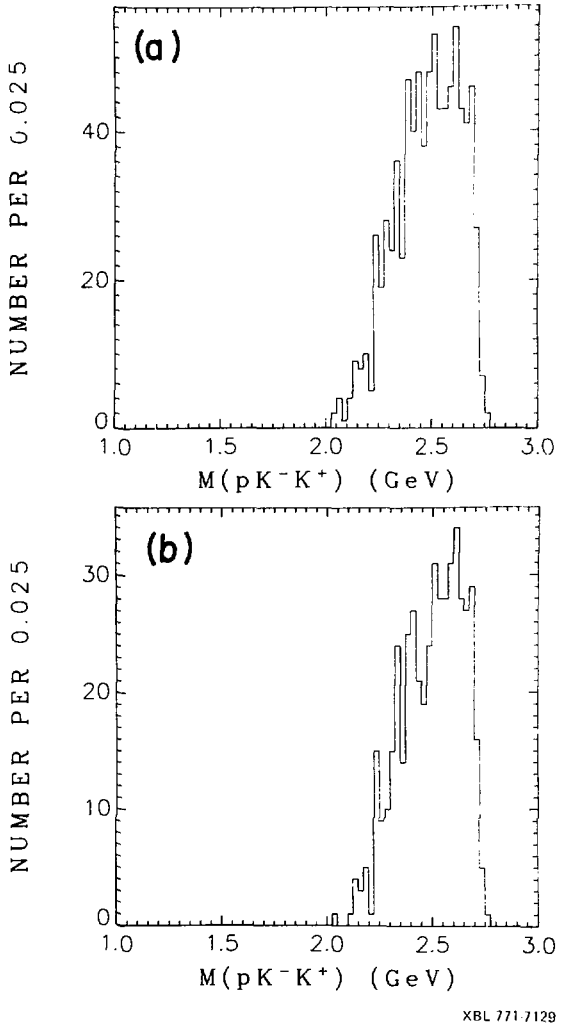
(a)
NUMBER PER 0.025
40
20
0
1.0
1.5
2.0
2.5
3.0
M(pK⁻K⁺) (GeV)
(b)
NUMBER PER 0.025
30
20
10
0
1.0
1.5
2.0
2.5
3.0
M(pK⁻K⁺) (GeV)
XBL 771-7129

Fig. 173

is the possibility of contamination from the $\pi^-\pi^-\pi^+p$ final state. However, there is no evidence of structure in the $\pi^-\pi^+p$ channel in that final state. Thus, the peak (if it is not a statistical fluctuation) has no apparent explanation.

G. $\underline{\pi^- p \to \pi^- K^+ \Lambda^0}$

The reaction

$$\pi^- p \to K^{*0}(892)\Lambda^0 \tag{44}$$

was analyzed, where the Λ^0 is produced forward. The differential cross section and the Λ^0 polarization for this reaction has been measured at higher energies with better statistics than are available from this experiment, but no analysis of the K^* decay has been published.

1. Event sample

There are 511 events which satisfy the hypothesis

$$\pi^- p \to \pi^- K^+ \Lambda^0, \tag{7}$$

with vertex fit χ^2 probability greater than or equal to 0.01 and kinematic fit χ^2 probability greater than or equal to 0.01. Of these, only 125 events have a fast Λ^0 which provided the trigger (with trigger acceptance greater than or equal to 0.10). The remainder of the events result from a K^+ trigger.

In Fig.174 is a histogram of the kinematic fit confidence level for this sample of events. Evidence for some background contamination is observed. The principal source of contamination is from the reaction

$$\pi^- p \to \pi^- K^+ \Sigma^0, \tag{45}$$

where the $\Sigma^0 \to \Lambda^0 \gamma$. In order to evaluate the relative production of reaction (45) as compared to reaction (7) (and to estimate the contamination of reaction (45) in reaction (7)), two methods of analysis were employed. The event sample pertinent to these analyses included all events with a forward Λ^0 which satisfied either hypothesis. The first method of analysis consisted of calculating the neutral missing mass from the

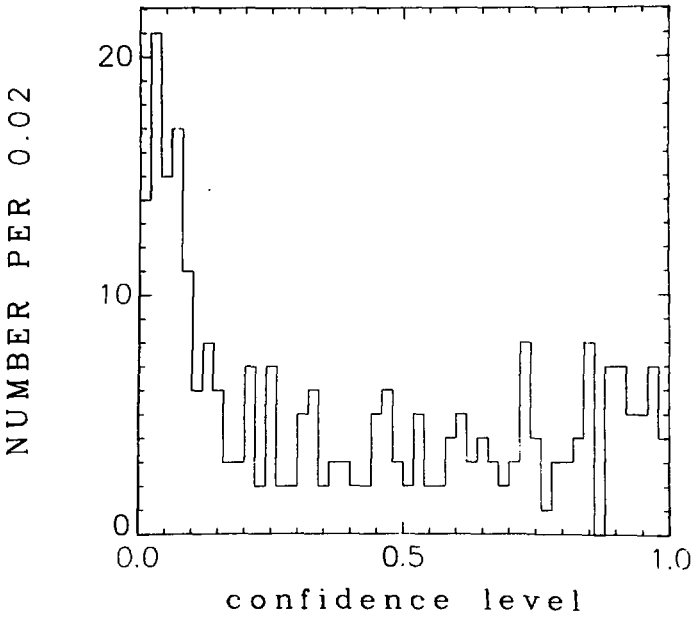

Fig. 174

unconstrained charged tracks (not including the Λ^0 decay prongs) and fitting the resulting mass distribution to the sum of a Λ^0 peak and a Σ peak (both widened to account for resolution broadening). The second method of analysis consisted of calculating the missing energy from the charged tracks (including the two prongs resulting from the Λ^0 which were constrained to satisfy a Λ^0 decay hypothesis) in the rest frame of the neutral system. The events satisfying reaction (7) were assumed to have a missing energy distribution symmetric around zero. The events satisfying reaction (45) were assumed to have a missing energy distribution centered at 0.074 GeV. The number of bona fide events satisfying reaction (7) was assumed to be twice the number of events with missing energy less than zero. The remaining number of events was assumed to represent the number of events satisfying reaction (45). The results of both analyses were consistent within errors, and the ratio of Λ^0 production to total Λ^0 plus Σ^0 production is

$$R = \frac{\sigma(\pi^- p \to \Lambda^0 K^+ \pi^-)}{\sigma(\pi^- p \to \Lambda^0 K^+ \pi^-) + \sigma(\pi^- p \to \Sigma^0 K^+ \pi^-)} = 0.71 \pm 0.05.$$

If both of these reactions are assumed to go by Σ exchange, a prediction for R can be made by utilizing the SU(3) Clebsch-Gordan coefficients and the experimental value of α (which is the ratio of the D coupling to the total D+F coupling), and by assuming the validity of factorization. α is experimentally determined to be approximately 0.64[100,101]. The predicted ratio is $R = 0.66 \pm 0.02$ where the error is based solely on the uncertainty in α. The agreement is excellent, indicating that the statistical separation of the two reactions is reasonable. A similar analysis involving only those events which satisfy the hypothesis of reaction (7), or both reactions (7) and (45), estimates that the

contamination from reaction (45) in the sample of events analyzed is 0.09 ± 0.07.

2. General features

In Fig.175(a) is the uncorrected $K^+\pi^-$ invariant mass distribution for all events in the sample. Fig.175(b) shows the same distribution for all events with Λ^o trigger acceptance greater than or equal to 0.10. Significant $K^*(892)$ production is observed, particularly in the total event sample. There appears to be an indication of structure at higher mass, but it is too low in mass for the $K^*(1420)$. Its nature (possibly statistical) is unknown. In Fig.176 is a Chew-Low plot of the π^-K^+ invariant mass squared vs u from the beam to the Λ^o. The curve represents the kinematic limit. Regions representing forward (meson exchange) and backward (baryon exchange) K^* production are observed to be cleanly separated.

In Fig.177 are the $\pi^-\Lambda^o$ invariant mass distributions. (In (b), events with Λ^o trigger acceptance less than 0.10 are eliminated.) A strong, forward $\Sigma^o(1385)$ signal is observed. In Fig.178 are the $K^+\Lambda^o$ invariant mass distributions (again with an acceptance cut in (b)). There is no evidence for resonance production in this channel.

3. K^* production

The analysis of reaction (46) was similar to the method employed for the analysis of ρ^- production in the 3-body final state . In Fig. 179 is the π^-K^+ invariant mass distribution (corrected up by the inverse of the Λ^o trigger acceptance). All events with trigger acceptance less than 0.10 are eliminated from the distribution. The distribution is scaled to be in units of cross section. The solid curve is a least squares fit to the data involving two Breit-Wigner resonance terms over an incoherent

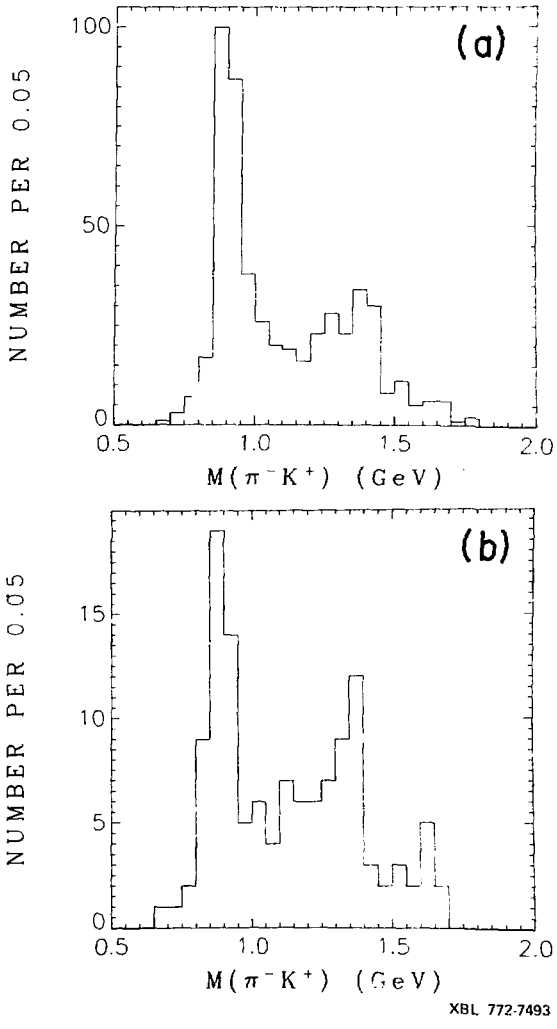
(a)
NUMBER PER 0.05
100
50
0
0.5
1.0
1.5
2.0
M(π⁻K⁺) (GeV)
(b)
NUMBER PER 0.05
15
10
5
0
0.5
1.0
1.5
2.0
M(π⁻K⁺) (GeV)
XBL 772-7493

Fig. 175

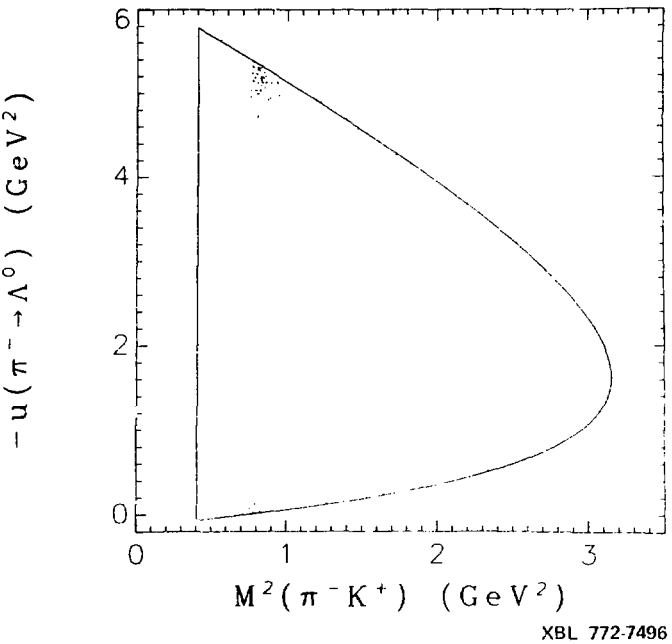

Fig. 176

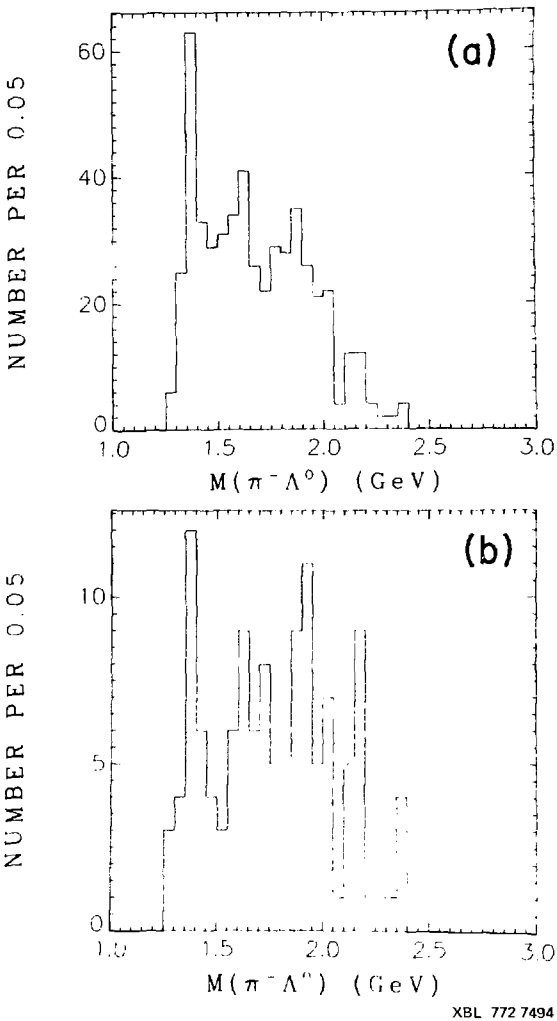
(a)
NUMBER PER 0.05
60
40
20
0
1.0
1.5
2.0
2.5
3.0
M(π⁻Λ°) (GeV)
(b)
NUMBER PER 0.05
10
5
0
1.0
1.5
2.0
2.5
3.0
M(π⁻Λ°) (GeV)
XBL 772 7494

Fig. 177

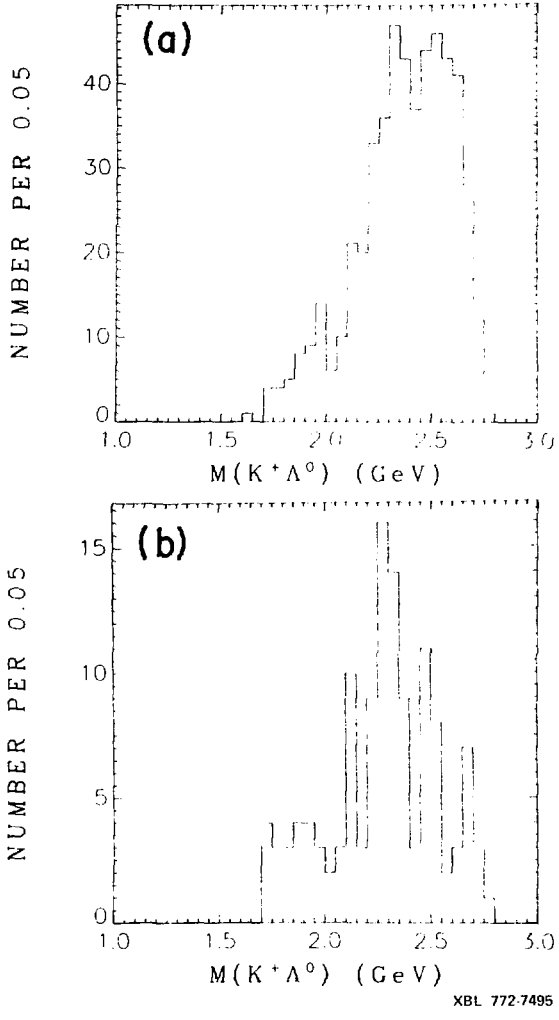
(a)
NUMBER PER 0.05
40
30
20
10
0
1.0
1.5
2.0
2.5
3.0
M(K⁺Λ⁰) (GeV)
(b)
NUMBER PER 0.05
15
10
5
0
1.0
1.5
2.0
2.5
3.0
M(K⁺Λ⁰) (GeV)
XBL 772-7495

Fig. 178

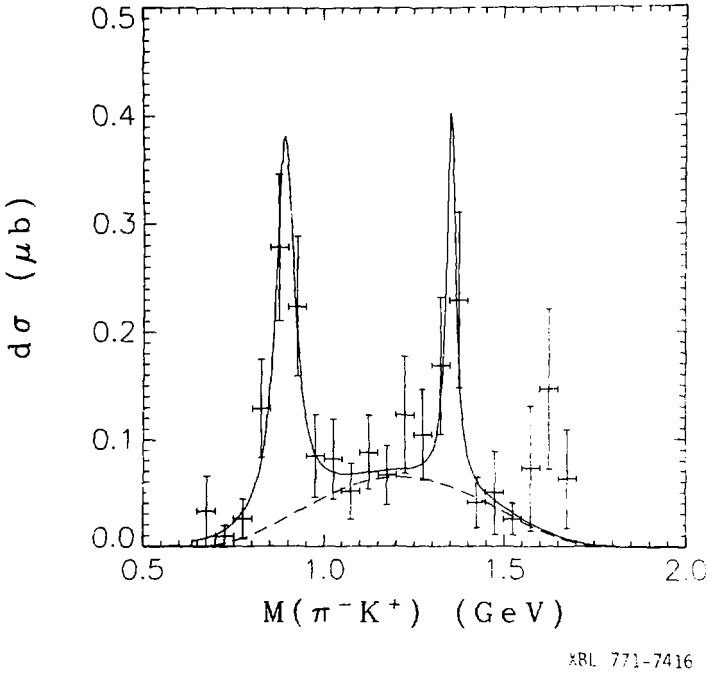

XBL 771-7416

Fig. 179

background term (represented by the dashed curve). The parameters obtained in the fit for the K^* are

$$M_{K^*} = 0.891 \text{ GeV}$$

$$\Gamma_{K^*} = 0.063 \text{ GeV}.$$

The mass is very close to the nominal value, and the width is only slightly greater, presumably due to resolution effects. A term was included in the fit to account for the enhancement at 1.35 GeV in order to minimize distortion of the K* parameters. The enhancement is of minimal statistical significance (approximately 2 standard deviations).

A background subtraction was made (for a signal region between 0.80 and 1.00 GeV in mass), and a Monte Carlo simulation was generated in order to correct for events lost because of poor trigger acceptance. This correction was found to be negligible over the interval $u' > -0.4$ GeV^2, and it was sufficient to correct the experimental data by the inverse of the trigger acceptance. The resulting differential cross section as a function of u' is shown in Fig. 180 along with data from Foley et al.[52] at 8 and 10.7 GeV/c and data from Fluri et al.[53] at 8 GeV/c. The data shown for this experiment is given in Table XXXVII. These data points include corrections for unobserved decay modes of both the K^* and the Λ^0 (a branching fraction of 0.642 into $p\pi^-$ is assumed).

In Fig. 181, a plot of the integrated cross section over the interval $u' > -0.2$ GeV^2 is shown for reaction (44) as a function of lab momentum. In addition to the data from this experiment, there is the data from Foley et al. and Fluri et al. All data points have statistical errors only. The straight line is a linear least squares fit (in log-log space) to the data points. The cross section is found to vary with lab momentum as

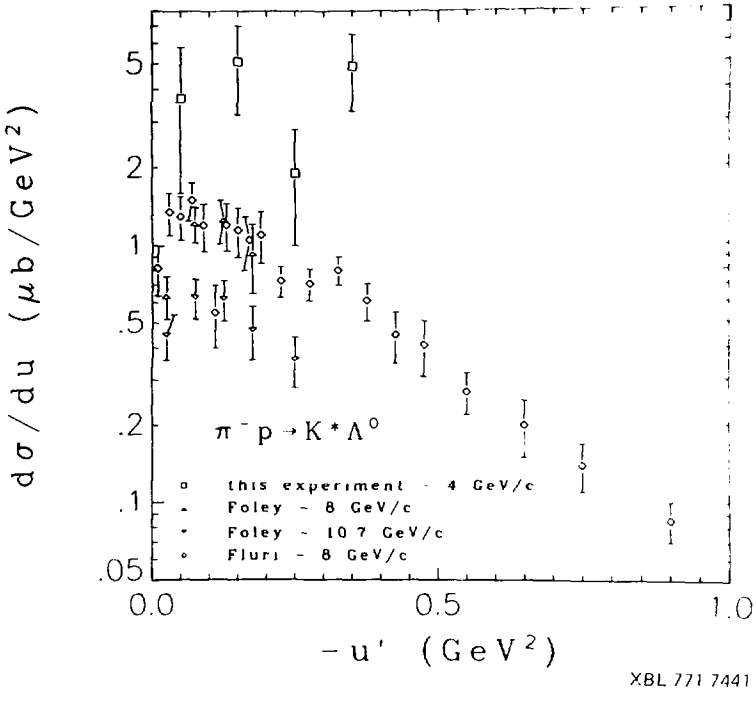
dσ/du (μb/GeV²)
5
2
1
.5
.2
.1
.05
0.0
0.5
1.0
−u' (GeV²)
π⁻p→K*Λ°
this experiment - 4 GeV/c
Foley - 8 GeV/c
Foley - 10.7 GeV/c
Fluri - 8 GeV/c
XBL 771 7441

Fig. 180

Table XXXVII. Differential cross section for $\pi^- p \to K^{*}\Lambda^{0}$ as a function of u'.

-u' (GeV^2)	Δu (GeV^2)	$d\sigma/du$ ($\mu b/GeV^2$)
0.05	0.10	3.7 ± 2.1
0.15	0.10	5.1 ± 1.9
0.25	0.10	1.9 ± 0.9
0.35	0.10	4.9 ± 1.6

Table XXXVIII. Average K^{*0} density matrix elements in the s-channel and u-channel helicity frames.

	UHF	SHF
ρ_{00}	0.55 ± 0.16	-0.01 ± 0.17
$Re(\rho_{10} - \rho_{0,-1})/2$	-0.10 ± 0.10	0.02 ± 0.08
$Im(\rho_{10} - \rho_{0,-1})/2$	-0.02 ± 0.11	-0.03 ± 0.08
$Re\ \rho_{1,-1}$	0.05 ± 0.14	-0.23 ± 0.14
$Im\ \rho_{1,-1}$	-0.09 ± 0.13	0.08 ± 0.17

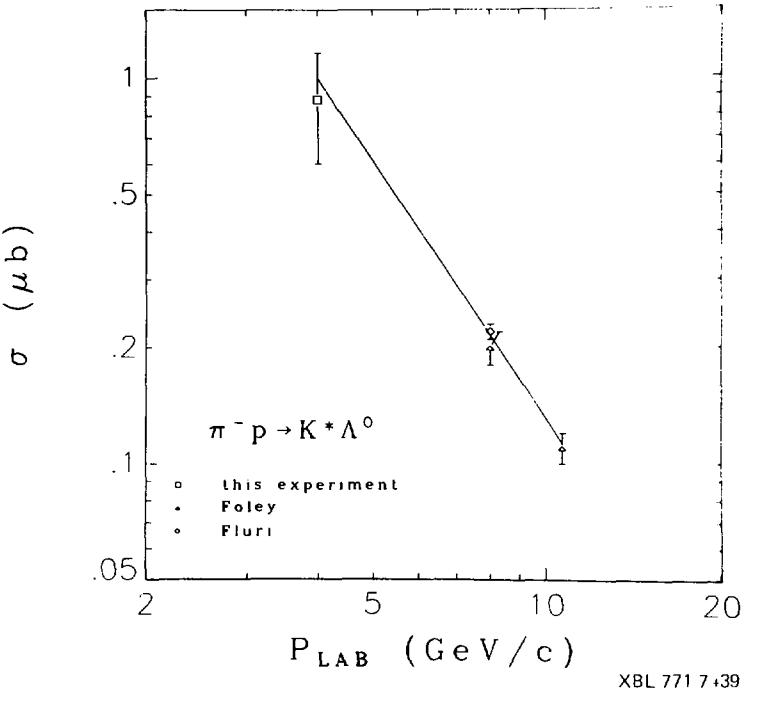
σ (μb)
1
.5
.2
.1
.05
2
5
10
20
P LAB (GeV/c)
π⁻p → K*Λ°
this experiment
Foley
Fluri
XBL 771 7439

Fig. 181

$$\sigma \propto P_{LAB}^{-(2.2 \pm 0.3)}.$$

The value of the exponent is consistent within errors with Regge expectations for Σ_α exchange.

An analysis of the K^* density matrix elements was done in the usual manner. However, contrary to the results of previous meson analyses discussed, the K^* density matrix elements seem to vary less as a function of u' when evaluated in the u-channel helicity frame than when evaluated in the s-channel helicity frame, although the errors are large. The resulting density matrix elements (averaged over the interval $u' > -0.4$ GeV^2) in both the u- and s-channel helicity frames are given in Table XXXVIII. It is observed that the s-channel helicity frame density matrix elements are quite consistent with the ρ^- s-channel helicity frame density matrix elements for events satisfying reaction (31).

4. Λ^0 polarization

In Table XXXIX is the Λ^0 polarization for all events with a fast forward Λ^0 (corrected up by the inverse of the trigger acceptance) as a function of the π^-K^+ invariant mass. Although the errors are large, it is clear that there is significant positive polarization in the region of the $K^*(892)$, whereas the polarization outside of this mass region is consistent with being zero or possibly slightly negative.

The Λ^0 polarization was examined for events in the background subtracted K^* peak as a function of u'. The results are shown in Table XL. The data is observed to be consistent with the data of Fluri et al. at 8 GeV/c, where the Λ^0 polarization is observed to be consistent with 1. at u'=0, dips to approximately 0. between u' = -0.10 and -0.15 GeV^2, and then rises to approximately 1. again.

Table XXXIX. Λ^0 polarization as a function of $\pi^- K^+$ invariant mass.

M (GeV)	ΔM (GeV)	Λ^0 polarization
0.70	0.20	-0.4 ± 0.9
0.90	0.20	1.1 ± 0.4
1.10	0.20	0.4 ± 0.6
1.30	0.20	-0.1 ± 0.4
1.50	0.20	-0.5 ± 1.2
1.70	0.20	-0.5 ± 1.2

Table XL. Λ^0 polarization as a function of u'.

u (GeV^2)	Δu (GeV^2)	Λ^0 polarization
0.05	0.10	3.2 ± 2.2
0.15	0.10	0.4 ± 1.0
0.25	0.10	0.4 ± 1.4
0.35	0.10	1.5 ± 0.9

VII. Conclusions

I have attempted to describe the results of this experiment in terms of a baryon exchange model. The clearest evidence for baryon exchange is observed in elastic scattering. The backward elastic differential cross section can be parameterized by

$$\frac{d\sigma}{du} \propto \sigma_T b e^{bu'},$$

where the total backward cross section is $\sigma_T = 5.47 \pm 0.91\mu b$ and the slope is $b = 3.77 \pm 0.43\ GeV^{-2}$. Comparison of this data with data at higher energies allows a determination of the energy dependence of the backward cross section:

$$\sigma_T \propto P_{LAB}^{-2.45 \pm 0.17}.$$

This energy dependence is consistent with expectations for delta Regge exchange.

Backward ρ production is observed in the final states $p\rho^-$ and $p\pi^-p'$. The ρ^- differential cross section as a function of u' displays an exponential falloff, indicative of baryon exchange. The measured cross section and slope are $\sigma_T = 8.2 \pm 1.9\mu b$ and $b = 3.9 \pm 1.2\ GeV^{-2}$. Comparison of this data with data at higher energies yields the energy dependence:

$$\sigma_T \propto P_{LAB}^{-2.33 \pm 0.28}.$$

This energy dependence is consistent with that of the elastic scattering cross section and with expectations for delta exchange.

On the other hand, although the ρ^0 production cross section in the backward region is considerably larger than the ρ^- cross section, it does not display the characteristic backward peaking expected for baryon

exchange processes. This behavior is partially explained by interference effects which appear to be taking place near u'=0, but a significant fraction of the cross section appears to result from processes other than a two-vertex, u-channel exchange process.

Backward ω^0 production is observed in the final state $p\pi^-\omega^0$. The differential cross section as a function of u' can be described in terms of a sharp peak (contained within the interval $u' > -0.05$ GeV^2) with cross section $\sigma_{peak} = 4.8 \pm 1.1\mu b$ superimposed on a flat term with cross section $\left\{\frac{d\sigma}{du}\right\}_{flat} = 61.3 \pm 7.4 \mu b/GeV^2$. Backward peaking is also observed in the $p\pi^- f^0$ and $p\pi^- \eta^0$ final states.

It is clear that the observed meson production cross sections are due, in part at least, to u-channel, baryon exchange processes. The two processes in which delta exchange is required, elastic scattering and ρ^- production, are observed to peak in the backward direction with slopes consistent with what is expected for baryon exchange. The processes which are allowed to go by nucleon exchange, e.g., ρ^0 and ω^0 production, have considerably larger cross sections than the delta exchange cross sections. However, the characteristic backward peak is either missing or superimposed on a large, roughly flat cross section component. Thus, one can not ascribe the entire backward cross section to nucleon exchange. A possible reason for the difference in structure between the delta exchange reactions and the nucleon exchange reactions is that the meson produced in a nucleon exchange reaction recoils against a $p\pi^-$ system rather than a single proton. The differences in structure can then be attributed to the differences between quasi two-body and quasi three-body processes.

No evidence for A_1 or A_2 production is observed in any channel. 95%

confidence level cross section upper limits for the final states pA_1^- and pA_2^- are $\sigma_{A_1^-} < 6.6\mu b$ and $\sigma_{A_2^-} < 7.6$ μb. Lack of evidence for A_1^- production is not very surprising in light of the fact that no A_2^- production is observed. The A_2^- cross section is expected to be comparable to the ρ^- cross section; hence, a cross section not too much lower than the upper limit established in this experiment is expected. Limits for A_1 and A_2 production in the final states $p\pi^- A^0_{1,2}$ and $p\pi^0 A^-_{1,2}$ are larger. (The 95% confidence level cross section upper limit for $p\pi^- A_2^0$ is 32μb.) Similarly, the final state pB^- is not observed and an upper limit of $\sigma_{B^-} < 4.6\mu b$ is found. Exotic meson production in the final states $p\pi^+ X^{--}$ and $p\pi^+\pi^0 X^{--}$ is not observed. Cross section upper limits (σ x B.R.) on the order of 5μb are found for the $\pi^-\pi^-$ and $\pi^-\pi^-\pi^0$ decay modes.

$\Delta(1232)$ and higher mass N* production is observed in many channels. The cross section for $\Delta^0(1232)\pi^0$ production is $\sigma = 7.5 \pm 2.4\mu b$ for the interval $u' > -0.4$ GeV^2. The differential cross section for $N^{*0}\pi^0$ production (where the N* consists of one or more resonances in the vicinity of 1.6 GeV which decay into $N\pi$) consists of a backward peak with $\sigma_{peak} = 17.6 \pm 5.1\mu b$ and slope $b = 8.9 \pm 3.7$ GeV^{-2} above a flat cross section component $\left(\frac{d\sigma}{du}\right)_{flat} = 43.2 \pm 6.8\mu b/\text{GeV}^2$. Considerable Δ^{++} production is observed in the 4- and 5-body final states. If resonance production is assumed to proceed via a single exchange in the u-channel, then Δ^{++} production can result only from exotic baryon exchange or from cascade decay of higher mass N* resonances. The data is inconsistent with either of these hypotheses.

In conclusion, the quasi two-body final states requiring delta exchange appear consistent with a u-channel, baryon exchange picture. The final states which can be produced via nucleon exchange are more complicated and lack the simple structure expected for baryon exchange reactions. These reactions (and the reactions producing Δ^{++}) indicate background from other processes such as 3-vertex diagrams or s-channel processes. In order to gain more information on baryon exchange processes, data should be taken at higher energy and with a π^+ beam. The advantage of taking data at higher energy (e.g., 8 GeV/c) is that s-channel effects are essentially eliminated and that kinematic overlap between different final states is reduced. The advantage of π^+p scattering is that simple final states (e.g., $p\rho^+$, $pA_{1,2}^+$) which might be of interest are allowed to go by nucleon exchange. If it is assumed that nucleon exchange couplings are larger than delta exchange couplings, then one would expect larger cross sections for these reactions than the corresponding π^-p reactions. π^+p scattering, however, requires a more sophisticated trigger than was used in this experiment to reject noninteracting beam particles.

A. Fitting Programs

In the analysis of the data from this experiment, two different types of fitting programs were utilized. To do most simple fits (e.g., fits involving fitting some functional form to a histogram), a program employing MINUIT[102] was used to perform least squares fits. The MINUIT package consists of a set of general purpose routines which can be used to find the minimum of a multiparameter function. This set of routines was used in conjunction with a routine to calculate the χ^2 deviation (the function to be minimized) of the experimental data from the theoretical expression as a function of the fit parameters. The definition of the χ^2 deviation is

$$\chi^2 = \sum_i \frac{[f(x_i) - y_i]^2}{\sigma_i^2},$$

where the summation in i varies over all the real data points (or histogram bins) and x_i and y_i are the abscissa and ordinate of real data point i. If a fit to a histogram is being made, y_i represents the number of weighted counts in the bin centered on x_i, $f(x_i)$ represents the value of the fitting expression at x_i. In order to insure accuracy in the fitting procedure when applied to histograms, the function $f(x_i)$ was numerically integrated over the domain of each bin (generally ten intervals were used in the integration). σ_i is the error associated with real data point i. For a histogram bin, this error is calculated as

$$\sigma^2 = \sum_n W_n^2,$$

where the summation in n varies over all the events falling into the histogram bin and W_n is the weight assigned to the event. In order to circumvent problems associated with empty bins, fits were only done over the domain

of x in which the bins were populated. When desired, a full error calculation was available in which each parameter was fixed at various values near the χ^2 minimum, and the remaining parameters fit to find a new minimum χ^2. When the new fit deviated from the original fit by one unit of χ^2, the error on the parameter in question was determined.

When a more complicated maximum likelihood fit was required which necessitated the generation of Monte Carlo events for normalization, the program OPTIME[103] was used in conjunction with the Monte Carlo event generator SAGE.[99] The OPTIME package consists of a set of routines specifically written to do maximum likelihood fitting. The expression for the logarithm of the likelihood which is to be maximized is

$$\ln(\mathcal{L}) = \sum_i n_i \ln(y(\xi_i)) - Y,$$

where

$$Y = \int y(\xi)\, d\xi .$$

The summation in i varies over all the real events. $y(\xi)$ is the distribution function to which the data is being fit. It is a function of the kinematic variables ξ and the fitting parameters (not explicitly shown). These kinematic variables consist of the final state invariant masses, momentum transfers, or whatever variables can be conveniently used to describe the distribution function. In a reaction producing an n-body final state, there are 3n-5 independent kinematic variables. n_i is the weight assigned to event i. It was set equal to 1 for all events in any fit discussed in this thesis. Y is the integral over all of the accepted phase space of the distribution $y(\xi)$. In order to determine this integral, SAGE was used to generate Monte Carlo events uniformly in phase space.

These events were corrected down by weighting each event by the acceptance as discussed in Ch. V. Any cuts which were imposed on the real data (e.g., eliminating events with small trigger acceptance, events in which a pion traversed the Cerenkov counter, and events in which the proton recoil system had poor geometric acceptance) were also imposed on the Monte Carlo event sample. The integral was proportional to the sum of the weighted probabilities (as determined by the distribution function).

This program is useful for doing multidimensional fits and fits in which the effects of acceptance must be included. It was utilized in the analysis of the 2-body and 3-body final states as described in Ch. VI. Independently of my development of this program, a similar program utilizing MINUIT was developed by my colleagues to do maximum likelihood fitting. It was applied to the 4- and 5-body final states.

B. Coordinate Systems

In order to be able to unambiguously compare the results of this experiment with those of other experiments, it is necessary to clearly specify the coordinate system employed when describing the decays of resonant systems. In all cases, except the Λ^{o} polarization, I describe the resonant spin state in terms of a helicity frame density matrix. For a meson system, the y-axis is defined as the production plane normal

$$\hat{y} = \frac{\bar{p}_B \times \bar{p}_{\pi^-}}{|\bar{p}_B \times \bar{p}_{\pi^-}|} ,$$

where

$\bar{p}_{\pi^-}$ = momentum of incoming pion beam

$\bar{p}_B$ = momentum of outgoing baryon system.

All momenta are defined in the rest frame of the meson system as shown in Fig. 182(a). The dashed line in the figure represents the exchanged particle.

Two commonly used helicity frames are the u-channel and the s-channel helicity frames. The u-channel helicity frame probably provides more insight into the spin properties of the exchanged trajectory while the s-channel helicity frame provides information more relevant to the resonance itself. In the u-channel helicity frame, the z-axis is defined to be

$$\hat{z} = - \frac{\bar{p}_p}{|\bar{p}_p|} ,$$

where

$\bar{p}_p$ = momentum of proton target.

The x-axis is constructed so as to give a right-handed coordinate system. In the s-channel helicity frame, the z-axis is defined to be

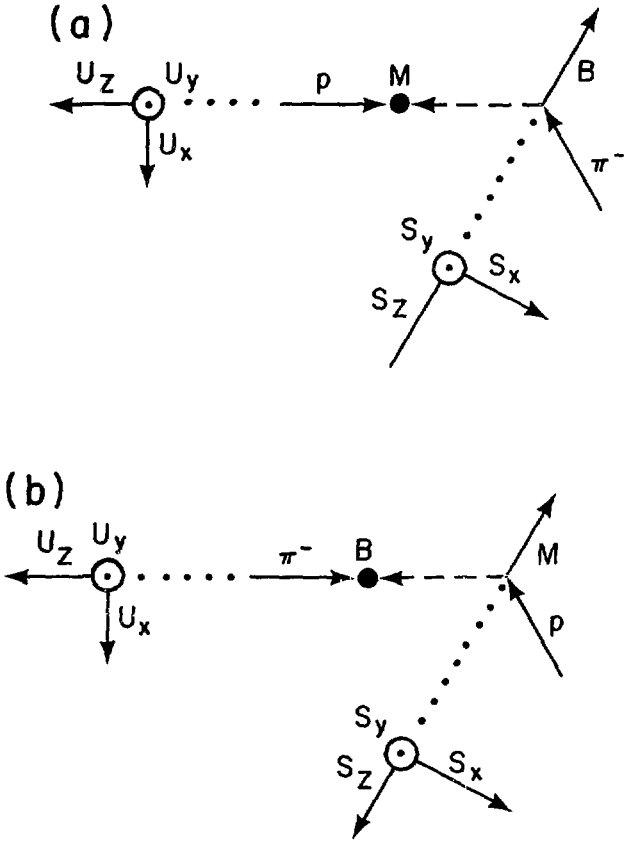

XBL 771-249

Fig. 182

$$\hat{z} = - \frac{\bar{p}_B}{|\bar{p}_B|}.$$

The coordinate systems are also shown in Fig. 182(a).

For a baryon system, the coordinate systems are similarly defined and are shown in Fig. 182(b). The y-axis is the same as that given above, but it can be rewritten as

$$\hat{y} = \frac{\bar{p}_\pi \times \bar{p}_M}{|\bar{p}_\pi \times \bar{p}_M|},$$

where

$\bar{p}_M$ = momentum of outgoing meson system.

The u-channel helicity frame z-axis is defined as

$$\hat{z} = - \frac{\bar{p}_\pi}{|\bar{p}_\pi|}$$

and the s-channel z-axis as

$$\hat{z} = - \frac{\bar{p}_M}{|\bar{p}_M|}.$$

For the Λ^0, the polarization is commonly defined in terms of a transversity frame in which the z-axis is the production plane normal,

$$\hat{z} = \frac{\bar{p}_\pi \times \bar{p}_M}{|\bar{p}_\pi \times \bar{p}_M|}.$$

C. Resonance Decay Angular Distributions

Expressions for decay angular distributions in terms of resonance production density matrix elements and expressions for density matrix elements in terms of expectation values of the spherical harmonics integrated over decay angular distributions are discussed in detail by Jackson.[104] The resonance decay angular distribution is given in terms of the production density matrix elements, for the decay $\gamma \to \alpha + \beta$, by the expression:

$$w(\theta,\phi) = \frac{2j+1}{4\pi} \left[\sum_{\lambda_\alpha,\lambda_\beta} |M(\lambda_\alpha,\lambda_\beta)|^2 \right]^{-1} \cdot$$

$$\cdot \sum_{\substack{\lambda_\alpha,\lambda_\beta \\ m,m'}} |M(\lambda_\alpha\lambda_\beta)|^2 \, D^{j*}_{m\lambda}(\phi,\theta,0) D^{j}_{m',\lambda}(\phi,\theta,0) \rho^{j}_{m\,m'} ,$$

where

θ = polar angle of α in γ rest frame

ϕ = azimuthal angle of α in γ rest frame

j = spin of γ

m, m' = components of spin along quantization axis

λ_α,λ_β = helicities of α and β

$M(\lambda_\alpha,\lambda_\beta)$ = decay amplitude

D^j = Wigner D function

ρ^j = production density matrix

$\lambda = \lambda_\alpha - \lambda_\beta$.

Note that the decay amplitude is a function only of the final helicity states.

If parity is conserved in the decay, the following relationship holds:

$$M(-\lambda_\alpha,-\lambda_\beta) = \eta_\alpha\eta_\beta\eta_\gamma(-1)^{j-s_\alpha-s_\beta} M(\lambda_\alpha,\lambda_\beta),$$

where

η_α, η_β, η_γ = intrinsic parities of α,β,γ

s_α, s_β = spins of α,β.

The density matrix satisfies certain requirements. Hermiticity requires that

$$\rho_{mm'} = \rho^*_{m'm}.$$

The normalization of the density matrix is defined by

$$Tr\rho = 1.$$

For the special case of a helicity frame (see Appendix B), if parity is conserved in the production of the resonant state, then

$$\rho_{mm'} = (-1)^{m-m'}\rho_{-m,-m'}.$$

The angular distribution can also be expressed in terms of multipole parameters:

$$w(\theta,\phi) = \frac{2j+1}{4\pi}\left[\sum_{\lambda_\alpha,\lambda_\beta}|M(\lambda_\alpha,\lambda_\beta)|^2 - 1\sum_{\substack{\lambda_\alpha,\lambda_\beta\\L,M}}|M(\lambda_\alpha,\lambda_\beta)|^2\right] \cdot$$

$$\cdot (-1)^{j-\lambda} <L0|jj\lambda-\lambda > t^*_{LM} Y_{LM}(\theta,\phi), \qquad (46)$$

where

L,M = multipole order

t_{LM} = multipole parameter

Y_{LM} = spherical harmonic.

Clebsch-Gordan coefficients are written in the form $< jm \mid j_1 j_2 m_1 m_2 >$ for the vector addition of $\bar{j} = \bar{j}_1 + \bar{j}_2$. The multipole parameters are related to the density matrix elements by

$$t^*_{LM} = \sum_{m,m'} < jm \mid jLm'M > \rho_{mm'} \tag{47}$$

$$\rho_{mm'} = \frac{1}{2j+1} \sum_{L,M} (2L+1) < jm \mid jLm'M > t^*_{LM}. \tag{48}$$

Corresponding to the hermiticity relation for the density matrix elements is the relation

$$t_{L,-M} = (-1)^M t^*_{LM}.$$

If parity is conserved in the resonance production.

$$t^*_{LM} = (-1)^L t_{LM}$$

in a helicity frame. Decay in a helicity frame will be assumed for the remainder of this appendix.

For the special cases of a meson decay into two spin 0 particles and a baryon decay into a spin 1/2 particle and a spin 0 particle, there is only one decay amplitude. For the meson decay case, Eq. (46) reduces to

$$w(\theta,\phi) = (-1)^j \frac{2j+1}{4\pi}^{\frac{1}{2}} \left[2 \sum_{\substack{L \text{ even} \\ M>0}} < L0 \mid jj00 > \mathrm{Re}(t_{LM}) \mathrm{Re}(Y_{LM}) \cdot \right.$$
$$\left. \cdot \sum_{L \text{ even}} < L0 \mid jj00 > t_{L0} Y_{L0} \right].$$

For the baryon decay case, Eq. (46) reduces to

$$w(\theta,\phi) = (-1)^{j-\frac{1}{2}} \frac{2j+1}{4\pi}^{\frac{1}{2}} \left[2 \sum_{\substack{L \text{ even} \\ M>0}} < L0 \mid jj \tfrac{1}{2} \; -\tfrac{1}{2} > \mathrm{Re}(t_{LM}) \mathrm{Re}(Y_{LM}) \cdot \right.$$
$$\left. \cdot \sum_{L \text{ even}} < L0 \mid jj \tfrac{1}{2} \tfrac{-1}{2} > t_{L0} Y_{L0} \right].$$

These expressions can be rewritten in terms of the density matrix elements by using Eq. (47). These expressions can be inverted by taking expectation values of the spherical harmonics integrated over the angular distribution. For meson decay

$$< Y_{LM} > = (-1)^j \left(\frac{2j+1}{4\pi}\right)^{\frac{1}{2}} < L0 \mid jj00 > t_{LM}.$$

For baryon decay

$$< Y_{LM} > = (-1)^{j-\frac{1}{2}} \left(\frac{2j+1}{4\pi}\right)^{\frac{1}{2}} < L0 \mid jj\ \tfrac{1}{2}\ -\tfrac{1}{2} > t_{LM}.$$

Using Eq. (48), the density matrix elements can be calculated in terms of the expectation values of the spherical harmonics.

Some explicit cases have been calculated and are presented here. For the decay of a spin 1 resonance, the angular distribution is given by

$$\begin{aligned} W(\theta,\phi) = {} & 0.0796 - 0.1262 < Y_{20} > \\ & - 0.3785\ \rho_{00} < Y_{20} > \\ & + 0.8740\ \mathrm{Re}\ \rho_{10} < \mathrm{Re}\ Y_{21} > - 0.6180\ \mathrm{Re}\rho_{1,-1} < \mathrm{Re}\ Y_{22} >. \end{aligned}$$

The density matrix elements are given in terms of the expectation values of the spherical harmonics in Table XLI. The special case of vector decay into three pseudoscalar mesons is also described by these results for a spin 1 decay, except that the angles θ and ϕ refer to the direction of the decay plane normal.

For a spin 2 meson decay, the decay angular distribution (ignoring the nondiagonal matrix elements) is given by

$$\begin{aligned} w(\theta,\phi) = {} & 0.0796 - 0.1802 < Y_{20} > + 0.0403 < Y_{40} > \\ & + 0.3604\ \rho_{00} < Y_{20} > + 0.2015\ \rho_{00} < Y_{40} > \\ & + 0.5407\ \rho_{11} < Y_{20} > - 0.4030\ \rho_{11} < Y_{40} >. \end{aligned}$$

Table XLI. Spin 1 density matrix elements in terms of expectation values of spherical harmonics.

$$\rho_{00} = 0.3333 + 2.6422 \langle Y_{20} \rangle$$

$$\mathrm{Re}(\rho_{10} - \rho_{0,-1})/2 = 2.2882 \langle \mathrm{Re}\ Y_{21} \rangle$$

$$\mathrm{Im}(\rho_{10} - \rho_{0,-1})/2 = -2.2882 \langle \mathrm{Im}\ Y_{21} \rangle$$

$$\mathrm{Re}(\rho_{1,-1}) = -3.2360 \langle \mathrm{Re}\ Y_{22} \rangle$$

$$\mathrm{Im}(\rho_{1,-1}) = 3.2360 \langle \mathrm{Im}\ Y_{22} \rangle$$

Table XLII. Spin 2 diagonal density matrix elements in terms of expectation values of spherical harmonics.

$$\rho_{00} = 0.2000 + 1.5853 \langle Y_{20} \rangle + 2.1269 \langle Y_{40} \rangle$$

$$(\rho_{1,1} + \rho_{-1,-1})/2 = 0.2000 + 0.7927 \langle Y_{20} \rangle - 1.4180 \langle Y_{40} \rangle$$

The diagonal density matrix elements are given in terms of the expectation values of the spherical harmonics in Table XLII.

For a spin 3/2 decay,

$$w(\theta,\phi) = 0.0796 - 0.1262 \langle Y_{20} \rangle + 0.5046\, \rho_{\frac{1}{2}\frac{1}{2}} \langle Y_{20} \rangle + 0.7136\, \mathrm{Re}\, \rho_{\frac{3}{2}\frac{1}{2}} \langle \mathrm{Re}\, Y_{21} \rangle - 0.7136\, \mathrm{Re}\, \rho_{\frac{3}{2}\,-\frac{1}{2}} \langle \mathrm{Re}\, Y_{22} \rangle .$$

The expressions for the density matrix elements are given in Table XLIII.

For a spin 5/2 decay,

$$\begin{aligned} w(\theta,\phi) = {} & 0.0796 - 0.1802 \langle Y_{20} \rangle + 0.0403 \langle Y_{40} \rangle \\ & + 0.6488\, \rho_{\frac{1}{2}\frac{1}{2}} \langle Y_{20} \rangle + 0.0806\, \rho_{\frac{1}{2}\frac{1}{2}} \langle Y_{40} \rangle \\ & + 0.4325\, \rho_{\frac{3}{2}\frac{3}{2}} \langle Y_{20} \rangle - 0.3224\, \rho_{\frac{3}{2}\frac{3}{2}} \langle Y_{40} \rangle \\ & + 0.7897\, \mathrm{Re}\rho_{\frac{5}{2}\frac{3}{2}} \langle \mathrm{Re}\, Y_{21} \rangle - 0.3221\, \mathrm{Re}\rho_{\frac{5}{2}\frac{3}{2}} \langle \mathrm{Re}\, Y_{41} \rangle \\ & + 0.4995\, \mathrm{Re}\rho_{\frac{3}{2}\frac{1}{2}} \langle \mathrm{Re}\, Y_{21} \rangle + 0.5097\, \mathrm{Re}\rho_{\frac{3}{2}\frac{1}{2}} \langle \mathrm{Re}Y_{41} \rangle \\ & - 0.5584\, \mathrm{Re}\rho_{\frac{5}{2}\frac{1}{2}} \langle \mathrm{Re}Y_{22} \rangle + 0.4836\, \mathrm{Re}\rho_{\frac{5}{2}\frac{1}{2}} \langle \mathrm{Re}Y_{42} \rangle \\ & - 0.7492\, \mathrm{Re}\rho_{\frac{3}{2}\,-\frac{1}{2}} \langle \mathrm{Re}Y_{22} \rangle - 0.3604\, \mathrm{Re}\rho_{\frac{3}{2}\,-\frac{1}{2}} \langle \mathrm{Re}Y_{42} \rangle \\ & - 0.6031\, \mathrm{Re}\rho_{\frac{5}{2}\,-\frac{1}{2}} \langle \mathrm{Re}Y_{43} \rangle + 0.6031\, \mathrm{Re}\rho_{\frac{5}{2}\,-\frac{3}{2}} \langle \mathrm{Re}Y_{44} \rangle . \end{aligned}$$

The density matrix elements are given in Table XLIV. Note that the imaginary parts of all density matrix combinations listed in Tables XLI-XLIV must vanish if parity is conserved.

Table XLIII. Spin 3/2 density matrix elements in terms of expectation values of spherical harmonics.

$$(\rho_{\frac{1}{2}\frac{1}{2}} + \rho_{-\frac{1}{2}-\frac{1}{2}})/2 = 0.2500 + 1.9817 \langle Y_{20} \rangle$$

$$\mathrm{Re}(\rho_{\frac{3}{2}\frac{1}{2}} - \rho_{-\frac{1}{2}-\frac{3}{2}})/2 = 2.8025 \langle \mathrm{Re}Y_{21} \rangle$$

$$\mathrm{Im}(\rho_{\frac{3}{2}\frac{1}{2}} - \rho_{-\frac{1}{2}-\frac{3}{2}})/2 = -2.8025 \langle \mathrm{Im}Y_{21} \rangle$$

$$\mathrm{Re}(\rho_{\frac{3}{2}-\frac{1}{2}} + \rho_{\frac{1}{2}-\frac{3}{2}})/2 = -2.8025 \langle \mathrm{Re}Y_{22} \rangle$$

$$\mathrm{Im}(\rho_{\frac{3}{2}-\frac{1}{2}} + \rho_{\frac{1}{2}-\frac{3}{2}})/2 = 2.8025 \langle \mathrm{Im}Y_{22} \rangle$$

Table XLIV. Spin 5/2 density matrix elements in terms of expectation values of spherical harmonics.

$$(\rho_{\frac{1}{2}\frac{1}{2}} + \rho_{-\frac{1}{2}-\frac{1}{2}})/2 = 0.1667 + 1.3211 \langle Y_{20} \rangle + 1.7725 \langle Y_{40} \rangle$$

$$(\rho_{\frac{3}{2}\frac{3}{2}} + \rho_{-\frac{3}{2}-\frac{3}{2}})/2 = 0.1667 + 0.3303 \langle Y_{20} \rangle - 2.6587 \langle Y_{40} \rangle$$

$$\mathrm{Re}(\rho_{\frac{5}{2}\frac{3}{2}} - \rho_{-\frac{3}{2}-\frac{5}{2}})/2 = 1.8090 \langle \mathrm{Re}Y_{21} \rangle - 1.7725 \langle \mathrm{Re}Y_{41} \rangle$$

$$\mathrm{Im}(\rho_{\frac{5}{2}\frac{3}{2}} - \rho_{-\frac{3}{2}-\frac{5}{2}})/2 = -1.8090 \langle \mathrm{Im}Y_{21} \rangle + 1.7725 \langle \mathrm{Im}Y_{41} \rangle$$

$$\mathrm{Re}(\rho_{\frac{3}{2}\frac{1}{2}} - \rho_{-\frac{1}{2}-\frac{3}{2}})/2 = 1.1441 \langle \mathrm{Re}Y_{21} \rangle + 2.8025 \langle \mathrm{Re}Y_{41} \rangle$$

$$\mathrm{Im}(\rho_{\frac{3}{2}\frac{1}{2}} - \rho_{-\frac{1}{2}-\frac{3}{2}})/2 = -1.1441 \langle \mathrm{Im}Y_{21} \rangle - 2.8025 \langle \mathrm{Im}Y_{41} \rangle$$

$$\mathrm{Re}(\rho_{\frac{5}{2}\frac{1}{2}} + \rho_{-\frac{1}{2}-\frac{5}{2}})/2 = -1.2792 \langle \mathrm{Re}Y_{22} \rangle + 2.6587 \langle \mathrm{Re}Y_{42} \rangle$$

$$\mathrm{Im}(\rho_{\frac{5}{2}\frac{1}{2}} + \rho_{-\frac{1}{2}-\frac{5}{2}})/2 = 1.2792 \langle \mathrm{Im}Y_{22} \rangle - 2.6587 \langle \mathrm{Im}Y_{42} \rangle$$

$$\mathrm{Re}(\rho_{\frac{3}{2}-\frac{1}{2}} + \rho_{\frac{1}{2}-\frac{3}{2}})/2 = -1.7162 \langle \mathrm{Re}Y_{22} \rangle - 1.9817 \langle \mathrm{Re}Y_{42} \rangle$$

$$\mathrm{Im}(\rho_{\frac{3}{2}-\frac{1}{2}} + \rho_{\frac{1}{2}-\frac{3}{2}})/2 = 1.7162 \langle \mathrm{Im}Y_{22} \rangle + 1.9817 \langle \mathrm{Im}Y_{42} \rangle$$

$$\mathrm{Re}(\rho_{\frac{5}{2}-\frac{1}{2}} - \rho_{\frac{1}{2}-\frac{5}{2}})/2 = -3.3160 \langle \mathrm{Re}Y_{43} \rangle$$

$$\mathrm{Im}(\rho_{\frac{5}{2}-\frac{1}{2}} - \rho_{\frac{1}{2}-\frac{5}{2}})/2 = 3.3160 \langle \mathrm{Im}Y_{43} \rangle$$

$$\mathrm{Re}(\rho_{\frac{5}{2}-\frac{3}{2}} + \rho_{\frac{3}{2}-\frac{5}{2}})/2 = 3.3160 \langle \mathrm{Re}Y_{44} \rangle$$

$$\mathrm{Im}(\rho_{\frac{5}{2}-\frac{3}{2}} + \rho_{\frac{3}{2}-\frac{5}{2}})/2 = -3.3160 \langle \mathrm{Im}Y_{44} \rangle$$

D. Stodolsky-Sakurai Model

The Stodolsky-Sakurai model[105] has been successful in predicting the Δ^{++} decay angular distribution (but not the u distribution) in the reaction[106, 107]

$$\pi^+ p \to \pi^o \Delta^{++}.$$

This reaction is assumed to result from the exchange of a ρ in the t-channel. The model is based on the assumption that the exchanged ρ behaves as if it were an M1 photon transition between the Δ^{++} and the proton states. In this experiment, the reaction

$$\pi^- p \to p\rho^-$$

is examined. If this reaction is assumed to result from the exchange of a Δ^{++} in the u-channel, the same $\rho\Delta p$ vertex appears in the u-channel exchange diagram for this reaction as was present in the t-channel exchange diagram for the Δ^{++} production reaction above. If it is assumed that the ρ produced at this vertex behaves like an M1 photon, even when the Δ^{++} is taken far off the mass-shell and the ρ is on the mass-shell, then a prediction can be made for the ρ^- density matrix elements.[108]

Let the amplitudes T_{LM} be the amplitudes for a multipole transition of order (L,M). For an M1 transition, the requirement of parity conservation yields only one independent amplitude:

$$T_{11} = -T_{1,-1} = T$$

$$T_{10} = 0.$$

Helicity amplitudes can be constructed in terms of these multipole amplitudes. The amplitudes are defined in the u-channel helicity frame where the Δ^{++} and the proton are collinear (the same configuration as was used in the original model). Factorization is assumed and the other vertex ($\pi\Delta p$) is

ignored.

$$H^{M}_{\lambda_N} = \sum_{L,M} (2L+1) \langle \tfrac{3}{2} \lambda_\Delta | \tfrac{1}{2} L \lambda_N - M \rangle T_{LM},$$

where

$H^{M}_{\lambda_N}$ = helicity amplitude

λ_Δ = delta helicity

λ_N = nucleon (target proton) helicity

$M = \rho^-$ helicity.

Note that $\lambda_\Delta = \lambda_N - M$. If only M1 transitions are considered, the only non-zero helicity amplitudes are:

$$H^{1}_{\frac{1}{2}} = \sqrt{3}\, T$$

$$H^{-1}_{-\frac{1}{2}} = -\sqrt{3}\, T$$

$$H^{-1}_{\frac{1}{2}} = -\,3\, T$$

$$H^{1}_{-\frac{1}{2}} = 3\, T.$$

The ρ^- density matrix elements can be constructed from these amplitudes using the expression

$$\rho_{M,M'} = \frac{\sum_{\lambda_N} H^{M}_{\lambda_N} H^{M'*}_{\lambda_N}}{\sum_{\lambda_N,M} |H^{M}_{\lambda_N}|^2}.$$

Inserting the expressions for the helicity amplitudes, the predictions for the density matrix elements are:

$$\rho_{00} = 0.$$

$$\rho_{10} = 0.$$

$$\rho_{1,-1} = -\sqrt{3}/4 \simeq -\,0.43.$$

References

1. V. D. Barger, D. B. Cline, Phenomenological Theories of High Energy Scattering, W. A. Benjamin, Inc. (1969).
2. V. Barger, D. Cline, Phys. Rev. Lett. 21, 392 (1968).
3. J. K. Storrow, G. A. Winbow, Nucl. Phys. B53, 62 (1973).
4. V. Barger, Phys. Rev. 179, 1371 (1969).
5. V. Barger, D. Cline, J. Matos, Phys. Lett. 29B, 121 (1969).
6. S. W. Kormanyos, A. D. Krisch, J. R. O'Fallon, K. Ruddick, Phys. Rev. Lett. 16, 709 (1966).
7. S. W. Kormanyos, A. D. Krisch, J. R. O'Fallon, K. Ruddick, L. G. Ratner, Phys. Rev. 164, 1661 (1967).
8. E. S. Meanley, R. W. Anthony, C. T. Coffin, J. E. Rice, N. R. Stanton, K. M. Terwilliger, Phys. Rev. D 6, 740 (1972).
9. C. T. Coffin, N. Dikmen, L. Ettlinger, D. Meyer, A. Saulys, K. Terwilliger, D. Williams, Phys. Rev. 159, 1169 (1967).
10. R. R. Crittenden, K. F. Galloway, R. M. Heinz, H. A. Neal, R. A. Sidwell, Phys. Rev. D 1, 3050 (1970).
11. J. P. Baton, G. Laurens, Nucl. Phys. B21, 551 (1970).
12. A. Brabson, G. Calvelli, S. Cittolin, P. DeGuio, F. Gasparini, S. Limentani, P. Mittner, M. Posocco, L. Ventura, C. Voci, M. Crozon, A. Diaczek, R. Sidwell, J. Tocqueville, Phys. Lett. 42B, 283 (1972).
13. E. W. Hoffman, R. L. Dixon, J. M. Fletcher, A. F. Garfinkel, F. J. Loeffler, S. Mudrak, E. I. Shibata, K. C. Stanfield, Y. W. Tang, Phys. Rev. Lett. 35, 138 (1975).

14. O. N. Baloshin, V. V. Vladimirskii, I. A. Dukhovskoi, V. V. Kishkurno, A. P. Krutenkova, V. V. Kulikov, E. S. Nikolaevskii, V. N. Petrukhin, S. A. Radkevich V. S. Fedorets, Yad. Fiz. 14, 131 (1971) [Sov. J. Nucl. Phys. 14, 74 (1972)].

15. E. W. Anderson, E. J. Blesser, H. R. Blieden, G. B. Collins, D. Garelick, J. Menes, F. Turkot, D. Birnbaum, R. M. Edelstein, N. C. Hien, T. J. McMahon, J. Mucci, J. Russ, Phys. Rev. Lett. 20, 1529 (1968).

16. W. F. Baker, D. P. Eartly, K. P. Pretzl, S. M. Pruss, A. A. Wehmann, P. Koehler, A. J. Lennox, J. A. Poirier, C. A. Rey, O. R. Sander, Phys. Rev. Lett. 32, 251 (1974).

17. D. J. Schotanus, C. L. Pols, D. Z. Toet, R. T. Van de Walle, J. V. Major, G. E. Pearson, B. Chaurand, R. Vanderhaghen, G. Rinaudo, A. E. Werbrouck, Nucl. Phys. B22, 45 (1970).

18. W. F. Baker, P. J. Carlson, V. Chabaud, A. Lundby, J. Banaigs, J. Berger, C. Bonnel, J. Duflo, L. Goldzahl, G. Plouin, Phys. Lett. 25B, 361 (1967).

19. J. Banaigs, J. Berger, C. Bonnel, J. Duflo, L. Goldzahl, F. Plouin, W. F. Baker, P. J. Carlson, V. Chabaud, A. Lundby, Nucl. Phys. B8, 31 (1968).

20. W. F. Baker, P. J. Carlson, V. Chabaud, A. Lundby, J. Banaigs, J. Berger, C. Bonnel, J. Duflo, L. Goldzahl, F. Plouin, Nucl. Phys. B9, 249 (1969).

21. W. F. Baker, P. J. Carlson, V. Chabaud, A. Lundby, E. G. Michaelis, J. Banaigs, J. Berger, C. Bonnel, J. Duflo, R. Goldzahl, F. Plouin, Phys. Lett. 23, 605 (1966).

22. H. Brody, R. Lanza, R. Marshall, J. Niederer, W. Selove, M. Shochet, R. Van Berg, Phys. Rev. Lett. 16, 828 (1966).

23. J. Orear, R. Rubinstein, D. B. Scarl, D. H. White, A. D. Krisch, W. R. Frisken, A. L. Read, H. Ruderman, Phys. Rev. 152, 1162 (1966).

24. A. Ashmore, C. J. S. Damerell, W. R. Frisken, R. Rubinstein, J. Orear, D. P. Owen, F. C. Peterson, A. L. Read, D. G. Ryan, D. H. White, Phys. Rev. Lett. 19, 460 (1967).

25. J. Orear, D. P. Owen, F. C. Peterson, A. L. Read, D. G. Ryan, D. H. White, A. Ashmore, C. J. S. Damerell, W. R. Frisken, R. Rubinstein, Phys. Rev. Lett. 21, 389 (1968).

26. D. P. Owen, F. C. Peterson, J. Orear, A. L. Read, D. G. Ryan D. H. White, A. Ashmore, C. J. S. Damerell, W. R. Frisken, R. Rubinstein, Phys. Rev. 181, 1794 (1969).

27. V. D. Antopolsky, G. L. Bayatyan, E. V. Brakhman, G. P. Eliceev, N. E. Emelyanov, Yu. V. Galaktionov, Yu. V. Gorodkov, L. G. Landsberg, N. N. Lugetsky, V. A. Lyubimov. I. V. Sidorov, F. A. Yetch, O. Ya. Zeldovich, Phys. Lett. 28B, 223 (1968).

28. V. Kistiakowsky, R. K. Yamamoto, R. D.Klem, P. Marcato, I. A. Pless, I. Spirn, E. G. Anelli, C. N. De Marzo, A. Romano, D. G. Crabb, A. C. Meyers, III, J. R. O'Fallon, Phys. Rev. Lett. 22, 618 (1969).

29. R. C. Chase, E. Coleman, H. W. J. Courant, E. Marquit, E. W. Petraske, H. F. Romer, K. Ruddick, Phys. Rev. D 2, 2588 (1970)

30. J. Schneider, V. Lepeltier, P. Bonamy, P. Borgeaud, O. Guisan, P. Sonderegger, Phys. Rev. Lett. 23, 1068 (1969).

31. J. P. Boright, D. R. Bowen, D. E. Groom, J. Orear, D. P. Owen, A. J. Pawlicki, D. H. White, Phys. Lett. 33B, 615 (1970).

32. J. P. Boright, D. R. Bowen, D. E. Groom, J. Orear, D. P. Owen, A. J. Pawlicki, D. H. White, Phys. Rev. Lett. 24, 964 (1970)

33. V. V. Vladimirskii, R. I. Dzhelyadin, I. A. Dukhovskoi, V. V. Kishkurno, A. P. Krutenkova, V. V. Kulikov. I. A. Radkevich, V. S. Fedorets, Yad. Fiz. 17, 788 (1973) [Sov. J. Nucl. Phys. 17, 411 (1973)].

34. R. C. Chase, E. Coleman, H. W. J. Courant, E. Marquit, E. W. Petraske, H. F. Romer, K. Ruddick, Phys. Lett. 30B, 659 (1969).

35. R. Anthony, C. T. Coffin, E. Meanley, J. Rice, N. Stanton, K. Terwilliger, Phys. Rev. Lett. 21, 1605 (1968).

36. J. E. Rice, R. W. Anthony, C. T. Coffin, E. S. Meanley, K. M. Terwilliger, N. R. Stanton, Phys. Rev. Lett. 27, 687 (1971).

37. S. Hagopian, V. Hagopian, E. Bogart, R. O'Donnell, W. Selove, Phys. Rev. Lett. 24, 1445 (1970).

38. T. Buhl, D. Cline, University of Wisconsin report (1971).

39. P. B. Johnson, J. A. Poirier, N. N. Biswas, N. M. Cason, T. H. Groves, V. P. Kenney, J. T. McGahan, W. D. Shephard, L. J. Gutay, J. H. Campbell, R. L. Eisner, F. J. Loeffler, R. E. Peters, R. J. Sahni, W. L. Yen, I. Derado, G. T. Guiragossian, Phys. Rev. 176, 1651 (1968).

40. E. W. Anderson, E. J. Bleser, H. R. Blieden, G. B. Collins, D. Garelick, J. Menes, F. Turkot, D. Birnbaum, R. M. Edelstein N. C. Hien, T. J. McMahon, J. Mucci, J. Russ, Phys. Rev. Lett. 22, 102 (1969).

41. E. W. Anderson, E. J. Bleser, H. R. Blieden, G. B. Collins, D. Garelick, J. Menes, F. Turkot, D. Birnbaum, R. M. Edelstein, N. C. Hien, T. J. McMahon, J. Mucci, J. Russ, Phys. Rev. Lett. 22, 1390 (1969)

42. A. Abashian, N. Beamer, A. Bross, B. Eisenstein, N. Gelfand, J. D. Hansen, W. Mollet, G. R. Morris, B. Nelson, T. O'Halloran, J. R. Orr, D. Rhines, P. Schultz, P. Sokolsky, R. G. Wagner, J. Watson, M. Buttram, Phys. Rev. Lett. 34, 691 (1975).

43. A. Abashian, B. Eisenstein, J.D. Hansen, W. Mollet, G. R. Morris, B. Nelson, T. O'Halloran, J. R. Orr, D. Rhines, P. Schultz, P. Sokolsky, R. G. Wagner, J. Watson, N. M. Gelfand, M. Buttram, Phys. Rev. D 13, 5 (1976).

44. C. L. Pols, D. J. Schotanus, D. Z. Toet, R. T. Van de Walle, K. Bockmann, K. Sternberger, B. Vagini, G. Winter, J. V. Major, E. Cirba, R. Vanderhaghen, G. Rinaudo, A. Werbrouck, Nucl. Phys. B25, 109 (1970).

45. P. J. Carlson, P. Fleury, A. Lundby, S. Mukhin, J. Myrheim, Phys. Lett. 33B, 502 (1970).

46. D. Cline, J. English, R. Terrell, W. Wilke, B. Chaudhary, H. Courant, E. Marquit, K. Ruddick, Phys. Rev. Lett. 23, 491 (1969).

47. M. J. Emms, J. B. Kinson, B. J. Stacey, M. F. Votruba, P. L. Woodworth, I. G. Bell, M. Dale, D. Evans, J. V. Major, K. Neat, J. A. Charlesworth, R. L. Sekulin, Phys. Lett. 51B, 195 (1974).

48. S. Dado, A. Engler, R. W. Kraemer, S. Toaff, F. Weisser, J. Diaz, F. Dibianca, W. Fickinger, D. K. Robinson, Phys. Lett. 50B, 275 (1974).

49. W. Beusch, A. Michelini, D. Websdale, W. E. Fischer, R. Frosch, P. Muhlemann, M. Pepin, E. E. Polgar, J. Codling, M. G. Green, Nucl. Phys. B19, 546 (1970).

50. P. Astbury, J. Gallivan, J. Jafar, M. Letheren, W. Steiner, J. A. Wilson, W. Beusch, M. Borghini, D. Websdale, L. Fluri, K. Freudenreich, F. X. Gentit, W. Wetzel, P. le Du, O. Guisan, Nucl. Phys. B99, 30 (1975).

51. M. Pepin, W. Beusch, W. E. Fischer, E. E. Polgar, R. Bowen, G. Brautti, A. Michelini, P. Astbury, D. Websdale, Phys. Lett. 26B, 35 (1967).

52. K. J. Foley, W. A. Love, S. Ozaki, E. D. Platner, A. C. Saulys, E. H. Willen, S. J. Lindenbaum, M. A. Kramer, Phys. Rev. D 10, 2763 (1974).

53. L. Fluri, H. Brundiers, R. Hartung, K. Runge, O. Schaile, C. Weber, F. Brun, G. Carles, M. Cribier, J. R. Hubbard, G. Laurens, L. Moscoso, A. Muller, S. Zylberajch, presented at the International Conference on Elementary Particles, Palermo, Italy (1975).

54. G. Goldhaber, J. L. Brown, S. Goldhaber, J. A. Kadyk, B. C. Shen, G. H. Trilling, Phys. Rev. Lett. 12, 336 (1964).

55. M. Aderholz, . Bondar, W. Brauneck, H. Lengeler, C. Thoma, C. Grote, H. Kaufmann, K. Lanius, R. Leiste, R. Pose, D. C. Colley, W. P. Dodd, B. Musgrave, J. Simmons, K. Bockmann, J. Moebes, B. Nellen, E. Paul, G. Winter, V. Blobel, H. Butenschon, P. von Handel, P. Schilling, G. Wolf, E. Lohrmann, J. M. Brownlee, I. Butterworth, F. Campayne, M. Ibbotson, M. Saeed, N. N. Biswas, K. H. Goihl, D. Luers, N. Schmitz, J. Weigl, Phys. Lett. 10, 226 (1964).

56. T. G. Trippe, A. Barbaro-Galtieri, R. L. Kelly, A. Rittenberg, A. H. Rosenfeld, G. P. Yost, N. Barash-Schmidt, C. Bricman, R. J. Hemingway, M. J. Losty, M. Roos, V. Chaloupka, B. Armstrong, Rev. Mod. Phys. 48, S1 (1976).

57. D. J. Herndon, P. Soding, R. J. Cashmore, Phys. Rev. D 11, 3165 (1975).

58. G. Ascoli, D. V. Brockway, L. Eisenstein, M. L. Ioffredo, U. E. Kruse, P. F. Schultz, C. Caso, G. Tomasini, P. von Handel, P. Schilling, G. Costa, S. Ratti, P. Daronian, L. Mosca, A. E. Brenner, W. C. Harrison, D. Heyda, W. H. Johnson, Jr., J. K. Kim, M. E. Law, J. E. Mueller, B. M. Salzberg, L. K. Sisterson,

T. F. Johnston, J. D. Prentice, N. R. Steenberg, T. S. Yoon, J. T. Carroll, A. R. Erwin, R. Morse, B. Y. Oh, W. Robertson, W. D. Walker, Phys. Rev. Lett. 26, 929 (1971).

59. G. Ascoli, D. V. Brockway, H. B. Crawley, L. B. Eisenstein, R. W. Hanft, M. L. Ioffredo, U. E. Kruse, Phys. Rev. Lett. 25, 962 (1970).

60. Y. M. Antipov, G. Ascoli, R. Busnello, M. N. Kienzle-Focacci, W. Kienzle, R. Klanner, A. A. Lebedev, P. Lecomte, V. Roinishvili, A. Weitsch, F. A. Yotch, Nucl. Phys. B63, 153 (1973).

61. G. Otter, G. Rudolf, H. Wieczorek, H. Bottcher, W. D. Nowack, K. Bockmann, H. Plothow, V. T. Cocconi, M. J. Counihan, J. D. Hansen, A. Kotanski, D. R. O. Morrison, D. Sotiricu, R. Stroynowski, H. Wahl, T. Hirose, E. Leitner, Nucl. Phys. B80, 1 (1974).

62. R. T. Deck, Phys. Rev. Lett. 13, 169 (1964).

63. E. L. Berger, Phys. Rev. 166, 1525 (1968).

64. G. Ascoli, L. M. Jones, B. Weinstein, H. W. Wyld, Jr., Phys. Rev. D 8, 3894 (1973).

65. M. G. Bowler, M. A. V. Game, I. J. R. Aitchison, J. B. Dainton, Nucl. Phys. B97, 227 (1975).

66. M. J. Emms, G. T. Jones, J. B. Kinson, B. J. Stacey, M. F. Votruba, P. L. Woodworth, I. G. Bell, M. Dale, J. V. Major, J. A. Charlesworth, D. J. Crennell, R. L. Sekulin, Phys. Lett. 60B, 109 (1975).

67. F. Wagner, M. Tabak, D. M. Chew, LBL - 3395 (1974).

68. F. Wagner, M. Tabak, D. M. Chew, Phys. Lett. 58B, 201 (1975).

69. G. L. Kane, in Proceedings of the Tenth Rencontre de Moriond, Meribel - les - Allues, France, 1975, edited by J. Tran Thanh Van, p. 337.

70. G. L. Kane, University of Michigan, private communication.

71. G. W. Brandenburg, R. K. Carnegie, R. J. Cashmore, M. Davier, W. M. Dunwoodie, T. A. Lasinski, D. W. G.S. Leith, J. A. J. Matthews, P. Walden, S. H. Williams, F. C. Winkelmann, Phys. Rev. Lett. 36, 703 (1976).

72. G. W. Brandenburg, R. K. Carnegie, R. J. Cashmore, M. Davier, W. M. Dunwoodie, T. A. Lasinski, D. W. G. S. Leith, J. A. J. Matthews, P. Walden, S. H. Williams, F. C. Winkelmann, Phys. Rev. Lett. 36, 706 (1976).

73. J. L. Basdevant, E. L. Berger, Phys. Rev. Lett. 37, 977 (1976).

74. G. H. Trilling, LBL - 5535, presented at the Summer Institute on Particle Physics, SLAC, Stanford, Ca. (1976).

75. H. Harari, Phys. Rev. Lett. 22, 562 (1969).

76. J. L. Rosner, Phys. Rev. Lett. 22, 689 (1969).

77. P. G. O. Freund, R. Waltz, J. Rosner, Nucl. Phys. B13, 237 (1969).

78. J. L. Rosner, Phys. Rev. Lett. 21, 950, 1468 (E) (1968).

79. J. Mandula, C. Rebbi, R. Slansky, J. Weyers, G. Zweig, Phys. Rev. Lett. 22, 1147 (1969).

80. H. J. Lipkin, Phys. Rev. D 7, 2262 (1973).

81. M. Jacob, J. Weyers, Nuovo Cimento 69A, 521 (1970), 70A, 285 (E) (1970).

82. M. A. Abolins, O. I. Dahl, J. Danburg, D. Davies, P. Hoch, D. H. Miller, R. Rader, J. Kirz, Phys. Rev. Lett. 22, 427 (1969).

83. D. J. Crennell, H. A. Gordon, K. W. Lai, J. Louie, J. M. Scarr, W. H. Sims, Phys. Rev. Lett. 26, 1280 (1971).

84. C. W. Akerlof, P. K. Caldwell, C. T. Coffin, P. Kalbaci, D. I. Meyer, P. Schmueser, K. C. Stanfield, Phys. Rev. Lett. 27, 539 (1971).

85. H. W. Atherton, L. M. Celnikier, B. R. French, B. Ghidini, L. Mandelli, J. P. Moebes, E. Quercigh, Phys. Lett. 42B, 522 (1972).

86. G. Yekutieli, D. Yaffe, S. Toaff, A. Shapira, E. E. Ronat, U. Karshon, B. Haber, Y. Eisenberg, Phys. Rev. Lett. 25, 184 (1970).

87. K. Igi, T. Eguchi, Phys. Lett. 42B, 449 (1972).

88. E. L. Berger, R. A. Morrow, Phys. Rev. Lett. 25, 1136 (1970).

89. D. Cohen, in Proceedings of the Fourth International Conference on Experimental Meson Spectroscopy, April 26-27, 1974, AIP, edited by D. Garelick.

90. B. B. Brabson, in Proceedings of Williamsburg Meeting, Sept. 5-7, 1974, AIP, edited by C. E. Carlson.

91. M. S. Alam, B. B. Brabson, K. Galloway, R. Mercer, N. V. Baggett, E. C. Flowler, M. L. Huebschman, A. E. Kreymer, A. H. Rogers, C. Baglin, J. Hanlon, R. Kamat, R. Panvini, E. Petraske, S. Stone, J. Waters, M. Webster, Phys. Lett. 53B, 207 (1974).

92. J. Mellema, UCLA High Energy Group Notes, Memo No. HC 141 (1971).

93. H. C. Albrecht, E. P. Binnall, R. W. Birge, M. H. Myers, P. W. Weber, UCRL - 18528 (1968).

94. F. T. Solmitz, A. D. Johnson, T. B. Day, Group A Programming Note No. P-117 (1966).

95. M. A. Garjnost, Group A Programming Note No. P-239 (1974).

96. O. I. Dahl, T. B. Day, F. T. Solmitz, N. L. Gould, Group A Programming Note No. P-126 (1968).

97. D. B. Chelton, D. B. Mann, UCRL - 3421 (1956).

98. Bevatron Experimenters Handbook, UCRL - 17333 (1972).

99. J. Friedman, Group A Programming Note No. P-189 (1971).

100. M. Roos, Phys. Lett. 36B, 130 (1971).

101. M. Roos, Nucl. Phys. B77, 420 (1974).

102. F. James, M. Roos, Cern Computer 7600 Interim Program Library D-516 (1971).

103. P. H. Eberhard, W. O. Koellner, UCRL - 20159 (1970), UCRL - 20160 (1971).

104. J. D. Jackson, Proc. Les Houches Summer School of Theoretical Physics, Ed. C. DeWitt, M. Jacob, Gordon and Breach Science Publishers, Inc. (1965).

105. L. Stodolsky, J. J. Sakurai, Phys. Rev. Lett. 11, 90 (1963).

106. J. Bartsch, M. Deutschmann, K. Eickel, H. Lengeler, Ch. Thoma, H. Kaufmann, U. Kundt, K. Lanius, R. Leiste, R. Pose, D. C. Colley, W. P. Dodd, B. Musgrave, J. Simmons, D. Hohne, E. Paul, V. Blobel, H. Butenschon, P. von Handel, P. Schilling, G. Wolf, J. M. Brownlee, I. Butterworth, F. Campayne, M. Ibbotson, M Saeed, N. N. Biswas, N. Schmitz, J. Weigl , Phys. Lett. 10, 229 (1964).

107. G. Gidal, G. Borreani, D. Grether, F. Lott, R. W. Birge, S. Y. Fung, W. Jackson, R. Poe, Phys. Rev. Lett. 23, 994 (1969).

108. P. G. Hoyer, Lawrence Berkeley Lab, private communication.